PFC/RR-86-13

DOE/ET-51013-184
UC20

ION AND ELECTRON PARAMETERS IN THE ALCATOR C TOKAMAK SCRAPE-OFF REGION

A. S. Wan

May 1986

Plasma Fusion Center
Massachusetts Institute of Technology
Cambridge, Massachusetts 02139 USA

ION AND ELECTRON PARAMETERS IN THE ALCATOR C TOKAMAK SCRAPE-OFF REGION

Alan Szu-Hsin Wan

B.S.N.E., University of Michigan
(1980)

Submitted to the
Department of Nuclear Engineering
in Partial Fulfillment of the Requirements
for the Degree of
DOCTOR OF SCIENCE
at the
MASSACHUSETTS INSTITUTE OF TECHNOLOGY
May 1986

Signature of Author 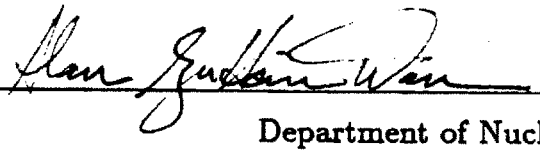
Department of Nuclear Engineering
May 1986

Certified by 
Professor Ronald R. Parker
Thesis Supervisor

Certified by 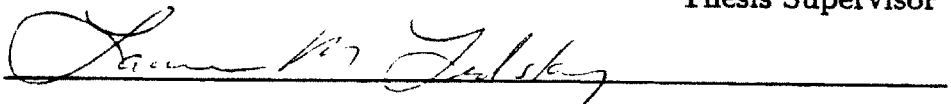
Professor Lawrence M. Lidsky
Thesis Reader

Accepted by _____
Professor Allen F. Henry
Chairman, Departmental Graduate Committee

ION AND ELECTRON PARAMETERS IN THE ALCATOR C TOKAMAK SCRAPE-OFF REGION

by

Alan Szu-Hsin Wan

Submitted to the Department of Nuclear Engineering
on May 21, 1986 in partial fulfillment of the
requirements for the Degree of Doctor of Science
in Nuclear Engineering

ABSTRACT

Janus is a bi-directional, multi-functional edge probe used to diagnose the ion and electron parameters in the Alcator C tokamak scrape-off region. Two mirror image sets of diagnostics are aligned to face the electron and ion sides (as defined by the plasma current, $\underline{I}_p$) along magnetic field lines. Each set of diagnostics consists of a retarding-field energy analyzer (RFEA), a Langmuir probe, and a calorimeter. The RFEA can alternatively sample both the ion and electron parallel energy distribution functions during a tokamak discharge. From the Langmuir probe, one can infer electron temperature, density, and the plasma floating potential. Simple Langmuir probe theory is found to yield the best agreement between the measured Langmuir probe characteristics and the RFEA-inferred T_e. The calorimeter independently detects the total parallel heat flux incident to an electrically floating plate. The measured sheath transmission coefficient, however, is typically lower than the theoretically predicted value by a factor of ~ 3. Together these diagnostics enable detailed, localized edge plasma characterization on Alcator C.

Large electron side/ion side parameter asymmetries were observed. Higher ion and electron temperatures and densities at the probe location occur on the electron side when the toroidal field ($\underline{B}_t$) is antiparallel to $\underline{I}_p$. The direction of $\underline{B}_t$ with respect to $\underline{I}_p$, and variations of the plasma in-out positions, change the magnitude of the asymmetry. Possible directional asymmetry mechanisms include poloidally asymmetric perpendicular diffusion and parallel flow. T_i is always greater than or equal to T_e. Minor equipartition contribution causes weakly coupled ion and electron energies. Large anomalous perpendicular conduction is necessary to balance the dominant parallel convection and compression losses for both the ion and electron species. During an ICRF fast wave experiment, evidence of direct edge heating in the immediate vicinity of the antenna is observed. Increasing rf power spreads the heating throughout the edge region, forcing flat temperature profiles. Observation of increasing high-Z impurities can be attributed to the increase in physical sputtering rate at both the antenna's Faraday shields and the limiter surfaces.

Thesis Supervisors:

Ronald R. Parker, Professor of Electrical Engineering, M.I.T.
Tien-Fang Yang, Senior Staff Scientist, Plasma Fusion Center, M.I.T.
Bruce Lipschultz, Principal Staff Scientist, Plasma Fusion Center, M.I.T.

Thesis Reader:

Lawrence M. Lidsky, Professor of Nuclear Engineering, M.I.T.

ACKNOWLEDGMENT

Many people have assisted me at various time, on various issues, in guiding me through my stay at M.I.T. It is a pleasure to acknowledge their support and friendship.

Dr. Ted Yang took me on since my first day of graduate school. His constant faith and guidance during the whole thesis research period guided and inspired me through the good and bad times. Dr. Bruce Lipschultz supported and advised me during my experimental period on Alcator C. He helped transform me into a genuine "experimentalist." Prof. Ron Parker served as my thesis supervisor and Prof. Larry Lidsky as my thesis reader. Their feedbacks and criticisms helped steer me toward the completion. Prof. Ian Hutchinson is always available to answer my questions. His insight into the edge plasma phenomena is unparalleled. Albe Dawson took time from her busy schedule to help edit my thesis.

I wish to thank Professors Jeff Friedberg and Dieter Sigmar who joined Prof. Hutchinson to form my defense committee. I would also like to thank the staff physicists of Alcator C for their continuous help and insightful questions, especially Drs. Jim Terry, Catherine Fiore, Scott McDermott, Earl Marmer, Steve Wolfe, Miklos Porkolab, and Martin Greenwald.

The best companions of a frustrated graduate student are his fellow graduate students. All the past and present students have helped me one way or another, whether it is answering a question, or lending a helping hand, their contributions and friendship are among the primary factors in surviving through the years of agony and transform this thesis into a fun and learning experience. The constant support of Dr. Brian LaBombard is especially appreciated. Brian not only provided the Langmuir probe hardware and analysis software, together we spent long hours puzzling over the peculiar edge phenomena on Alcator C. Many of the physics interpretations of this thesis are the by-products of our

brain storms. Special thanks also go to Dr. Herb Manning, Tom Shepard, and John Moody for providing the necessary data for analyzing ICRF discharges.

Many people helped me to design and build my experiment. Bob Childs taught me the importance of keep "clean" and personally took care of the diagnostics in alignment and maintenance. Guy Pollard, Paul Dozois, and Mark Iverson built most of the probe. The tungsten components are made by Prospect Tool and Die Co., Inc., and the alumina pieces are made by Ceramics Grinding Co. The Alcator electronics shop built all the electronics with speed and craftsmanship.

The running of a large experiment such as Alcator C requires a total team effort. Frank Silva and Charley Park provide the leadership in keeping the machine running reliably. Scott MeDermott, Dave Gwinn, and Bruce Lipschultz served as the chief machine operators during my tenure on Alcator C.

No word can describe my love and gratitude to my parents, my fiancée, Ellen, and my family. The lifelong encouragement of my parents is the main reason that led me to this goal. Ellen provides a constant source of love and moral support throughout the difficult period of this thesis. She also served as my chief graphics consultant. Without my family I would not be where I am today. It is to them that this thesis is dedicated.

TABLE OF CONTENTS

LIST OF FIGURES

Chapter 4. Operation and Data Reduction

Chapter 5. RFEA and Langmuir Probe data

Chapter 8. Calorimeter Data and Analysis

Chapter 9. Effect of ICRF on the Edge Plasma

LIST OF TABLES

CHAPTER 1

INTRODUCTION

In the process of reaching toward commercial realization of fusion reactors, the role of the edge plasma becomes more and more prominent as each new experimental device reaches for higher and higher density, temperature, and confinement time. The edge plasma is defined as the buffer region between the core (or bulk) plasma and the vacuum wall. It is a region in which the plasma first intersects a solid material surface. It is also a region in which the primary fuel enters the experimental configuration. Thus the edge plasma is a complex region governed by a variety of different physics processes, including plasma processes, molecular and atomic processes, and plasma-surface interactions.

The separation between the bulk plasma and the edge plasma can be achieved by using either mechanical or magnetic techniques. These two techniques are illustrated in figure 1.1. The mechanical scheme employs solid material apertures, or limiters, to limit the bulk plasma dimension. The magnetic scheme uses magnetic divertors to create localized magnetic perturbations to the normal magnetic topology and generate a separatrix surface. All field lines outside of this separatrix surface will eventually be diverted into a separate vacuum chamber where they intersect a target plate. Typically the divertor-controlled discharges run at higher edge temperatures and lower densities as compared to the limiter-controlled discharges. Therefore the physics processes governing the edge plasma are different for each of the operating scheme.

Regardless of the operating scheme, the presence of a solid material interface creates a strong perturbation to the edge plasma. Appendix A describes some of the processes occurring at this plasma-material interface which can be categorized into three mechanisms: recycling, low-Z, and high-Z impurity release mechanisms. An excellent review is given by McCracken and Stott[1].

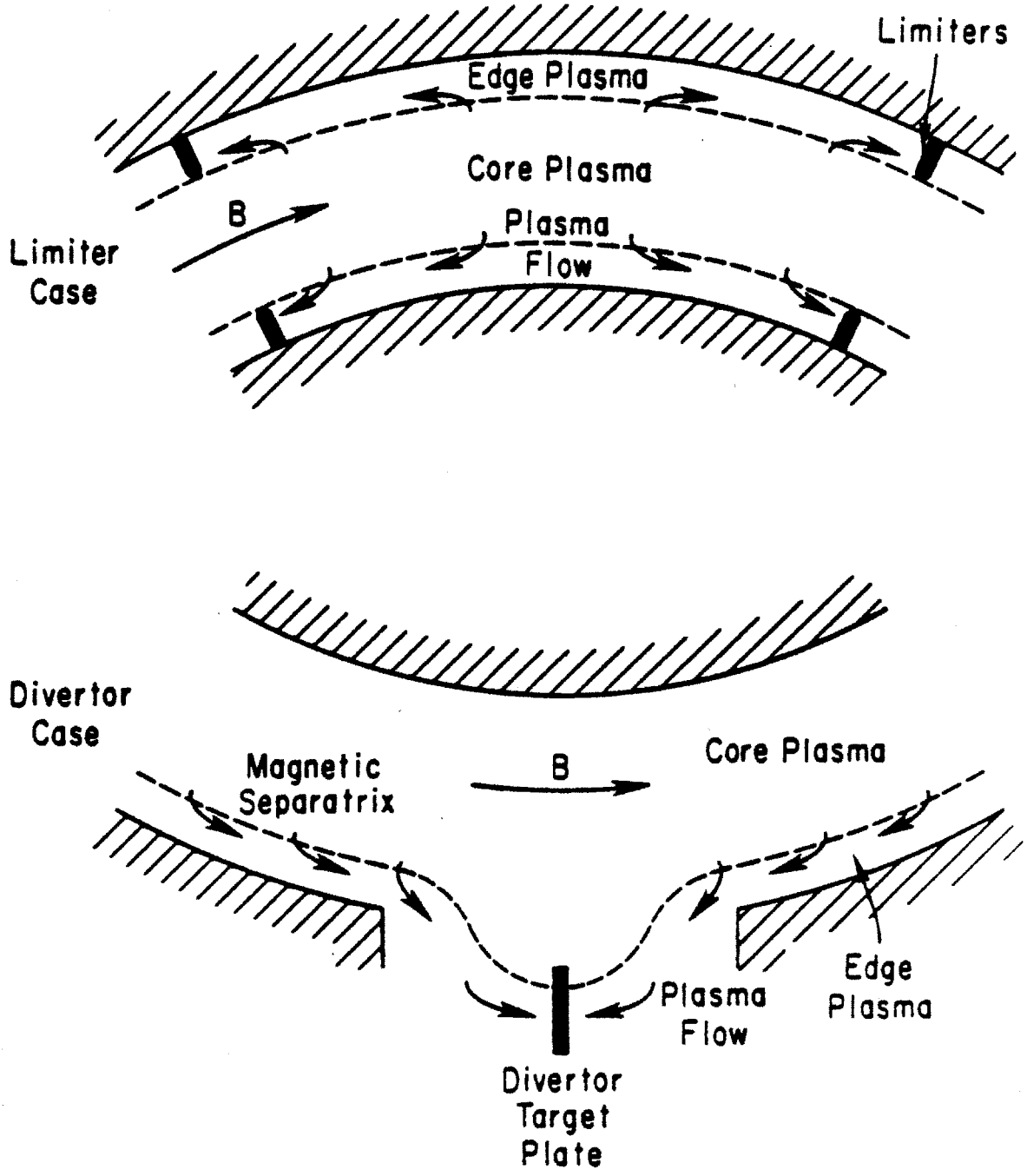

Figure 1.1 Magnetic divertor and mechanical limiter configurations.

Recycling can be defined as the processes which allow a fuel ion incident on a wall surface to return to the plasma. These processes are strongly influenced by the incident ion energy and the target conditions. Typically the re-emitted particles are neutrals possessing different energies than their initial incident energies. By introducing additional fuel particles back into the edge plasma, recycling would have a major impact on the overall particle and energy balances in this region.

Oxygen and carbon are the two most populous low-Z impurities in a typical fusion device. Oxygen is present due to the abundance of water molecules in air. Carbon is present due to the difficulty of purging carbon once it is introduced into the experimental system. These low-Z gases are adsorbed onto wall surfaces by either chemical or Van der Waal forces. They are released by different desorption processes such as thermal, particle, or chemical desorptions.

During the early days of tokamak experiments, the low-Z impurities were the dominant impurities in the edge plasma. It was believed that the presence of low-Z gases helped in achieving higher core plasma temperatures since fully stripped low-Z ions would increase the Spitzer resistivity which results in better bulk heating. However, low-Z particles ionize at low plasma temperatures. Thus regions near the limiter typically have lower temperature due to the large abundance of partially striped low-Z impurities which radiate away a large fraction of the local energy. This causes the current profile to peak on axis and leads to unfavorable changes in the MHD stability properties of the discharge[1]. Using various vacuum techniques such as discharge cleaning we can reduce the population of low-Z impurities. This pre-experimental cleaning has allowed tokamaks to operate at much higher densities than before.

The high-Z impurities are either wall or limiter materials. Their release mechanisms are different than the two previously described mechanisms, and include processes such as evaporation, sputtering, arcing and blistering. It is these high-Z impurities that ultimately dominate overall energy balance pictures for

reactor-relevant tokamak conditions. Extrapolating the high-Z impurity concentration of present day experiments to future reactor conditions, the energy loss due to line and bremsstrahlung radiation could exceed the fusion energy released, thus quenching the burn[2]. In addition, partially stripped high-Z impurities tend to radiate away most of the energy near the center of the core plasma, yielding a hollow temperature profile which inadvertently would also generate instabilities leading toward plasma disruptions.

In addition to the different types of particles entering the edge plasma due to plasma-surface interactions, the fuel particles also pass through the edge region. Gases are typically puffed through a local access port into the edge region where they are ionized while drifting toward the core plasma region. The presence of these fuel particles along with the particles released by plasma-surface interactions create a complicated environment for the plasma diffusing into the edge from the bulk plasma. Appendix B describes some of the relevant molecular and atomic processes that may occur in the edge plasma.

The performance of the core plasma depends largely on the behavior of the edge plasma. By controlling the edge plasma by reducing the ill effects the plasma-surface interactions, better core plasma parameters can be achieved. For example, utilizing a "closed" poloidal divertor configuration, a high confinement (H-mode) operating regime was discovered during neutral beam injection[3]. The attainment of H-mode can be correlated with recyling phenomena. Due to the increased confinement, edge recycling is reduced which leads to a hotter, less dense edge plasma. Forced edge cooling by enhanced recycling or by the injection of impurities would quench the H-mode.

Another prominent example is the occurrence of Marfes, which is the manifestation of thermal instability when localized regions of the edge plasma enter a radiation-dominated mode. The Marfe phenomenon has a threshold that is proportional to $\bar{n}/I_p$, where $\bar{n}$ is the line averaged electron density and I_p is the plasma current[4,5].

As discussed in Appendix A, the plasma-surface interactions are strongly dependent on the local plasma parameters. Until the past few years, the edge plasma region was a poorly diagnosed area as scientists concentrated on monitoring only the core plasma parameters. As the importance of the edge plasma becomes recognized, the task of monitoring the edge plasma becomes more and more crucial.

The focus of this thesis is to develop an edge plasma diagnostic capable of monitoring most of the relevant information that governs plasma-surface interactions. By applying this diagnostic on Alcator C, we can perform a detailed study of the edge plasma as a function of core plasma parameters. Furthermore, by coupling our findings with other Alcator C measurements we can study the correlation of the measured edge parameters with the observed impurity behaviors that can be connected to plasma-surface interaction mechanisms.

1.1 Alcator C

The Alcator C tokamak is a compact toroidal device characterized by operating at high magnetic field. Figure 1.2 shows a cartoon of the device along side of a "standard" 2-meter man. The main difference between Alcator C and other tokamaks lies in the toroidal magnet design. Instead of discrete TF coils, Alcator C employs the "Bitter plate" magnet design which uses a continuous winding of copper plates in the toroidal direction. The plates are interlocked and reinforced with stainless steel, allowing them to withstand the large forces while operating at high magnet field. Furthermore, the entire magnet is immersed in a liquid nitrogen Dewar. Since the copper resistivity reduces by factor of 7 when cooled to liquid nitrogen temperature, the total electrical requirement of Alcator C is drastically reduced, even with the expense of the refrigeration requirement of using liquid nitrogen as coolant.

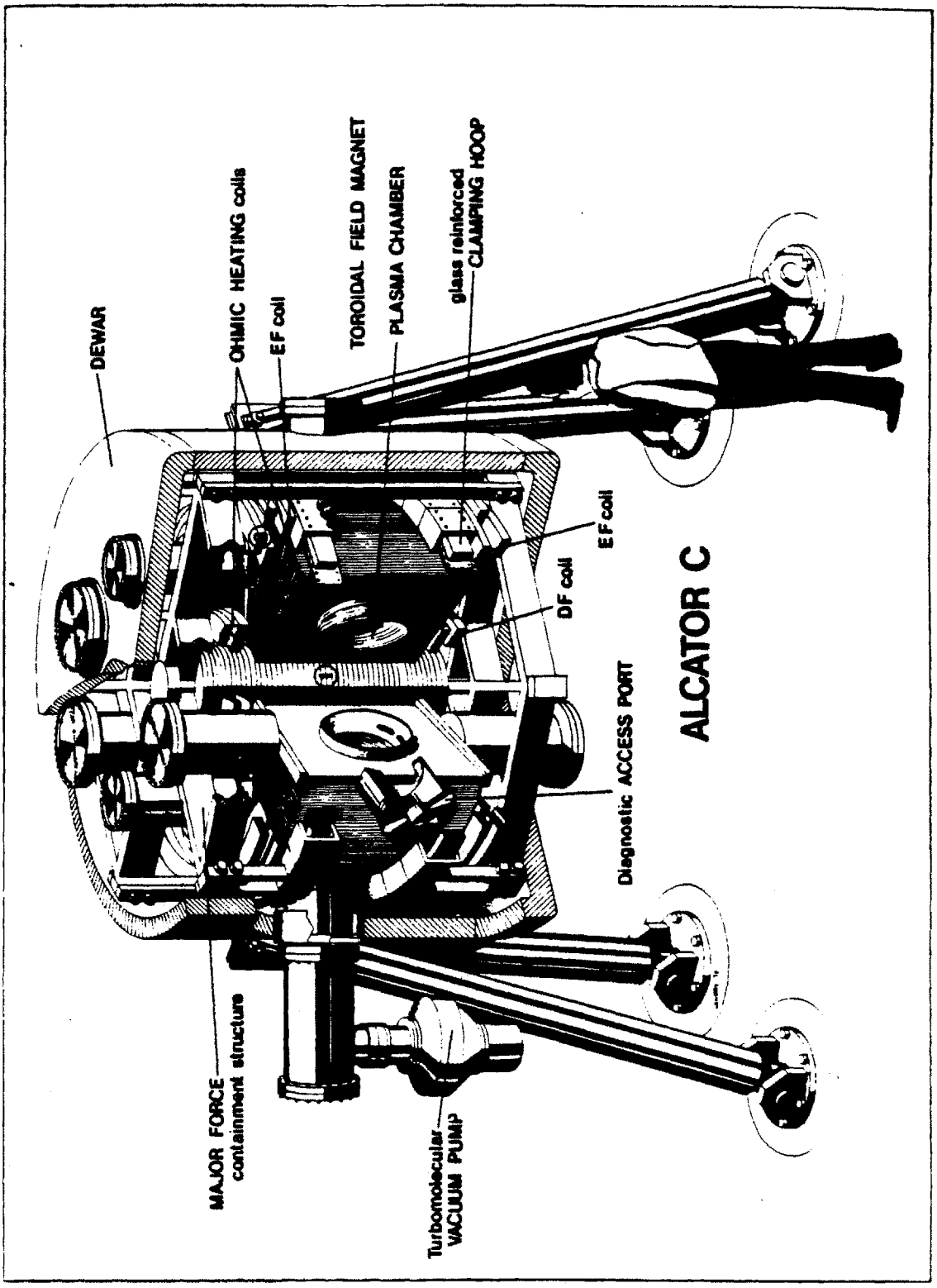

Figure 1.2 Alcator C.

By operating at high field, and by enforcing strict vacuum requirements, Alcator C can operate in a wide range of parameters, Table 1.1 summarizes typical and maximum operating parameters of Alcator C.

Major experiments carried out on Alcator C include RF heating and current drive[6,7], pellet injection[8,9], impurity injection and transport analysis[9,10]. By injecting frozen hydrogen pellets into the plasma and raising the central density, Alcator C became the first device to surpass the Lawson Criterion for breakeven ($n\tau_E$) in 1983. It also has the distinction of demonstrating the current drive at a higher core plasma density than any other experiment.

1.2 Thesis Outline

This thesis is divided into 5 major sections. The first section provides the introduction and background. In the next chapter, the relevant theoretical background is discussed and will be used in later chapters. The second section describes the instrumentation aspect while chapter 3 discusses the instruments and chapter 4 discusses the operational and analytical techniques. Most of the experimental data and their interpretation are presented in section III. Chapter 5 contains the data from two of the instruments, the Langmuir probe and the retarding-field energy analyzer, as a function of various core plasma parameters. Chapters 6 and 7 present feasible explanations to two commonly observed edge phenomena on Alcator C. Chapter 8 presents the data and interpretation of the other instrument used, the calorimeter. In section IV (chapter 9) we present a specific example of plasma-surface interactions on Alcator C. Through correlation with other measurements, a consistent picture of the Alcator C edge plasma during the ICRF heating experiment is presented. Finally section V (chapter 10) summarizes the findings and offers the author's opinion on needed future activities.

Alcator C Parameters	Standard Values	Range of Values
R_{major}	64 cm	$57 - 71$ cm
r_{minor}	16.5 cm	$10 - 16.5$ cm
$B_{toroidal}$	8 tesla	$5.5 - 13$ tesla
I_p	400 kA	$100 - 700$ kA
$n_e(central)$	2×10^{14} cm^{-3}	$0.1 - 20. \times 10^{14}$ cm^{-3}
T_e	1500 eV	$1000 - 3000$ eV
T_i	1100 eV	$500 - 2000$ eV

Table 1.1 Typical and range of operating parameters of Alcator C.

References

[1] McCracken, G. M., Stott, P. E., "Plasma-Surface Interactions in Tokamaks," *Nucl. Fusion*, **19** 7, 889 (1979).

[2] Meade, D., *Nuclear Fusion* **14**, 289 (1974).

[3] Wagner, F., Keilhacker, M., and the ASDEX and NI Teams, "Importance of the Divertor Configuration for Attaining the H-Regime in ASDEX," *J. Nucl. Mat.* **121**, 103–113 (1984).

[4] Lipschultz, B., LaBombard, B., Marmer, E. S., Pickrell, M. M., Terry, J. L., Watterson, R., Wolfe, S. M., "MARFE : An Edge Plasma Phenomenon," *Nucl. Fusion* **24**, 977 (1984).

[5] LaBombard, B., "Poloidal Asymmetries in the Limiter Shadow Plasma of the Alcator C Tokamak," M.I.T. Doctoral Thesis, April 1986.

[6] Knowlton, S., *et al.*, 11^{th} Int'l. Conf. on Plasma Physics and Controlled Nucl. Fusion Research, Budapast, Hungary (Sept 1985).

[7] Porkolab, M., *et al.*, "Lower Hybrid Heating and Current Drive, and Ion Cyclotron Heating Experiments on the Alcator C and Versator II Tokamaks," 10^{th} Int'l. Conf. on Plasma Physics and Controlled Nucl. Fusion Research, London (September 1984).

[8] Greenwald, M., Gwinn, D., Milora, S., Parker, J., Parker, R., Wolfe, S., and Alcator Group, "Energy Confinement of High-Density Pellet-Fueled Plasmas in the Alcator C Tokamak," *Phys. Rev. Let.* **53**, 352 (1984).

[9] Terry, J. L., *et al.*, "Observation of an Increase in Impurity Particle Confinement After Injection of Large Pellets," *Bull. Amer. Phys. Soc.* **30**, paper 3F4, 1413 (Nov 1985).

[10] Marmer, E. S., Rice, J. E., Terry, J. L., Seguin, F. H., "Impurity Injection Experiments on the Alcator C Tokamak," *Nucl. Fusion* **22** (12), 1567 (1982).

CHAPTER 2

THE EDGE PLASMA

Alcator C is a limiter-controlled device, employing two sets of full-poloidal ring limiters to create the buffer edge region between the core plasma and the stainless steel vacuum wall. Particle and energy fluxes diffuse perpendicularly from the core plasma into the edge plasma and are lost along the magnetic field lines to the limiters. This simple picture of the edge plasma is presented in figure 2.1.

In reality the edge plasma is a complex region. A complete model of the edge plasma must properly balance the plasma, neutral, and impurity particle, momentum, and energy sources and sinks. Thus plasma, atomic, molecular, and surface physics effects must be considered. It is a difficult task and much effort has been devoted to the modelling of the edge plasma[1,2,3,4,5].

The goal of this thesis is to provide an experimental investigation of the edge plasma phenomena. In light of the difficulty of accurately modelling the edge plasma, the author will instead employ simple theoretical arguments to justify the observed phenomena at the Alcator C edge plasma. This chapter presents the background of some of the theories that will be used in the later parts of this thesis. Section 2.1 presents a summary of the physics behind the formation of a stable plasma sheath. A simple model of the edge plasma that considers both the radial and parallel terms is discussed in section 2.2. Finally, the entire edge plasma is strongly perturbed by virtue of inserting a large probe into the region. Section 2.3 discusses some of the possible perturbing effects of a large probe and techniques of recovering the unperturbed parameters using a theorem by Stangeby.

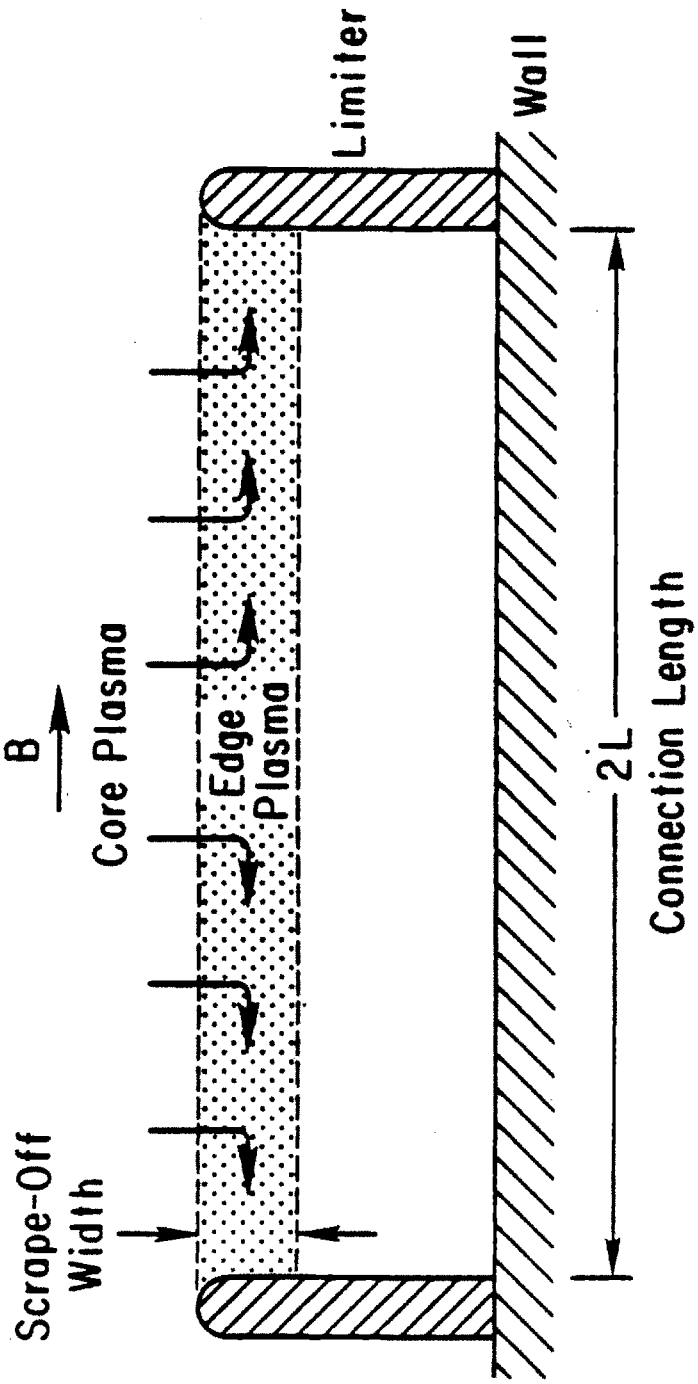

Figure 2.1 A simple picture of the edge plasma.

2.1 The Plasma Sheath

What will happen when an electrically isolated solid is suddenly immersed into a plasma? In the beginning, both the electrons and ions will strike the solid at their random flux values equalling

$$\Gamma_{\parallel}^{e,i} = \frac{1}{4}\, n_{e,i}\, \bar{C}_{e,i}, \qquad (2.1),$$

$$\text{where} \quad \bar{C}_{e,i} = \sqrt{\frac{8\,kT_{e,i}}{\pi\, m_{e,i}}}. \qquad (2.2)$$

$\bar{C}$ is the averaged velocity; T and n are the particle's temperature and density respectively; m_e and m_i are the electron and ion masses; and k is the Boltzmann constant. By quasineutrality, $n_e = Zn_i$ to a high order, where Z is the ion charge state. (n_p, defined as the plasma density, will often be used in place of n_e and Zn_i for convenience). Unless $T_i \gg T_e$, the random electron flux will greatly exceed the ion flux due to the large mass difference between the electrons and ions. Thus the solid will quickly gain a negative charge after the initial contact with the plasma. In order to preserve the neutrality of the plasma, the solid will develop a negative potential difference between the solid and the plasma potential. This potential difference is defined as the sheath potential, V_{sheath}. And the region where the potential drop occurs is called the sheath region. An excellent review of the sheath theory is presented by Stangeby[6].

A crude estimate of V_{sheath} can be arrived by modifying the electron flux by the Boltzmann factor $\exp(eV_{sheath}/kT_e)$, where $q_e \equiv$ electron charge $= -e$. Equating the modified electron flux and the ion flux, for an electrically floating solid, we get

$$\frac{1}{4}\, n_p\, \bar{C}_i = \frac{1}{4}\, n_p\, \bar{C}_e\, e^{eV_{sheath}/kT_e}. \qquad (2.3)$$

Thus

$$eV_{sheath} = \frac{kT_e}{2} \ln \frac{m_e T_i}{m_i T_e}. \tag{2.4}$$

Assuming a hydrogen plasma and $T_i = T_e$, $eV_{sheath}/kT_e \simeq -3.8$.

From a simplistic point of view, both the ions and electrons retain their Maxwellian distribution functions before entering the sheath region. In traversing the sheath, the majority of the electrons are repelled before striking the solid surface. Electrons with sufficiently high energies to allow them to overcome the potential barrier will each lose an amount of energy equal to eV_{sheath}. In the meantime all ions entering the sheath region will reach the solid surface. Each ion will be accelerated by the negative sheath, picking up an energy equal to $eZ|V_{sheath}|$, where $q_i \equiv$ ion charge $= eZ$. Therefore, despite the fact that ions arrive at the solid carrying significantly more energy, in reality each ion only contributes its thermal energy toward the overall heat flux incident on the solid. The primary contributors to the overall heat flux are the electrons since they are the species that must maintain the negative sheath. So the electrons not only contribute their thermal energy, but they also add a component associated with the sheath potential. More detailed heat flux analysis will be discussed in Chapters 6 and 8.

How far does the sheath potential extend into the plasma? Detailed theoretical modelling shows that the sheath structure can be divided into two components: a localized sheath region and a presheath region which extends far into the plasma. The presheath effect will be treated later. But first let us obtain an approximate extent of the sheath by using a simple model. Since the majority of the electrons are repelled, inside the sheath region n_i dominates over n_e. Applying this approximation to the 1-D (x) Poisson's equation, we get

$$\frac{d^2 V(x)}{dx^2} = \frac{-e}{\varepsilon_0}\,(Z n_i(x) - n_e(x)), \tag{2.5}$$

$$\sim \frac{-e\,Z\,n_i(x)}{\varepsilon_0}, \tag{2.6}$$

where $V(x)$ is the potential as a function of parallel position x, and ε_0 is the free space permittivity. For simplicity $Z = 1$ is used for this analysis. The ion current, I^i, is defined as a constant and equal to

$$I^i \equiv e\,n_i(x)\,v_i(x), \tag{2.7}$$

$$\text{where } v_i(x) = \sqrt{\frac{2\,e\,V(x)}{m_i}}. \tag{2.8}$$

Assuming the flow is space-charge-limited, or $\frac{dV}{dx}\,|_{x=0} = 0$, and further assuming $V(x = 0) = 0$, we can solve equation (2.6) and obtain

$$I^i = \frac{4\,\varepsilon_0\,\sqrt{2e/m_i}}{9\,\delta^2_{sheath}}\,|V_\delta|^{\frac{3}{2}}, \tag{2.9}$$

where δ_{sheath} is the sheath thickness, and V_δ is the potential difference over δ_{sheath}. Equation (2.9) is also known as the Child-Langmuir Law[7] for current in a space-charge limited diode.

From equation (2.1) we have a crude estimate of $I^i \sim e\Gamma^i_\parallel$. Using equation (2.4), we can approximate V_δ as V_{sheath}, and solve for δ_{sheath}. We get

$$\delta_{sheath} \approx 1.255\,(f_s)^{\frac{3}{4}}\,(\frac{T_e}{T_i})^{\frac{1}{4}}\,\lambda_{Debye}, \tag{2.10}$$

$$\text{where } \lambda_{Debye} = \text{electron Debye length,}$$

$$\equiv \sqrt{\frac{\varepsilon_0\,T_e}{n_e\,e^2}}. \tag{2.11}$$

The coefficient f_s equals $|eV_{sheath}/kT_e|$. Assuming a hydrogen plasma and $T_e = T_i$, $\delta_{sheath} \approx 3.4\,\lambda_{Debye}$. Despite the crudity of this model, the δ_{sheath} value obtained gives us an order of magnitude estimate of the thickness of the sheath region. Including the electron density terms in equation (2.5) would yield a slightly larger δ_{sheath}. Using a more complete model, Self[8] estimates the sheath thickness to be on the order of $10\,\lambda_{Debye}$.

A fundamental characteristic of the behavior of a plasma is its ability to shield out any applied potential if the system dimension is much larger than the electron Debye length. However, the presence of the sheath potential has a strong effect on the plasma beyond the sheath region. This effect is called the presheath effect and was first derived by Langmuir[9] and Bohm[10]. In their treatment they assumed monoenergetic ions with initial velocity v_1. Electron distribution is Maxwellian. Integrating the distribution functions over the velocity space, we can obtain expressions of n_i and n_e as a function of the potential $V(x)$. By substituting these density expressions into equation (2.5) we arrive at the following form of Poisson's equation:

$$\frac{d^2\eta}{d\xi^2} = n_p\left[(1+\eta\,u_1^{-2})^{-\frac{1}{2}} - e^{-\eta}\right], \tag{2.12}$$

$$\text{where} \quad \eta \equiv \frac{-eV(\xi)}{kT_e}, \tag{2.13}$$

$$u_1 \equiv v_1\sqrt{\frac{m_i}{2\,kT_e}}, \quad \text{and} \tag{2.14}$$

$$\xi \equiv x\sqrt{\frac{n_p\,e^2}{\epsilon_0\,kT_e}}. \tag{2.15}$$

Equation (2.12) can be solved by using an integration factor $\frac{d\eta}{d\xi}$, and assume $\frac{d\eta(\xi=0)}{d\xi} \sim 0$. Finally, expanding the solution near the origin $\eta = 0$, we obtain the necessary inequality in order for equation (2.12) to have a solution:

$$u_1 \geq \frac{1}{\sqrt{2}}, \tag{2.16}$$

$$\text{or} \quad v_1 \geq \sqrt{\frac{kT_e}{m_i}}. \tag{2.17}$$

Equation (2.17) states that in order for a stable sheath to form, the ions must be drifting toward the solid surface with a velocity equaling the ion sound speed, C_s ($\equiv \sqrt{kT_e/m_i}$), at the sheath edge. This effect is also known as the Bohm Sheath Criterion. For $T_i \neq 0$, the sound speed is defined as

$$C_s \equiv \sqrt{\frac{k(T_e + T_i)}{m_i}}. \tag{2.18}$$

For analysis of waves in plasmas, C_s in equation (2.18) includes an adiabatic index γ_a in front of T_i, where $gamma_a$ ranges from 1 to 3. It is not clear what value of $gamma_a$ should be used. For this thesis C_s is defined with $\gamma_a = 1$.

Using kinetic theory formulation, where the ion velocity distribution function, f_i, is allowed to be general, the Bohm Sheath Criterion is generalized to be

$$\int_0^\infty \frac{f_i(v_z)}{v_z^2}\, dv_z \leq \frac{m_i}{T_e}, \tag{2.19}$$

where v_z is the parallel ion velocity. From the Bohm Sheath Criterion, we can obtain an approximate expression for the ion and electron fluxes:

$$\Gamma_\parallel^e \approx \Gamma_\parallel^i \approx \frac{1}{2} n_p C_s. \tag{2.20}$$

The "exact" plasma sheath problem has yet to be solved. Thus far Emmert and co-workers[11] have offered the closest approach by solving the plasma-sheath equation for a collisionless plasma with arbitrary ion temperature in plane geometry. The electron density still follows the Maxwellian distribution. The ion densities are derived by assuming the presence of a source function $S(E_x, x)$, which depends on both the parallel position x and parallel energy E_x. E_x is a constant of motion defined as

$$E_x(x) \equiv \frac{1}{2} m_i v_x(x)^2 + q_i V(x). \tag{2.21}$$

Substituting the ion and electron expressions into the Poisson's equation, they obtain the integral-differential form of the plasma-sheath equation:

$$\begin{aligned} \frac{d^2 V(x)}{dx^2} &= \frac{e n_p(x=0)}{\varepsilon_0} e^{eV(x)/kT_e} \\ &\quad - \frac{2 q_i Z}{\varepsilon_0} \int_0^L dx' \int_{E_x(x=0)}^{\infty} dE_x \frac{S(E_x, x')}{v_x(E_x, x)}, \end{aligned} \tag{2.22}$$

where L is the distance to the solid surface. The ion distribution function and the particle and energy fluxes to the solid are all independent of the function $S(E_x, x)$. Figure 2.2 plots the resultant $e|V_{sheath}|/kT_e$ as a function of $\tau(\equiv T_i/T_e)$. The same parameter obtained by equation (2.4) is also plotted for comparison.

By solving for the spatial dependence of $V(x)$, a spatial profile of the evolution of the ion distribution function can be obtained using Emmert's kinetic model. Figure 2.3 plots the ion distribution functions at four spatial positions corresponding to $x = 0$, at the sheath edge, at the wall, and at an intermediate point between $x = 0$ and the sheath edge. The dashed line traces out a shifted half Maxwellian at the sheath edge, offset by the ion sound speed. The

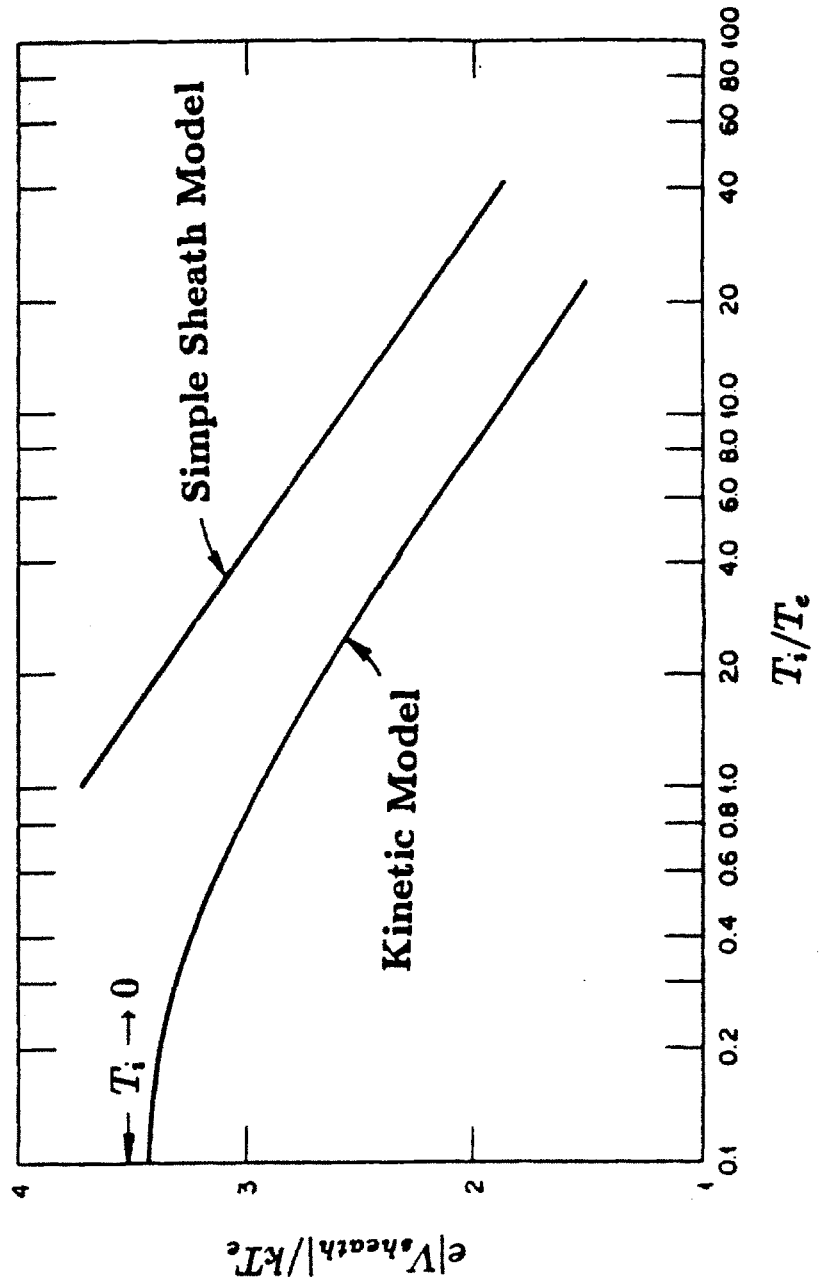

Figure 2.2 Comparisons of $e|V_{sheath}|/kT_e$ using Emmert's kinetic model and the simple sheath model.

difference between the two distribution functions due to presheath effect is also incorporated into Emmert's model as multipliers which depend on T_i/T_e. The application of Emmert's solution in modelling the edge plasma will be described in later sections.

The plasma-sheath problem is a nontrivial problem. By incorporating in the finite ion temperature, Emmert's model takes a step toward simulating the edge plasma of fusion devices. However, for high edge density devices such as Alcator C, the edge plasma could be collisional and Emmert's model would eventually fail. Furthermore, Emmert's model fails to properly account for the source diffusion in and out of the sampling flux tube, where the source function is derived from the unperturbed distribution function far away from the probe surface. In reality, particles diffuse into the flux tube at the unperturbed distribution function while diffusing out of the flux tube at the localized, accelerated distribution. More extensive modelling of the plasma-sheath problem is currently under way[12] in an attempt to provide more thorough understanding of the plasma in both the presheath and sheath regions.

2.2 A Simple Edge Plasma Model

The Alcator C edge plasma is a complicated region with parameter variations in the radial[13,14], poloidal[13,14], and toroidal[15,16] directions. It is difficult to model these asymmetries while including the various physics phenomena. Instead this thesis intends to explore the edge plasma experimentally. A previous study using a full poloidal array of Langmuir probes at three different radii has been conducted on Alcator C[13] to examine the radial and poloidal variations. This thesis concentrates on examining more edge parameters, both ions and electrons, located at one poloidal location while monitoring parallel and antiparallel to the field lines simultaneously.

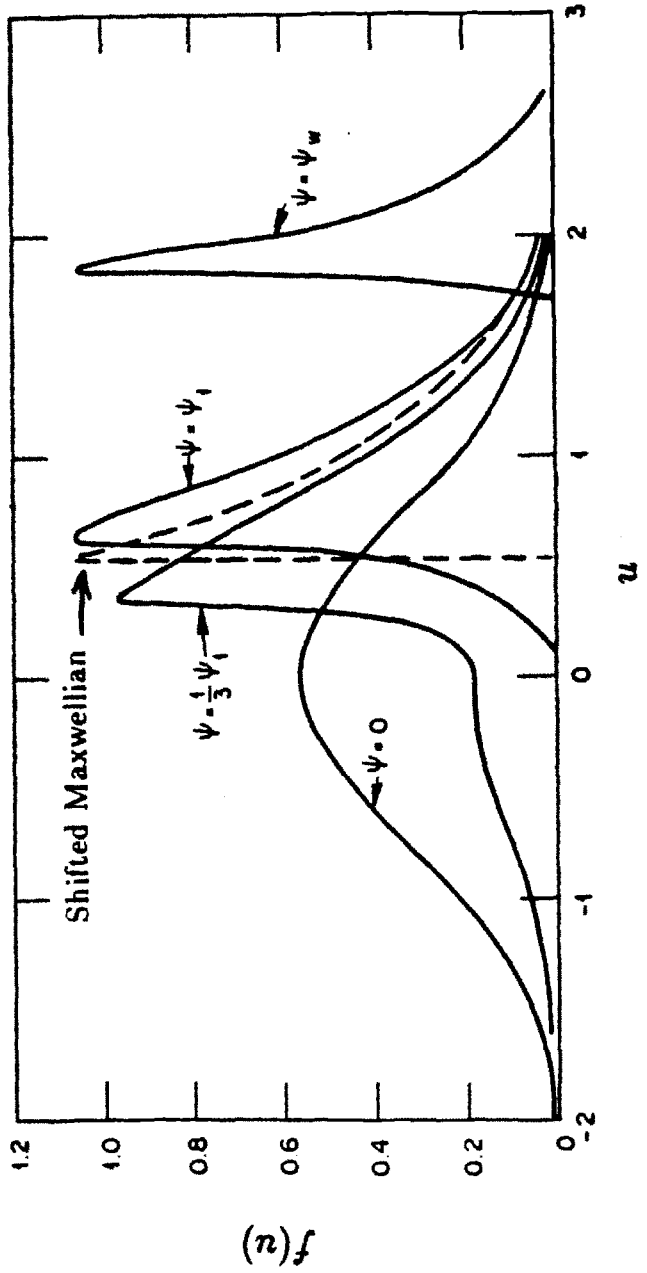

Figure 2.3 The ion distribution function $f(u)$ vs u (equation (2.14)) at the center ($\Psi = 0$), somewhere between the center and the sheath edge ($\Psi = \Psi_{edge}/3$), at the sheath edge ($\Psi = \Psi_{edge}$), and at the wall ($\Psi = \Psi_{wall}$). $\Psi \equiv -eV(x)/kT_e$. The shifted half Maxwellian at the sheath edge is represented by the dashed line.

This section provides a simple edge plasma model that will be used in the later parts of this thesis in order to explain some of the observed edge phenomena. The model includes the parallel (or toroidal) contributions by using the results of Stangeby[6] and Emmert[11] and radial contributions by approximating the perpendicular transport coefficients. The first three subsections will discuss the continuity, momentum, and energy equations. The fourth subsection will briefly examine the validity of the fluid approximation.

2.2.1 Continuity Equation

A simple model of the edge plasma is presented in figure 2.1. In this model, the particles diffused into the edge plasma region (or scrape-off layer) are all lost via parallel convection to the limiter surfaces. In reality there are also particle sources in the edge region. Therefore the steady state continuity equation can be written as

$$\nabla \cdot \underline{\Gamma} = S_p, \tag{2.23}$$

where S_p is the particle source. Typically the dominating source is due to ionization of background neutrals by various impact ionization and dissociation processes. A more detailed description of these mechanisms is presented in Appendix B. Grouping all ionization mechanisms together, S_p can be represented by

$$S_p = n_p\, n_n \langle \sigma v \rangle_{ioniz}, \tag{2.24}$$

where n_n is the neutral density and $\langle \sigma v \rangle_{ioniz}$ is the total ionization rate coefficient.

$\underline{\Gamma}$ is the particle flux. A simplified representation of the parallel particle flux at the solid surface is given by equation (2.20). The kinetic model[11] replaces the factor of $\frac{1}{2}$ by a density reduction factor $f(\tau)$. $f(\tau) \sim 0.487$ at $T_i/T_e = 0$, and $f(\tau) \sim 0.798$ as $T_i/T_e \rightarrow \infty$. The parallel flux of equation (2.23) varies along field lines and can be expressed as

$$\Gamma_{\parallel}(x) \quad = \quad n_p \, v_{\parallel}, \tag{2.25}$$

where x is the distance along a field line. Both n_p and the parallel velocity $v_{\parallel}$ can vary along x. The perpendicular (or radial) particle flow can be approximated by using Fick's Law

$$\Gamma_{\perp} \quad = \quad \Gamma_r \quad = \quad -D_{\perp} \frac{\partial n_p}{\partial r}, \tag{2.26}$$

where $D_{\perp}$ is the perpendicular diffusion coefficient. Combining equations (2.24)-(2.26), the complete continuity equation becomes

$$\frac{\partial}{\partial x}\left(n_p \, v_{\parallel}\right) \; + \; \frac{\partial}{\partial r}\left(-D_{\perp} \frac{\partial n_p}{\partial r}\right) \quad = \quad n_p \, n_n \, \langle \sigma v \rangle_{ioniz}. \tag{2.27}$$

Using the kinetic model to express $\nabla \cdot \Gamma_{\parallel}$, we get

$$\frac{f(\tau) \, n_p \, C_s}{L_{\parallel}} \; - \; \frac{\partial}{\partial r}\left(D_{\perp} \frac{\partial n_p}{\partial r}\right) \quad = \quad n_p \, n_n \, \langle \sigma v \rangle_{ioniz}, \tag{2.28}$$

where $L_{\parallel}$ is defined as the parallel scale length.

If there are no momentum sources, for Alcator C's limiter setup $L_{\parallel}$ can be approximated as half the distance between the limiters. Furthermore, assuming

n_p as the only variable in minor radius with boundary conditions $n_p(r = a) = n_a$ and $n_p(r \to \infty) = 0$, where a is the minor radius, we can solve equation (2.28) for $n_p(r)$

$$n_p(r) = n_a\, e^{-(r-a)/\lambda_n}, \tag{2.29}$$

$$\text{where } \lambda_n = \text{density scrape-off length}$$

$$= \sqrt{\frac{D_\perp}{(f(\tau)C_s/L_\parallel) - n_n \langle\sigma v\rangle_{ioniz}}}. \tag{2.30}$$

The source term can be neglected if it is much smaller than the parallel loss term, yielding the criterion

$$\lambda_n = \sqrt{\frac{D_\perp L_\parallel}{f(\tau)\, C_s}}, \quad \text{if} \tag{2.31}$$

$$\frac{f(\tau)\, C_s}{L_\parallel} \gg n_n \langle\sigma v\rangle_{ioniz}. \tag{2.32}$$

Appendix B contains the $\langle\sigma v\rangle_{ioniz}$ values for various ionization processes. Assuming the dominating process is due to electron impact ionization of neutral hydrogen atoms, $\langle\sigma v\rangle_{ioniz} \approx 2 \times 10^{-8}\text{cm}^3/\text{s}$ for $10\text{eV} \leq T_e \leq 100\text{eV}$. Applying typical Alcator C edge conditions of $T_i \sim 25$ eV, $T_e \sim 15$ eV, and $L_\parallel \sim 67$ cm to equation (2.32), we get

$$n_n \leq 2.3 \times 10^{12}\ \text{cm}^{-3}. \tag{2.33}$$

Therefore as long as $n_n \ll 2.3 \times 10^{12}$ cm^{-3}, equation (2.31) is applicable. Edge neutral density is typically $\sim 10^{10} - 10^{11}$ cm-3. Unfortunately there is no edge

diagnostic available to measure the edge neutral density profile on Alcator C. Thus the validity of equation (2.31) is in question.

Assuming equation (2.31) holds, we can obtain a rough estimate of the perpendicular transport characteristic of the Alcator C edge plasma in terms of measurable parameters. The perpendicular diffusion coefficient is approximately

$$D_\perp = \frac{\lambda_n^2 C_s f(\tau)}{L_\parallel}. \tag{2.34}$$

Experimentally measured $\lambda_n \sim 0.4$ cm. Therefore $D_\perp \sim 7400$ cm^2/s. This value is several orders of magnitude greater than the neoclassical value. Typically in tokamaks bulk ion transport is about 5 times the neoclassical values while electrons behave anomalously[17]. However the edge transport is always anomalous[18,19]. Past experiments[20,21,22,23] have observed that the edge particle diffusion scales approximately to the Bohm diffusion coefficient

$$D_{Bohm} = \frac{625\ T_e\ (\text{eV})}{B\ (\text{tesla})}\ \ (\text{cm}^2/\text{s}), \tag{2.35}$$

where B is the magnetic field strength which ~ 8 tesla for routine Alcator C operation. $D_{Bohm} \sim 1172$ cm^2/s for typical Alcator C edge conditions. Therefore $D_\perp/D_{Bohm} \sim 5$.

2.2.2 Momentum Equation

In the edge plasma region, parallel (or toroidal) flow with flow velocity on the order of sound speed has been experimentally observed[24]. In modelling the parallel flow it is essential to study the momentum equation. And due to the mass difference, only the ion momentum equation needs to be considered. Taking

the first moment of the Vlasov-Boltzmann equation we obtain the complete ion momentum equation[25]

$$m_i n_i \left(\frac{\partial \underline{v}^i}{\partial t} + \underline{v}^i \frac{\partial \underline{v}^i}{\partial \underline{x}}\right) = -\nabla P_i - \nabla \cdot \underline{\underline{\pi}} + q_i n_i \left(\underline{E} + \underline{v}^i \times \underline{B}\right) - \underline{R} + \underline{S}_m, \quad (2.36)$$

where m_i, n_i, and q_i are the ion's mass, density, and charge. $P_i(= n_i T_i)$ is the total pressure; $\underline{\underline{\pi}}$ is the viscosity tensor; $\underline{R}$ is the mean change of momentum of the ions due to collisions with all other particles; and $\underline{v}^i$ is the ion mean velocity. $\underline{E}$ and $\underline{B}$ are the external electric and magnetic fields. $\underline{S}_m$ is the momentum source which can be described by[26]

$$\underline{S}_m = S_p m_i \left(\underline{v}^i - \underline{v}_0\right), \quad (2.37)$$

where S_p is the particle source function of equations (2.23) and (2.24), and $\underline{v}_0$ is the initial particle velocity as it enters the sampling flux tube.

Compared to $\nabla \cdot P_i$, the viscosity and collisional effects are negligible[27]. Since only the parallel component of equation (2.36) is investigated here, $\underline{v}^i \times \underline{B} = 0$. The parallel electric field term can be approximated by the presheath effect[26] described in section 2.1

$$q_i n_i E_{\parallel} \approx -kT_e \frac{\partial n_i}{\partial x}. \quad (2.38)$$

Finally, assuming the temperature profile along the x direction is constant and taking the steady state approximation of the parallel component of equation (2.36), we get

$$v_{\parallel}^{i}\,\frac{dv_{\parallel}^{i}}{dx} = -\frac{kT_i}{n_i m_i}\,\frac{dn_i}{dx} - \frac{kT_e}{n_i m_i}\,\frac{dn_i}{dx} - \frac{S_p}{n_i}\left(v_{\parallel}^{i} - v_0\right),$$

$$= -\frac{C_s^2}{n_i}\,\frac{dn_i}{dx} - \frac{S_p}{n_i}\left(v_{\parallel}^{i} - v_0\right). \qquad (2.39)$$

Defining $M \equiv v_{\parallel}^{i}/C_s$ and $M_0 \equiv v_0/C_s$, equation (2.39) and the continuity equation can be reduced[26] to

$$\frac{n(M)}{n_0} = \frac{1}{1 + M^2 - M_0 M}, \quad \text{and} \qquad (2.40)$$

$$\frac{dM}{dx} = \frac{S_p}{n_0 C_s}\,\frac{(1 + M^2 - M M_0)^2}{(1 - M^2)}, \qquad (2.41)$$

where $n_i = n_0$ at $M = M_0$. Integrating equation (2.41) we get

$$\left.\frac{S_p\, x}{n_0 C_s}\right|_{x=x_i}^{x=x_f} = \left.\frac{M}{1 + M^2 - M_0 M}\right|_{M=M_i}^{M=M_f}, \qquad (2.42)$$

where i and f are initial and final positions, respectively.

The relevance of the momentum equation in explaining the possible effects of toroidal flow will be discussed in Chapter 7. In this treatment of the ion momentum equation, we have already assumed an isothermal condition. To properly solve the momentum equation detailed energy equation must also be solved. In this section the need to solve the energy equation is removed by the assumption of isothermal ions.

2.2.3 Energy Equation

Considering the number of different processes occurring in the edge plasma region, it is a nontrivial task to balance an individual species' energy. Unlike the momentum equation, both the ions and electrons must be considered. Detailed experimental investigation of the ion and electron energy balances are presented in Chapter 6.

The energy equation for species j can be expressed as[25]

$$\begin{aligned} \frac{3}{2} n_j \left(\frac{\partial T_j}{\partial t} + \underline{v}^j \frac{\partial T_j}{\partial \underline{x}} \right) &= -P_j \nabla \cdot \underline{v}^j - \nabla \cdot \underline{q}_j \\ &\quad - \underline{\underline{\pi}} : \nabla \underline{v}^j + Q_j^c + Q_j^s, \end{aligned} \tag{2.43}$$

where $\underline{q}_j$ is the heat flux carried by the particles; Q_j^c is the heat generated in the plasma of particles of specie j as a consequence of collisions with particles of other species; and Q_j^s is the heat source or sink due to other possible edge processes.

Each term of equation (2.43) has a radial ($\perp$ to $\underline{B}$) and a parallel (to $\underline{B}$) component. Once again, parallel gradients of the temperatures are neglected. Therefore, in steady state, the left hand side of equation (2.43), or the convective energy term, can be reduced to

$$\frac{3}{2} n_j \left(\frac{\partial T_j}{\partial t} + \underline{v}^j \frac{\partial T_j}{\partial \underline{x}} \right) \sim \frac{3}{2} n_j v_\perp^j \frac{dT_j}{dr}, \tag{2.44}$$

$$\sim -\frac{3}{2} D_\perp \left(\frac{dn_j}{dr}\right)\left(\frac{dT_j}{dr}\right), \tag{2.45}$$

by using Fick's Law (equation (2.26)).

Starting from zero net drift velocity, the ions are accelerated to the sound speed along the field line due to presheath effects. To maintain quasineutrality, the electrons also assume the sound speed flow. Therefore, for a floating plate,

$$\nabla_{\parallel} \cdot \underline{v}^j \sim \frac{C_s}{L_{\parallel}}. \tag{2.46}$$

In another words, each of the plasma species is loosing a certain amount of *parallel compressive energy* due to presheath effects.

$\nabla \cdot \underline{v}^j_{\perp}$ is difficult to estimate. If Fick's Law is valid, then

$$v^j_{\perp} \sim -\frac{D_{\perp}}{n_p}\frac{dn_p}{dr}. \tag{2.47}$$

Experimentally we typically observed that the plasma density n_p decays exponentially in the edge plasma region. Therefore $(\nabla_{\perp} n_p)/n_p \sim$ constant. If $D_{\perp}$ is constant with respect to the minor radius, then $\nabla_{\perp} \cdot \underline{v}^j \sim 0$. That is, if $D_{\perp}$ varies with minor radius, then the density profile observed would not obey simple exponential profiles.

If the velocity distribution function, $f_j(\underline{v}^j)$, is known, the parallel heat flux can be directly integrated. As a first cut approximation, for cartesian coordinates, the parallel heat flux equals

$$q^j_{\parallel} = \int_{v_{cut}}^{\infty} dv_{\parallel} \int_{-\infty}^{\infty} dv_{\perp 1} \int_{-\infty}^{\infty} dv_{\perp 2} \frac{m_j v_{\parallel}}{2} \left(v^2_{\parallel} + v^2_{\perp 1} + v^2_{\perp 2}\right) f_j(\underline{v}^j), \tag{2.48}$$

where $v_{\perp 1}$ and $v_{\perp 2}$ are the perpendicular velocity components and v_{cut} is the parallel cut-off velocity which is different for ions and electrons and is dependent on the sheath potential. If no presheath effect is present,

$$v_{cut} = 0, \quad \text{for ions, and} \tag{2.49}$$

$$v_{cut} = \sqrt{\frac{2\,|eV_{sheath}|}{m_e}}, \quad \text{for electrons.} \tag{2.50}$$

Figure 2.4 plots the electron and ion parallel velocity distribution function far away from a solid surface. The shaded portions of the distributions are the regions of the distribution functions that ultimately strike the solid and contribute toward $q_{\parallel}^{j}$.

Substituting $v_{cut} = 0$ for a Maxwellian ion distribution function, we obtain

$$q_{\parallel}^{i} = 2\,kT_i\,n_p\sqrt{\frac{kT_i}{2\,\pi\,m_i}}. \tag{2.51}$$

Using Emmert's kinetic model[11], the ion distribution function is modified due to the presheath. Equation (2.51) is then adjusted to be

$$q_{\parallel}^{i} = \mu_E\,\beta_E\,2\,kT_i\,n_p\sqrt{\frac{kT_i}{2\,\pi\,m_i}}. \tag{2.52}$$

The two coefficients μ_E and β_E arise from the presheath. They represent, respectively, the enhancement of the energy and particle flux over what they would have been if the ions possessed a half-space Maxwellian distribution at the sheath edge. Both coefficients approach large positive values as $T_i/T_e \rightarrow 0$. For $T_i/T_e \geq 1$, $\mu_E \rightarrow 1$, and $\beta_E \rightarrow 2.1$. Stangeby[6] modified equation (2.52) and expresses the parallel heat flux to resemble equation (2.20)

$$q_{\parallel}^{i} = 2\,\mu_E\,kT_i\,n_p\,C_s\,f(\tau). \tag{2.53}$$

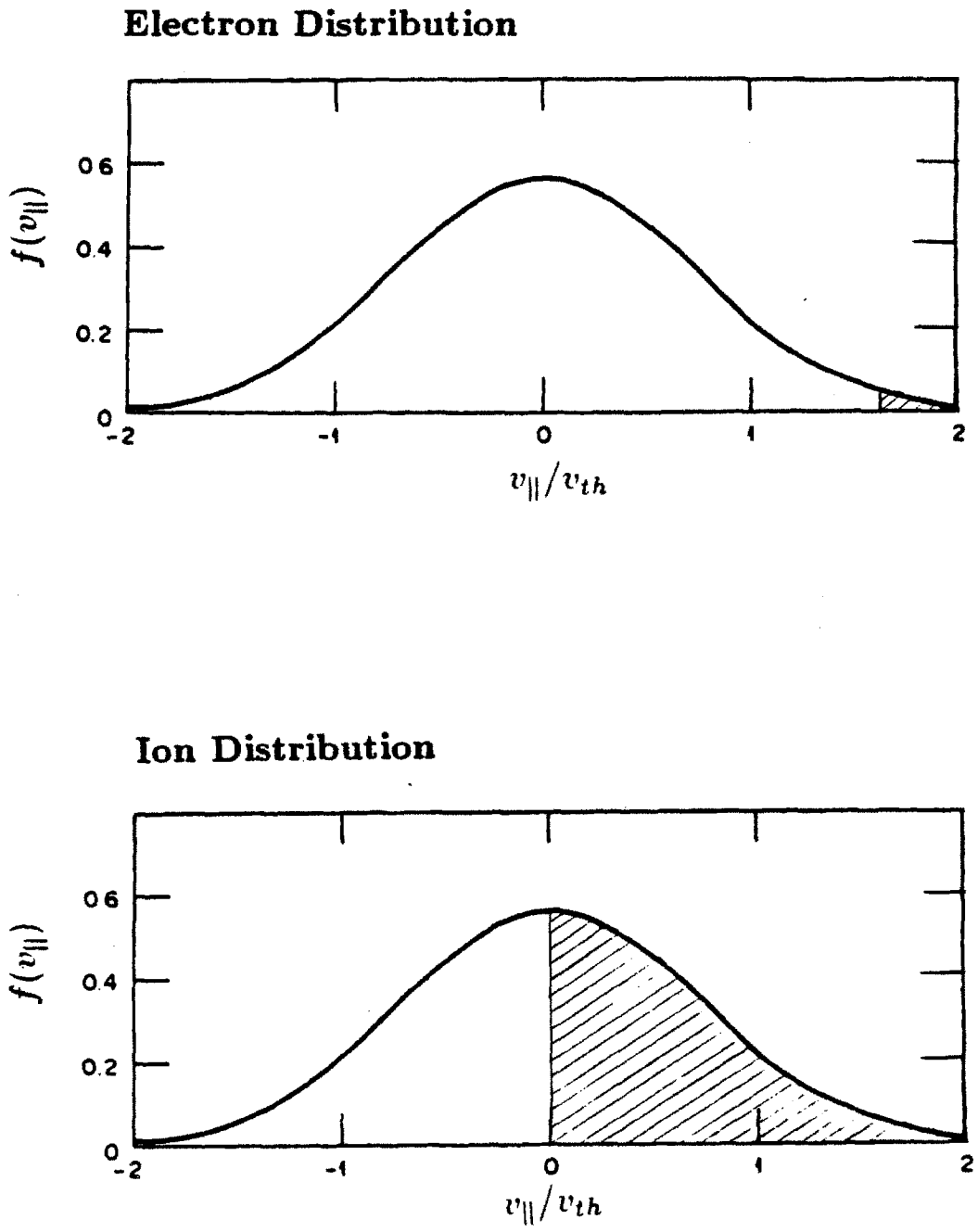

Figure 2.4 Electron and ion parallel velocity distribution function far away from the solid surface. The shaded regions represent the portions of distribution functions that will penetrate the negative sheath potential. $e|V_{sheath}|/kT_e \sim 3$ is assumed.

The value $(2\mu_E\tau)$ represents the ion contribution of the sheath transmission coefficient[28].

Using the sheath potential value to obtain v_{cut} for the electron parallel heat flux, we obtain

$$q_{\parallel}^{e} = \left(2 + \frac{e|V_{sheath}|}{kT_e}\right) kT_e \left(n_p\, e^{eV_{sheath}/kT_e}\right) \sqrt{\frac{kT_e}{2\pi m_e}}, \qquad (2.54)$$

where $n_p \exp(eV_{sheath}/kT_e)$ represents the portion of electrons possessing high enough energy to penetrate the sheath, and $(2\,kT_e + e|V_{sheath}|)$ is the average amount of energy lost by each of the penetrating electrons, and is defined as the electron portion of the sheath transmission coefficient[28], γ_e. Kinetic treatment[11] assumed that the electron distribution function remains as a Maxwellian. And since $\Gamma_{\parallel}^{e} = \Gamma_{\parallel}^{i}$, the electron parallel heat flux is

$$q_{\parallel}^{e} = \gamma_e\, kT_e\, n_p\, C_s\, f(\tau). \qquad (2.55)$$

Combining equations (2.53) and (2.55), the total parallel heat flux equals to

$$q_{\parallel}^{total} = q_{\parallel}^{i} + q_{\parallel}^{e} \qquad (2.56)$$

$$= (2\mu_E\tau + \gamma_e)\, kT_e\, n_p\, C_s\, f(\tau). \qquad (2.57)$$

$(2\mu_E\tau + \gamma_e)$ is defined as the total sheath transmission coefficient[28], γ_{total}. Multiplying with the electron temperature, $\gamma_{total}\, kT_e$ can be viewed as the total amount of energy deposited onto the material surface by an ion-electron pair. In a realistic situation, γ_{total} not only depends on the sheath and presheath effects, but also depends on plasma-surface interactions, such as secondary electron

emission, ion and electron particle and energy backscattering, and plasma-surface incident angles[6].

Since far away from the material surface the parallel heat flux is 0, the divergence of $q_{\parallel}^{j}$ can be approximated by the change of $q_{\parallel}^{j}$ over the entire parallel scale length $L_{\parallel}$. Therefore,

$$\nabla_{\parallel} \cdot q_{\parallel}^{j} \sim \frac{q_{\parallel}^{j}}{L_{\parallel}}. \tag{2.58}$$

The perpendicular heat flux, $q_{\perp}^{j}$, is assumed to be anomalous and can be modelled by a dependence similar to Fick's Law

$$q_{\perp}^{j} = -n_p \chi_{\perp}^{j} \frac{dT_j}{dr}, \tag{2.59}$$

where $\chi_{\perp}^{j}$ is the perpendicular thermal diffusivity of species j. Unlike $D_{\perp}$, where we can approximate its value by using the continuity equation, $\chi_{\perp}^{j}$ is a unknown coefficient. INTOR[29] uses the ratio for $\chi_{\perp}^{j}/D_{\perp} \sim 5 - 10$. The perpendicular scale length on Alcator C is typically much smaller than the plasma minor radius. Therefore, $\nabla_{\perp} \sim d/dr$.

The viscosity term is a difficult term to treat. An order of magnitude estimate of $\underline{\underline{\pi}}$ can be obtained using Braginskii's[25] transport coefficients. Comparing with the parallel heat flux term,

$$\frac{\underline{\underline{\pi}} : \nabla \underline{v}^{j}}{\nabla_{\parallel} \cdot \underline{q}^{j}} \sim \frac{\tau_j C_s}{L_{\parallel}}, \tag{2.60}$$

where τ_j is the dominating 90° scattering time for specie j. From Braginskii[25]

$$\tau_i \sim \tau_{ii} = 2.1 \times 10^7 \frac{\mu_i^{\frac{1}{2}} T_i^{\frac{3}{2}}}{Z^3 n_p (\ln \Lambda)}, \quad \text{and} \tag{2.61}$$

$$\tau_e \sim \tau_{ei} = 3.5 \times 10^5 \frac{T_e^{\frac{3}{2}}}{Z n_p (\ln \Lambda)}, \tag{2.62}$$

where μ_i is the atomic mass unit of the ion and $(\ln \Lambda)$ is the Coulomb Logarithm which is a slowly variating function in the range of 10 - 15 in the edge region of Alcator C.

Plugging in the set of Alcator C edge parameters used in this chapter, we found that the electron viscosity can be neglected. However, the ion viscosity can have significant effect on the ion energy balance. If there exists a strong radial gradient of the parallel flow, then the viscosity term produces a significant amount of shear drag energy into the edge plasma region. However, it is difficult to estimate the true contribution of the ion viscosity term since the perpendicular edge transport is anomalous in nature. Although there is claim of the existence of a perpendicular gradient in the parallel flow[30], we can neither measure this phenomenon nor accurately model it. Therefore the ion viscosity term is also neglected in our simple model of the energy equation.

Q_j^c is the heat exchange between different species as the result of collisions. Assuming that the plasma is dominated by only the ions and the electrons, Q_j^c can be viewed as the energy equipartition term and $Q_i^c = Q_{ie} = -Q_e^c = Q_{ei}$. From Braginskii[25], the equipartition term can be modelled as

$$Q_{ie} = -Q_{ei} = \frac{3 m_e n_p}{m_i \tau_{ei}} k(T_e - T_i). \tag{2.63}$$

If Q_j^c is small in comparison with the other terms of the energy equation, then T_i is not necessarily equal to T_e due to the small energy coupling mechanism.

As the result of the presence of neutrals and impurities, there are additional energy sources or sinks, Q_j^s, that must be considered in the energy equations. For the electrons, the presence of low or high Z impurities would result in radiation power loss Q_{rad} due to radiative decay and recombination. Photons are emitted when a bound state electron decays from an excited level to a lower, more stable configuration. Photons will also be emitted when a free electron is captured by, or recombined with an ion. The amount of steady state radiative energy loss due to the presence of different impurities ($2 \leq Z \leq 92$) was compiled by Post, Jensen, and co-workers[31], and can be expressed as

$$Q_{rad} = n_Z n_p P_Z, \tag{2.64}$$

where n_Z is the impurity density and P_Z is the cooling rate.

The neutrals impact the energy balances in two separate ways: ionization and charge exchange. The mean free path of molecular hydrogen is approximately 4 cm for $T_e \sim 15$ eV, and $n_e \sim 1 \times 10^{13}$ cm^{-3}. Therefore, far away from the limiters and the gas puffing port, and away from the vacuum wall surfaces, most of the neutrals are atoms instead of molecules, then electron impact ionization is the dominant process. For each atom, there is an associated threshold ionization energy ξ_e which the free electrons must reach to ionize the neutral. For ground state atomic hydrogen, $\xi_e \sim 13.6$ eV. Excitation processes would raise the value of ξ_e. $\xi_e \sim 30$ eV is used by Matthews in the edge region of DITE[32]. Further, for each ionization process, an ion with energy equal to the original neutral energy E_n is produced. $E_n \sim 2-3$ eV for atomic hydrogen as the result of dissociation of Frank-Condon molecules. Therefore, in association with the ionization process, the ion and electron energies are altered and are equal to

$$Q_{iz}^e = n_n n_p \langle \sigma v \rangle_{ioniz} \xi_e, \quad \text{and} \tag{2.65}$$

$$Q_{iz}^{i} = -n_n n_p \langle \sigma v \rangle_{ioniz} E_n. \quad (2.66)$$

Charge exchange occurs when an ion collides with a neutral and an electron is transferred from the neutral to the ion. The addition of a new ion with different energy than the original ion can cause a change in the overall ion energy balance. This term can be modelled as

$$Q_{cx} = \frac{3}{2} n_n n_p \langle \sigma v \rangle_{cx} k(T_i - E_n), \quad (2.67)$$

where $\langle \sigma v \rangle_{cx}$ is the rate coefficient for the charge exchange process.

In summary, the ion and electron energy equations can be reduced to

$$\frac{3}{2} D_\perp (\frac{dn_p}{dr})(\frac{dT_i}{dr}) + \frac{d}{dr}(n_p \chi_\perp^i \frac{dT_i}{dr}) = n_p T_i \nabla \cdot \underline{v}^i + \frac{q_\parallel^i}{L_\parallel} + Q_{ie} + Q_{cx} + Q_{iz}^i, \quad \text{and} \quad (2.68)$$

$$\frac{3}{2} D_\perp (\frac{dn_p}{dr})(\frac{dT_e}{dr}) + \frac{d}{dr}(n_p \chi_\perp^e \frac{dT_e}{dr}) = n_p T_e \nabla \cdot \underline{v}^e + \frac{q_\parallel^e}{L_\parallel} + Q_{ei} + Q_{rad} + Q_{iz}^e. \quad (2.69)$$

Ion and electron energy balances using equations (2.68) and (2.69) will be carried out in Chapter 6.

2.2.4 Validity of the Fluid Approximation

The approach of the previous sections in examining the particle continuity, momentum, and energy equation incorporates the assumption of the edge

plasma as a multi-specie fluid. This section will examine the validity of the fluid approximation in the edge region of Alcator C.

The fluid approximation is valid if the plasma is sufficiently magnetized and the particle's collisional mean free path is small in comparison with the parallel scale length $L_{\|}$. The magnetization requirement can be expressed as $\omega_{ci}\tau_i \gg 1$, and $\omega_{ce}\tau_e \gg 1$. ω_c is the cyclotron frequency or gyrofrequency, defined as

$$\omega_c^j = \frac{q_j |B|}{m_j}, \tag{2.70}$$

τ_e and τ_i are defined in equations (2.61) and (2.62). For typical Alcator C edge parameters,

$$\omega_{ci}\tau_i \sim 1.6 \times 10^4, \quad \text{and} \tag{2.71}$$

$$\omega_{ce}\tau_e \sim 2.3 \times 10^5. \tag{2.71}$$

The magnetization requirement is easily satisfied in the Alcator C edge plasma region.

The collisional mean free path, λ_j, is defined as the product of the j specie's thermal velocity and the 90° scattering time. Once again, substituting in the typical Alcator C edge condition, we obtain

$$\lambda_{ii} = v_{th}^i \tau_{ii} \sim 147 \text{ cm}, \quad \text{and} \tag{2.72}$$

$$\lambda_{ei} = v_{th}^e \tau_{ei} \sim 37 \text{ cm}, \tag{2.73}$$

$L_\parallel$ is defined as half of the distance between the limiters, which is $\sim$ 100 cm. Therefore, the Alcator C edge plasma is not very collisional. For operation at higher n_p, λ_j's will be reduced correspondingly.

The effect of collisions is to "Maxwellianize" the distribution function such that the derivations[25] of the continuity, momentum, and energy equations remain valid. If the ion and electron distribution functions are already Maxwellians in the edge region, then the fluid approach is still valid. This assumption was verified using the retarding-field energy analyzer described in Chapters 3 and 4. Therefore, despite the long collisional mean free paths, the fluid approach used in this section is still valid. Furthermore, the collisionless assumption used by the kinetic model[11] is also reasonable.

2.3 The Perturbing Effects of a Large Probe in the Edge Plasma

By inserting a solid probe, the plasma is perturbed such that the parameters measured at the probe surface may be different from the unperturbed parameters in the absence of the probe[33,34]. The degree of perturbation is determined by the dimension of the inserted solid. Corresponding to each solid there exists an ambipolar disturbance length, $L_{\parallel a}$. $L_{\parallel a}$ is the parallel length required such that the parallel flux lost to the solid can be balanced exactly by the perpendicular flux entering the collecting flux tube. The flux tube is defined by extending the field lines intersecting the solid into the plasma. This concept is sketched out in figure 2.5. The probe is large, i.e. perturbing, if

$$L_{\parallel a} \geq L_\parallel. \tag{2.74}$$

In other words, the probe acts effectively as a limiter.

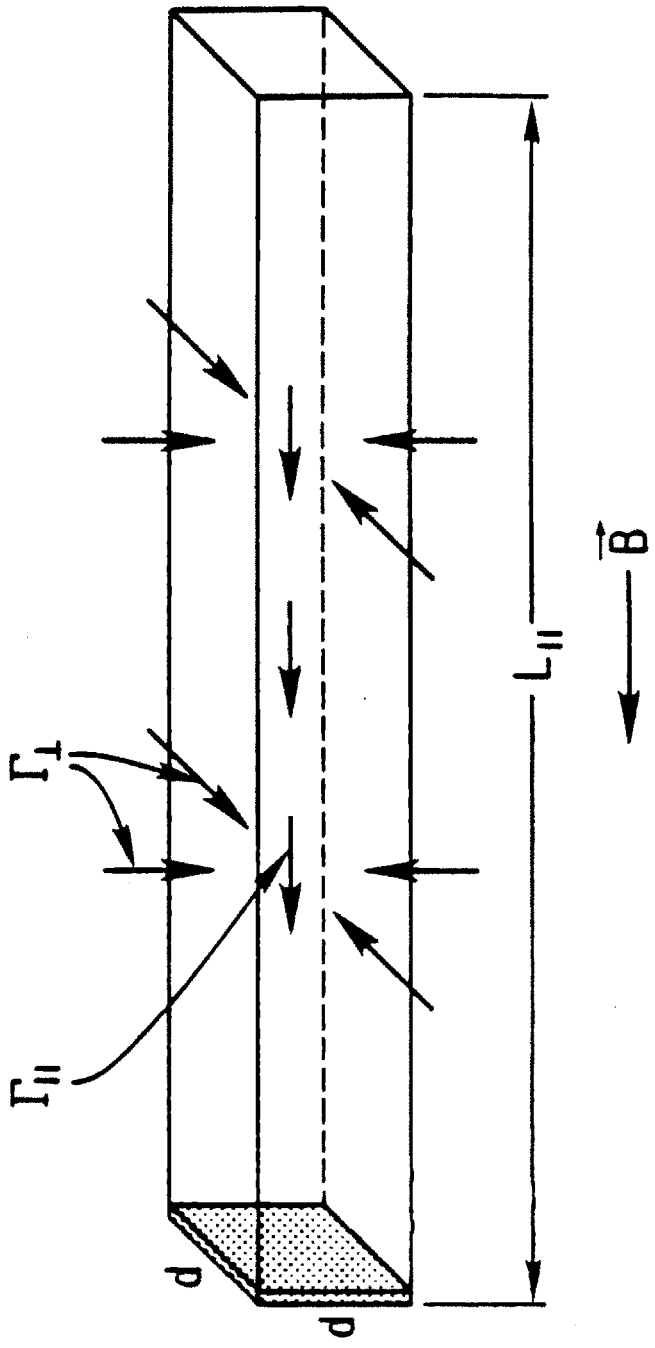

Figure 2.5 Balance of parallel and perpendicular fluxes entering a flux tube defined by a solid square probe housing with dimension d_h.

$L_{\|a}$ can be estimated by integrating the continuity equation (2.23) and assuming $S_p = 0$ inside the flux tube:

$$A_\perp \Gamma_\perp = A_\| \Gamma_\|, \tag{2.75}$$

$$\text{where } A_\perp = 2 d_h L_{\|a}, \text{ and} \tag{2.76}$$

$$A_\| = d_h^2. \tag{2.77}$$

Using the parallel and perpendicular fluxes used in section 2.2.1, and assuming $dn_p/dr \sim n_p/d_h$, equation (2.75) is reduced to

$$L_{\|a} = \frac{C_s f(\tau) d_h^2}{2 D_\perp}. \tag{2.78}$$

For an Alcator C edge probe with a length on the order of 2.5 cm, $L_{\|a} \sim$ 1200 cm, which is an order of magnitude greater than $L_\|$. Thus the probe can approximate a limiter and will command its own scrape-off layer. A typical Langmuir probe with dimension $\sim$ 1 mm, $L_{\|a} \sim$ 2 cm; The probe is therefore unperturbing probe and requires no further interpretation.

The process of unfolding the unperturbed values from the perturbed measurements is difficult and thus far only a simplified approach by Stangeby[33,34] has been proposed. In Stangeby's large probe analysis, 4 different probe configurations were discussed. However, most of the large probes used in the edge plasma region, including the edge probe used in this research, assumed the most complicated configuration which is sketched out in figure 2.6. In this configuration, the probe housing and the diagnostic sensors are fixed together, with the sensors recessed back by a distance Δ_p. The entire assembly is allowed to move radially. ϱ_B and ϱ_C represent the measured edge parameters at side B and side

C. As shown in figure 2.6, the leading edge of the probe housing is located at r_p while the perturbed parameters are measured at $r_p + \Delta_p$.

To unfold the unperturbed parameters, Stangeby assumes that the ϱ's follow exponential profiles with scrape-off lengths λ_A, λ_B, and λ_C for each of the regions labelled in figure 2.6. Then the perturbed parameters $\varrho_{B,C}(r_p + \Delta_p)$ can be unfolded as

$$\varrho_{B,C}\,(r_p + \Delta_p) \quad = \quad \varrho_0\, e^{-r_p/\lambda_A}\, e^{-\Delta_p/\lambda_{B,C}}, \tag{2.79}$$

where ϱ_0 is the unperturbed value at the limiter edge.

If the edge region is collisionless with no particle, momentum, or energy sources, and the perpendicular transport into the sampling flux tube is independent of r and poloidally and toroidally symmetric, then a radial scan would yield a measurement of λ_A since $\exp(-\Delta_p/\lambda_B)$ and $\exp(-\Delta_p/\lambda_C)$ are constants throughout the scan. λ_B and λ_C can be deduced from the geometric relation

$$\lambda_{B,C} \quad = \quad \lambda_A \sqrt{\frac{L_{B,C}}{L_A}}, \tag{2.80}$$

since

$$\lambda \quad \propto \quad \sqrt{\frac{D_\perp L}{C_s}}. \tag{2.81}$$

Therefore, if C_s is constant in regions B and C, then the only variable in equation (2.81) is L, the connection length to the closest limiter surface. Once ϱ_0 and the λ's are known, unperturbed values of ϱ can be easily deduced at any radial position.

Realistically the assumptions that went into Stangeby's large probe model are not valid in the Alcator C edge region. Experimentally the scrape-off lengths

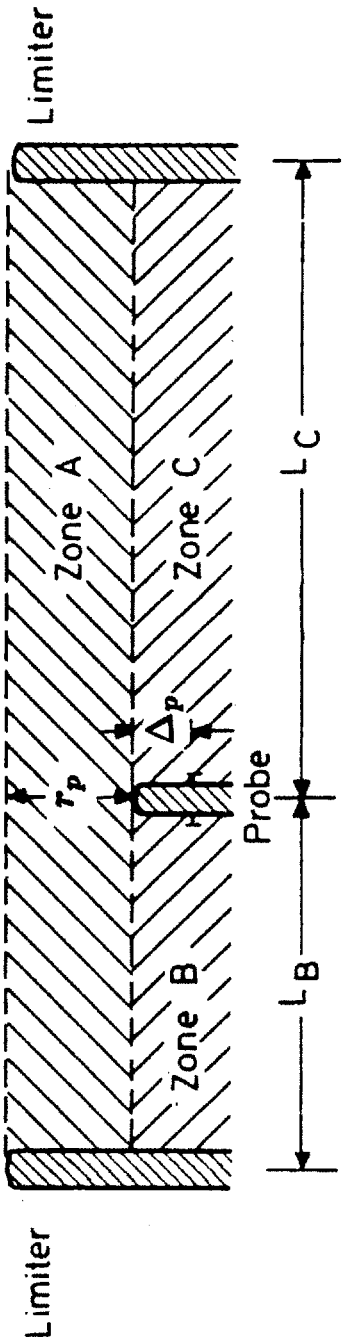

Figure 2.6 Large probe in the edge plasma region with recessed (by Δ_p) sensors facing both sides along the field line (labelled as regions B and C). Region A is the unperturbed region.

measured on both sides of the two-sided probe used in these experiments differ for different operational conditions and the probe's poloidal position. In view of the complexity of the edge region, there is no simple, immediately available solution to unfold the unperturbed parameters from our measurements. Thus the results obtained here are not modified by the benefit of any large probe analysis.

References

[1] Gierszewski, P. J., "Plasma/Neutral Gas Transport in Divertors and Limiters," M.I.T. ScD Thesis, September 1983.

[2] Prinja, A. K., Conn, R. W., "An Axially Averaged-Radial Transport Model of Tokamak Edge Plasmas," *J. Nucl. Mat.* **128 & 129**, 135–140 (1984).

[3] Ulrickson, M., Post, D. E., "Particle and Energy Transport in the Plasma Scrape-Off Zone and Its Impact on Limiter Design," *J. Vac. Sci. Technol. A* **1**, 907 (1983).

[4] Waltz, R. E., Burrell, K. H., "Tokamak Boundary in Contact with a Limiter," *Nuclear Fusion* **17**, 1001 (1977).

[5] Braams, B. J., Harbour, P. J., Harrison, M. F. A., Hotston, E. S., Morgan, J. G.,, "Modelling of the Boundary Plasma of Large Tokamaks," *J. Nucl. Mat.* **121**, 75 (1984).

[6] Stangeby, P. C., "Sheath Lecture," Proceedings of NATO Advanced Study Institute on Plasma Surface Interactions, Val Morin P.Q., Canada (August 1984).

[7] Langmuir, I., Compton, K. T., *Rev. Mod. Phys.* **3**, 244 (1931).

[8] Self, S. A., "Exact Solution of the Collisionless Plasma-Sheath Equation," *Phys. of Fluids*, **6** 12, 1762 (1963).

[9] Langmuir, I., *Phys. Rev.*, **33**, 954 (1929).

[10] Bohm, D., Burhop, E. H. S., Massey, H. S. W., The Characteristics of Electrical Discharges in Magnetic Fields, Editors: Guthrie, A., Wakerling, K. R., McGraw Hill, New York (1949).

[11] Emmert, G. A., Wieland, R. M., Mense, T. A., Davidson, J. N., "Electric Sheath and Presheath in a Collisionless, Finite Ion Temperature Plasma," *Phys. Fluids* **24**, 803 (1980).

[12] Hutchinson, I. H., Chung, K., private communications, 1986.

[13] LaBombard, B., "Poloidal Asymmetries in the Limiter Shadow Plasma of the Alcator C Tokamak," M.I.T. Doctoral Thesis, April 1986.

[14] Lipschultz, B., LaBombard, B., Marmer, E. S., Pickrell, M. M., Terry, J. L., Watterson, R., Wolfe, S. M., "MARFE : An Edge Plasma Phenomenon," *Nucl. Fusion* **24**, 977 (1984).

[15] Wan, A., Lipschultz, B., Yang, T., LaBombard, B., "Directional Measurement of Edge Electron and Ion Parameters on Alcator C," *Bull. Amer. Phys. Soc.* **30**, paper 3F6, 1413, (Nov 1985).

[16] Hayzen, A. J., Overskei, D. O., Moreno, J., "Probe Measurements of the Boundary Plasma in Alcator C," M.I.T. Plasma Fusion Center Report No. PFC/JA-81-10 (April 1981)

[17] Hugill, J., "Transport in Tokamaks - a Review of Experiments," *Nuclear Fusion* **23**, 331 (1983).

[18] Liewer, P. C., "Measurements of Microturbulence in Tokamaks and Comparisons with Theories of Turbulence and Anomalous Transport," *Nuclear Fusion* **25**, 543 (1985).

[20] Liewer, P. C., McChesney, J. M., Zweben, S. J., Gould, R. W., "Temperature Fluctuations and Heat Transport in the Edge Regions of a Tokamak," *Phys. Fluids* **29**, 309 (1986).

[20] Zweben, S. J., Taylor, R. J., "Edge-Plasma Properties of the UCLA Tokamaks," *Nucl. Fusion* **23** 4, 513 (1983).

[21] Zweben, S. J., Liewer, P. C., Gould, R. W., *J. Nucl. Mat.* **111 & 112**, 87 (1982).

[22] Gomay, Y., Fujisawa, N., Maeno, M., Suzuki, N., Uehara, K., Yamamoto, T., Konoshima, S., *Nuclear Fusion* **18**, 849 (1978).

[23] Staudenmaier, G., Staib, P., Behrish, R., *Nucl. Fusion* **20** 1, 96 (1980).

[24] Harbour, P. J., Proudfoot, G., "Mach Number Deduced from Probe Measurements in the Divertor and Boundary Layer of DITE," *J. Nucl. Mat.* **121**, 222 (1984).

[25] Braginskii, S. I., "Transport Processes in a Plasma," *Reviews of Plasma Physics* **1**, 205–311 (1965).

[26] Stangeby, P.C., "Measuring Plasma Drift Velocities in Tokamak Edge Plasmas using Probes," *Phys. Fluids* **27**, 2699-2704 (1984).

[27] LaBombard, B., "Reduced Transport Equations for the Edge Plasma in Alcator C," M.I.T. Plasma Fusion Center Report to be published.

[28] Stangeby, P. C., "Plasma Sheath Transmission Factors for Tokamak Edge Plasmas," *Phys. Fluids* **27**, 682 (1984).

[29] "International Tokamak Reactor, Phase Two A, Part I, Report of the INTOR Workshop 1981-83," 196 (IAEA, Vienna, 1983).

[30] Proudfoot, G., Harbour, P. J., Allen, J., Lewis, A., "Poloidal and Radial Variations in Plasma Transport in a Limiter Scrape-Off Layer in DITE," *J. Nucl. Mat.* **128 & 129**, 180–185 (1984).

[31] Post, D. E., Jensen, R. U., Tarter, C. B., Grasberger, W. H., Lokke, W. A., "Steady State Radiative Cooling Rates for Low-Density, High-Temperature Plasma," *Atomic Data and Nuclear Tables* **20**, 397 (1977).

[32] Matthews, G. F., "The Measurement of Ion Temperature in Tokamak Edge Plasmas," Oxford University Doctoral Thesis (1985).

[33] Stangeby, P. C., "The Disturbing Effect of Probes Inserted into Edge Plasmas of Fusion Devices," *J. Nucl. Mat.* **121**, 36–40 (1984).

[34] Stangeby, P.C., "Large Probes in Tokamak Scrape-off Plasmas. The Collisionless Scrape-off Layer: Operation in the Shadow of Limiters or Divertor Plates," *J. Phys. D: Appl. Phys.* **18**, 1547–1559 (1985).

CHAPTER 3

INSTRUMENTATION

To understand the mechanisms of plasma-surface interactions requires knowledge of a number of "essential" edge plasma parameters including ion and electron energy distribution functions, densities, local potentials, heat fluxes, and their fluctuations. Manos and McCracken[1] and Cohen[2] have recently summarized the capabilities of edge diagnostics. Most of the previous edge plasma studies employed either an array of single purpose diagnostics or tried to piece together information from different diagnostics at different poloidal and toroidal locations. However, many tokamaks have observed strong poloidal[3,4,5,6] and toroidal[7,8,9] asymmetries of edge plasma parameters. Consequently a proper correlation between various edge parameters requires a local, directional measurement. Ideally, one would like to measure all the "essential" edge plasma parameters at many spatial locations. However this task is formidable even at only one spatial position.

No diagnostic is capable of measuring all the desired parameters directly without using some theoretical assumptions. The measurement of ion parameters is especially difficult. During the early stage of this thesis research, a detailed study of viable ion diagnostics was performed. A sample of those previously used are surface probes[10,11], $E \times B$ probes[12,13], aperture transmission probes[14], Katsumata probes[15], biased heat flux probes[16], carbon resistance probes[17], and retarding-field energy analyzers[18,19,20,21]. Matthews[21] gives an excellent review on these diagnostics, both the principles and usefulness for fusion plasma applications. The retarding-field energy analyzer is assessed to be the best overall ion parameter diagnostics for its versatility and reliability.

A prototype retarding-field energy analyzer (RFEA) was constructed and installed on a low energy ion beam device[22]. An improved model was used on

Alcator C for short periods of time during the spring and summer of 1984. The main task of this experiment was to study the feasibility of an RFEA-type of device in the scrape-off region of a tokamak and to determine possible applications of the RFEA. This proof-of-principle experiment used a simple RFEA that could be scanned in the minor radial direction and could also rotate with respect to the toroidal field. Therefore, the rotational capability allowed the probe to face either the electron side, the ion side, or anywhere in between, thus allowing us to determine the proper alignment of the probe with respect to the magnetic field.

Although the success[23] of the proof-of-principle experiment showed that the RFEA is a viable edge plasma diagnostic, this experiment also exposed some shortcomings. We found the need to diagnose other edge plasma parameters that the RFEA cannot measure. We also found significantly different edge conditions as the probe is rotated about the toroidal field. Subsequently these findings led to the design of the final instrument: a bi-directional, multi-functional probe herein denoted by Janus which features two mirror-image sets of diagnostics. Each set of diagnostics consists of a retarding-field energy analyzer, a Langmuir probe, and a calorimeter. The Langmuir probes and calorimeters are added to supplement the RFEA so directional measurements of the "essential" parameters at a single location are now possible. The diagnostics are aligned such that one set faces the ion side and the other faces the electron side (as defined by the plasma current, I_p).

Unlike simple Langmuir probes which makes only minor perturbation to the plasma, Janus is a "large" probe. The implication of using a large probe in the tokamak edge is discussed previously in section 2.3.

Section 3.1 describes the overall experimental setup and some general design considerations of Janus. Section 3.2-3.4 will go into detail mechanical and electrical design considerations and constraints of the RFEA, Langmuir probe,

and calorimeter respectively. Section 3.5 briefly describes the data acquisition procedures featuring the MDS system[24].

3.1 Overall Experimental Setup and Considerations

Figure 3.1 shows an unscaled artist's conception of the experimental setup of Janus looking perpendicular to its "viewing" length along a field line. Typically Janus is inserted from the top of Alcator C, directly centered over the magnetic axis. Due to the limitation of probe components and insulator designs, the diagnostic sensors are recessed by about 0.5 cm from the leading edge of the probe. The relevance of this design feature on the interpretation of results will be discussed in part III of this thesis.

Alcator C typically operates with two sets of full poloidal ring limiters. Each set of limiters consists of two full ring limiters. Limiter radii of 16.5 cm, 12.5 cm, and 11.5 cm were used during the Janus experimental period. For the sake of easy labelling, we defined the two sides of Janus in accordance with the plasma current direction. Therefore, as indicated by figure 3.1, the Janus electron side flux tube has a limiter connection length that is twice as long as the ion side.

Figure 3.2 shows a poloidal cross-sectional view of the overall Janus setup, including all the vacuum components. Utilizing a combination of bellows and a Thermionics bellows actuator, Janus can be scanned in the minor radial direction (perpendicular to the magnetic field). The motion is limited by the vacuum wall at one extreme and the limiter radius defining the main plasma edge at the other extreme. The probe is supported by a tube guide installed within the port slot. This feature prevents the probe from extensive movement during the discharge.

Janus is constructed with a molybdenum casing and Al_2O_3 insulators to allow for operating at high temperature. In addition, in order to allow for easy maintenance, the probe head is detachable. This detachment scheme is sketched

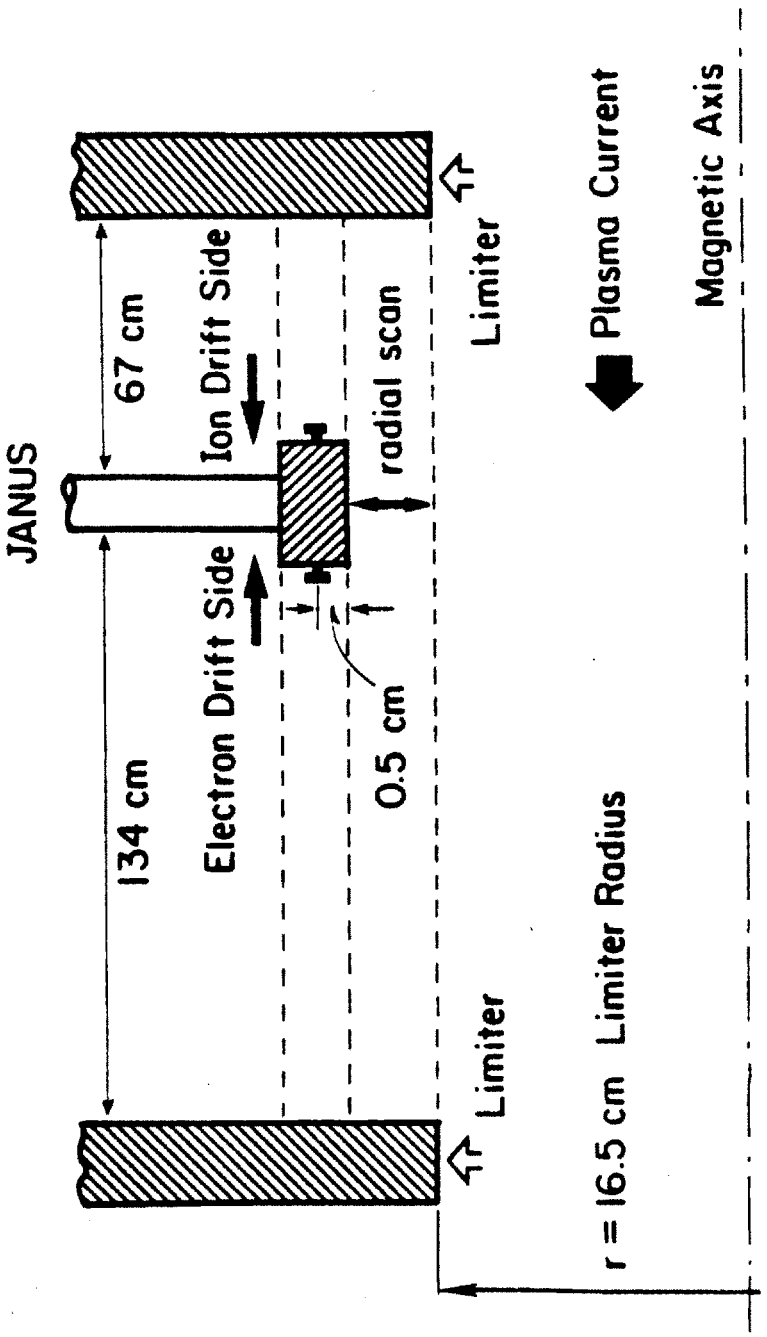

Figure 3.1 Unscaled artist's conception of the Janus experiment setup looking perpendicular to Janus "viewing" length along a field line.

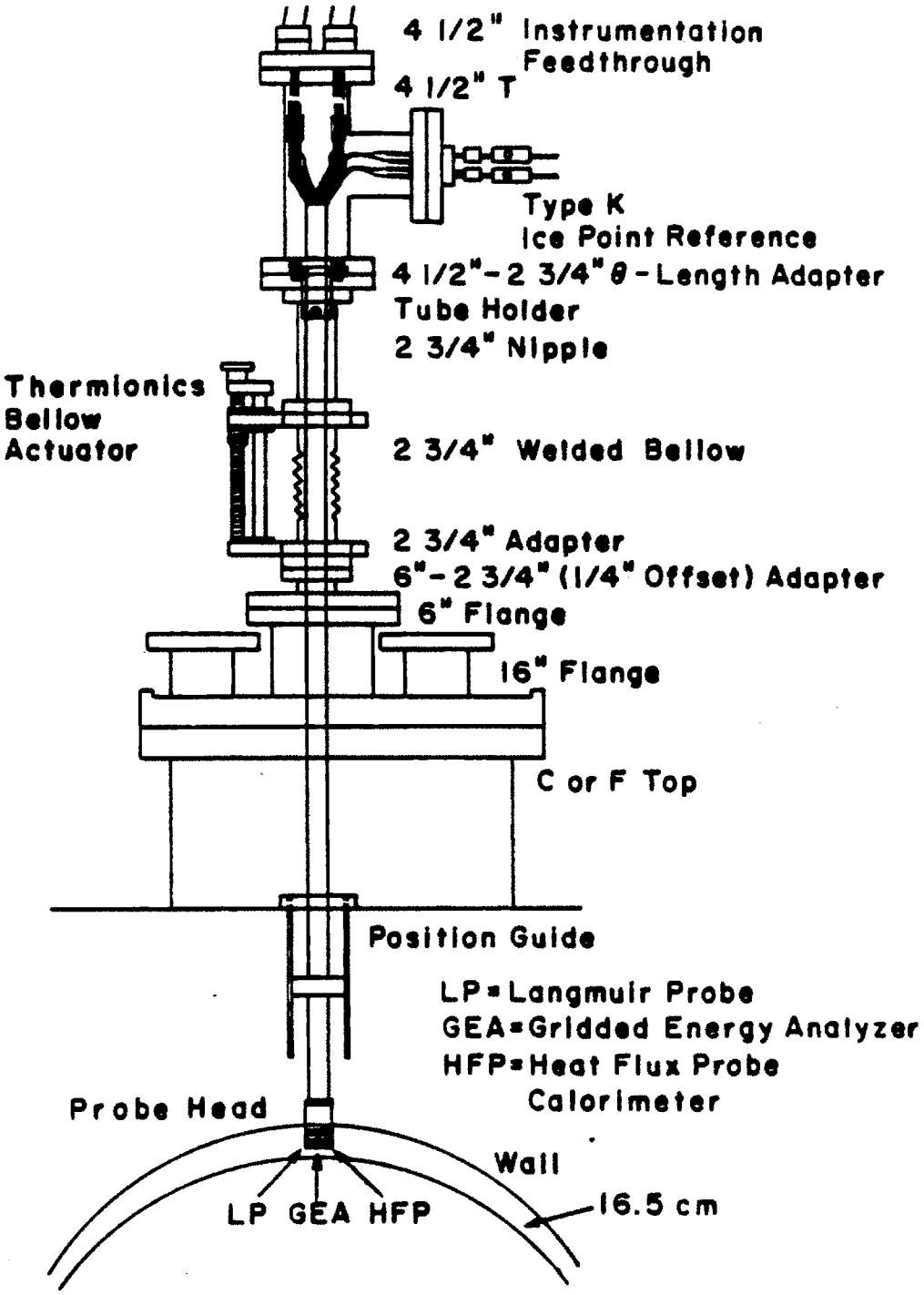

Figure 3.2 Poloidal view of the probe and vacuum assembly of Janus.

in figure 3.3. The connections between the wires originating from the probe head and the wires from the vacuum feedthroughs are achieved by using Be-Cu spring electrodes confined by carefully machined matching slot insulators shown in figure 3.3. The hole patterns of the insulators match the wire patterns from the probe head and from the feedthrough. The elastic property of the upper spring electrodes are produced by carefully baking the Be-Cu under set conditions. Since the electrodes are confined by the matching slots of the insulators, when the probe head is secured onto the tube assembly, the electrodes make excellent electrical contacts.

Figure 3.4 shows a 3-D view of a set of diagnostics on a single side of Janus. The retarding-field energy analyzer is flanked by the Langmuir probe on the inside (smaller major radius, see figure 3.2) and the calorimeter on the outside. A U-shaped spring is inserted between the two sets of diagnostics in order to secure all components in place. The entire Janus assembly is less than 1 inch perpendicular (poloidal) and $1\frac{7}{8}$ inches parallel (toroidal) to the view shown in figure 3.1.

The associated electronics are all grounded at one point on the Alcator C vacuum vessel with electrically isolated trays supporting the wires between the probe and the electronics. Electronics for the diagnostics will be discussed in the subsequent sections.

3.2 Retarding-Field Energy Analyzer (RFEA)

The RFEA is a versatile edge diagnostic designed to measure the ion and/or electron energy distribution functions. Early versions of the RFEA were used on beam-type devices[25,26] and for space applications[27] to measure the behavior of the space plasmas.

In a magnetized environment, the RFEA measures the *parallel* energy distributions of ions and electrons along magnetic field lines. Previously, different

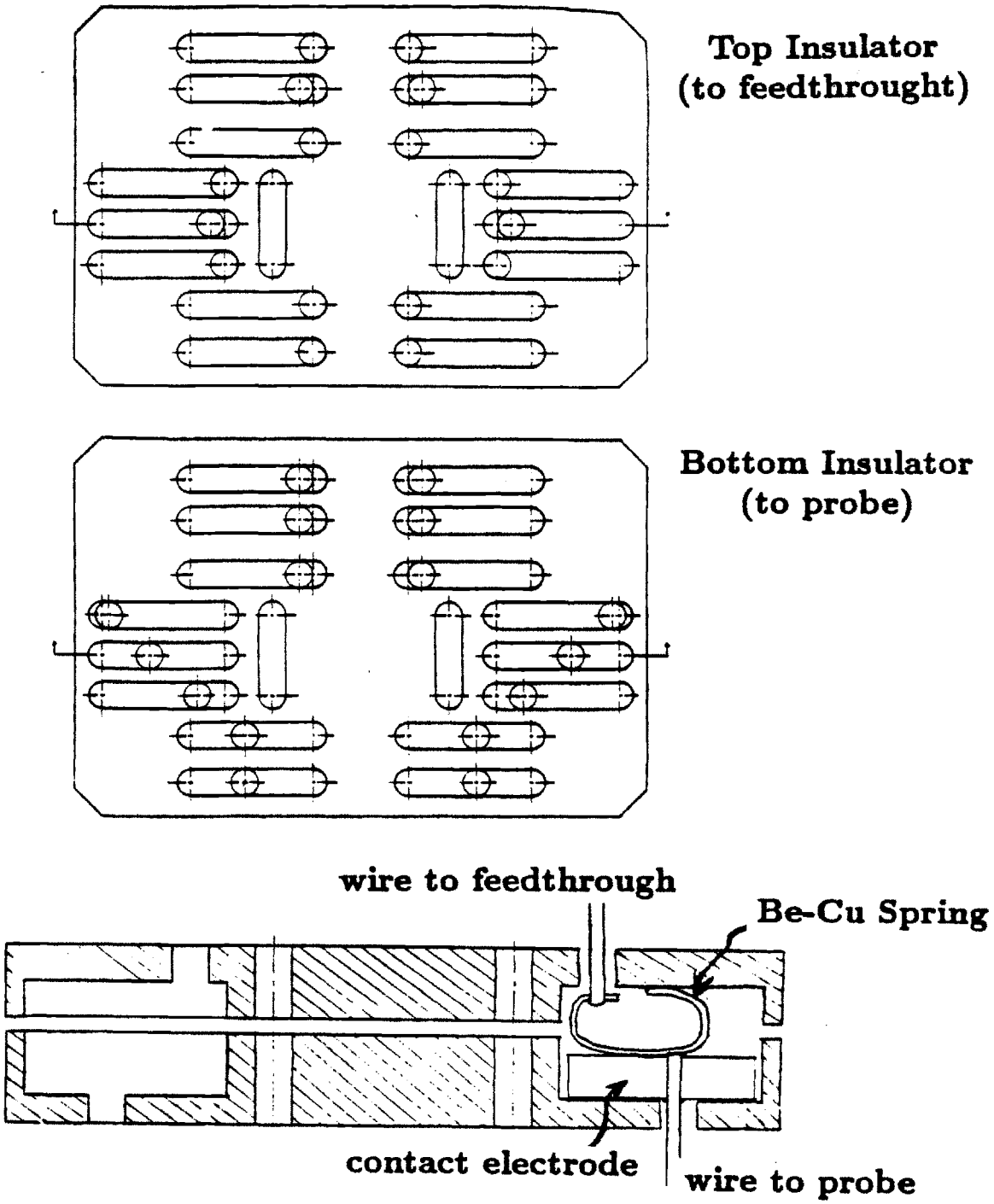

Figure 3.3 Detachable probe head scheme.

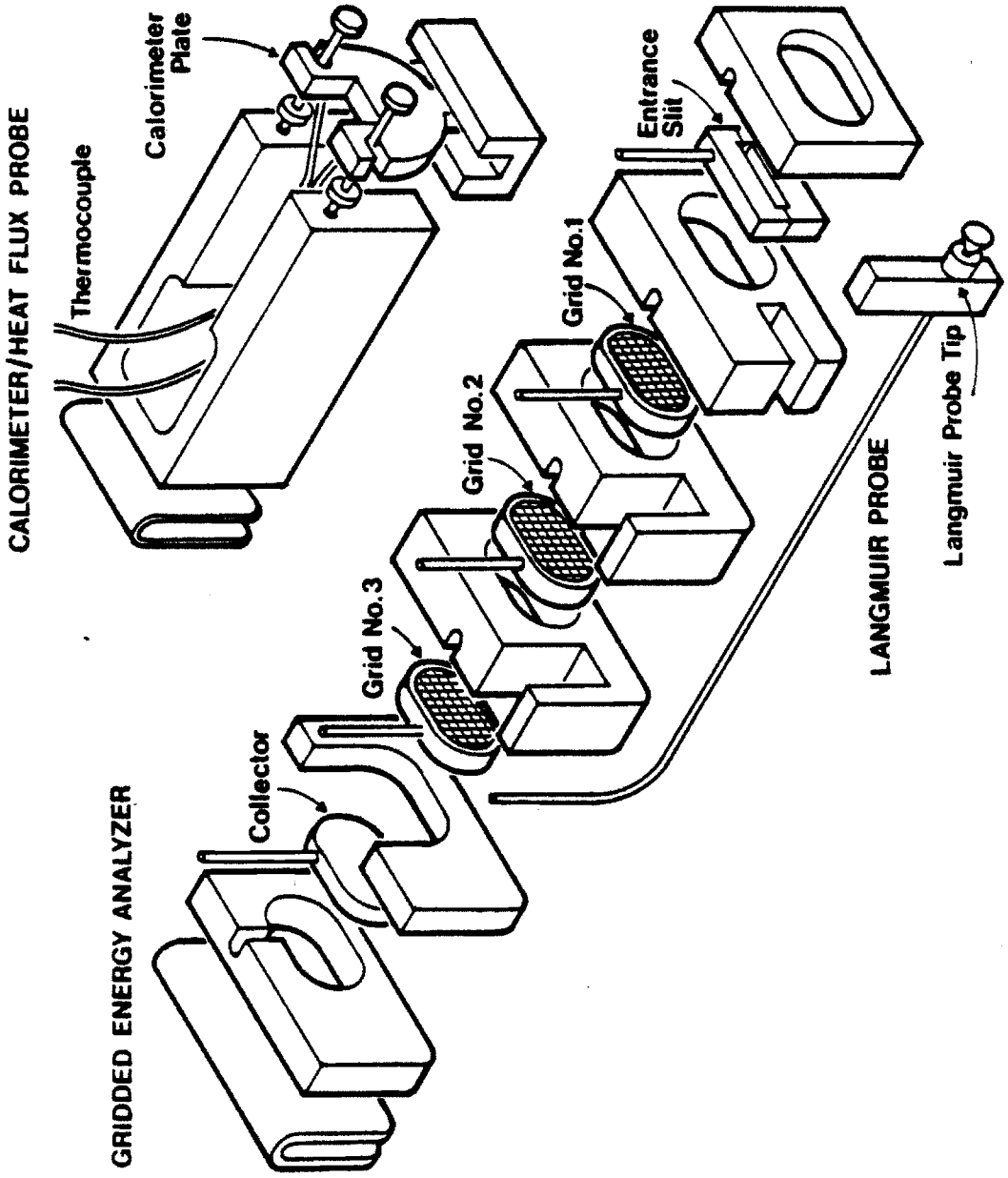

Figure 3.4 3-D view of a set of diagnostic on a single side of Janus.

versions of the RFEA have been used successfully in various fusion devices for different purposes[18,19,20,21]. An excellent review of the design principles of the RFEA is given by Molvik[20].

Figure 3.5 shows a cross-sectional view of the RFEA used for Janus. It consists of 5 components: a knife-edge slit, 3 double-sided mesh electrodes, and a collector. All components rest in Al_2O_3 insulators and are pressed together by using a flat, U-shaped, stainless steel spring. Detailed operational and analysis techniques will be discussed in section 4.1.

If enough particles enter the analyzer and are neutralized, there is a possibility that neutral density may build up inside the analyzer. This consideration is taken into account in the design of the analyzer by providing a neutral pump-out passage just before the collector plate (see figure 3.5). Photoelectrons can also contribute to the total collector current. However, given the geometry of Alcator C, the high energy photon flux is unlikely to produce significant contributions. This is verified in the proof-of-principle experiment.

In the subsequent sections we will go into detail regarding the design considerations of the entrance slit and the gridded electrodes. The collector does not have much restriction as long as it has good electrical, mechanical, and vacuum properties.

3.2.1 The Entrance Slit

The knife-edge slit is the most difficult component of the RFEA to design and manufacture. It is the piece that separates the edge plasma and the analyzer chamber and is constantly facing a large heat flux. Therefore, the slit must possess sufficient thermal mass and superior thermophysical properties to withstand the heat flux. In addition, the slit is designed to be biasable. These requirements impose a strict limitation on the possible materials that can be used.

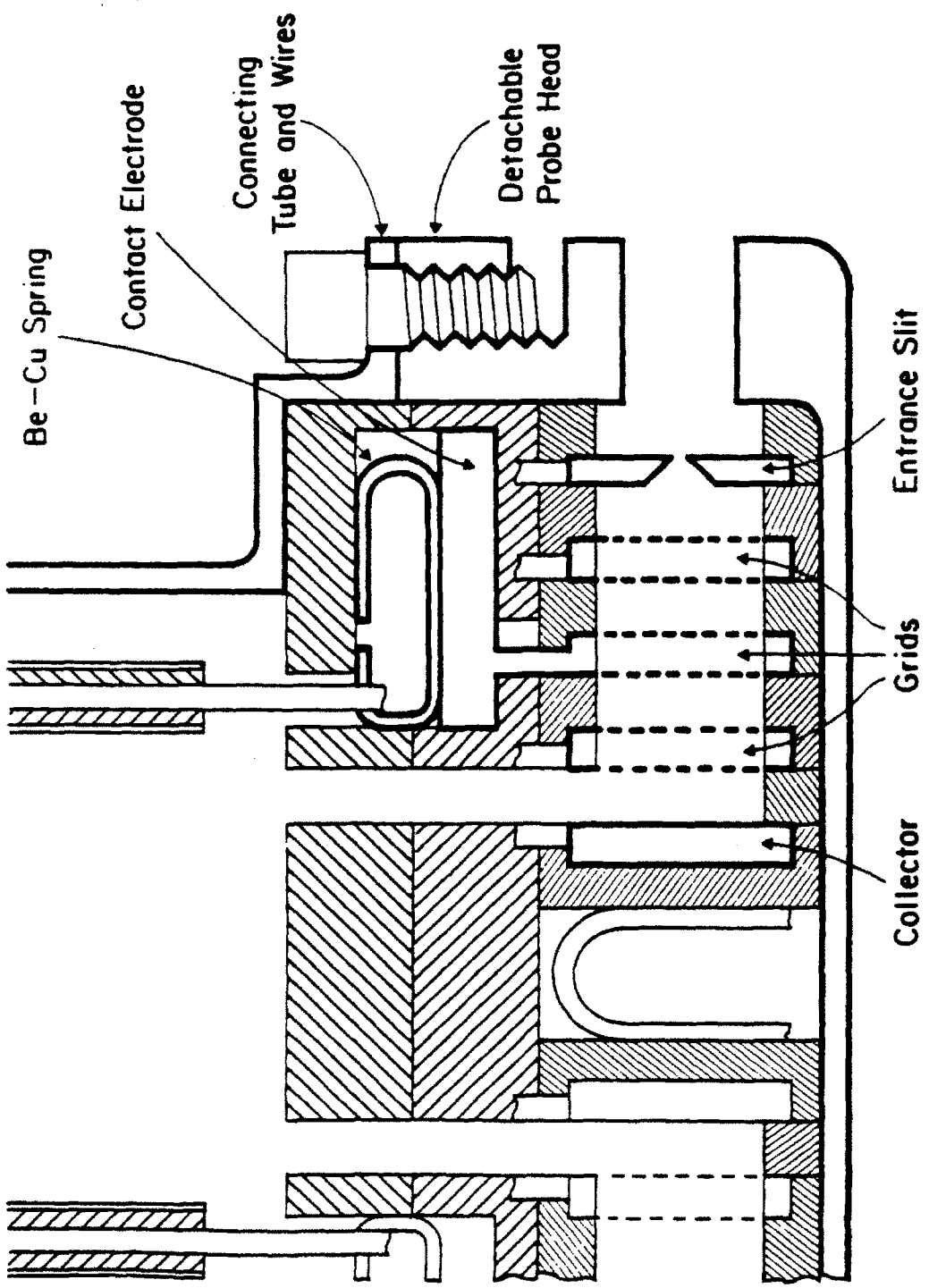

Figure 3.5 Cross-sectional view of the Janus retarding-field energy analyzer.

Tungsten was chosen due to its overall thermal properties and high melting point ($\sim 3600\,K$). (Detailed material selection criteria will be discussed in section 3.4). However, tungsten is difficult to machine and to weld. Each slit is comprised of two half pieces which are "carved" out of tungsten by using wire EDM processes. The knife-edges are machined by using conventional EDM processes and a notch besides the knife-edge defines the slit width. The two half pieces are welded together by electron beam. The weld joints are easily oxidized, thus they are very brittle. A superior mechanical design of making the two pieces with portions of each piece overlapping the other piece was designed (but never used) to reduce the fragility of the weld joints.

The slit opening at the plasma side must be less than twice the sheath thickness, δ_{sheath}, in order to assure the continuity of sheath potential surface across the the front of the slit. This design constraint assures that the charge particle distribution functions are not perturbed by a uneven distribution of the sheath potential. And the particle distributions and fluxes are the same quantities as those experienced by a limiter surface. Theoretically δ_{sheath} is characterized as[21,28,29]:

$$\delta_{sheath} \leq 10\ \lambda_{Debye}, \tag{3.1}$$

$$\text{where } \lambda_{Debye} = 743\ \sqrt{\frac{T_e}{n_p}}\ \text{(cm)}. \tag{3.2}$$

Here T_e is the electron temperature in eV and n_p is the plasma density in cm^{-3}. Applying typical Alcator C edge conditions of $T_e \sim 15$ eV and $n_p \sim 1 \times 10^{13}$ cm^{-3}, we obtain $\lambda_{Debye} \sim 9\ \mu\text{m}$. The RFEA slits for Janus are designed with a width of 30 μm. The continuity of the potential across the slit gap will be demonstrated in section 4.1.

In magnetized plasma, charged particles gyrate about magnetic field lines with a gyroradius ρ, which for ions is defined as:

$$\rho_i \approx 1.02 \times 10^{-2} \frac{\sqrt{\mu T_i}}{Z B} \text{ (cm)}, \tag{3.3}$$

where μ is the mass (in amu) of the ion with charge Z; T_i is the perpendicular ion temperature in eV; and B is the magnetic field in tesla. For hydrogen ions at 8 tesla and 25 eV, $\rho_i \sim 60\,\mu$m, which is larger than the designed slit width. A large fraction of the ions with large gyroradii (compared to the slit width) can be scraped off as they pass through the slit, never reaching the RFEA chamber. To minimize this effect, the slit is designed like a knife-edge. In this way, as soon as an ion enters the slit the overall aperture for transmission is enlarged. The electron gyroradius, ρ_e, is smaller than ρ_i by $\sqrt{m_e/m_i}$. Thus the electron transmission characteristics are not strongly affected by the slit geometry.

The transmission properties of various slit geometries are studied using a 3-dimensional, Monte-Carlo, true orbit following code. The code uses the 3-D velocity launching technique employed by Gierszewski[30]. The true orbit of each particle is calculated for each time step as the particles travel through a 3-D geometric grid. The grid points simulate the geometry of the slit and any particle intersecting a solid interface is stopped and recorded. Detailed code structures and assumptions are presented in Appendix C.

Figures 3.6.1 and 3.6.2 compare the transmission characteristics of the three velocity components between a straight entrance slit and a 45° knife-edge slit. For this transmission experiment, we used $T_i = 25\,$eV, $T_e = 15\,$eV, and the parallel distribution function (v_z) is shifted in energy by $\sim 2.8\,T_e$, which corresponds to Emmert's predicted V_{sheath} value plotted in figure 2.2. The launched velocity distributions are shown in figure C.1. The transmission characteristics are shown as the percentage of the particles within a velocity strip that penetrated the slit. The slit width is aligned with the v_x component.

For a straight slit (figure 3.6.1), due to the thick slit design, only a very small percentage of the particles with very small v_x and v_y components can enter

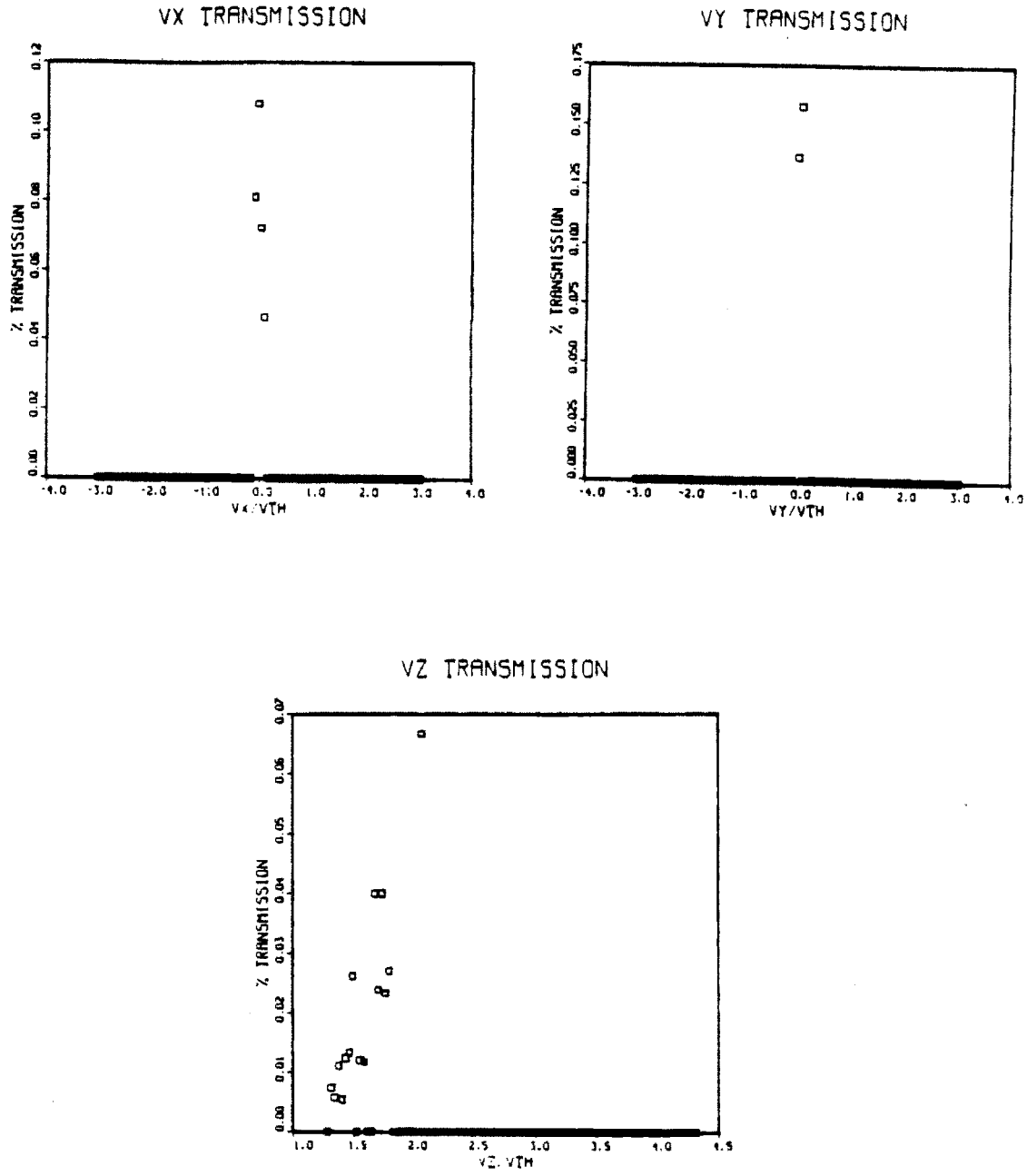

Figure 3.6.1 Velocity transmission characteristic of a straight edge slit.

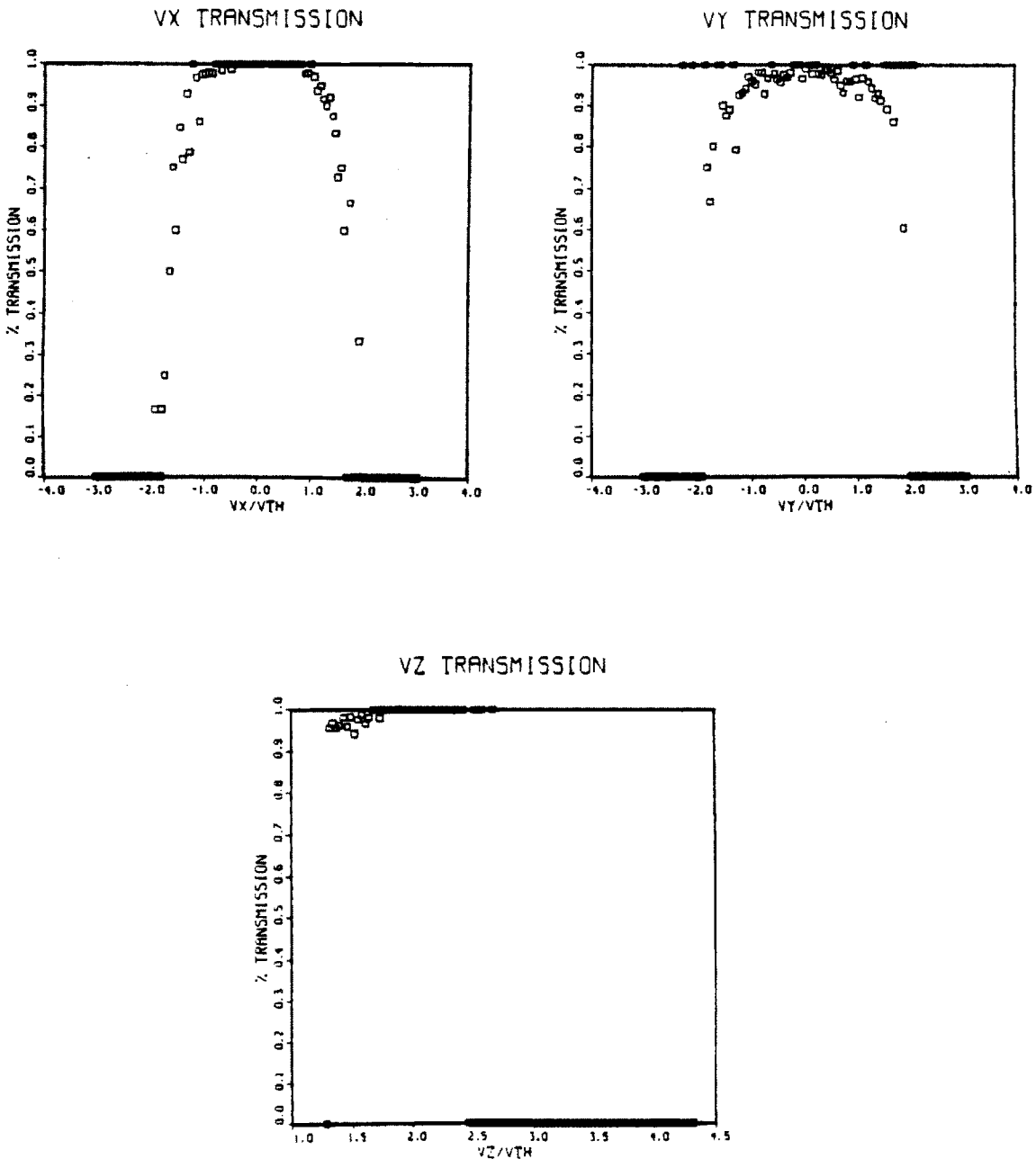

Figure 3.6.2 Velocity transmission characteristic of a 45° knife-edge slit.

the RFEA chamber. The rest of the particles will intersect the slit wall before entering the analyzer chamber. A simple approximation shows that for the RFEA slit design width, only particles with *both* perpendicular energy components less than 20% of T_i can actually penetrate a straight slit. For a knife-edge slit the perturbations to the transmission characteristics are minimized as the result of the enlarged slit region. Although the high perpendicular components are still cut off, as long as the perturbation to the parallel component is small, the slit design will not jeopardize the the RFEA performance.

3.2.2 The Grids

3.2.2.1 Mesh Spacing and Debye Shielding

All three grids (mesh electrodes) employ the double-sided mesh design[25] to avoid potential shielding by the electrons inside the analyzer and to avoid the field penetration effect from adjacent electrodes. The mesh spacing is chosen based on the estimated electron density inside the analyzer chamber. Therefore the mesh closest to the slit faces the most stringent spacing requirement.

To avoid Debye shielding, the first electrode has a mesh spacing of 250 lines/inch with a line weight of 0.001 inch. For $T_e \sim 15$ eV, the maximum allowable electron density at the first mesh is around 5.6×10^{11} cm^{-3}. If there is a negative sheath potential at the slit surface, a majority of electrons are repelled away before entering the analyzer chamber. Assuming the sheath potential affects only the v_z component, then the fraction of electrons that the first mesh will encounter is

$$\% \text{ transmitted} = \frac{2}{\pi v_{th}} \int_{\sqrt{\frac{2e|V_{sheath}|}{m_e}}}^{\infty} e^{-v^2/v_{th}^2}\, dv$$

$$= erfc\left(\sqrt{\frac{e|V_{sheath}|}{kT_e}}\right), \tag{3.4}$$

$$\text{where } erfc(x) \equiv \frac{2}{\pi} \int_x^{\infty} e^{-y^2}\, dy. \tag{3.5}$$

V_{sheath} is the sheath potential; v_{th}, $(\equiv \sqrt{\frac{2kT_e}{m_e}})$, is the electron thermal velocity; and $erfc(x)$ is the complementary error function. Taking the classical sheath potential of $3T_e$, only 1.44% of the electrons will penetrate through the negative sheath. Therefore, the first mesh is designed for an incident electron density up to 4×10^{13} cm^{-3}. Since each mesh also physically absorbs a large fraction of incident electrons, the Debye shielding limitation for the ensuing meshes is further reduced. The next two electrodes in the RFEA employ 150 lines/inch meshes with similar line weight.

3.2.2.2 Grid Transmission

The separation between the 2 meshes within the same electrode are chosen to avoid the existence of Móire fringes[20]. Then the transmission characteristics of each mesh are independent of the characteristics of the other meshes. The velocity transmission characteristic is in general a function of the component geometry, the particle energetics, the applied potential, and magnetic field strength and direction. Once again we can use the 3-D Monte-Carlo code to predict the transmission characteristics of particles through the meshes. By simulating the geometry of the meshes and stipulating a potential distribution function that simulates the analyzer's operation, we can conduct a study of the velocity

transmission characteristics as a function of applied mesh potential. A sheath acceleration component is added onto v_z (see Appendix C).

The transmission experiment is carried out by simulating a biased double-sided mesh electrode. The mesh position is determined by choosing a starting position of the mesh by random numbers generated by the code. Therefore the two meshes within the same electrode will have different alignment with respect to the slit position. This should not be an important factor if the meshes are sufficiently far apart as stipulated by the Móire fringe test. In other words, the process of particle transmission through each mesh should be a Markoff process, i.e. each process is independent of the next and the particles *forget* all previous encounters.

Figure 3.7 shows the transmission characteristics for all three velocity components while the electrode is biased at +10 volts. The launched distribution functions were described in the previous section. The fraction of particles reflected by the mesh potential is monitored and found to be in excellent agreement with equation (3.5) if V_{sheath} is replaced by the mesh potential.

No apparrent preferential cut-off for any region of the perpendicular velocity components is noticeable. The parallel transmission characteristic remains constant throughout most parts of the distribution. At large v_z, the transmission coefficient is increased. This is partially due to poor statistics, but the transmission characteristic may also change as a function of the parallel velocity and the mesh biased potential. These are important considerations in determining the viability of the RFEA as an edge plasma diagnostic. Experimentally the ion parallel energy distribution function is found to be a Maxwellian (see section 4.1). Therefore if higher v_z components possess better transmission, the measured distribution function does not reflect its importance.

During the process of varying the mesh potential the particles are decelerated, and the gyrating particles now require a longer period of time to pass through a mesh opening. Therefore the probability of particle interaction with

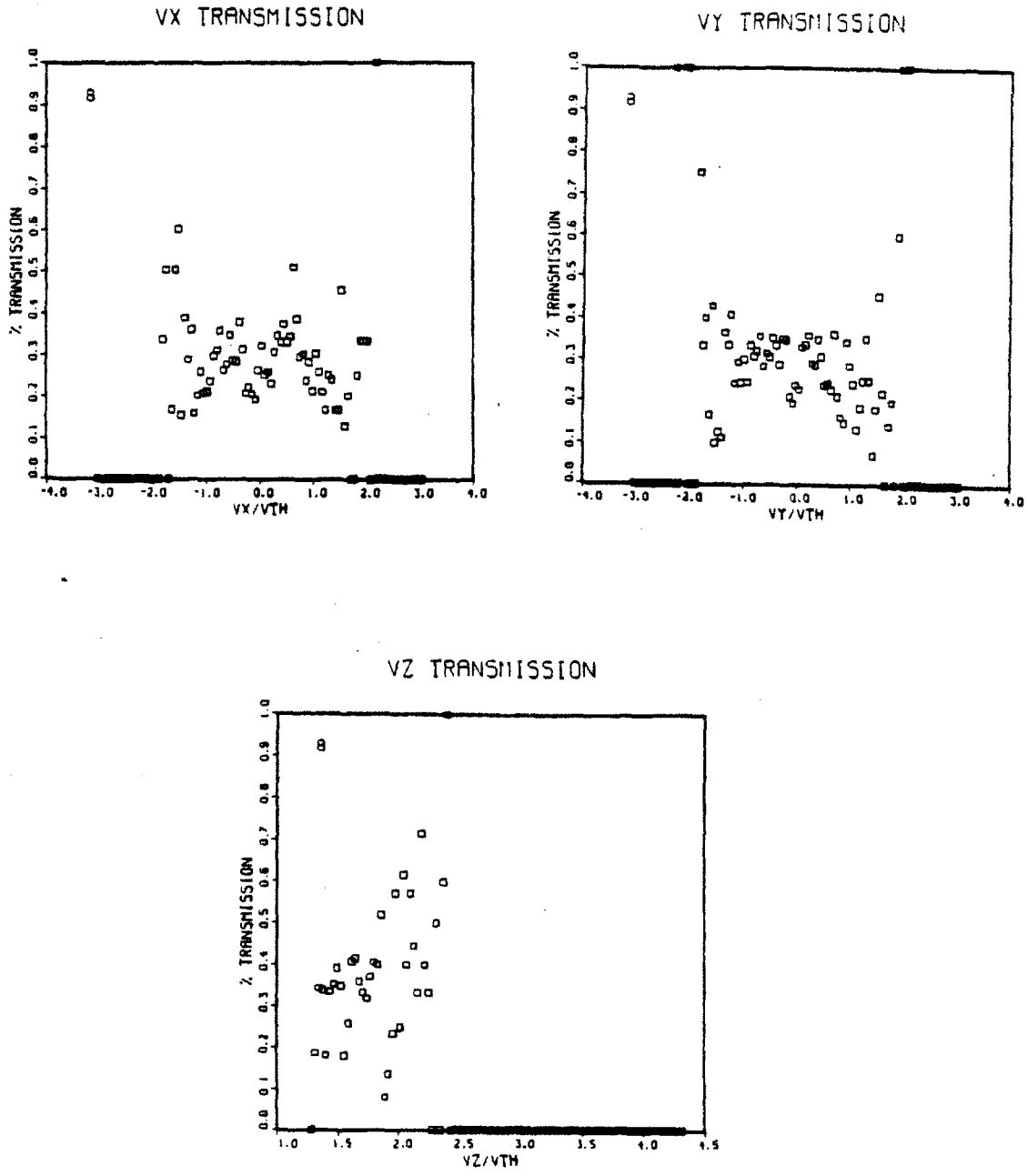

Figure 3.7 Transmission characteristics for the three velocity components of particles through a biased double-sided mesh electrode.

the mesh structure is also increased. If the transmission coefficient is a strong function of mesh potential, then the collected signal will not reflect the true distribution of the particles before the entering the analyzer chamber. Then the RFEA will not be a viable diagnostic in terms of measuring the particles' parallel energy distribution functions. Using the Monte-Carlo code, it is found that both the mesh geometries and biasing schemes used for the Janus RFEA design produce very weak perturbations in the overall parallel energy distribution functions. Therefore the overall transmission coefficient, T_T, is just the multiple of all the individual component's transmission coefficient, T_j:

$$T_T = \prod_{j=1}^{n} T_j. \tag{3.6}$$

Here T_j's designate the contributions of the slit and meshes totalling n components.

3.2.2.3 Space Charge Limitation

In the absence of magnetic field, the maximum allowed incoming current density due to space charge limitation, J_{max}^{C-L}, is determined by the analyzer's biasing scheme and the electrode separation distance[20,31]. This space charge limitation is often referred to as the Child-Langmuir Law. A simple derivation of the Child-Langmuir Law is presented in section 2.1. This law can pose a severe limitation upon the operating limit of the RFEA. For an RFEA setup with a deuterium Maxwellian, Molvik[20] calculated the current density limit, yielding:

$$J_{max}^{C-L} = 3.85 \times 10^8 \frac{(V+\Phi)^{1.5}}{(z-z_m)^2} \left[1 + 0.0247\sqrt{\frac{T_i}{V+\Phi}}\right] (\mathrm{A/cm^2}), \tag{3.7}$$

where V is the potential between grids in eV, Φ is the averaged particle energy in eV, and $z - z_m$ is the maximum grid spacing in cm. Therefore J_{max}^{C-L} is raised when the grid spacing reduces or the grid potential difference increases, allowing the particle to have higher parallel energy such that the beam diverges at a slower pace for the same distance travelled.

In a highly magnetized environment such as that in Alcator C, the charged particles observe Brillouin flow[21,32,33]. The particles gyrate about the magnetic field with the gyrofrequency, ω_c, defined in equation (2.70). In this rotating system a particle is moving along a field line with a centripetal force, $F_{centripetal}$, where

$$F_{centripetal} = m\rho\omega_c^2. \tag{3.8}$$

ρ is the Larmor radius of the charged particle (equation 3.3).

Brillouin flow occurs when the outward electrostatic force due to the space charge effect is balanced by the centripetal force imposed by the magnetic field. By equating $F_{centripetal}$ to the space charge force, one obtains the maximum current density that can be confined to a beam without divergence:

$$J_{max}^{Brillouin} = 5.86 \times 10^{-4}\ \mu^{-1.5}\ B^2\ \Phi^{0.5}\ (\mathrm{A/cm^2}), \tag{3.9}$$

where B is in tesla. Assuming $B \sim 8$ tesla, $\Phi \sim 30$ eV, and a deuterium plasma, $J_{max}^{Brillouin} \sim 0.073$ A/cm^2. This is about a factor of 600 greater than J_{max}^{C-L} at a comparable condition. However, $J_{max}^{Brillouin}$ is also about 2 orders of magnitude smaller than the expected plasma current density for a 1×10^{13} cm^{-3} deuterium plasma.

Several factors need to be keep in mind in determining the proper current density limit. Since the particles are gyrating, the area occupied by the charged

particles after entering the narrow slit region are enlarged, effectively reducing the actual current density within the analyzer chamber. In addition, before encountering the first mesh, there are both ions and electrons present in the charged particle beam, adding a neutralizing effect in reducing the diverging action of a single species beam. However, this is also a complicated phenomenon to analyze since ions and electrons have very different Larmor radii and the electrons reside near the central portions of the beam. After the first electrode, a large fraction of the particles are absorbed on the meshes, once again reducing the actual current density in the succeeding stages of the analyzer.

These analytic current density limits can only provide rough estimates of the limitations. The only thorough solution would be provided by solving the problem with a 3-D numerical solution of Poisson's equation combined with particle tracing capability in a complicated magnetized environment. However, we can experimentally investigate the space charge problem by studying the pattern of the collected current as a function of the biased voltage. By sweeping the mesh voltage up and down, for example by using a triangular sweep, if the space charge limit is violated, the collected current will exhibit a hysteresis pattern instead of retracing the same pattern during ramp-up and ramp-down[25]. This biasing technique is also the standard operating mode of the Janus RFEA. Successive traces can be overlapped to examine the space charge effects. Thus far there is no apparent violation of the space charge limitation within the operating regime of Janus.

3.2.2.4 Perturbation to the Parallel Energy Distribution Function

For accurate parallel distribution measurements it is important to study any possible mechanism that might shift parallel energy into the perpendicular components, and vice versa. This type of defocusing action can occur if there are nonuniform potential surfaces and/or lens effects.

A likely cause of nonuniformities at the potential surfaces inside the analyzer is the shape of the meshes. Etched meshes are used instead of woven meshes in order to minimize local potential perturbations. When welding the meshes onto electrodes, the meshes must be stretched uniformly in order to ensure a flat mesh surface.

Lens effect produced by the mesh opening can be characterized by the Davisson-Calbrick formula[34],

$$|f| = \frac{4\Phi}{|E_2 - E_1|}, \tag{3.10}$$

where f is the focal length, and E_2 and E_1 are the electric field intensities on the two sides of the opening. For RFEA parameters, $|f|$ is on the order of meters, much larger than the mesh opening which has dimension of order 10^{-4} m. Another way of examining the lens effect is to calculate the energy resolution of the particle as it passes through the mesh opening. The energy resolution can be characterized as

$$\frac{\Delta\Phi}{\Phi} \approx \frac{a_{mesh}^2 (E_2 - E_1)^2}{16\ V_{mesh}^2} \approx \frac{a_{mesh}^2}{16\ d_{grid}^2}, \tag{3.11}$$

where a_{mesh} and V_{mesh} are the effective mesh radius and mesh potential respectively, and d_{grid} is the separation distance between two adjacent meshes. The energy resolution for the Janus RFEA is on the order of 10^{-5}.

3.2.2.5 Other Considerations

The meshes are subjected to large heat flux and may be damaged by melting. This is especially crucial for the first mesh after the slit. The electron microscopic photograph (figure 3.8) shows a damaged stainless steel electrode

that was used in the proof-of-principle experiment. The area that was melted was positioned directly behind the slit. Only the first mesh was partially melted; the second mesh was undamaged. For the Janus design, etched tungsten meshes replaced the stainless steel meshes.

3.2.3 Electronics

Two different types of electronics are required to operate the RFEA: those that supply the biased potentials and those that link the analyzer output to the CAMAC data acquisition system. One of the main limitations of the proof-of-principle experiment lies in the available programmable power supplies. To study high temperature plasmas the mesh must be biased at really high voltages. KEPCO BOP-72M was used in the first experiment which can only be biased up to ± 72 volts.

For the Janus operation, we employed the KEPCO BOP-500 operational amplifiers which can go up to ± 500 volts. The waveforms input to the amplifiers are generated by using a programmable LeCroy 8601/8201 complex function generator. Before every shot the computer searches for a special input file that contains the bit-by-bit information of the desired waveforms. A total of 4 independent complex waveforms can be contained in the input file, generated by the function generator, and fed into the programmable amplifiers. Thus we have the freedom to control the RFEA operation by manipulating the input file.

Figure 3.9 illustrates the electrical network that runs the RFEA. For typical operations only two of the electrodes are needed. Furthermore, due to the limitation of available power amplifiers and for simplicity of operation and analysis, the electrodes on both sides of Janus that perform the same function share the same amplifier. This poses a problem on the total allowable operating current of the BOP-500. At extremely high plasma densities the impinging ion current on the meshes could saturate the amplifiers

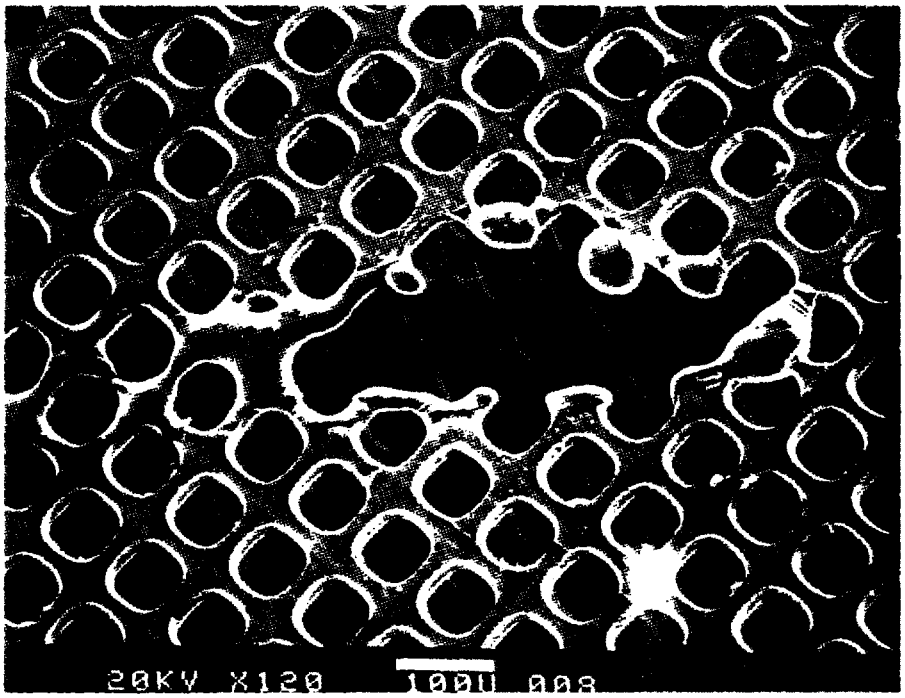

Figure 3.8 Photomicrograph showing partial melting of the first mesh that was place immediately behind the slit. The second mesh was undamaged.

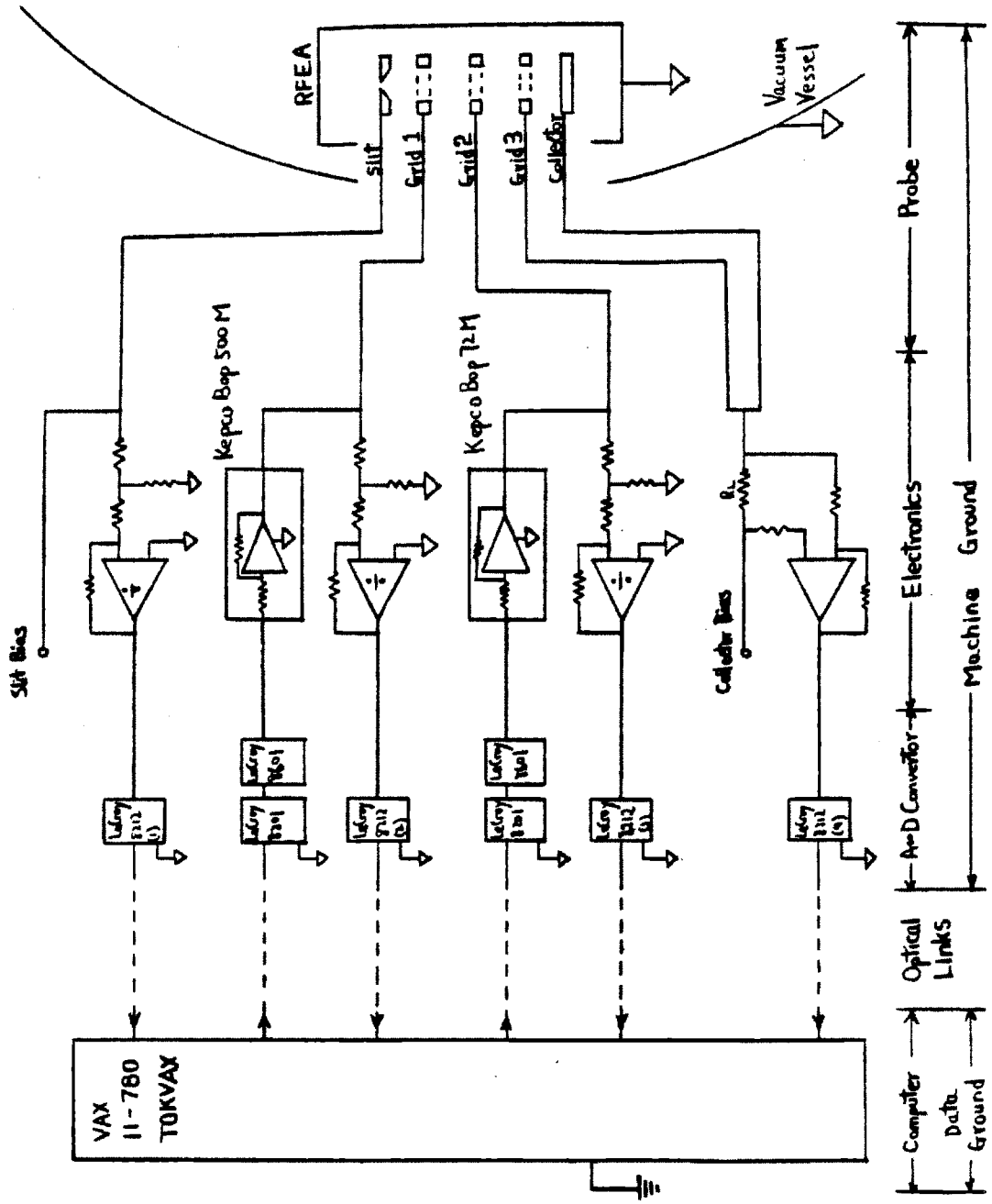

Figure 3.9 RFEA electrical network.

The electronics linking the electrodes and collectors to the CAMAC modules must be designed such that the output of the electronics must be less than ± 5 volts. Each electrode potential must be monitored for analysis purposes. Since the electrodes can be biased to really high voltages, the associated electronics are just carefully calibrated voltage dividers. Figure 3.10 shows a divided by 60 circuit.

The collector electronics must monitor the collected current. Two circuits are used for this purpose and work equally well. They are illustrated in figures 3.11.1 and 3.11.2. The load resistances (both circuits) and the circuit gains (circuit B only) must be constantly adjusted to maximize the output voltage without going over the ± 5 volt limit. Circuit A uses an isolated instrumentation amplifier set up in differential mode. Circuit B is more flexible, but also more complicated. The first stage of the circuit has two carefully balanced voltage dividers to reduce the input voltage down to the operating limit of the operational amplifier. The second stage differentiates the reference leg and the signal leg before the final stage amplifying the output back up to $\sim \pm 5$ volts.

3.3 Langmuir Probe

Due to its simplicity and versatility, the Langmuir probe is probably the most frequently used edge plasma diagnostic[35,36]. Depending on the variety of Langmuir probe used and the operational and analysis techniques, the Langmuir probe offers a wealth of valuable plasma information. Thus the Langmuir probe is an excellent complementary diagnostic to the RFEA. Besides providing an independent check on the measured T_e, the Langmuir probe also measures the plasma density, the ion saturation current, the floating potential, and edge fluctuations. Section 4.2 will go into detail on the probe theory used for the Janus Langmuir probe analysis.

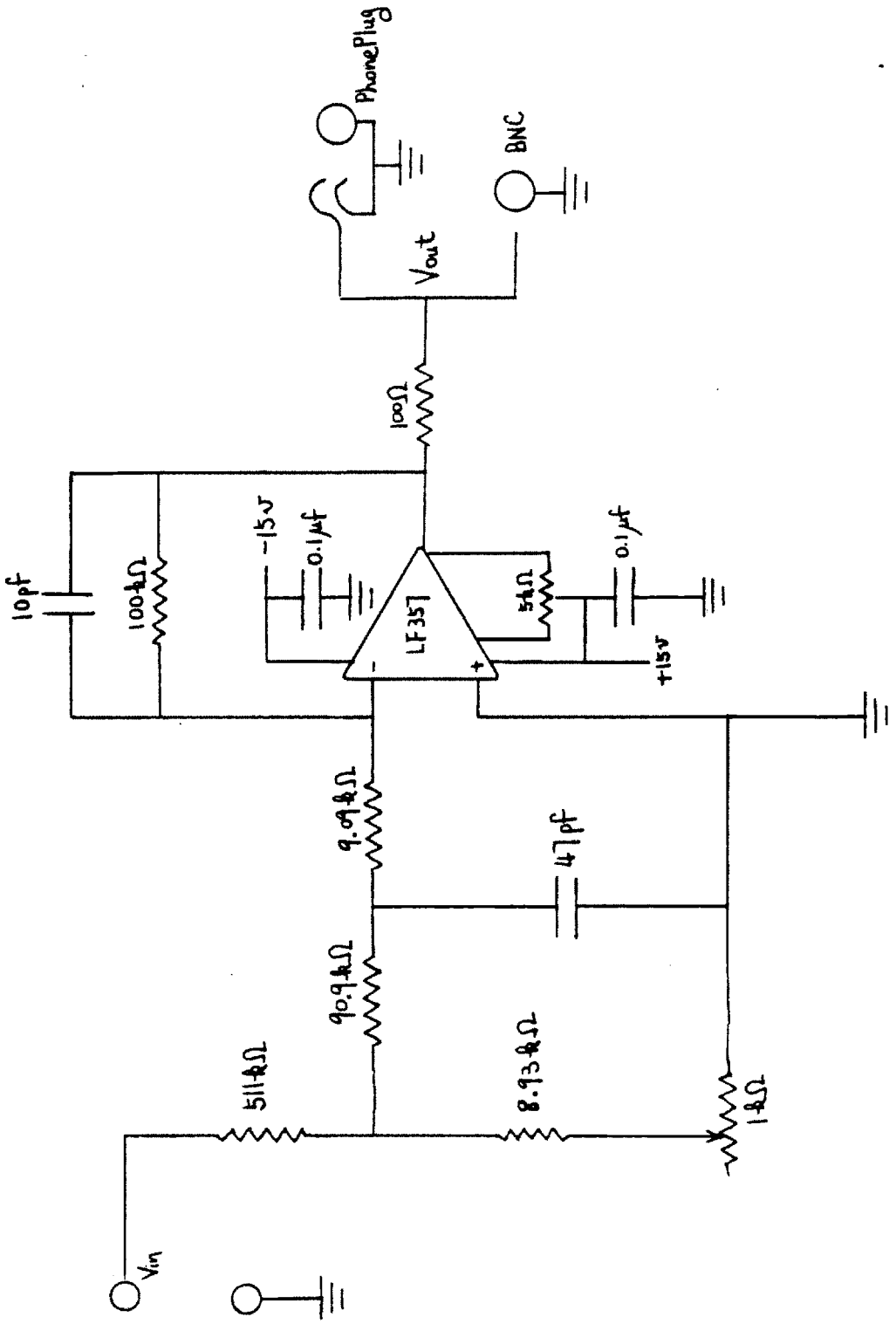

Figure 3.10 Circuit diagram of a divided by 60 circuit used for monitoring the bias voltage of the RFEA electrodes.

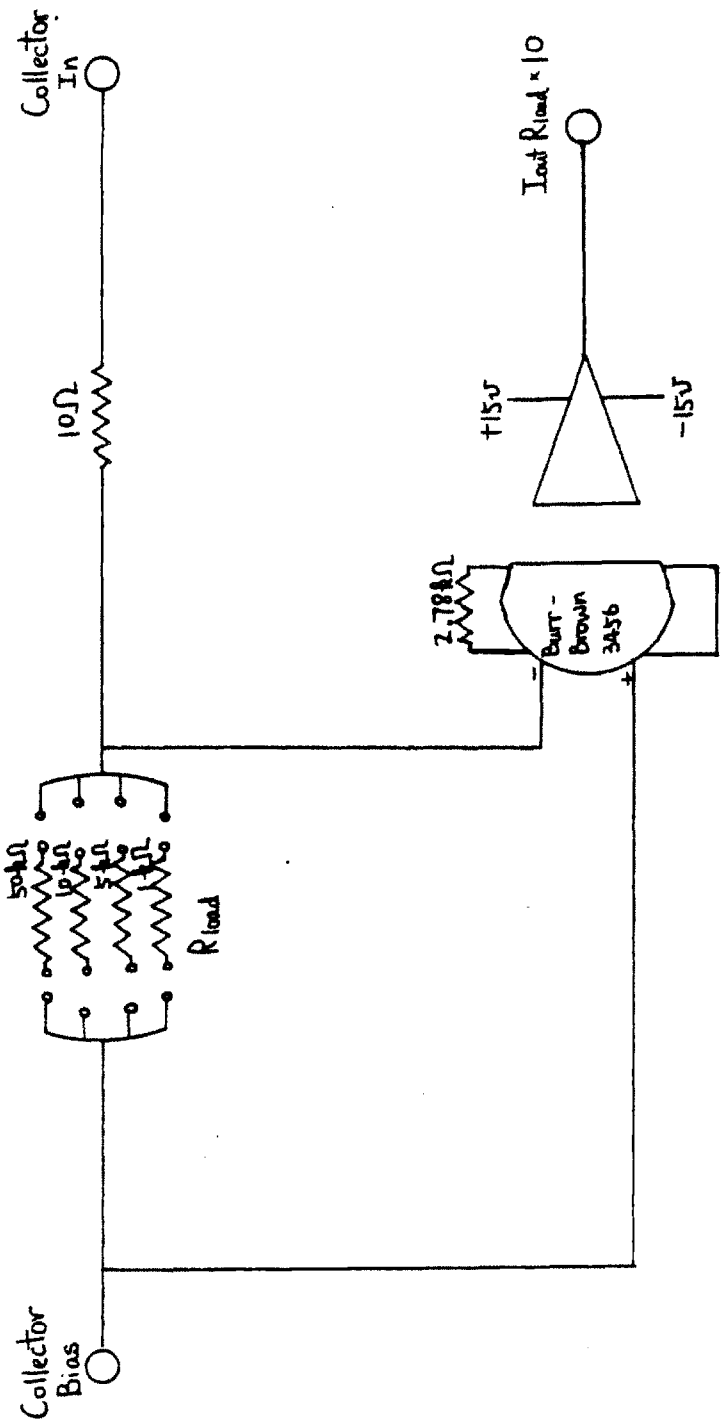

Figure 3.11.1 Circuit A used for monitoring the collected current.

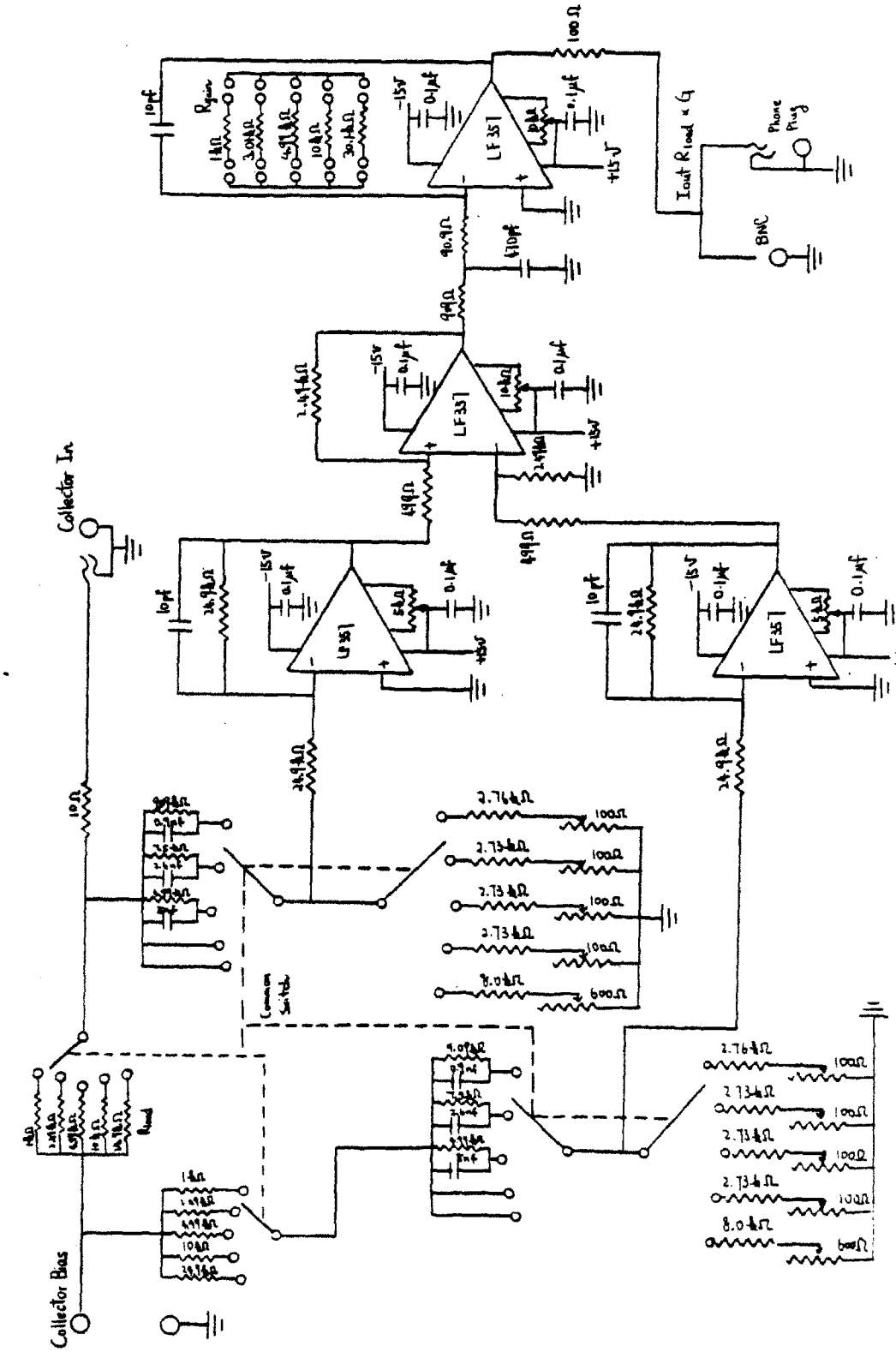

Figure 3.11.2 Circuit B used for monitoring the collected current.

The Janus Langmuir probe is a simple, single conductor probe that protrudes from the Janus housing. The center of the probe is aligned with the RFEA slit position. The Langmuir probe consists of a cylindrical tip supported on a smaller-diameter ceramic-insulated wire which makes the electrical connection back through the housing. The tip is also larger in diameter (along a field line) than the ceramic insulator covering the support wire in order to avoid metallic deposition onto the insulator which might cause an electrical connection of the probe to the Janus housing. The entire Langmuir probe is made of molybdenum and no melting or arcing was evident during the entire operation of the Janus. Figure 3.12 shows the cross-sectional view of the Janus Langmuir probe assembly. As figure 3.4 illustrates, the Langmuir probe actually nests within the RFEA insulators.

The Langmuir probe electronics used are similar to the RFEA electronics and are described in more detail elsewhere[5]. The power supply used is a high power audio amplifier made by TECRON. The input waveforms are generated by a Tektronix function generator.

3.4 Calorimeter (Heat Flux Probe)

The calorimeter is designed to infer the real time parallel plasma heat flux, $q_{\parallel}(t)$, incident onto an electrically floating plate. The calorimeter must be designed to handle high heat flux and to have a fast thermal response time for real time measurements.

Figure 3.13 shows a cross-sectional view of the Janus calorimeter. The design is basically divided into two separate sections: the thermocouple and the calorimeter plate. The plate is pinned to the calorimeter holder by two ceramic pin-and-washer assemblies which isolate the plate electrically (see figure 3.4). The thermocouple is spot-welded onto the plate. Each thermocouple wire passes through the detachable probe head region previously described, before

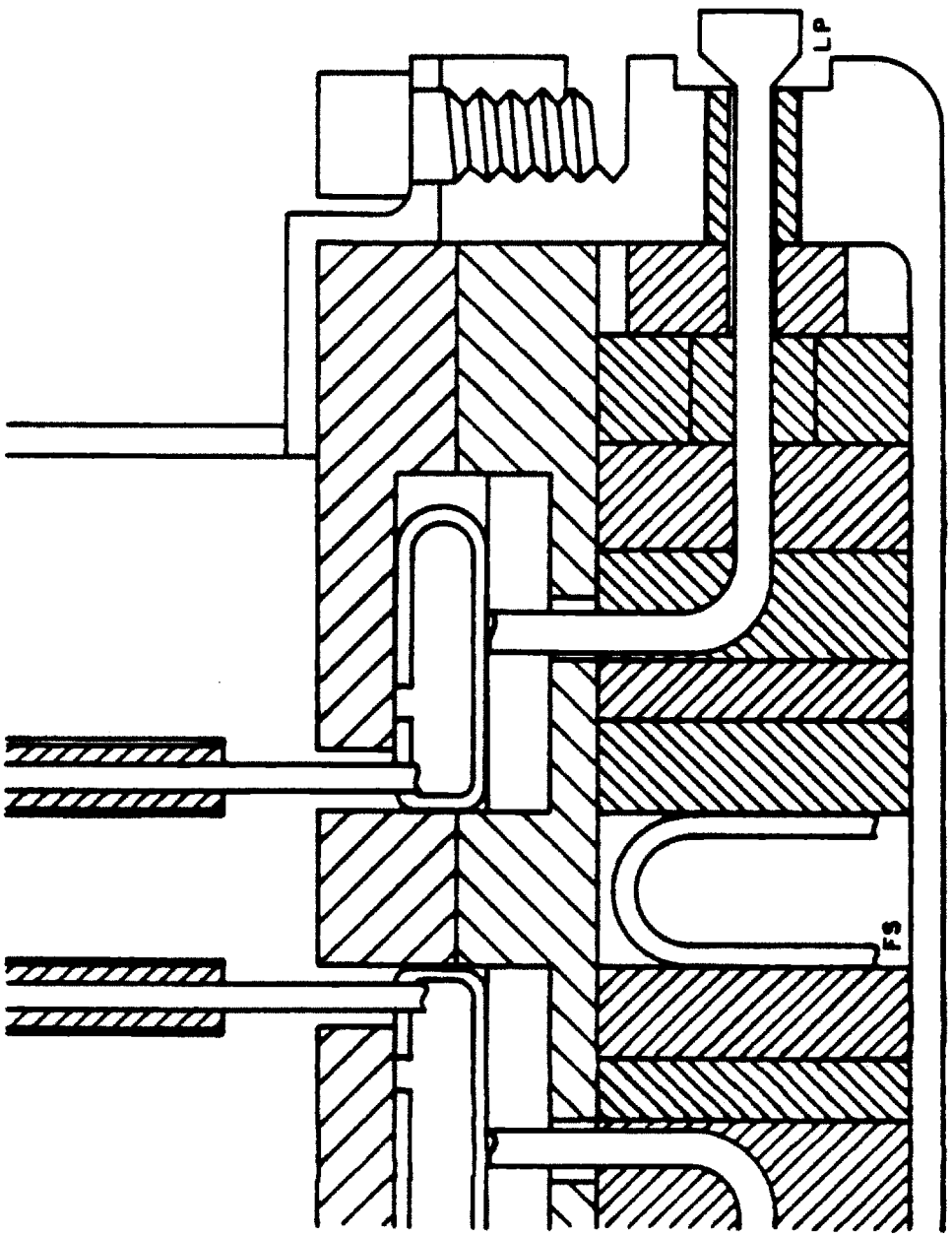

Figure 3.12 Cross-sectional view of the Janus Langmuir probe assembly.

reconnecting onto a connecting thermocouple wire. As long as there is no large temperature gradient in the detachable region, no significant error should occur as the result of the addition of two more thermocouple junctions. At the other end of the vacuum feedthrough, ice-point references are used before the wires change into standard shielded twisted pairs.

The calorimeter electronics are quite simple. The operational amplifiers must be isolated while providing excellent common-mode rejection and gain functions. A Burr-Brown 3456 isolation instrumentation amplifier with variable gain settings serves these needs well. In the meantime the potential of one of the thermocouple legs is monitored to determine the floating potential.

3.4.1 The Calorimeter Thermocouple

There are several criteria to use in choosing a proper thermocouple. For operation at high temperatures, three types of thermocouples were considered: chromel-alumel (type K), tungsten-rhenium, and platinum-rhodium. In addition, in a noisy environment such as the tokamak edge it is desirable to have a large change in the induced emf, i.e., Δemf, for a small change in the plate temperature.

Platinum-rhodium thermocouples are easily reduced and can only operate in a vacuum for a very short period of time unless they are properly coated. Tungsten-rhenium thermocouples are easily oxidized and are extremely brittle. In addition, both of these thermocouples have smaller change of induced emf per degree temperature rise as compared with the chromel-alumel thermocouples. Chromel and alumel are very easy to machine and the thermocouple can come in various shapes and sizes. The Janus design utilizes this machineability property and uses the NANMAC flat ribbon thermocouple to minimize the thermal response time. Therefore, despite a lower operating temperature limit

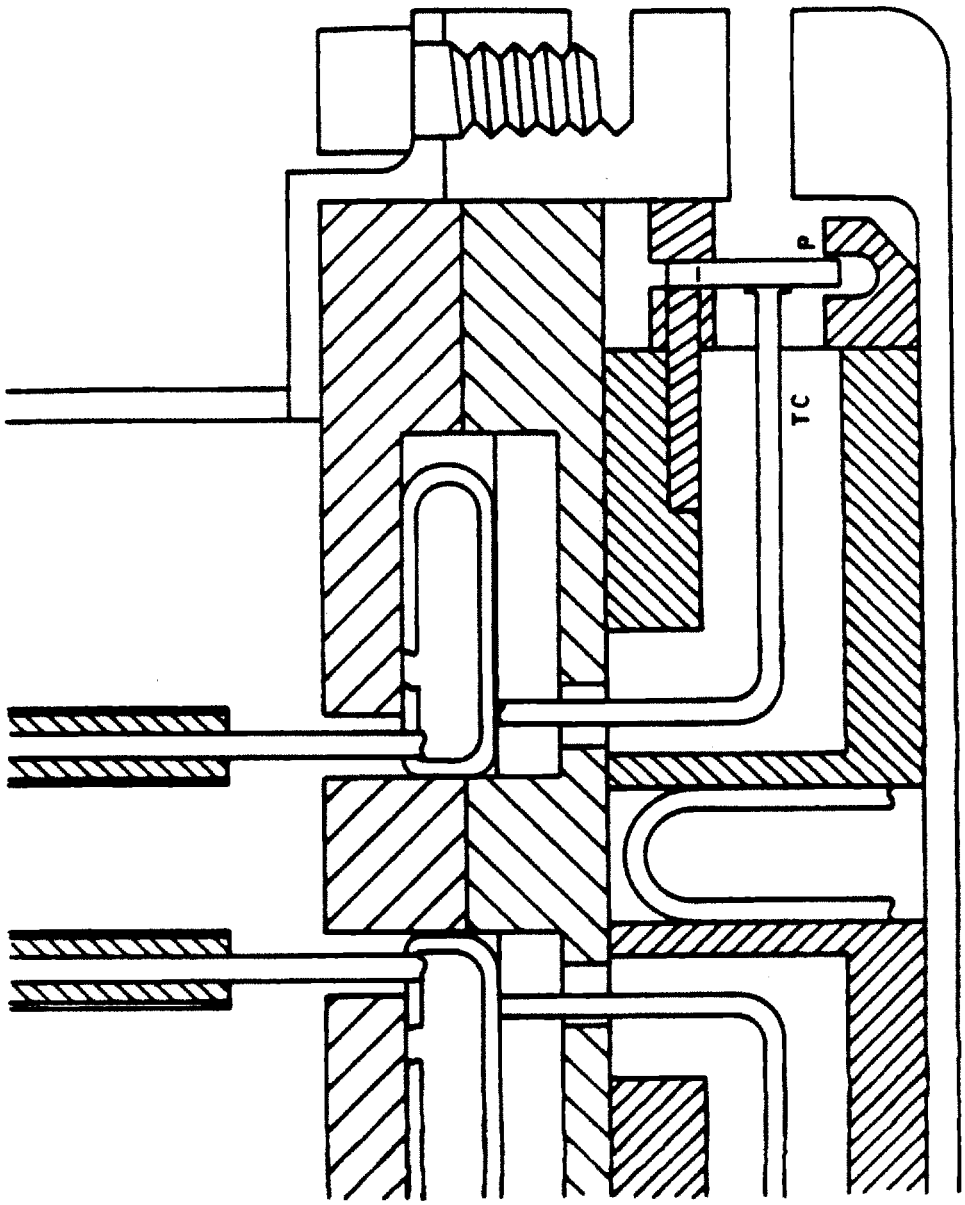

Figure 3.13 Cross-sectional view of the Janus calorimeter.

($\sim$ 1300°C), a chromel-alumel thermocouple was chosen over the other candidates.

3.4.2 The Calorimeter Plate

The calorimeter plate must have fast thermal response while still being able to withstand high heat fluxes. Table 3.1 lists the thermal properties of the materials under consideration, including tungsten, molybdenum, and tantalum. Properties been compared include the melting point (T_{melt}), and room temperature values of thermal conductivity (k_c), specific heat (C_p), and density (ρ_D). All thermal properties, however, vary with respect to the material temperature. These temperature dependences are tabulated in reference 37.

A simple comparison between the materials on their ability to withstand high heat fluxes can be achieved by performing a simple energy balance while neglecting the temperature dependence of the thermal properties:

$$q_{max} = \frac{\Delta T\ \rho_D\ C_p\ V_c}{\Delta t\ A_{exp}}. \tag{3.12}$$

Here q_{max} is the maximum permissible heat flux that would cause a temperature rise ΔT during a period of time Δt. ΔT is set equal to the difference between the melting point and the initial temperature. V_c equals the total calorimeter volume and A_{exp} is the plate area exposed to the incident heat flux.

Figure 3.14 shows the plot of q_{max} versus Δt for the materials under consideration. q_{max} is set to the maximum operating limit of a chromel-alumel thermocouple. Initial plate temperature is set at $300\,K$ and the plate thickness is 0.635 mm. For a typical Alcator C discharge lasting $\sim$ 500 ms, both tungsten and molybdenum can withstand constant heat fluxes exceeding 1 kW/cm^2.

material	T_{melt} K	k_c W/(m-K)	C_p J/(kg-K)	ρ_D kg-m^{-3}
Tungsten	3683	163.0	134.7	1.93×10^4
Molybdenum	2890	135.0	249.8	1.02×10^4
Tantalum	3269	57.7	139.7	1.67×10^4

Table 3.1 Room temperature thermal properties of the calorimeter plate materials under consideration.

Molybdenum is slightly better due to its higher C_p value. The temperature dependence of the thermal properties would produce a variation by approximately 10%.

In the Janus design tungsten was chosen over molybdenum due to its superior thermal response time, yielding a better measurement of the real time heat flux. Ideally the calorimeter should be able to record instantaneous temperature changes while having sufficiently long cool-down time such that the cool down would not affect the real time heat flux measurement. The calorimeter, however, must be cooled back down to the ambient temperature before the next plasma discharge.

By using an infinite thin plate approximation, we can reduce the problem down to a 1-D (x), time (t) dependent problem:

$$\frac{\partial^2 T(x,t)}{\partial x^2} = \frac{1}{\alpha}\frac{\partial T(x,t)}{\partial t}, \tag{3.13}$$

$$\text{where } \alpha \equiv \frac{k_c}{\rho_D C_p}. \tag{3.14}$$

$T(x,t)$ is defined as the plate temperature, and α is the thermal diffusivity. Initially the plate is at a uniform temperature T_0. Then a constant heat flux q_0 is imposed on the $x = \delta_L$ surface starting at $t = 0$. δ_L equals the thickness of the thin plate. At $x = 0$ we assume a perfectly insulated surface. The boundary conditions can be mathmatically described as:

$$@\, x = 0, \quad \frac{\partial T}{\partial x} = 0, \tag{3.15}$$

$$@\, x = \delta_L, \quad \frac{\partial T}{\partial x} = \frac{q_0}{k_c}. \tag{3.16}$$

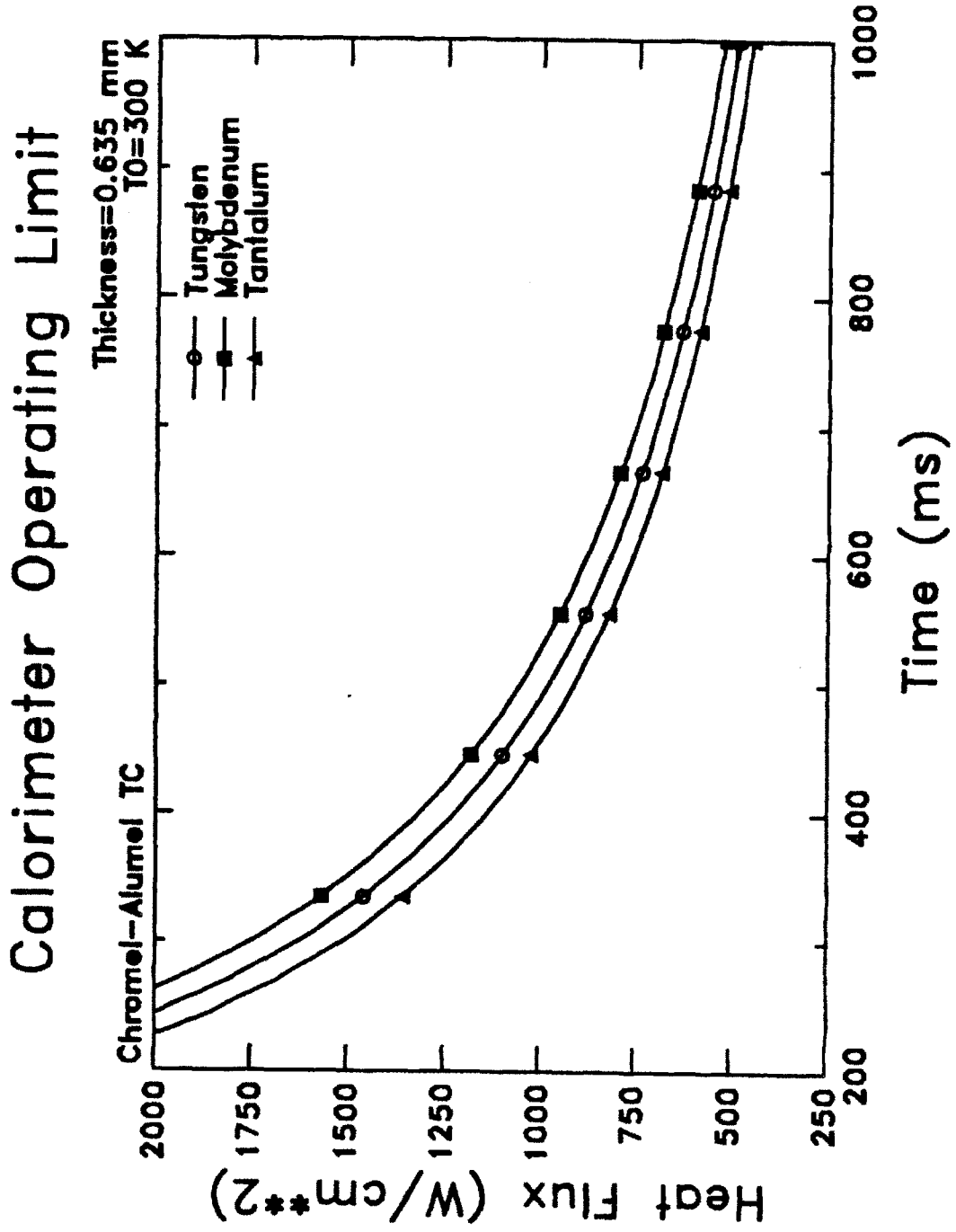

Figure 3.14 q_{max} versus Δt for various calorimeter plate materials under consideration.

This problem can be solved analytically to obtain the time and spatial dependences of the plate temperature evolution. The solution includes a transient contribution ($T_{tr}(x,t)$) due to the onset of the heat flux, and a steady state component ($T_{ss}(x,t)$) from the ensuing constant heat flux. Solving for equations 3.13-3.16, we obtain:

$$T_{ss}(x,t) = \frac{q_0 t}{\rho_D C_p \delta_L} + \frac{q_0 x^2}{2k_c \delta_L}, \text{ and} \tag{3.17}$$

$$T_{tr}(x,t) = T_0 - \frac{q_0 \delta_L}{6k_c} - \sum_{n=1}^{\infty} \frac{2q_0\delta_L}{n^2\pi^2 k_c} (\cos n\pi)(\cos \frac{n\pi x}{\delta_L}) e^{-n^2\pi^2 \alpha t/\delta_L^2}. \tag{3.18}$$

In the actual Janus calorimeter design only about 40% of the total plate area is exposed to the incident plasma. The rest of the area is hidden behind the aperture to protect the Al_2O_3 insulators and the pin-washer combination previously described. To analyze this 3-D effect properly we would need a 3-D thermal transport code to examine the time dependence of the temperature spreading. As a refinement of the infinite plate approximation we can define δ_L to be the ratio of the plate volume over the exposed area. In addition, the additional thermal mass of the thermocouple welded at the rear of the plate must also be considered in estimating the final response time $\tau_{response}$. The exact determination of $\tau_{response}$ is not critical in that its value does not affect the accuracy of the data analyzed.

Using equations 3.17 and 3.18, figure 3.15 shows of time histories of the temperature evolutions at several locations of the calorimeter plate, at $x = 0$, $x = \delta_L$, and at the mid-plane. For this calculation we chose a 0.635 mm thick tungsten plate with a chromel-alumel thermocouple. The plate is initially at a uniform temperature of $300\,K$ and is subjected to an incident heat flux of 1

kW/cm^2. The transient contribution dies down within the first 10 ms following the onset of the heat pulse. We also see that the temperature differential between the front and rear surfaces is about $40\,K$ and the time required ($\sim \tau_{response}$) for the rear surface (temperature) to reach that of front surface (temperature) is about 20 ms.

From equations 3.17 and 3.18 we can once again derive a method to judge the merits of the materials under consideration. By adding the two equations together and setting

$$T(\delta_L, t_1) \quad = \quad T(0, t_2), \tag{3.19}$$

we can the determine the thermal response time:

$$\begin{aligned} \tau_{response} &= t_2 - t_1, \\ &= \frac{\rho_D \; C_p \; \delta_L^2}{2 \; k_c}. \end{aligned} \tag{3.20}$$

From table 3.1, we determine that tungsten has the best overall thermal properties handling high heat fluxes while maintaining a fast thermal response time. Unfortunately the energy and particle backscattering coefficients of plasma incident upon a certain material are ignored in the design process. Tungsten has one of the highest *predicted* reflection coefficients which yields a smaller temperature increase per incident heat load. The uncertainty of the values of the actual reflection coefficients also brings a high degree of uncertainty into the analysis process. This problem will be discussed in more detail in section 4.3 and in chapter 8.

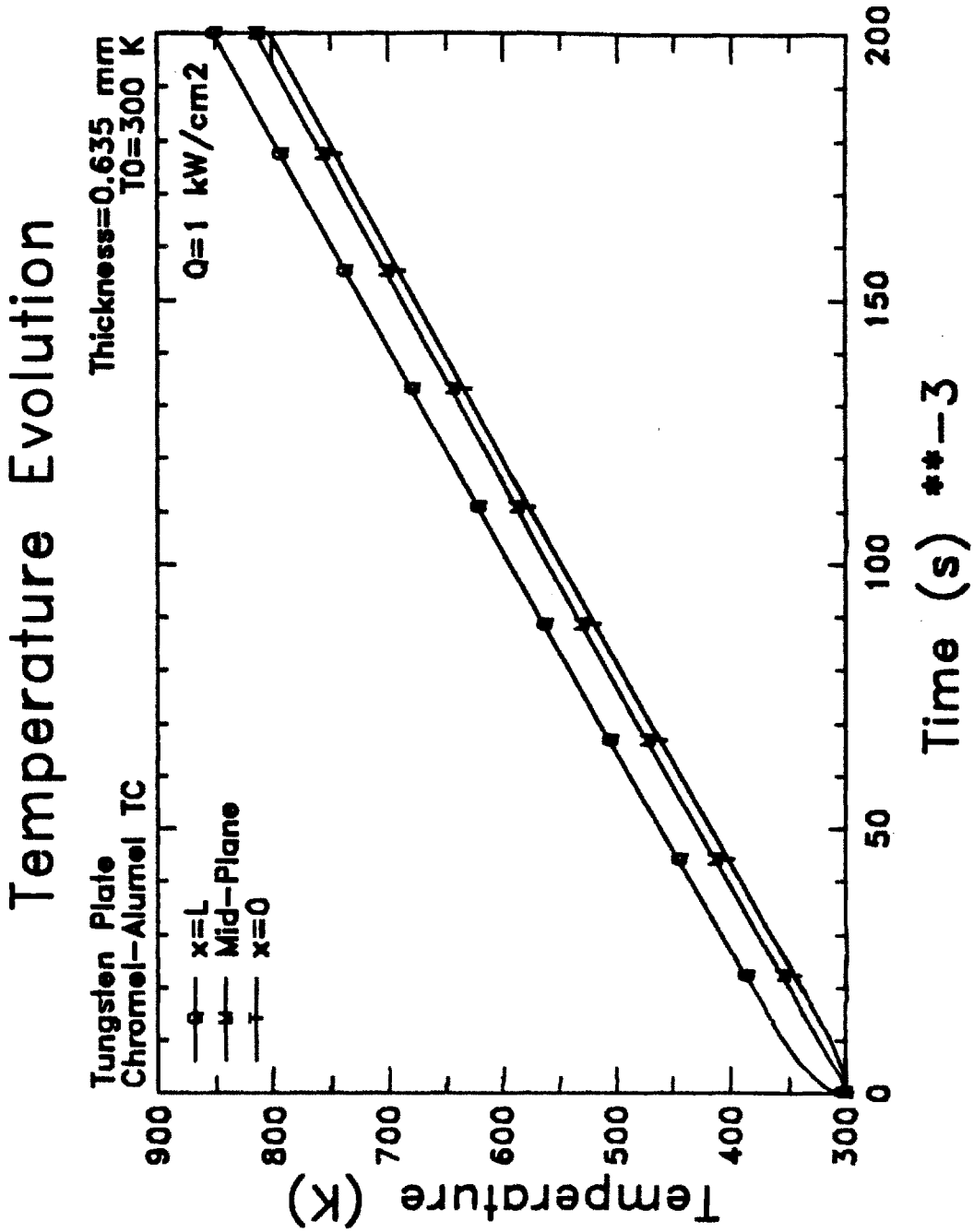

Figure 3.15 Time histories of the temperature evolutions at $x = 0$, $x = \delta_L$, and at mid-plane of a tungsten calorimeter plate. $q_0 = 1$ kw/cm^2, and $T_0 = 300°K$.

3.5 Data Acquisition

The data acquisition setup utilizes the MDS system[24] which controls all the CAMAC modules including the LeCroy 8212/32 Channel Digitizer and the LeCroy 8601/8201 Complex Function Generator previously mentioned (in section 3.2.5). The 8212 is an analog-to-digital convertor that links between the output electronics of each diagnostic and the VAX 11/780 computer (TOKVAX).

Typically the 8212 digitizes at 10 kHz. Therefore, by monitoring only 16 of the 32 channels, the memory space allows us to sample 6144 data points. The digitizer is typically triggered at 30 ms before the initiation of the discharge breakdown. Aside from recording the output channels of the Janus diagnostics, it is necessary to record the input bias voltage readings for analysis purposes. In addition, a separate header file is recorded for every shot to keep track of the operating settings for all the electronics.

References

[1] Manos, D. M., McCracken, G. M., "Probes for Plasma Edge Diagnostics in Magnetic Confinement Fusion Devices," Proceedings of NATO Advanced Study Institute on Plasma Surface Interactions, Val Morin P.Q., Canada (August 1984).

[2] Cohen, S. A., "Measuring Hydrogen Isotope Density and Velocity Distributions of the Tokamak Edge Plasma," Proceedings of IEEE Int'l. Conf. on Plasma Science, Montreal, Canada (1979).

[3] Lipschultz, B., LaBombard, B., Marmer, E. S., Pickrell, M. M., Terry, J. L., Watterson, R., Wolfe, S. M., "MARFE : An Edge Plasma Phenomenon," *Nucl. Fusion* **24**, 977 (1984).

[4] Boody, F. P., Bush, C. E., Medley, S. S., Park, H., Schivell, J., "Macroscopic Edge Phenomena in TFTR: MARFEs, Moving MARFEs, and Detached Plasmas," *Bull. Amer. Phys. Soc.* **30**, 1518, paper 6P7 (Nov 1985).

[5] LaBombard, B., "Poloidal Asymmetries in the Limiter Shadow Plasma of the Alcator C Tokamak," M.I.T. Doctoral Thesis, April 1986.

[6] Gentle, K. W., Klepper, C. C., Rowan, W. L., "Possible Poloidal Asymmetries in Particle Transport in Edge Region of Tokamaks," *Bull. Amer. Phys. Soc.* **30**, 1567, paper 7R10 (Nov 1985).

[7] Stangeby, P. C., McCracken, G. M., Erents, S. K., Matthews, G., "DITE Langmuir Probe Results Showing Probe-Size and Limiter-Shadow Effects," *J. Vac. Sci. Technol. A* **2**, 702 (1984).

[8] Zweben, S. J., Taylor, R. J., "Edge-Plasma Properties of the UCLA Tokamaks," *Nucl. Fusion* **23** 4, 513 (1983).

[9] Wan, A., Lipschultz, B., Yang, T., LaBombard, B., "Directional Measurement of Edge Electron and Ion Parameters on Alcator C," *Bull. Amer. Phys. Soc.* **30**, paper 3F6, 1413, (Nov 1985).

[10] Cohen, S., "Tokamak Plasma Diagnostics by Surface Physics Techniques," *J. Nucl. Mat.* **76 & 77**, 68–77 (1978).

[11] Staudenmaier, G., Staib, P., Behrish, R., *Nucl. Fusion* **20** 1, 96 (1980).

[12] Staib, P., "An E × B Analyzer to Study the Particle Fluxes, Energy, and Charge State in the Scrape-Off Layer of Tokamaks," *J. Nucl. Mat.* **93 & 94**, 351–356 (1980).

[13] Matthews, G. F., "A Combined Retarding Field Analyzer and E × B Probe for Measurement of Ion and Electron Energy Distribution in Tokamak Edge Plasmas," *J. Phys. D: Appl. Phys.* **17**, 2243–2254 (1984).

[14] Staudenmaier, G., Staib, P., Porschenrieder, W., "Determination of Ion Temperatures in the Edge Plasma from Ion Flux Transmission of Apertures," *J. Nucl. Mat.* **93 & 94**, 121–126 (1980).

[15] Katsumata, I., Obazaki, M., *Jap. J. Appl. Phys.* **6**, 123 (1967).

[16] Stangeby, P. C., *et. al.*, "Edge Measurements of T_e, T_i, n, E_r on the DITE Tokamak Using a Biased Power Bolometer," *J. Vac. Sci. Technol. A* **1**, 1302 (1983).

[17] Wampler, W. R., Manos, D. M., *J. Vac. Sci. Technol.* **1** (2), 827 (1983).

[18] Kimura, H., *et. al.*, "Heat Flux to the Material Surfaces in a Tokamak," *Nuclear Fusion* **18** 9, 1195 (1978).

[19] Blackwell, B., private communication (1985).

[20] Molvik, A. W., "Large Acceptance Angle Retarding-Potential Analyzers," *Rev. Sci. Inst.* **52** 5, 704 (1981).

[21] Matthews, G. F., "The Measurement of Ion Temperature in Tokamak Edge Plasmas," Oxford University Doctoral Thesis (1985).

[22] Fiore, C., Judd, S., private communication (1983).

[23] Wan, A. S., Yang, T. F., Parker, R. R., "A Localized, Directional Edge Plasma Diagnostic on Alcator C," Bull. Amer. Phys. Society, **29**, paper 2V7, 1223 (Nov 1984).

[24] Fredian, T. W., Stillerman, J. A., "MDS Run-Time Library Routines Reference Manual," M.I.T. Plasma Fusion Center PFC/IR-85-7, June 1985.

[25] Stephanakis, S., Bennett, W. H., "Electrostatic Energy Analyzer for Studying Gas-Focused Electron Beams and Their Background Media," *The Rev. of Sci. Inst.* **39** 11, 1714 (1968).

[26] Simpson, J. A., *The Rev. of Sci. Inst.* **32**, 1283 (1961).

[27] Bonetti, A., *et. al.*, "Explorer 10 Plasma Measurements," *J. Geophysical Research*, **68**, 4017 (1963).

[28] Tonks, L., Langmuir, I., "A General Theory of the Plasma of an Arc," *Phys. Rev.* **34** 6, (1929).

[29] Self, S. A., "Exact Solution of the Collisionless Plasma-Sheath Equation," *Phys. Fluids*, **6** 12, 1762 (1963).

[30] Gierszewski, P. J., "Plasma/Neutral Gas Transport in Divertors and Limiters," M.I.T., ScD Thesis (September 1983).

[31] Langmuir, I., Compton, K. T., *Rev. Mod. Phys.* **3**, 244 (1931).

[32] Brillouin, L., "A Theorem of Larmor and Its Importance for Electrons in Magnetic Fields," *Phys. Rev.* **67**, 260 (1945).

[33] Wan, A. S., Yang, T. F., Lipschultz, B., LaBombard, B., "Janus, a Bi-Directional, Multi-Functional Plasma Diagnostic," M.I.T. Plasma Fusion Center PFC JA/85-44 (December 1985), to be published in *Rev. Sci. Inst.*

[34] Klemperer, O., Electron Optics, Cambridge University Press, New York (1953).

[35] Chen, F. F., "Electric Probes," Chapter 3 in Plasma Diagnostic Techniques, Editors: Huddlestone, R. H., and Leonard, S. L., Academic Press, New York (1965).

[36] Lipschultz, B., Hutchinson, I., LaBombard, B., Wan. A, "Electrical Probes in Plasmas," M.I.T. Plasma Fusion Center Report PFC/JA-85-29 (August 1985).

CHAPTER 4

Operational and Data Reduction Techniques

The ability to measure the proper edge parameters relies on the ways to obtain and manipulate the raw data. Sections 4.1-4.3 of this chapter will discuss in detail the operational and reductional techniques of the retarding-field energy analyzers (RFEA), the Langmuir probes, and the calorimeters respectively.

4.1 Retarding-Field Energy Analyzer

4.1.1 Operation

Provided that the RFEA components introduce negligible perturbations to both the electron and ion parallel energy distributions, the grid electrodes between the collector and the slit can be biased to collect the integrated parallel energy distribution functions of the ions and electrons. In Janus, the first 2 grids are sufficient for RFEA operation. The third grid is used as an emergency backup in case the first grid is damaged. It is usually electrically tied to the collector. The probe casing is grounded to the vacuum vessel at the access flange. All electronics are referenced with respect to this ground.

Using a LeCroy 8601/8201 Complex Function Generator we can produce the complex waveforms shown in figure 4.1. The first grid (closest to the slit) always serves as the ion repeller. The second grid serves as the primary electron repeller as well as the secondary electron suppressor. The secondary electron suppression function is achieved when the collector is biased more positively than the grid adjacent to it. Then any secondary electron emitted from the collector region will turn back to the collector as the result of the favorable electric field configuration.

During the first part of the voltage sweep shown in figure 4.1, the analyzer is operating in *ion mode*. The first electrode is swept with a triangular waveform from a large positive potential to probe ground. The action of this grid is to repel away all ions with energies less than the applied electrode potential. Simultaneously the second electrode is held at a large negative potential to repel away all primary electrons. The collector is typically at ground potential for suppressing secondary electrons.

Measurement of the electron distribution function (*electron mode*) starts after the first grid completes its triangular sweep in voltage. This part is labeled as (b) of figure 4.1. Now the first electrode is held at a very high positive potential to repel away all the primary ions. At the point where the first electrode potential levels off, the second electrode now starts to sweep from a large negative potential to probe ground and back. Thus all electrons with energies less than the second grid potential are repelled. Secondary electrons are still suppressed since during this sweep the collector is still at a more positive potential than the second grid.

The collected current is shown as solid circles in figure 4.1. It follows the behavior predicted by

$$I(V_{bias}) \quad = \quad q\, A_{slit}\, T_T \int_{qV_{bias}}^{\infty} v_{\|}\, f(E_{\|})\, dE_{\|}, \tag{4.1}$$

where A_{slit} is the total slit area and V_{bias} is the biasing potential of the primary retarding electrode. $v_{\|}$ and $E_{\|}$ are defined as the particle parallel velocity and parallel energy respectively. T_T is the total transmission coefficient calculated by equation 3.6. q is the charge of the incoming particle. Keep in mind that $q_i \equiv$ ion charge $= Ze$, where Z is the ion charge state, and $q_e \equiv$ electron charge $= -e$. All particles possessing parallel energy, $E_{\|}$, larger than the biased potential, V_{bias}, will be collected provided they are transmitted through all analyzer components.

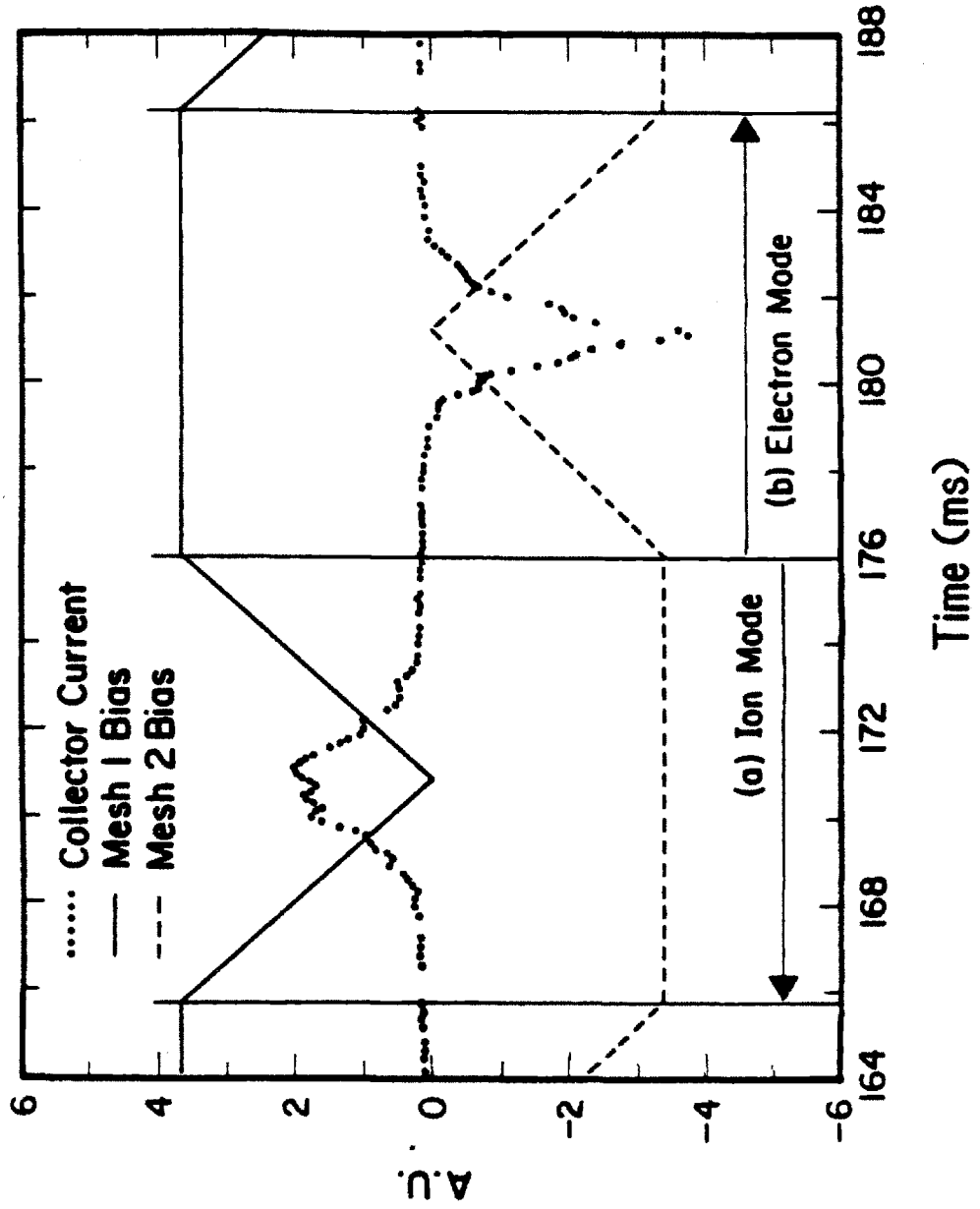

Figure 4.1 Bipolar biasing scheme and collected current.

Typically the RFEA bias is sweeping at 50 Hz, or at 20 ms interval the grid bias will repeat the pattern shown in figure 4.1, which contains 2 full sweeps through both the ion mode and electron mode. This sweep rate is limited by the digitizing frequency of the CAMAC module (10 kHz). Even at 50 Hz, each ion (or electron) sweep contains only 100 data points. For typical ion mode operation, the difference of the bias voltage between successive data points exceeds 1 volt, which may ultimately affect the accuracy of the RFEA measurements.

Since an ion (or electron) requires a finite time of flight (t_{flight}) to reach the collector from the time it passes through the slit, we can define a parallel energy resolution, $\Delta E_{\|}$, which corresponds to the voltage sweep-rate limit[1]:

$$\Delta E_{\|} = q\, t_{flight} \frac{dV_{bias}}{dt}, \tag{4.2}$$

$$\text{where} \quad t_{flight} = \delta_{RFEA} \sqrt{\frac{m}{2\, E_{\|}}}. \tag{4.3}$$

δ_{RFEA} is defined as the distance from the slit to the collector in the RFEA. For typical Janus operation, $\frac{\Delta E_{\|}}{E_{\|}}$ is less than 0.05%. Therefore, if we have a faster digitizer with the necessary supporting memory modules, we can operate the RFEA at a much higher sweep frequency.

$f(E_{\|})$ is the parallel energy distribution function of the charged particle of interest. In the edge plasma, however, it is possible that the measured $f(E_{\|})$ will not reflect the actual distribution due to potential variation along the field line[2]. According to the Bohm Sheath Criterion[3] (chapter 2), a presheath potential drop on the order of $T_e/2$ is needed to accelerate the ions to sound speed before a stable sheath can form. Therefore, if $T_i \leq T_e$, it is possible that the energy spread measured by $f_i(E_{\|})$ is really a reflection of ions drifting into the flux tube at different points. Thus the ions will possess energy spread due to various potentials they will encounter as they accelerate toward the probe surface. Typically $T_i > T_e$, so this effect should be minimal in our operating regime.

If it is necessary to monitor only the ions or the electrons, the RFEA can also employ a sweep function that strictly follows either the ion mode or the electron mode of figure 4.1. Another possible use of the RFEA is to investigate the existence of high energy tails on the distribution functions. In the bulk plasma, it is common that high energy tails exist during neutral beam injection[4,5], lower-hybrid current drive and heating[6,7], and ion-cyclotron resonance heating[8,9]. Run away electrons[10,11] are another source of a high energy tail in the electron distribution that will reach the edge plasma before they can equilibrate collisionally.

The DIVA group[12] had employed a simple RFEA and found two temperature electron distribution functions in the scrape-off region. The source of the high energy tails on DIVA is attributed to the misalignment of the TF coil which produces nonaxisymmetric perturbations that caused the destruction of magnetic surfaces near the separatrix. The Janus RFEA can also be biased at high voltages such that only high energy tails can reach the collector. However, the scrape-off length of the runaway electrons is extremely short[10], preventing us from directly measuring the confinement time of the high energy component of the distribution which may have different confinement characteristics as compared with the bulk distribution[13]. An attempt to find the presence of any high energy tail during ICRF was also unsuccessful.

A very important issue that was discussed in section 3.2 is the continuity of the slit potential across the slit gap. Since the Janus RFEA is designed with a biasable slit, we can test the effectiveness of the slit in holding its potential against incoming charged particles. Figure 4.2.1 and 4.2.2 show a series of curves plotting the collected current against the bias voltage of the ion repeller grid. Each curve represents a different slit bias potential. For all positively biased slit potentials (figure 4.2.1), the collected ion currents also exhibit energy shifts corresponding to the value of the bias potentials. This kind of response reflects the continuity of the slit potential across the gap. Since the slit now acts as an ion repeller, if the potential surface is continuous across the gap, then all

ions with incoming energy less than the slit potential will be reflected before entering the RFEA chamber. Therefore, when the ion repeller grid starts to ramp positively up from ground potential, the collected current should remain constant until the grid bias voltage exceeds the slit bias voltage.

On the other hand the no bias and negatively biased slit potentials (figure 4.2.2) show no associated energy shifts. This is also expected. Although ions are accelerated by a negative potential, as soon as they cross the slit gap, the negative slit bias starts to work against the accelerated ions to decelerate them to their original energies. Therefore, the negatively biased cases behave similarly the no-bias reference case.

4.1.2 Analysis Techniques

To unfold the ion or electron parallel energy distribution function we can, in principle, take the numerical derivative of equation 4.1 and solve for $f(E_{\|})$ such that

$$f(E_{\|} = V_{bias}) \quad = \quad \frac{-m}{q^2 \; A_{slit} \; T_T} \; \frac{dI(V_{bias})}{dV_{bias}}. \tag{4.4}$$

However $I(V_{bias})$ is typically noisy due to large edge density fluctuations and is therefore difficult to differentiate. A much more practical technique is to assume a form for $f(E_{\|})$ and compare $I(V_{bias})$ obtained from equation 4.1 with the experimental data.

Kinetic theory[14] (Emmert) predicts that the ion distribution at the material surface approximates that of a Maxwellian with a positive energy shift corresponding to the sheath potential $|V_{sheath}|$. This potential shift V_{shift} is equal to the difference between the plasma potential, V_{plasma}, and the probe ground. In reality, the tokamak's magnetic geometry is very complicated, and

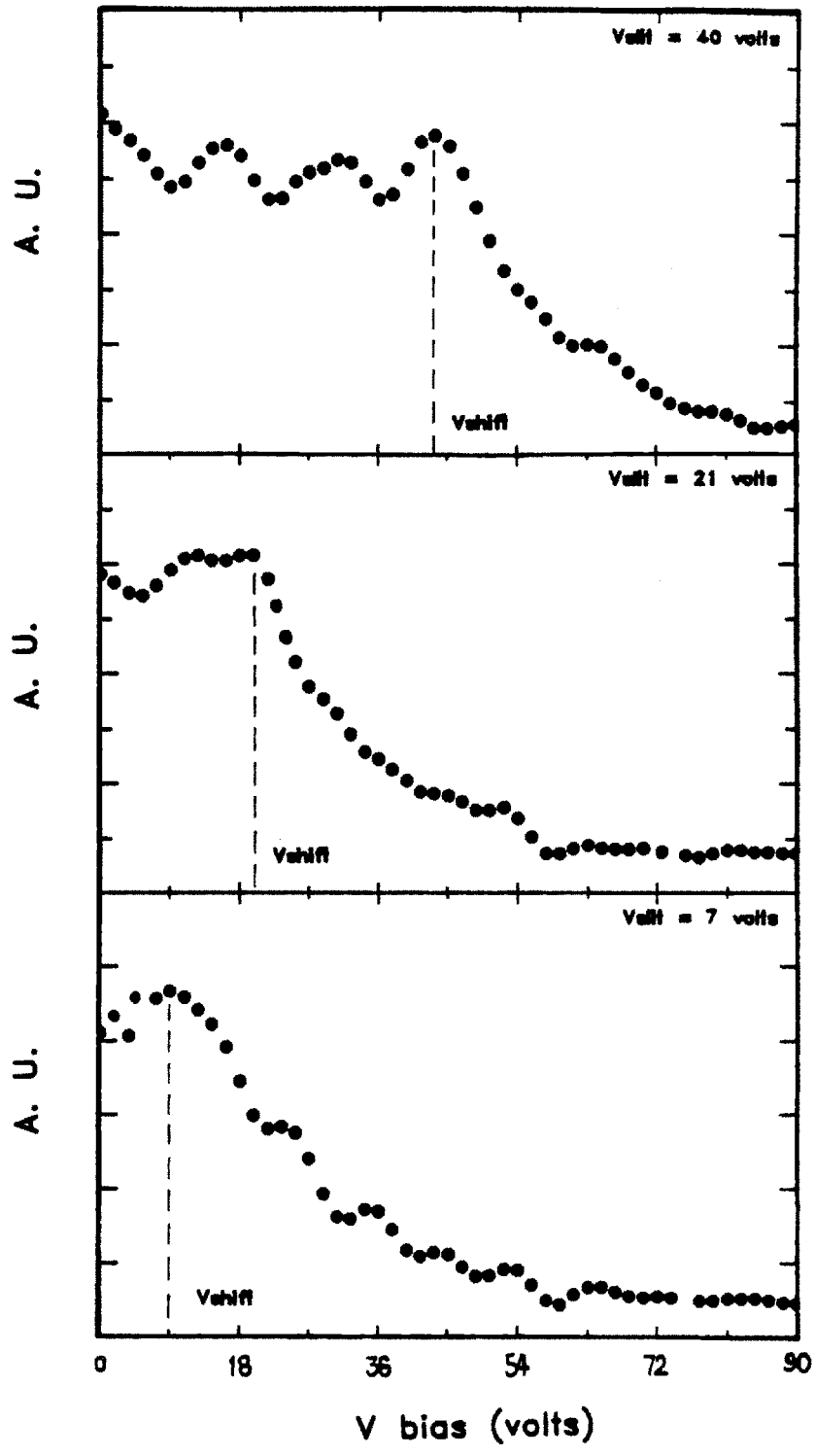

Figure 4.2.1 Current-voltage characteristics of a series of curves at positively slit biased potentials, V_{slit}.

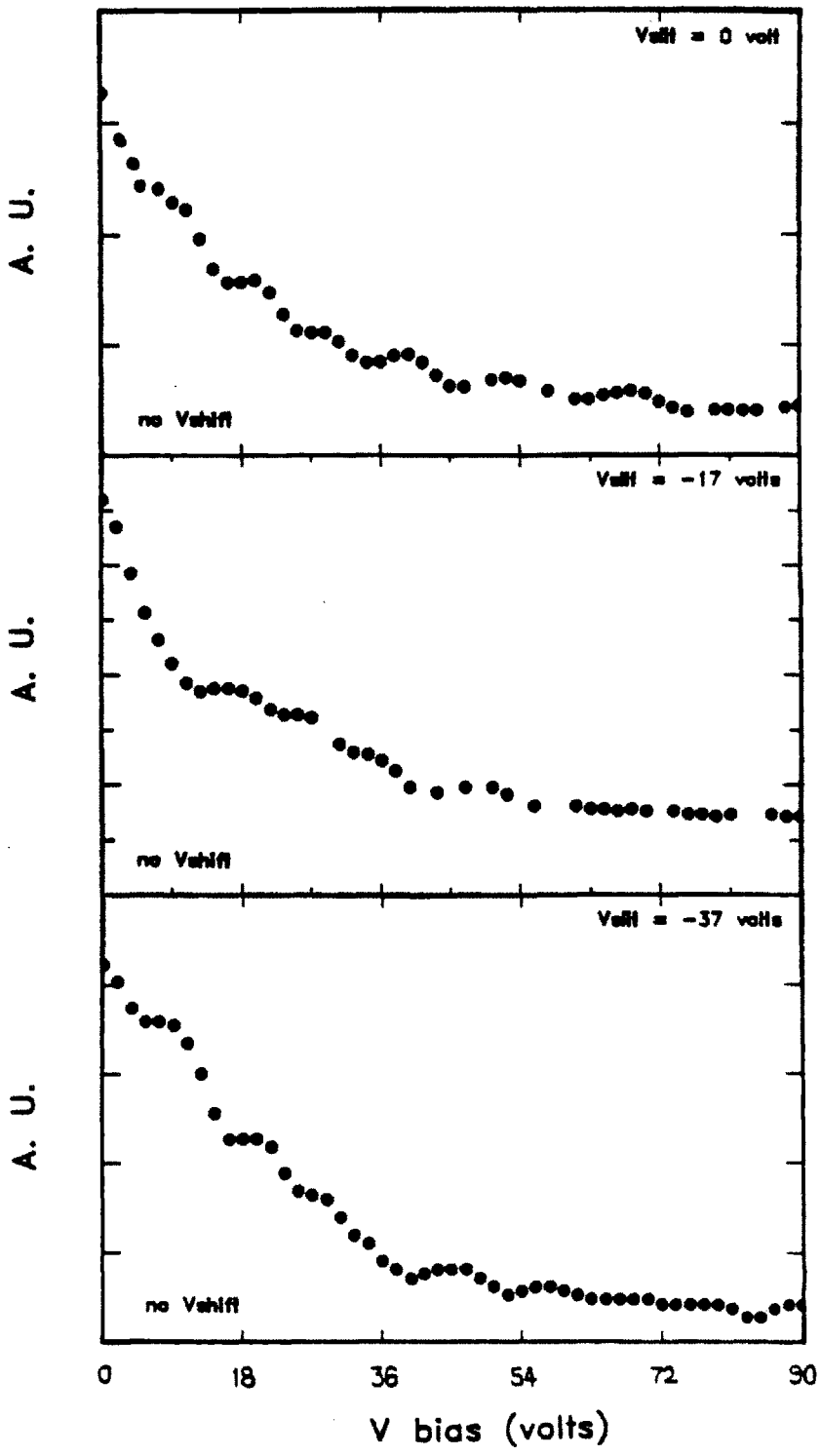

Figure 4.2.2 Current-voltage characteristics of a series of curves at no-bias and negatively slit biased potentials, V_{slit}.

the measured V_{sheath} would probably not be equal to the theoretical prediction. For example, Emmert assumes a 1-D geometry parallel to the magnetic field. Along the magnetic field lines electrons are much more mobile than ions and a negative V_{sheath} is necessary to force equal fluxes of ions and electrons. However, cross-field diffusion is dominated by ions due to their large Larmor radii. Then surfaces parallel to the field would charge positively.

From equation 4.1, the ion current as a function of the retarding potential V_{bias} is

$$\begin{aligned} V_{bias} \leq V_{shift}, \qquad I_i(V_{bias}) &= I_{oi}, \qquad \text{and} \\ V \geq V_{shift}, \qquad I_i(V_{bias}) &= I_{oi}\, e^{-q_i(V_{bias}-V_{shift})/kT_i}. \end{aligned} \tag{4.5}$$

I_{oi} is the ion current collected when none of the ions is repelled by the retarding potential. Its value depends on the edge model we employ. Assuming that both the ions and electrons exhibit sonic flows to the probe surface (see section 2.1), we can approximate I_{oi} as

$$I_{oi} = q_i\, f(\tau)\, n_i\, C_s\, T_T\, A_{slit}, \tag{4.6}$$

$$\text{where } C_s = \text{sound speed,}$$

$$\equiv \sqrt{\frac{k\,(T_e + T_i)}{m_i}}; \text{ and} \tag{4.7}$$

$$\tau \equiv \frac{T_i}{T_e}. \tag{4.8}$$

n_i is defined as the ion density. $f(\tau)$ equals an ion density reduction factor described in section 2.2. Simple probe theory typically uses an equivalent $f(\tau)$ value of 0.5.

If T_T can be estimated accurately, and given the value of T_e, we can obtain an approximate ion density using equation 4.6. Experimentally $T_i/T_e \geq 1$ (see Chapters 5 and 6). Since the value of T_T is highly uncertain, and for simplicity of calculation, the T_e dependence in equation 4.6 is typically ignored. The determination of T_T is achieved by using the 3-D Monte-Carlo code outlined in Appendix C. In studying the transmission characteristic of each of the RFEA components, we arrived at an averaged "magnetic" effect of the ion transmission characteristic in addition to the reduced transmission caused by the presence of the mesh (see Appendix C). Operating with the first two grids as the ion and electron repeller electrodes, the total transmission coefficient is about 5%.

Typical fits to the ion part of the previously shown raw data (figure 4.1) are shown in figure 4.3. These data were taken with a 2 kHz 6-pole active Butterworth filter to reduce the fluctuation level. Residual oscillations under 2 kHz are still evident in this data.

The only tricky aspect of fitting the ion characteristic is the determination of V_{shift}. Once this potential is found, T_i is calculated by least square fitting the $V_{bias} > V_{shift}$ portion of the voltage-current characteristic with a function of the form:

$$I(V_{bias} - V_{shift}) \quad = \quad I_{dc} + I_{oi}\, e^{-q_i(V_{bias}-V_{shift})/kT_i}. \tag{4.9}$$

I_{dc} is just equal to a shift in current of the entire curve, which can occur from electronic offset or insufficient biasing of the electrons.

V_{shift} is determined by using an iterative scheme of fitting. For the first time through, the voltage corresponding to a certain percentage of the peak current (typically 70%) is chosen as the initial guess of V_{shift}. Then we fit the portion above the initial guess using equation 4.9. The new V_{shift} is determined by

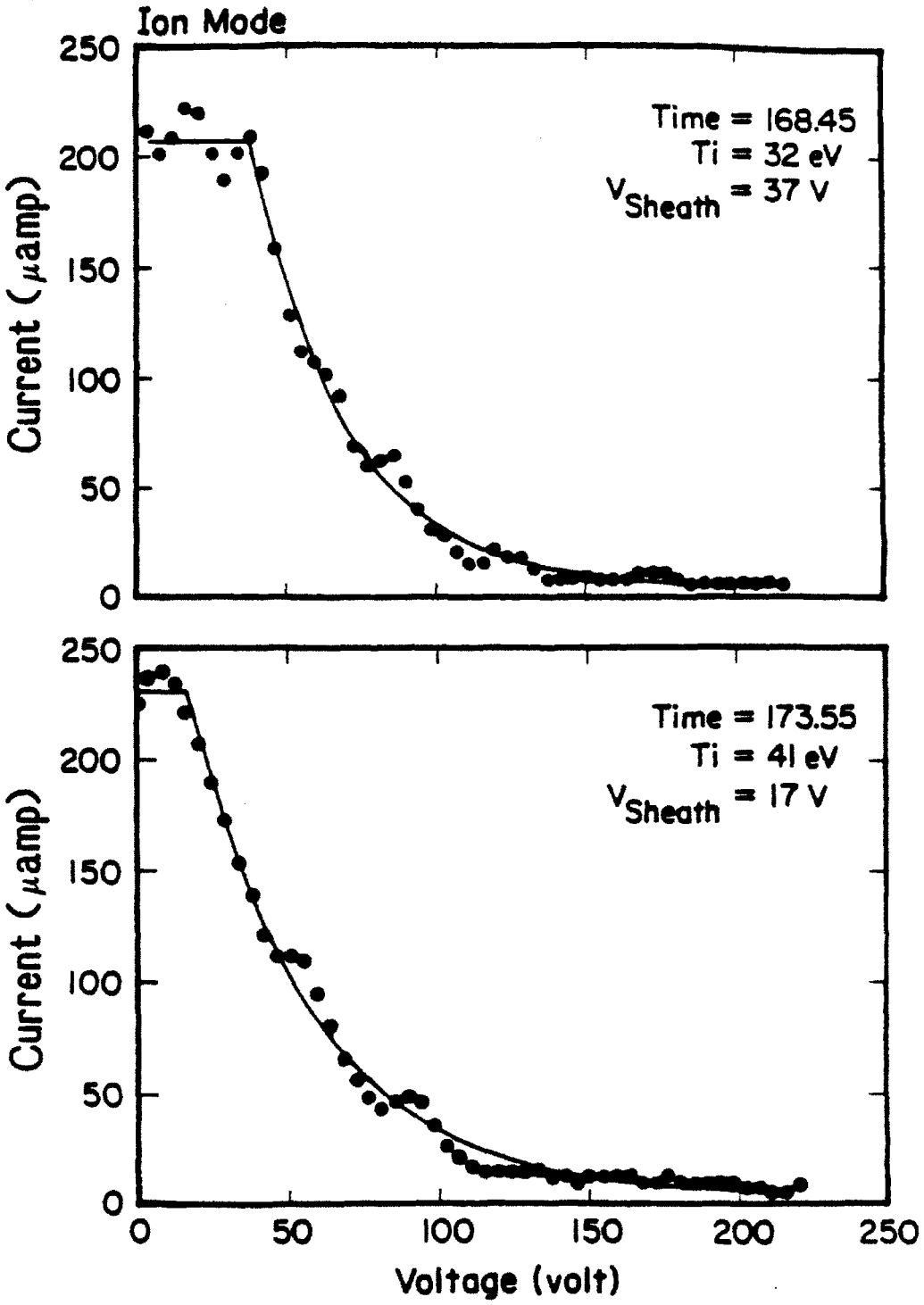

Figure 4.3 Fits corresponding to the two ion portions of the raw data shown in figure 4.1.

$$q V_{shift}^{new} = k T_i^{old} \left(\ln \frac{I_{peak}}{I_{ave}} \right), \tag{4.10}$$

$$\text{where } I_{ave} = \frac{1}{n} \sum_{i}^{n} I^i, \quad \text{for all } V_{bias}^i < V_{shift}^{old}. \tag{4.11}$$

I_{peak} is defined as the peak current at $V_{bias} = 0$, if we project the fitted current trace back as demonstrated in figure 4.4. This iteration will continue, with the new V_{shift} replacing the old V_{shift} as the next guess, until the difference in the V_{shift} between two successive iterations falls below a specified error margin. Figure 4.4 illustrates the technique and terminologies used in the iterative scheme.

Due to the formation of the negative sheath potential between the slit surface and the unperturbed plasma, the bulk of the electron distribution is repelled. Only the high energy portion of the electron distribution is collected. Again assuming a Maxwellian for the electron distribution function, we can obtain a version of equation 4.5 for electrons:

$$I_e(V_{bias}) = I_{oe}\, e^{eV_{bias}/kT_e}, \tag{4.12}$$

where I_{oe} is the electron current at $V_{bias} = 0$ volts. Measurement of electron density is more uncertain than the ion density measurement since accurate knowledge of V_{sheath} is necessary in order to determine the fraction of electrons repelled by the negative slit potential. As discussed earlier, V_{shift} may not be an accurate reflection of the local sheath potential. The electron transmission coefficient, however, should be much simpler to estimate when compared with the ion transmission coefficient. Due to its small Larmor radius, electron transmission can be treated approximately as photon transmission, equaling the total

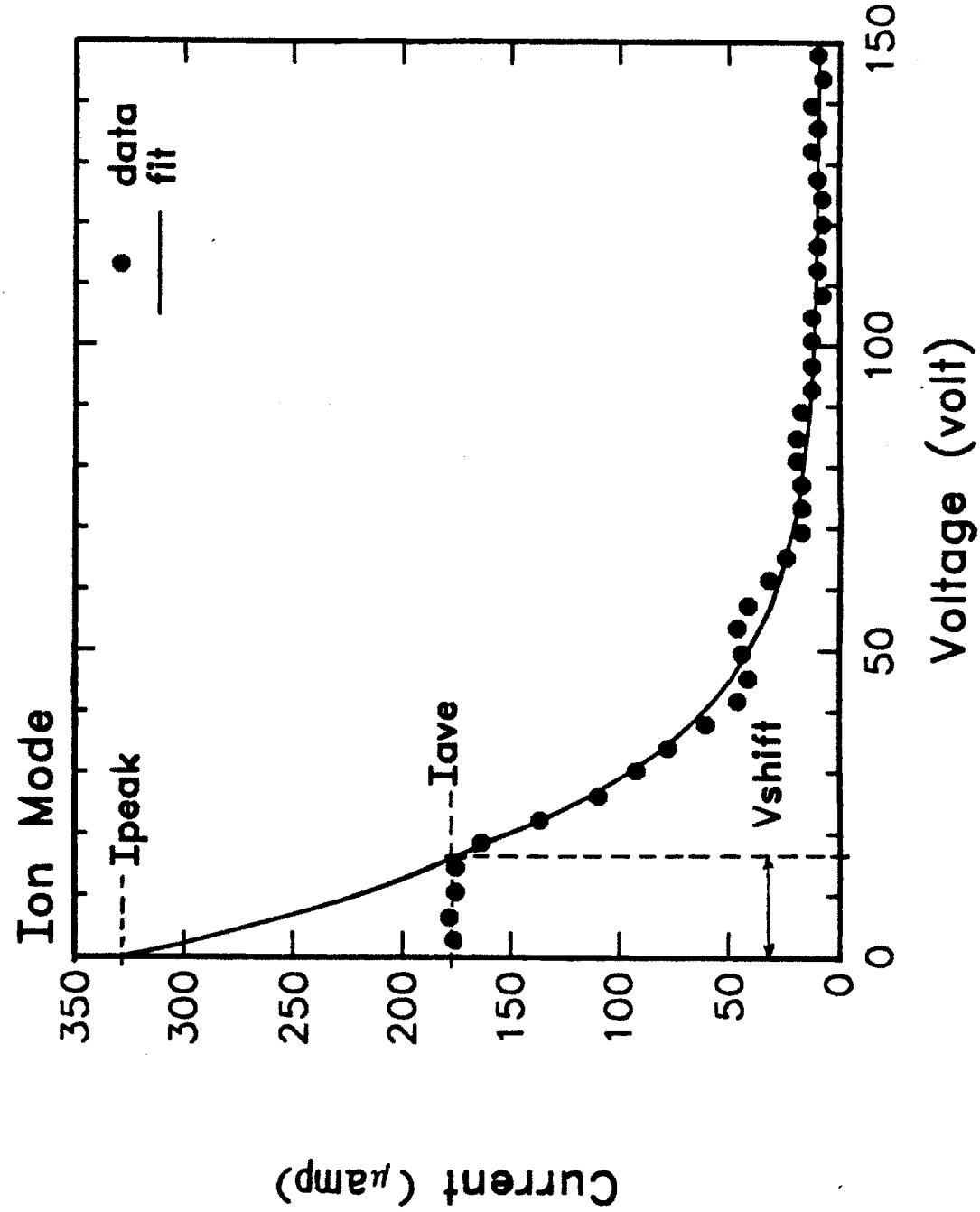

Figure 4.4 Iterative scheme to solve for V_{shift}

geometric transmission coefficient of the meshes. Figure 4.5 shows typical fits of the electron portions of the raw data in figure 4.1.

Another important issue here is the effect of a perturbing probe (Janus) on the measured plasma parameters. This effect has previously been addressed by Stangeby[15,16]. The insertion of a large, perturbing probe in the scrape-off layer creates new scrape-off lengths on both sides of Janus. Therefore the measured parameters are different from the natural, unperturbed plasma parameters. The relation of the perturbed parameters and the unperturbed parameters are dependent on the tokamak's limiter (or divertor) configuration and the probe geometry. Technique of analyzing "large" probe data was presented in Chapter 2. Unfortunately the necessary conditions for using Stangeby's "large" probe theory are not met in the Alcator C edge region. More theoretical work is necessary before we can accurately account for the effect of large edge probe housing.

4.2 Langmuir Probe

The Langmuir probe analysis technique used for this high magnetic field application is well documented[17,18,19]. The Janus Langmuir probe surface is aligned perpendicular to magnetic field lines and the surface is large compared to ion gyroradii. Therefore the collection area is assumed to be planer. The analysis used in this thesis utilizes the algorithms and methodology of LaBombard[17]. Since the RFEA can provide an independent check of the electron temperature, Janus provides an excellent opportunity to cross-check the different Langmuir probe theories.

For our analysis we principally employ a simple probe theory and obtain T_e by fitting only the exponential portion of the probe characteristic [17,20]. However, an important question here is the validity of the simple probe theory in a magnetized environment. A magnetized probe theory by Stangeby[21] was also used for electron temperature analysis.

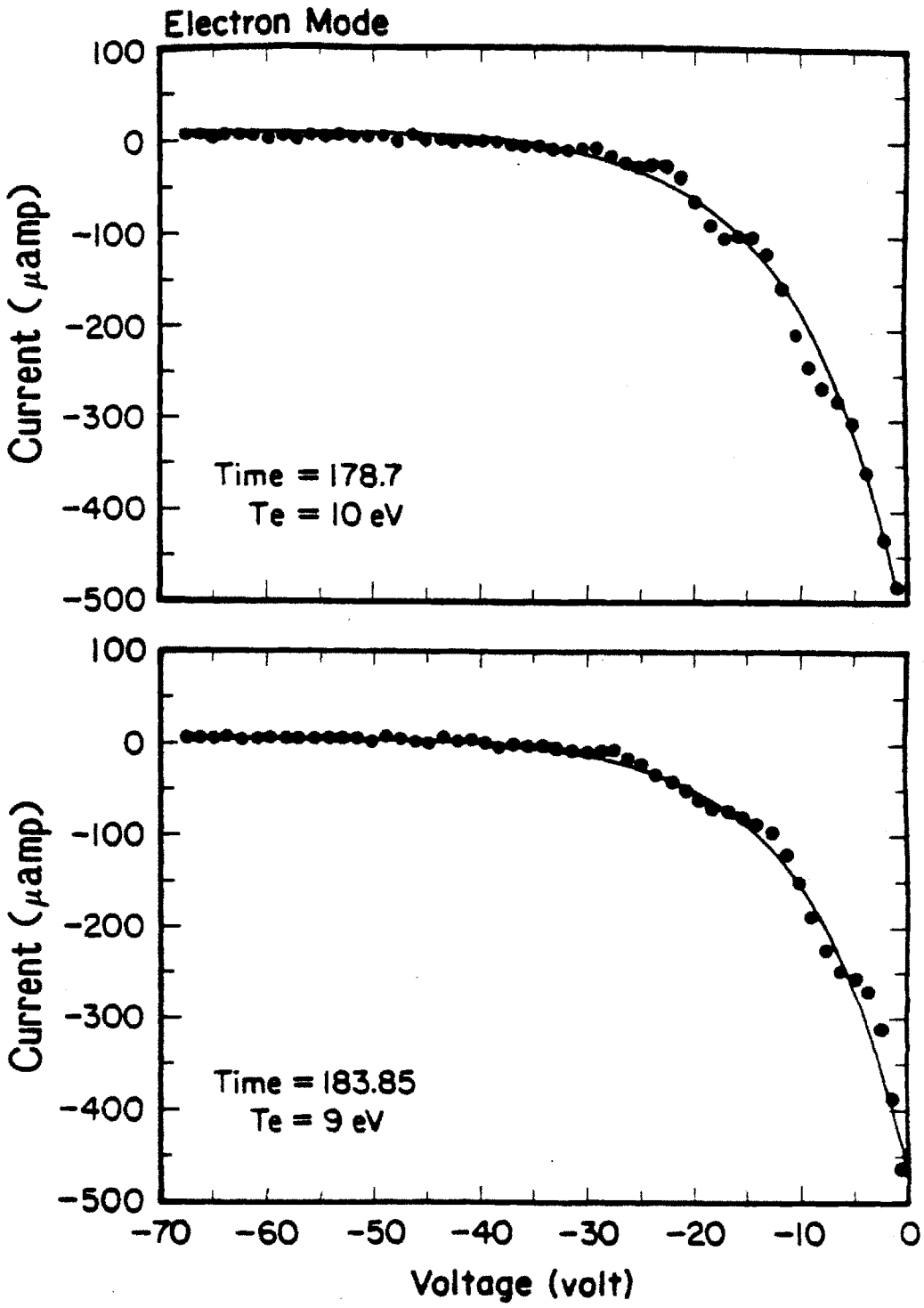

Figure 4.5 Fits corresponding to the two electron portions of the raw data shown in figure 4.1.

4.2.1 Simple Probe Theory

Figure 4.6 shows a schematic of a typical, collisionless, nonmagnetized Langmuir probe current-voltage characteristic. The characteristic can be divided into 3 regions separated by the voltage references V_{space} and V_{float}. These points are referenced with respect to the probe ground potential, which is the potential of the entry flange of Janus.

When the probe is biased very negatively with respect to the probe ground and V_{float}, all but a very small number of high energy electrons are repelled before reaching the probe. Therefore the collected current is dominated by positive ions, which are attracted by the negative bias potential. Once the bias reaches the point where all the ions are collected and electrons repelled, any further increase the negative bias would only accelerate the ions but would not affect the current drawn. This region is termed the "ion saturation region." The saturation current is defined as the ion saturation current, I^i_{sat}.

As the probe bias is increased, more and more electrons are capable of overcoming the repelling potential and contribute a negative current on top of I^i_{sat}. V_{float} is defined as the point at which the probe potential is negative enough to repel all the electrons except a flux equal to the incoming ion flux. This is an especially easy reference point in the Langmuir probe analysis since all we need to do is to locate the potential corresponding to the zero current position of the probe characteristic.

Continual increase of the probe potential would further increase the collection of electron flux, and eventual decrease of the ion flux as the probe starts to repel the ions. This region is characterized by the rapid change of the collected current from a positive I^i_{sat} to a region dominated by the electrons, and it is typically referred to as the "transition region." Due to their small mass, the electrons are travelling at a much faster speed than the ions. Therefore this transition region is dominated by the electron response and reflects a measurement of T_e.

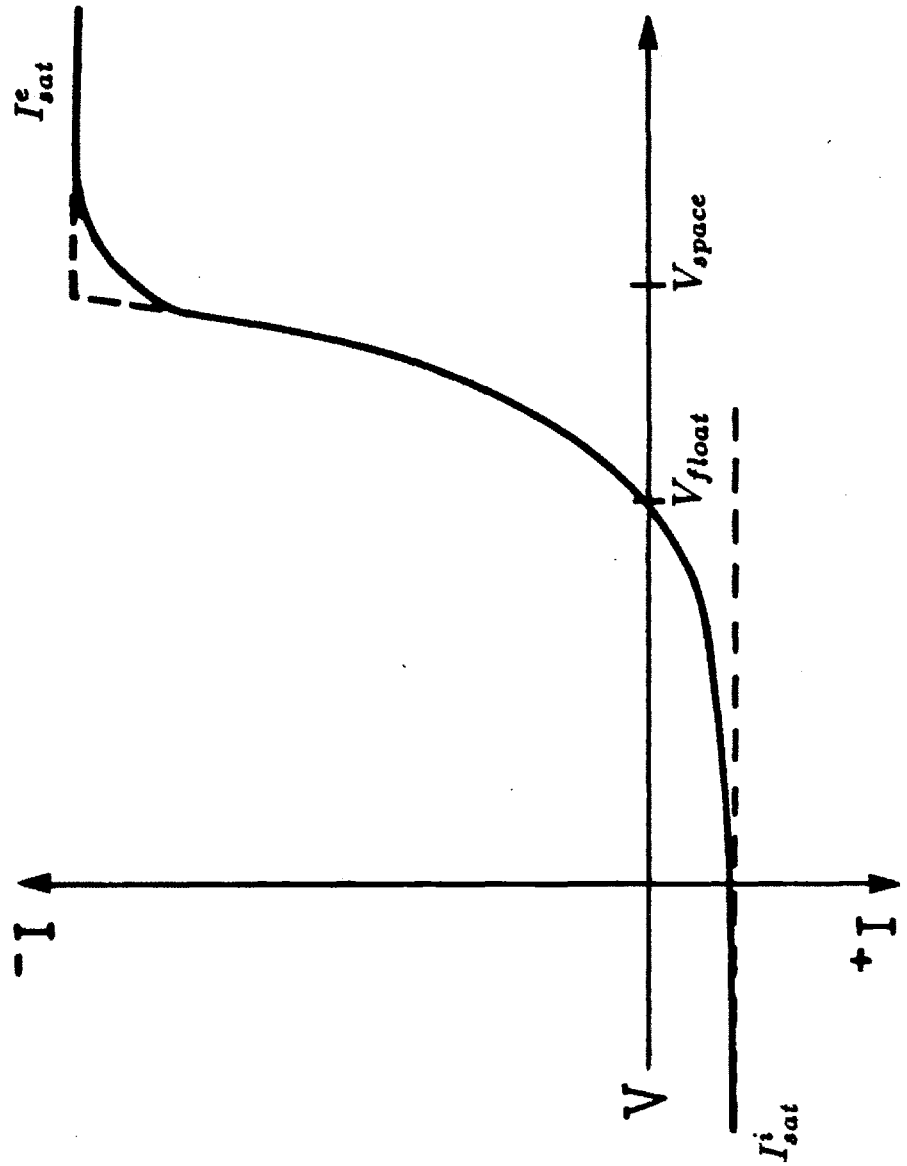

Figure 4.6 Schematic of a typical, collisionless, nonmagnetized Langmuir probe current-voltage characteristic.

V_{space} is defined as the plasma space potential. There should be no electric fields at this point and the charged particles migrate to the probe because of their thermal velocities, v_{th}. $v_{th} \propto \sqrt{\frac{1}{m}}$. Therefore, what is collected by the probe at V_{space} is dominantly electron current. Further increase of the probe potential above V_{space} allows the electron current to completely dominate the total collected current. This region is typically labelled as the "electron saturation region."

In practice, the sharp "knee" at V_{space} in figure 4.6 is not observed. The electron saturation region is also not seen despite very positive bias potentials. These observations will be discussed further in the next section.

As a first-cut approximation, we can describe the three regions of the simple probe theory by

$$\text{for } V_p < V_{space}, \quad \frac{I(V_p)}{eA_p n_p} \approx \frac{1}{2} C_s - \frac{1}{4} \bar{C}_e \, e^{e(V_p - V_{space})/kT_e}; \tag{4.13}$$

$$\text{for } V_p \geq V_{space}, \quad \frac{I(V_p)}{eA_p n_p} \approx \frac{1}{4} \bar{C}_e. \tag{4.14}$$

V_p is the probe bias potential; n_p is the plasma density far away from the probe (i.e. unperturbed); and A_p is the effective probe area which is just equal to the probe surface area normal to the magnetic field. If the ion charge state, Z, exceeds 1, then n_p should be replaced by the electron density n_e $(=Zn_i)$. C_s is defined in equation 4.7. $\bar{C}_e$ is the averaged electron velocity defined by equation 2.2.

The fitting of equations 4.13 and 4.14 is achieved by an iterative scheme written by LaBombard[17]. First I^i_{sat} is estimated by utilizing the knowledge that it equals the total current at large negative values of V_p. Then straight lines are fitted to the function $\ln(I(V_p) - I^i_{sat})$ on either side of an estimated knee

potential V_{knee}. The intersection of the two fitted lines provides the next V_{knee}. The iteration is continued until convergence is achieved.

Approximating $V_{knee} \approx V_{space}$, we can choose the data points satisfying the condition of equation 4.13, i.e. $V_p < V_{space}$, and least-square fit them to the equation

$$I(V_p) = I^i_{sat} + I_0\, e^{-eV_p/kT_e}, \tag{4.15}$$

where I_0 is a constant. Equation 4.15 is a linear function in I^i_{sat} and I_0, but nonlinear in T_e. By defining a function equal to $\exp\left(\frac{-eV_p}{kT_e}\right)$, then I^i_{sat} and I_0 can be solved for in terms of T_e through the usual linear least-square fit. Therefore, by iterating T_e, we can nonlinearly least-square fit all three unknown parameters.

By knowing I^i_{sat}, we can obtain an approximate plasma density by using the first part of equation 4.13, which describes the ion saturation region with the assumption of a sonic flow to the probe edge:

$$I^i_{sat} \approx \frac{1}{2}\, n_p\, C_s\, e\, A_p. \tag{4.16}$$

The factor of $\frac{1}{2}$ is an approximation of the density reduction factor $f(\tau)$. Although within the Janus package the RFEA measures T_i, we typically assume $T_i/T_e \sim 2$ in calculating C_s for simplicity.

4.2.2 Magnetized Langmuir Probe Theory

In the presence of collisions or magnetic field, the probe current depends also on the transport coefficients of the plasma. Collisional mean free path in the Alcator C scrape-off region is much longer than the probe dimension,

so this effect can typically be ignored in the analysis. However, the addition of magnetic field really complicates the probe theory. Since charged particle motion parallel and perpendicular to $\underline{B}$ are governed by different mechanisms, the effective collection area, i.e. the surface area across which all particles will be collected, is strongly perturbed by both the magnetic field and probe bias. For example, the effective length of the flux tube into which electrons can diffuse to reach the probe increases continuously with voltage. And due to their small Larmor radii, the motion of the electrons is always much more affected by the magnetic field than the motion of the ions.

Stangeby[21] provides an analysis that models the particle and energy flow to an electrically biasable probe immersed in the magnetic field. Figure 4.7 plots a series of potential variations along the field line as a function of probe bias potential. Profile A of figure 4.7 corresponds to collecting ion saturation current; C corresponds to electron saturation current collection, and B is biased at an intermediate potential. Looking at profile B, we see that for a negatively biased probe, a positive hill potential, V_h, is present before the drop off due to sheath potential.

Aside from incorporating potential variation along magnetic field lines into his model, Stangeby also considered the restrictions on the flow to the probe imposed by the continuity of parallel and cross-field transport. The effect of the perpendicular and parallel diffusions are incorporated in a reduction factor r, which is defined as

$$r \equiv \frac{16\,\lambda_e\sqrt{D_\perp/D_\parallel}\,(1+\tau)}{\pi\,d}, \tag{4.17}$$

where λ_e is defined as the electron mean free path, d is the probe dimension, and $D_\perp$ and $D_\parallel$ are the perpendicular and parallel diffusion coefficients respectively.

Defining a dimensionless parameter η where

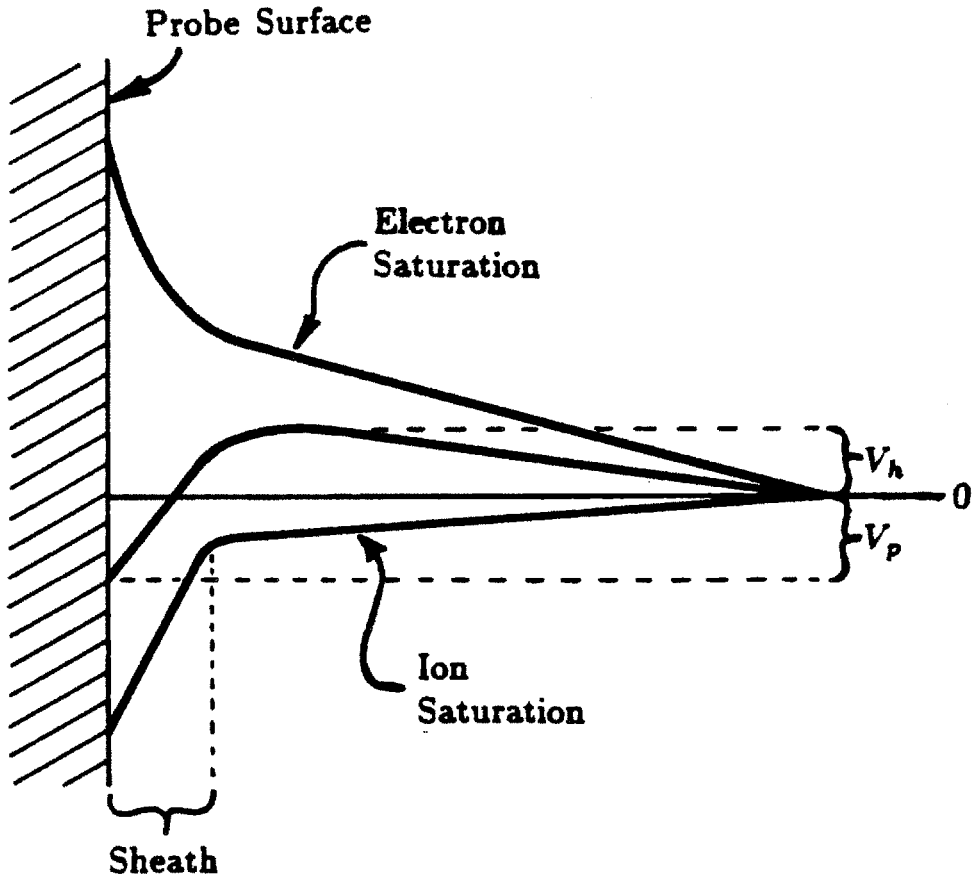

V_h = 'Hill' Potential
V_p = Probe Potential

Figure 4.7 Potential variation along a field line as a function of the probe bias potential.

$$\eta_p \equiv \frac{eV_p}{kT_e}, \text{ and} \tag{4.18}$$

$$\eta_h \equiv \frac{eV_h}{kT_e}. \tag{4.19}$$

we can summarize Stangeby's magnetized probe theory by separating the probe characteristic into two zones. For $\eta_p \leq \tau \ln\left[\frac{(1+\tau)}{\tau}\right]$,

$$\frac{I(\eta_p)}{eA_p n_p} = f(\tau) C_s e^{-\eta_h/\tau} - \frac{1}{4}\bar{C}_e \left[\frac{\tau}{1+\tau e^{\eta_h - \eta_p}}\right], \tag{4.20}$$

and for $\eta_p > \tau \ln\left[\frac{(1+\tau)}{\tau}\right]$,

$$\frac{I(\eta_p)}{eA_p n_p} = f(\tau) C_s e^{-\eta_h/\tau} - \frac{1}{4}\bar{C}_e \left[\frac{\tau}{1+\tau}\right]. \tag{4.21}$$

Equations 4.20 and 4.21 together yield a complete description of the magnetized Langmuir probe characteristic, with the first part of each equation describing the ion response and the second part describing the electron response. Actually in Stangeby's model, the ion response of equation 4.21, C_s is replaced by $\sqrt{\frac{2kT_i}{\pi m_i}}$. This causes a discontinuity of the probe characteristic at $\eta_p = \tau \ln\left[\frac{(1+\tau)}{\tau}\right]$. Since, at large positive probe biases, electrons dominate the overall probe characteristic and ions make little contribution, continuity equation 4.21 is modified accordingly.

The "Stangeby fit" is achieved by first finding the initial conditions using the simple probe model and then equations 4.20 and 4.21 are fit throughout the entire probe characteristic. More detailed description of the numerical fitting can be found in reference 15.

4.2.3 Validation of the Langmuir Probe Theories

Since two independent measurements of T_e are obtained by using the RFEA and the Langmuir probe, we can cross-check the T_e measurements and attempt to verify the validity of the probe theory. Figure 4.8 shows time histories of the electron side and ion side T_e's obtained by the RFEA, and by Langmuir probe using both the simple and magnetized (Stangeby) probe models. For this discharge, the RFEA measurements agree much better with the T_e obtained by using the simple probe theory, or simple fits to the exponential portion of the probe trace. The averaged T_e values at the flattop, or stable portion of the discharge, show that $T_e(RFEA)$ agrees to within 15% of the simple probe theory average. However, the same agreement was not found with the use of the Stangeby fit, which is lower than the other measurements by approximately 50%.

Comparisons among the three T_e measurements have been conducted for various plasma conditions. The RFEA result typically lies in between the fitted results of the simple probe model and the Stangeby model. It is expected that $T_e(RFEA)$ should be slightly lower than the Langmuir probe measured T_e since the Langmuir probe tip extends a bit further toward the limiter edge. Since the temperature gradient in the scrape-off region is typically flat, this effect should not be significant. Overall we typically found the best agreement between the RFEA results and the results obtained using the simple probe theory. Therefore the Langmuir probe results presented in this thesis are obtained strictly by fitting the data using the simple probe model.

4.2.4 Operation

Routinely the Langmuir probes within Janus are operating in a sweep mode, ramping with a 100 Hz triangular waveform that sweeps from a negative to a positive potential. The two potential limits are defined by the potential required

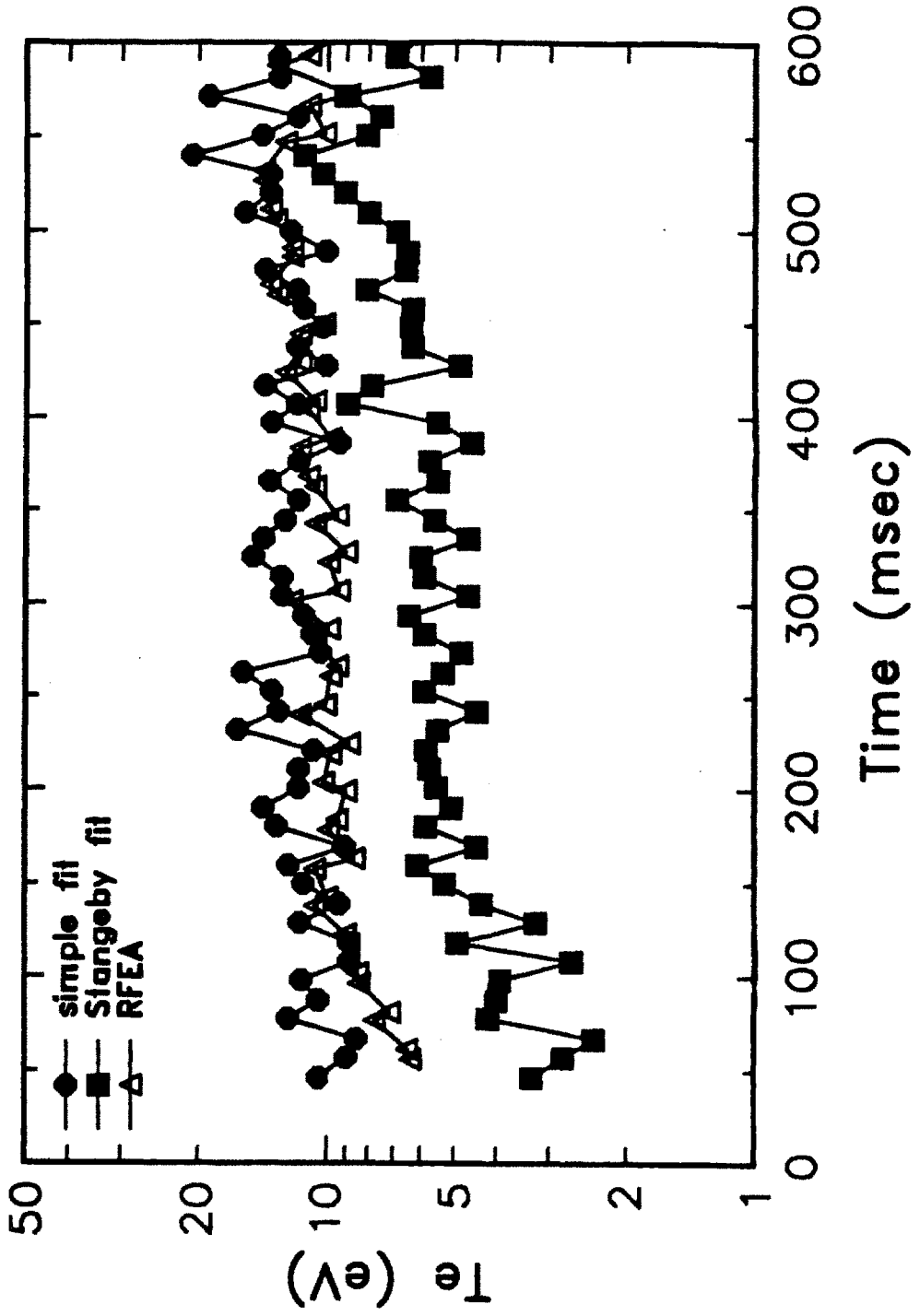

Figure 4.8.1 Time histories of the electron side T_e's obtained by the RFEA and by using the simple and magnetized probe theories.

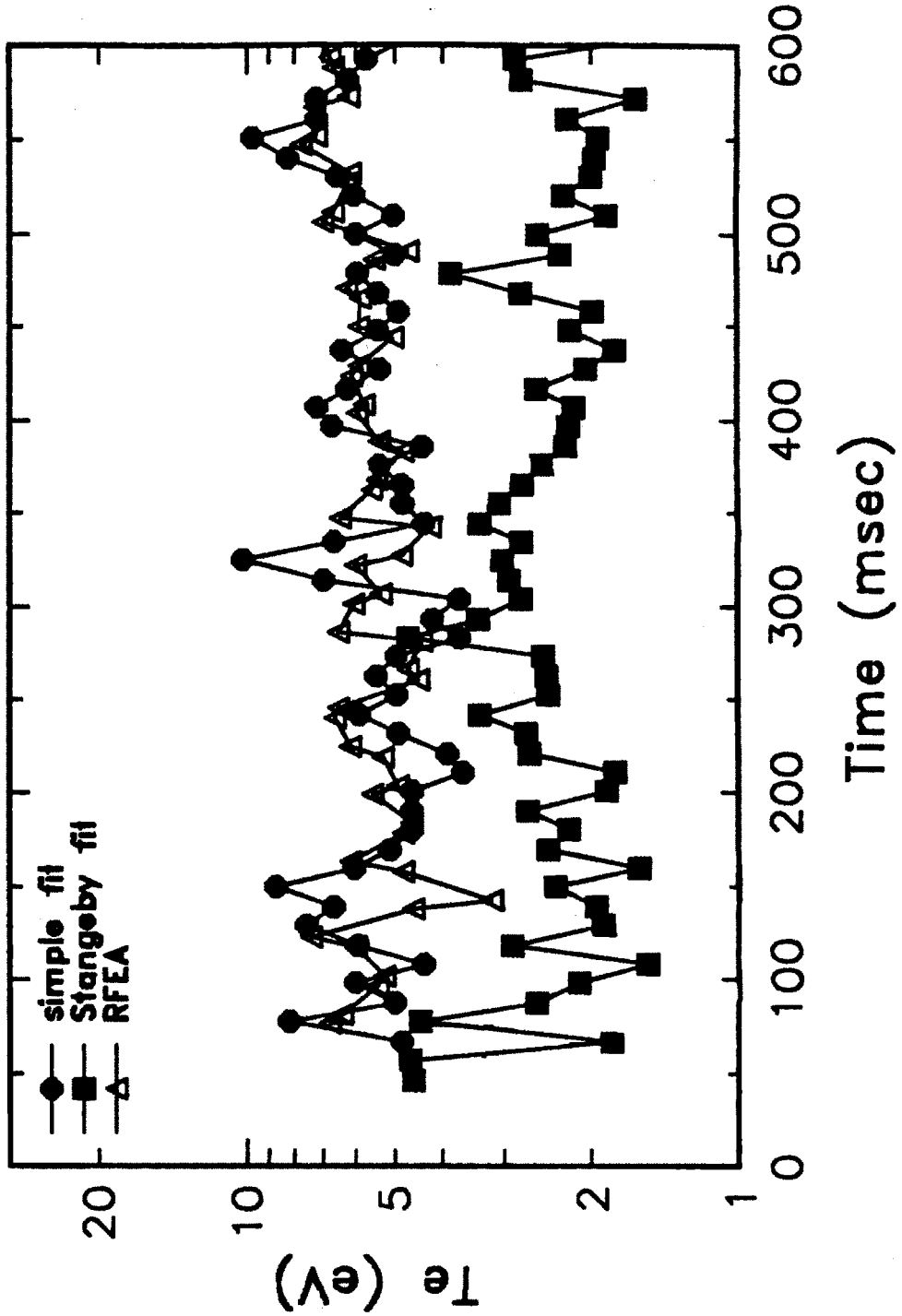

Figure 4.8.2 Time histories of the ion side T_e's obtained by the RFEA and by using the simple and magnetized probe theories.

to bias toward ion or electron saturation. A higher positive voltage is required to bias toward electron saturation while a high negative voltage will bias toward ion saturation. Typically the Langmuir probe is biased from −30 to +50 volts.

By biasing the probe at a constant negative voltage that is sufficiently into the ion saturation region, we can monitor the fluctuation levels of the edge plasma. Although I^i_{sat} is dependent on both the temperatures and plasma density, typically the fluctuations are attributed to variation in density.

The edge density fluctuation, $\tilde{n}_p$, along with possible potential fluctuation, $\tilde{\Phi}$, can be a possible cause of anomalous transport in the edge plasma[10] when both fluctuations are driven in phase with respect to each other. However it is not possible to measure both fluctuation levels simultaneously using the Janus Langmuir probe setup. LaBombard[17] has used a poloidal array of Langmuir probes to monitor $\tilde{n}_p$ in an attempt to correlate the fluctuation levels with the observed poloidal asymmetries on Alcator C. The finding was inconclusive since $\tilde{\Phi}$ could not be monitored. A multiple probe has been proposed[17]to monitor $\tilde{n}_p$ and $\tilde{\Phi}$ simultaneously .

4.3 Calorimeter

The analysis of the calorimeter output follows the treatment of Manos, et al.[22] Any change in temperature of the calorimeter plate is principally caused by three processes: the plasma heat flux, radiation loss from the hotter plate to a cooler vacuum vessel surface, and conduction loss from the hot plate to a cooler probe box. They can be expressed as

$$\begin{aligned} q_{\|}(t)\, A_{exp} &= \rho_D V_c C_p \frac{dT(t)}{dt} + \epsilon_t k_B A_{rad} \left(T(t)^4 - T_s^4\right) \\ &\quad + \frac{\rho_D V_c C_p}{\tau_d} \left(T(t) - T_s\right). \end{aligned} \tag{4.22}$$

$q_{\|}(t)$ is the incident parallel heat flux; $T(t)$ is the time dependent temperature measured by the thermocouple at the back of the calorimeter plate; T_s is the surrounding temperature which is measured by registering the plate temperature before each discharge; ϵ_t is the total radiative emissivity of the calorimeter plate material; k_B is the Stefan-Boltzmann constant; A_{rad} is the total effective radiating area; and τ_d is the decay time constant of the calorimeter plate due to conduction. The rest of the variables are defined above in section 3.4.

τ_d can be measured experimentally by applying a short-pulsed heat flux to the calorimeter and observe the decaying temperature characteristic. We used a 0.5 joule ruby-laser[23] with a pulse length of $\sim$ 0.5 ms as the heat source. Figure 4.9 plots the time histories of the laser pulse and the temperature evolution. Unfortunately only about 0.3 second was recorded and it is very difficult to estimate τ_d. Roughly τ_d is estimated to be in the range of 20 seconds, which is sufficiently long to eliminate the conduction loss as a major source of heat sink during the discharge. It is also short enough such that the calorimeter plate is cooled back down to T_s before the next discharge.

A more interesting measurement using this simple experiment is the determination of the time response of temperature rise as the result of this short heat flux. Exponentially fitting the temperature characteristic we found a rise time of approximately 8.2 ms, which is lower than our analytically predicted value by a factor of 2.

Previous experiments using calorimeters[24,25] included a biasable lead which allowed simultaneous operation as both heat flux and Langmuir probes. Furthermore, the calorimeter can now measure the contribution toward $q_{\|}$ from a different part of the Langmuir probe spectrum (figure 4.6). Unfortunately, an extra bias lead on the calorimeter was not incorporated into the Janus design. Any attempt to either ground or bias the calorimeter plate would draw too

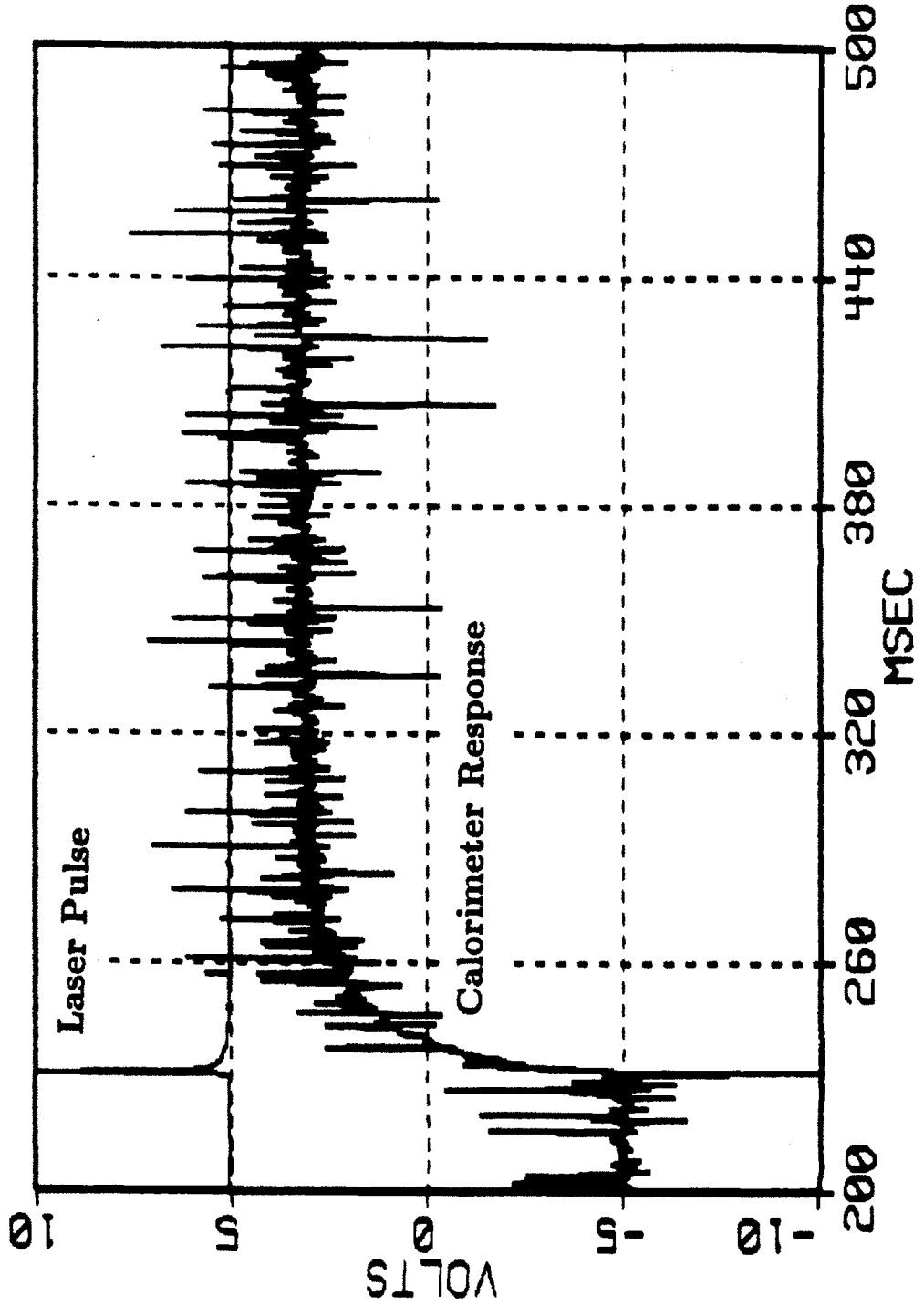

Figure 4.9 Experimental investigation of the calorimeter time response property using a short pulse ruby laser.

much current into the electronics such that the input to the CAMAC is always saturated. Therefore the calorimeter is typically left floating.

The calorimeter measurement is also prone to pick up noise due to the changing ohmic and toroidal field coil currents, although typically the toroidal field magnet current is constant during the plasma discharge. In addition, if the plate is subjected to large fluctuating floating potentials, it is difficult for a simple differential op-amp circuit to deduce the induced emf reading without extraordinarily high common mode rejection ratios. The reasons for the pick-up are two-fold. The first source is from dB/dt which induces current (Lenz' Law) within the circuit. Some of the ways to reduce this type of pick-up are better magnetic shielding or more tightly twisted wires. The calorimeter design is also susceptible to electrical pick-up due to large conducting surfaces exposed to an electrically noisy environment.

The analysis technique for a simple, floating calorimeter is trivial. With ice-point references right after the vacuum feedthrough, the measured emf readings can be easily translated to temperature $T(t)$[26]. The rest of the analysis follows equation 4.22. However, the data are extremely noisy, which might cause large fluctuations while numerically differentiating $T(t)$. To avoid this problem a specified number of data points are averaged to smooth the $T(t)$ profile before differentiation.

All material properties are evaluated at the plate temperature using the data compiled by Touloukian[27]. The energy reflection coefficient is also an adjustable input. For tungsten it is typically set at 0.5, although theoretically predicted values up to 0.6-0.8 have been reported[28,29]. Furthermore, since the particles are gyrating about magnetic field lines, they may strike the calorimeter plate at oblique angles[30]. This would produce additional uncertainty in the reflection coefficient.

References

[1] Molvik, A. W., "Large Acceptance Angle Retarding-Potential Analyzers," *Rev. Sci. Inst.* **52** 5, 704 (1981).

[2] Hutchinson, I., private communication (1986).

[3] Bohm, D., Burhop, E. H. S., Massey, H. S. W., The Characteristics of Electrical Discharges in Magnetic Fields, Editors: Gutherie, A., Wakerling, K. R., McGraw Hill, New York (1949).

[4] Kobayashi, T., *et al.*, "Langmuir Probe Measurements in Beam-Heated Divertor Discharge in D-III," *J. Nucl. Mat.* **121**, 10 (1984).

[5] McCormick, K., Murmann, H., El Shaer, M., and the ASDEX and NI Teams, "Temporal Behavior of the Electron Density Profile in the Scrape-Off Layer of Neutral-Beam-Heated ASDEX Plasmas," *J. Nucl. Mat* **121**, 41 (1984).

[6] Porkolab, M., *et al.*, "Lower Hybrid Heating and Current Drive, and Ion Cyclotron Heating Experiments on the Alcator C and Versator II Tokamaks," Proc. 10^{th} Int'l. Conf. on Plasma Physics and Controlled Nucl. Fusion Research, London (Sept 1984).

[7] Fisch, N. J., *Phys. Rev. Lett* **41**, 873 (1978).

[8] Fiore, C., private communication (1986).

[9] TFR Group, Sands, F., "ICRF Heating Experiments in TFR Using a Low-Field-Side Antenna," *Nuclear Fusion* **25**, 1719 (1985).

[10] Zweben, S. J., Taylor, R. J., "Edge-Plasma Properties of the UCLA Tokamaks," *Nucl. Fusion* **23** 4, 513 (1983).

[11] Barnes, C. W., Strachan, J. D., "Sawtooth Oscillation in the Flux of Runaway Electrons to the PLT Limiter," *Nuclear Fusion* **22**, 1090 (1982).

[12] Kimura, H., *et. al.*, "Heat Flux to the Matial Surfaces in a Tokamak," *Nuclear Fusion* **18** 9, 1195 (1978).

[13] Texter, S. C., "Plasma X-Ray Spectroscopy During Lower Hybrid Current Drive on Alcator C," M.I.T., Doctoral Thesis (December 1985).

[14] Emmert, G. A., Wieland, R. M., Mense, T. A., Davidson, J. N., "Electric Sheath and Presheath in a Collisionless, Finite Ion Temperature Plasma," *Phys. Fluids* **24**, 803 (1980).

[15] Stangeby, P. C., "The Disturbing Effect of Probes Inserted into Edge Plasmas of Fusion Devices," *J. Nucl. Mat.* **121**, 36–40. (1984).

[16] Stangeby, P.C., "Large Probes in Tokamak Scrape-off Plasmas. The Collisionless Scrape-off Layer: Operation in the Shadow of Limiters or Divertor Plates," *J. Phys. D: Appl. Phys.* **18**, 1547–1559 (1985).

[17] LaBombard, B., "Poloidal Asymmetries in the Limiter Shadow Plasma of the Alcator C Tokamak," M.I.T. Doctoral Thesis, April 1986.

[18] Chen, F. F., "Electric Probes," Chapter 3 in Plasma Diagnostic Techniques, Editors: Huddlestone, R. H., and Leonard, S. L., Academic Press, New York (1965).

[19] Lipschultz, B., Hutchinson, I., LaBombard, B., Wan. A, "Electrical Probes in Plasmas," M.I.T. Plasma Fusion Center Report PFC/JA-85-29 (Aug. 1985).

[20] Manos, D. M., McCracken, G. M., "Probes for Plasma Edge Diagnostics in Magnetic Confinement Fusion Devices," Proceedings of NATO Advanced Study Institute on Plasma Surface Interactions, Val Morin P.Q., Canada (August 1984).

[21] Stangeby, P. C.,"Effect of Bias on Trapping Probes and Bolometers for Tokamak Edge Diagnosis," *J. Phys. D: Appl. Phys.* **15**, 1007–1029 (1982).

[22] Manos, D. M., Budny, R., Satake, T., Cohen, S. A., "Calorimeter Probe Studies of PDX and PLT," *J. Nucl. Mat.* **111 & 112**, 130–136 (1982).

[23] Terry, J. L., private communications, 1985.

[24] Stangeby, P. C., *et al.*, "Edge Measurements of T_e, T_i, n, E_r on the DITE Tokamak Using a Biased Power Bolometer," *J. Vac. Sci. Technol. A* **1**, 1302 (1983).

[25] Erents, S. K., "Measurements of Edge Temperature and Density Profiles in the DITE Tokamak, using a Voltage Scanned Heat Flux Probe," *Fusion Technology* **6**, 453 (1984).

[26] "1984 Omega Temperature Measurement Handbook and Encyclopedia," Editor: Omega Engineering, Inc., Stamford CT (1984).

[27] Thermophysical Properties of High Temperature Solid Materials, Elements, Editor: Touloukian, Y. S., MacMillian, New York (1970).

[28] Eckstein, W., Verbeek, H., "Data on Light Ion Reflection," Max-Planck Institute Report No. IPP 9/32 (August 1979).

[29] Ito, R., Tabata, T., Itoh, N., Morita, K., Kato, T., Tawara, H., "Data on the Backscattering Coefficients of Light Ions from Solids (A Revision)," Institute of Plasma Physics (Nagoya University) Report No. IPPJ-AM-41.

CHAPTER 5

RFEA and Langmuir Probe Data Presentation

The present understanding of the edge plasma behavior is very limited. In the scrape-off region many different processes occur simultaneously, including plasma and atomic phenomena and plasma-surface interactions. Numerical models using a variety of assumptions have been proposed[1,2,3,4,5]. However, in view of the complexity of the problem, it is difficult to approach the level of reality using analytical or even computational models. It is not the goal of this thesis to come up with yet another attempt to theoretically or computationally describe the edge plasma.

Using Janus, we have conducted a detailed study of a variety of edge plasma parameters for various operating conditions. The experimental results will be presented separately from the physics interpretations. These physics interpretations will primarily focus on possible mechanisms which will justify the observations and no detailed theoretical model will be presented.

Data will be presented and then interpreted in both sections III and IV of the thesis. In section III we will concentrate on presenting some of the edge plasma phenomena observed on Alcator C, including correlations of edge parameters with central (bulk) plasma parameters and operating conditions; in section IV we will correlate the Janus results with possible mechanisms of plasma-surface interactions during ICRF heating[6,7]. Spectroscopy measurements of impurity concentration and confinement time will also be presented to support and to explain the Janus results.

In this chapter we will present the non-ICRF data of the RFEA and Langmuir probe. The calorimeter results will be presented in chapter 8. To illustrate some of the observed edge phenomena, a time history of a single Alcator C

discharge will be presented in section 5.1. Section 5.2 will present the dependence of edge parameters on several key central plasma parameters and operating conditions: including the peak plasma current, I_p ($\equiv |\underline{I}_p|$), peak line-averaged central electron density, $\bar{n}_e$, probe position, toroidal magnetic field magnitude and direction, $\underline{B}_t$, and plasma positions. Physics interpretations relevant to the data contained in this chapter will be presented in Chapters 6 and 7.

5.1 Time History of a Single Shot

The purpose of designing a Janus-type diagnostic is to be able to simultaneously monitor a variety of relevant edge plasma parameters that may affect plasma-surface interactions. Ion and electron parameters are monitored on both the ion side and the electron side (as defined by $\underline{I}_p$, see figure 3.1). From the proof-of-principle RFEA experiment, we located several interesting edge phenomena that warranted further investigation, including parameter asymmetries between the electron side and the ion side, and also a higher edge ion temperature than electron temperature. During the design phase of Janus, these findings helped determine the Janus setup and operational techniques.

To illustrate the edge phenomena observed by Janus, time histories of the results obtained by the RFEA's and the Langmuir probes for a single plasma discharge are presented in this section. The plasma shot presented here is an 8 tesla, hydrogen discharge. The magnetic configuration is aligned in the "normal" direction where $\underline{B}_t$ is antiparallel with respect to $\underline{I}_p$. The plasma current is flowing clockwise looking from the top. Figure 5.1 shows the two principal central parameters, I_p and $\bar{n}_e$. Compared to typical Alcator operating conditions (see Table 1.1), this discharge is running at relatively low plasma density. Minor central density variations are evident throughout the entire discharge.

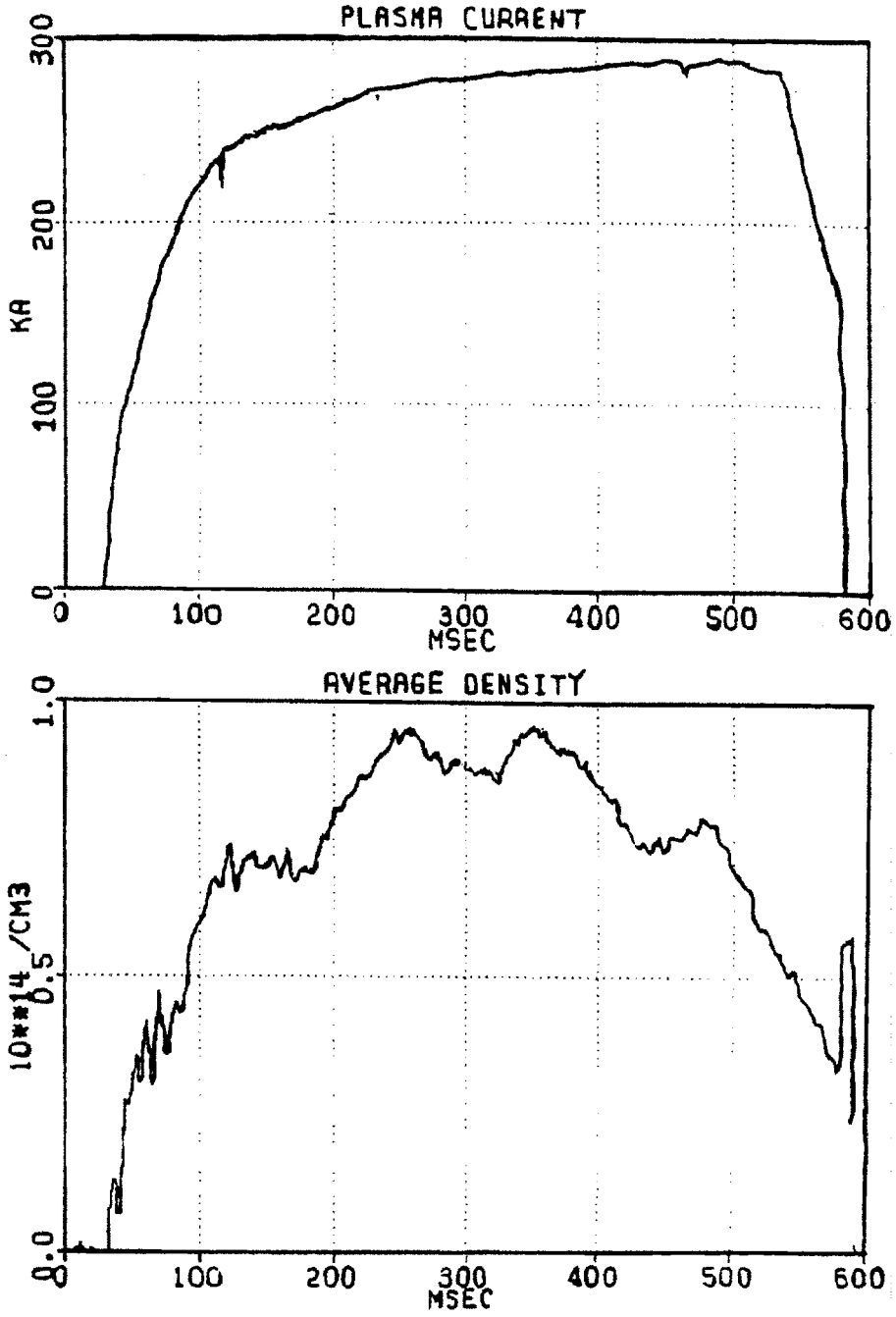

Figure 5.1 Time histories of I_p and $\bar{n}_e$, shot 61 on June 27, 1985.

For this plasma shot the edge of the Janus housing is located at approximately 17.3 cm in the minor radial direction, 0.8 cm into the shadow of the limiter. Janus is inserted from the top of the machine and the probe-limiter configuration is as presented in figure 3.1. The RFEA slit is recessed back from the probe edge by 0.5 cm, or 17.8 cm in minor radius. It is grounded at the probe housing. The center positions of the Langmuir probe and the calorimeter are aligned with respect to the slit position. The probe position, a_s, used in this thesis is defined as the RFEA slit position in the minor radial direction.

Time histories of the electron side and ion side RFEA and Langmuir probe results are presented in figures 5.2 and 5.3 respectively. The axes scales of the figures for the electron side and ion side are the same to allow for direct comparisons. Discharge starts at $\sim$ 30 ms. In each of the figures, the first subplot presents the RFEA measured ion temperature, T_i, and the Langmuir probe measured electron temperature, T_e, obtained from the simple probe theory. The RFEA measured T_e agrees reasonably well with the Langmuir probe T_e (see section 4.2.3) and will not be presented. The second subplot shows the plasma density deduced by the Langmuir probe using equation (4.16), which assumes quasineutral sonic flow to the probe surface. The third subplot plots the Langmuir probe floating potential, V_{float}, and the last subplot shows the energy shift of the ion distribution function with respect to the probe ground as measured by the RFEA, V_{shift} (approximately equal to the difference between the RFEA slit and the plasma potential far away from the probe). V_{shift} on the ion side remains at 0 for the entire discharge and is not plotted out.

The densities deduced from the RFEA are not shown in the figures. Using the transmission coefficients derived from the Monte-Carlo code, we found the RFEA-measured ion density is larger than $n_p(LP)$ by factors of $2 \sim 3$. Aside from the uncertainty of the code in calculating the transmission coefficients, the uncertainty of the simple probe theory will also affect the $n_p(LP)$ measurement. Agreement within a factor of 3 is quite reasonable under these circumstances.

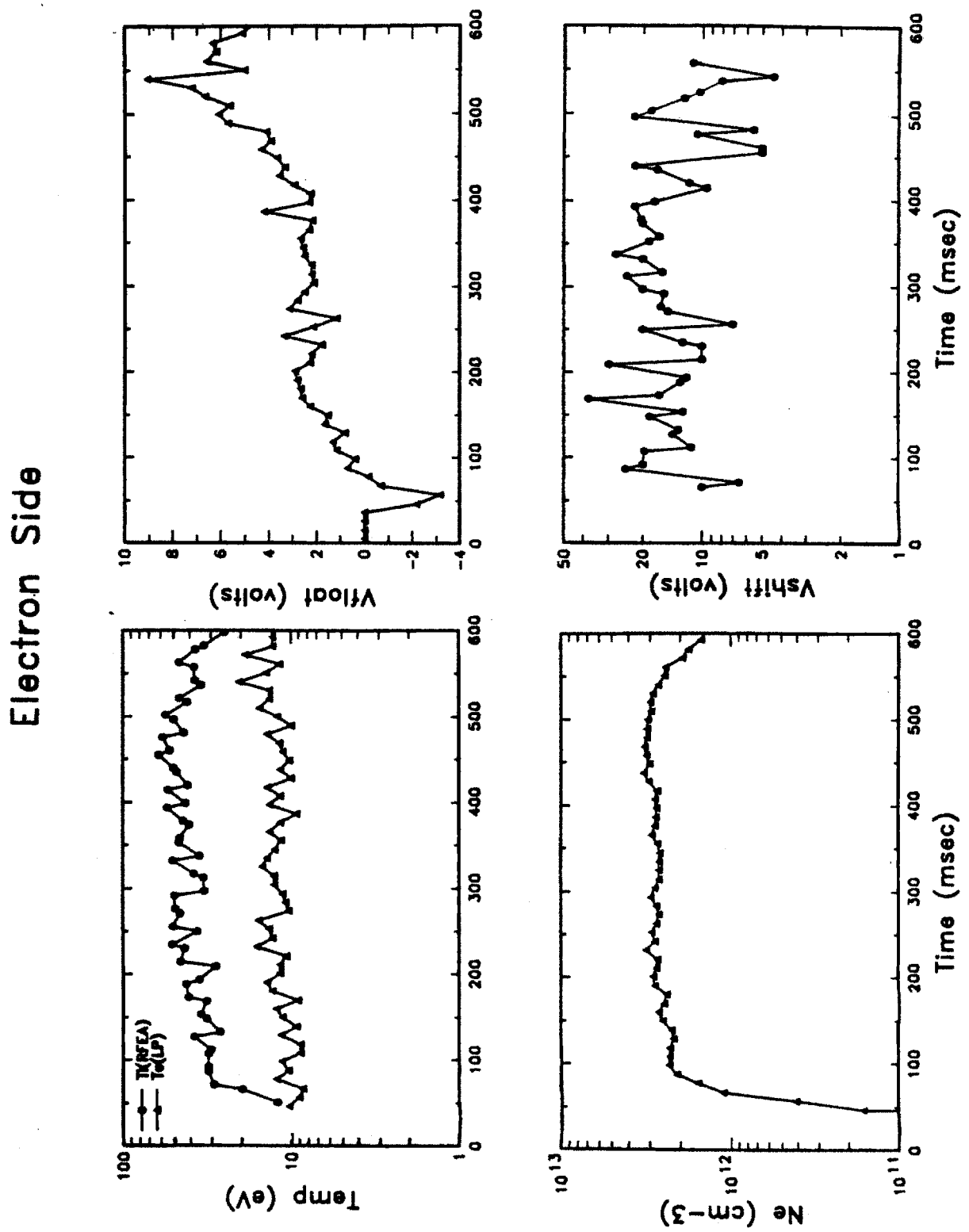

Figure 5.2 Electron side time histories of the edge plasma parameters.

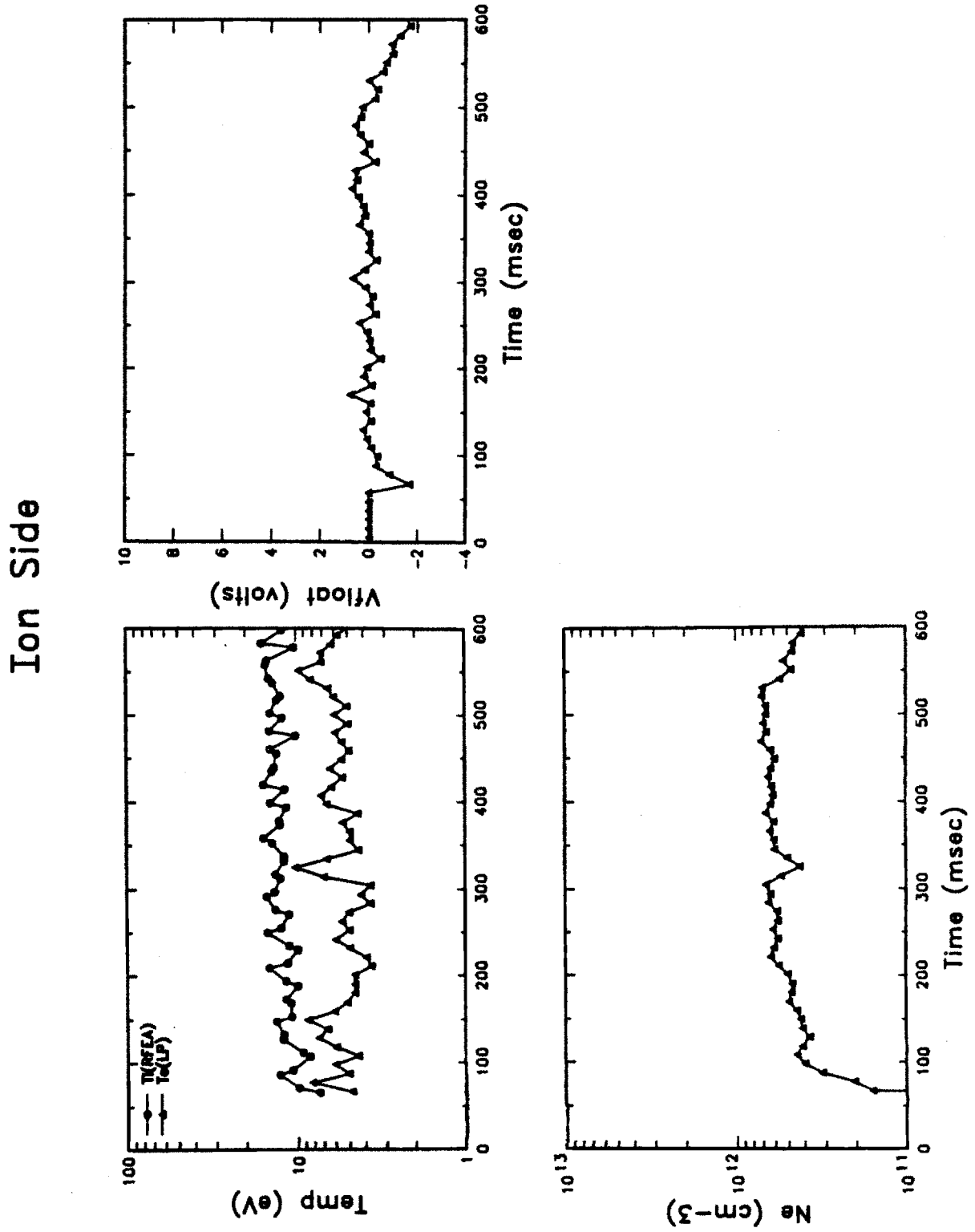

Figure 5.3 Ion side time histories of the edge plasma parameters.

The temperature profiles rise quickly during the ohmic (or plasma current) ramp-up period and stabilize during flattop. Both T_i and T_e typically decay quickly when the plasma shot ends. The end of this shot is not shown due to the shortage of memory space for a long-pulse discharge. Examining the temperature time histories, we found large T_i's compared to T_e's. $T_i/T_e \sim 4$ on the electron side and $T_i/T_e \sim 2.5$ on the ion side. Possible causes of the ion and electron energy decoupling will be investigated in more detail in Chapter 6 when we examine the ion and electron energy balances individually.

Similar time histories are observed for the plasma density. However, it is difficult to interpret the potential behaviors. V_{shift} appears to be roughly constant during the plasma current flattop at approximately 15-20 volts ($\sim 1-2T_e$) on the electron side, much lower than the theoretically predicted value of $\sim 3T_e$ for a floating probe. On the ion side, both V_{float} and V_{shift} are near the probe ground throughout the entire discharge.

Comparing the parameters on both sides of Janus, we found large asymmetries, favoring higher temperatures, densities, and V_{shift} and more positive V_{float} on the electron side. The electron side/ion side ratio for T_i is around 3; T_e ratio is around 2; and n_p ratio is around 5. The V_{float} difference between the electron side and ion side is around 2 volts. Although the electron side has a longer connection length to the next limiter surface, the degree of asymmetry is much larger than from the geometrical effects alone. Detailed analysis of this electron side/ion side asymmetry will be performed in Chapter 7.

5.2 Varying Operating Parameters

One of the primary goals of Janus is to conduct a detailed study of the edge plasma as a functions of the operating parameters. With the amount of data generated by Janus, it is necessary to examine the edge-central and edge-operating parameter correlations in a systematic fashion. To this purpose a database code

is developed. The data stored in the database code are each measured edge parameter averaged over current (I_p) flattop. The relevant parameters stored into the database for every discharge include I_p, $\bar{n}_e$, $|B_t|$, RF power, type of fuel gas, and probe (RFEA slit) position (in minor radius), a_s. Utilizing this database code, we can examine the edge parameters as a function of a specific central parameter or operating condition while limiting the rest of the parameters to a finite range of interest. No observable difference between hydrogen and deuterium discharges was found. So these discharges are not distinguished from each other. Scans of edge parameters as a function of $\bar{n}_e$, I_p, probe positions, $\bar{n}_e/I_p$, toroidal field strength and direction, and plasma positions will be presented in the following sections. The results presented for the first four operating parameters are all for 8 tesla discharges with $\underline{B}_t$ aligned antiparallel with respect to $\underline{I}_p$.

The results presented here are categorized by geometrical configurations, including the limiter dimension and the probe's poloidal location. Most of the time Janus is located on the top of Alcator C, aligned on the magnetic axis (see figure 3.1). Janus has also been installed from the side, positioned slightly (by $\sim$ 1 cm) above the midplane to reduce runaway electron damage. These two cases are distinguished by the notations "Top" and "Side". Three limiter radii have also been used during the tenure of Janus: 16.5 cm, 12.5 cm, and 11.5 cm. The cases presented in the first 4 subsections of this section represent the scans results using the "16.5 cm Top", "12.5 cm Top", and "12.5 cm Side" configurations. The only parameter scans performed using the 11.5 cm limiter are for varying plasma positioning.

The operating window for the two small limiter radius cases is very limited. The smaller limiters are designed to accommodate the ICRF antennas. Therefore the operating conditions are tailored to match the desirable ICRF operating conditions. The "12.5 cm Top" configuration was employed for ICRF Fast Wave Antenna[7], while the "12.5 cm Side" configuration was used for ICRF Bernstein

Wave Antenna[6]. Due to the smaller plasma volume, it is much more difficult to run at high plasma current. One method to quantify the operating current limit is to evaluate the safety factor at the limiter, q_{lim}, defined as

$$q_{lim} \equiv \frac{B_t\, a_{lim}}{B_p\, R_{major}}, \tag{5.1}$$

where B_p is the poloidal magnetic field strength and a_{lim} and R_{major} are the minor and major radii of the tokamak. Using Ampere's Law to relate the plasma current with B_p, and using the Alcator dimension of $R_{major} = 64$ cm, equation (5.1) is reduced to

$$q_{lim} = 0.781 \frac{a_{lim}^2\, B_t}{I_p}, \tag{5.2}$$

where a_{lim} is in cm, B_t is in tesla, and I_p is in kA. $q_{lim} \geq 2-3$ is required for stable tokamak operation.

5.2.1 Maximum Cord-Averaged Central Density

Alcator C primarily uses gas puffing as the refueling mechanism. Pellet experiments have also been successfully demonstrated on Alcator C, resulting in improved central density and overall energy confinement time[8], thus allowing Alcator C to become the first fusion device to surpass the Lawson Criterion for breakeven at higher $T_i(0)$. Results presented in this section are all gas puffing discharges. In performing a proper parameter scan, it is important that other operating parameters are held fixed during the scan. Using the database code, we can preferentially select discharges with similar operating parameters while allowing only the scan parameter to vary.

This section presents the dependence of the edge parameters on the maximum cord-averaged central density, $\bar{n}_e$, as recorded by the laser interferometer[9]. Figures 5.4-5.6 plot the "16.5 cm Top", "12.5 cm Top", and "12.5 cm Side" cases respectively. The "16.5 cm Top" case is obtained for $I_p \sim 400 - 470$ kA while the probe is positioned between 17.5 and 17.6 cm. Due to operating limitations, the bulk plasma parameters for the 12.5 cm configuration cannot match the operating parameters of the "16.5 cm Top" case. The "12.5 cm Top" case is obtained at probe positions between 13.6 and 13.7 cm with $I_p \sim 280 - 300$ kA. The "12.5 cm Side" case is obtained for $I_p \sim 240 - 260$ kA while the probe is positioned between 13.2 and 13.3 cm.

Each case presents both the electron side and ion side edge parameters as a function of $\bar{n}_e$. The edge parameters considered include T_i measured by the RFEA, and T_e, n_e, and V_{float} from the Langmuir probe. In this chapter these four parameters will be used to represent the behavior or the edge plasma.

The dependence of the edge parameters as a function of $\bar{n}_e$ is not obvious. For similar operating conditions, large edge parameter scatterings exist. The cause of these scatterings is unclear. The measured parameters, however, are sensitive to a variety of operating conditions. As we will examine later, the plasma position plays an important role in the measured edge parameters. The wall condition, which affects plasma-surface interaction mechanisms, will also cause edge parameters to fluctuate. For example, after a major disruption, for several successive discharges the edge parameters will behave quite differently despite apparently constant operating conditions. Typically, the edge densities will be lower, by almost an order of magnitude, right after the disruption as compared with later discharges. The presence of large quantities of wall impurities after a disruption may play an important role in the edge particle and energy balances. Finally, edge density and potential fluctuations[11] can be the cause of anomalous transport in the edge plasma region and may also contribute toward the measured scattering.

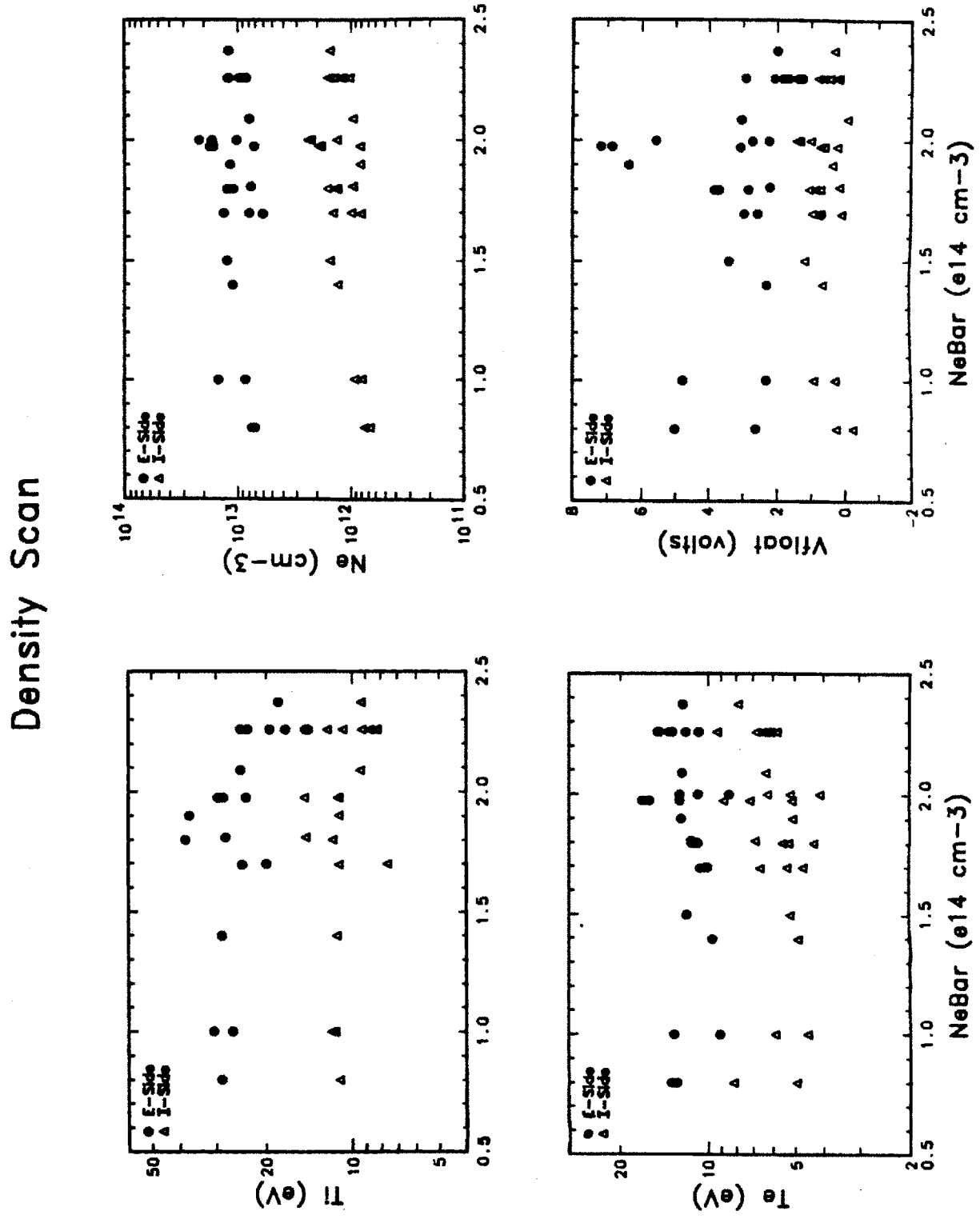

Figure 5.4 Edge parameters as a function of $\bar{n}_e$ for the "16.5 cm Top" configuration.

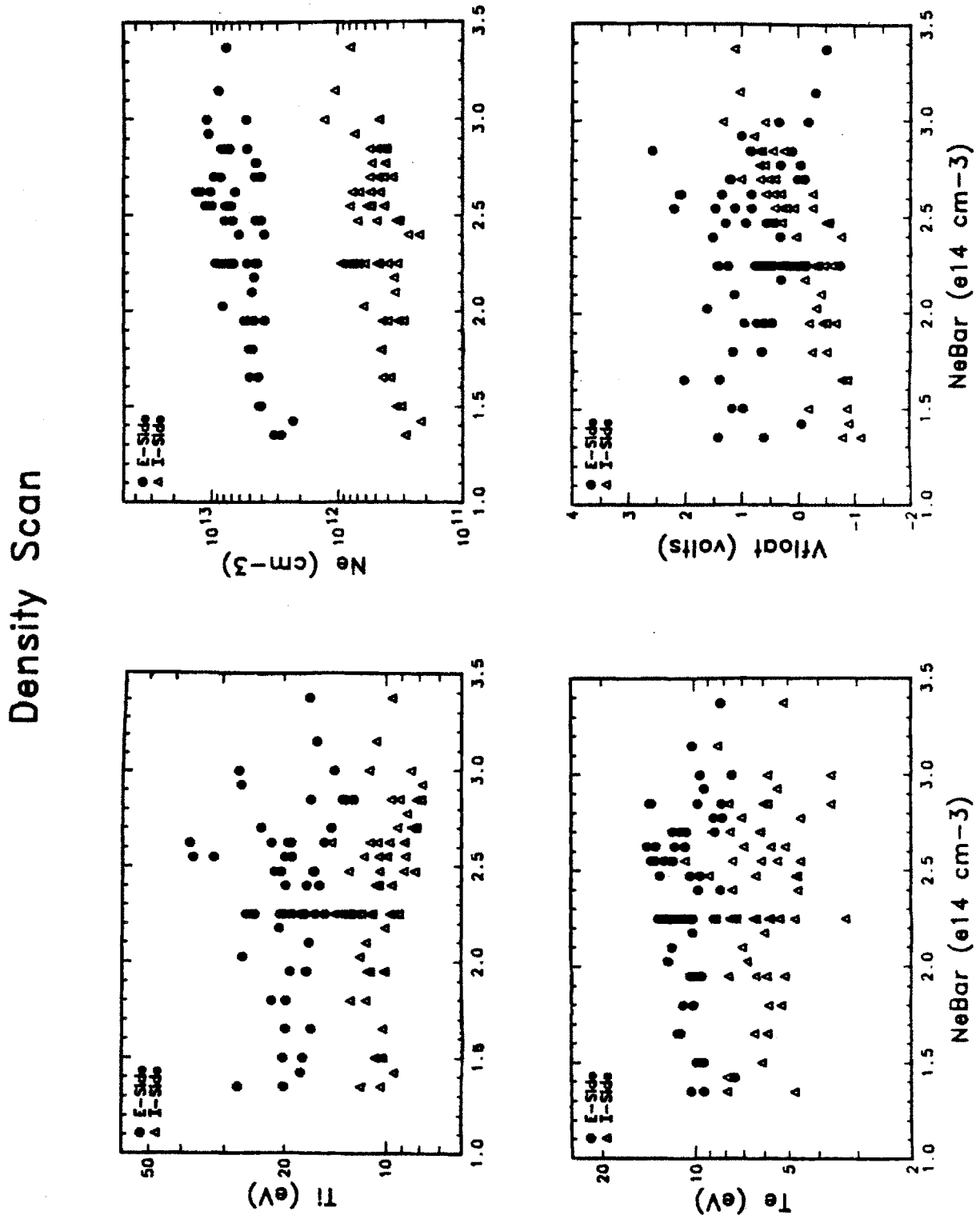

Figure 5.5 Edge parameters as a function of $\bar{n}_e$ for the "12.5 cm Top" configuration.

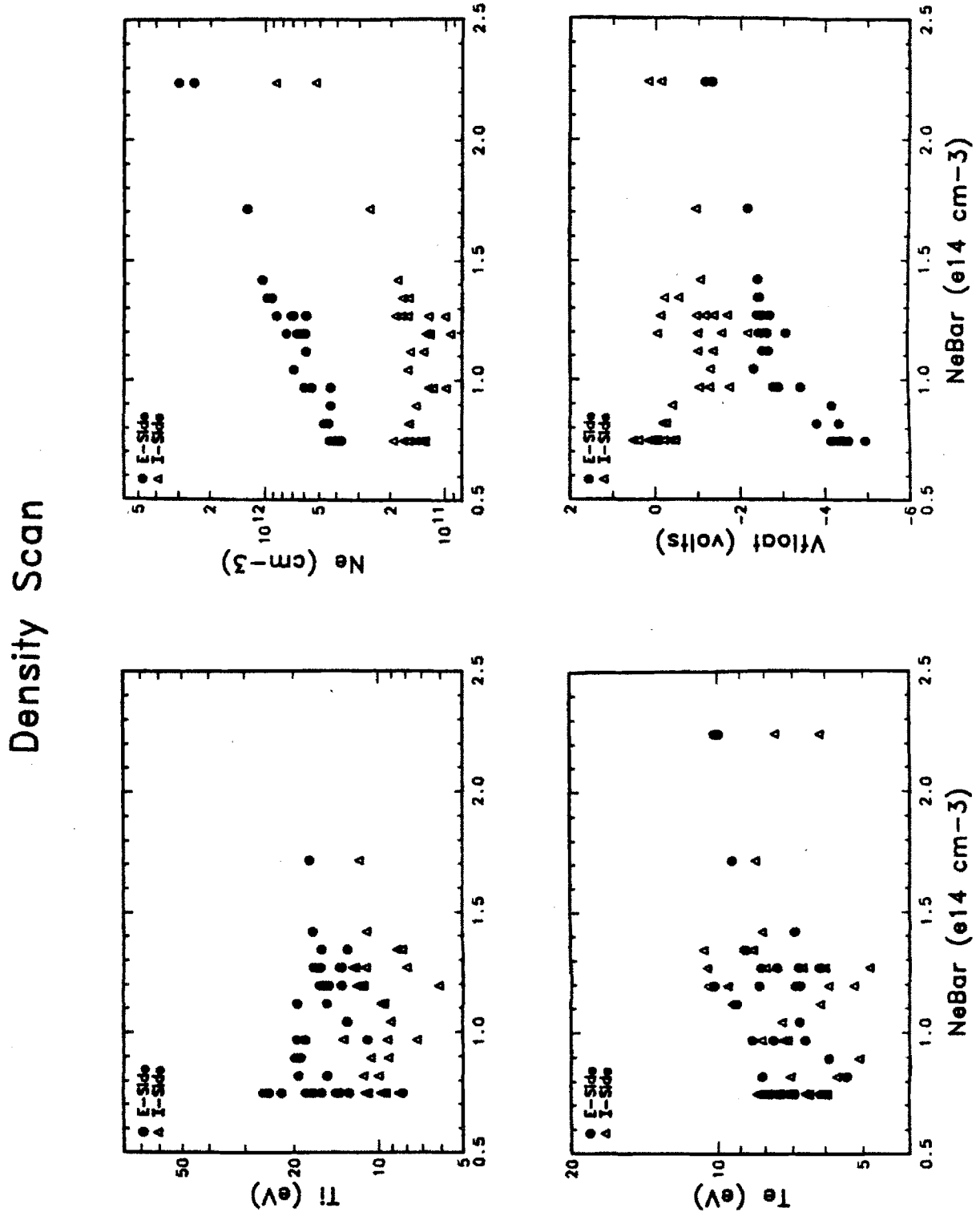

Figure 5.6 Edge parameters as a function of $\bar{n}_e$ for the "12.5 cm Side" configuration.

Looking at all three cases, no systematic variations of T_i and T_e can be deduced. The edge plasma densities, on both the electron and ion sides, increase as $\bar{n}_e$ is increased. For Janus locating at the top, the electron side is always hotter than the ion side. Calculating the electron side/ion side temperature ratios, both the T_i and T_e two-sided ratios fluctuate between 1.5 and 3. The side entry geometry produces a different result. The two-sided T_e ratio hovers around 1. The electron side T_i's are still hotter, but the electron side/ion side ratios drop to the 1-2 range.

The ion temperature remains higher than for electrons, but the behavior of the T_i/T_e ratios act differently for each of the three cases. They also behave differently between the electron and ion sides. For the "16.5 cm Top" case, the T_i/T_e ratios on both the electron and ion sides are around 3 at low central densities, but decay toward 1 as central density increases. No systematic T_i/T_e variation is seen for the "12.5 cm Top" case. The ratios fluctuate between 1 and 2.5 as we scan through in $\bar{n}_e$. From the side, the electron side T_i/T_e ratio drops from 3 to 2 as $\bar{n}_e$ is increased. The ion side ratio ranges from 1 to 2, without any indication of systematic variation.

Although the "16.5 cm Top" case is conducted at higher plasma current, the measured T_i and T_e values match closely with the "12.5 cm Top" case. Keep in mind that the probe positions for both cases are about 1-1.2 cm into the limiter shadow region. The "12.5 cm Side" case yields lower temperatures despite being positioned closer to the bulk plasma. Between the top and side mount geometries, uncertainties of ± 2 mm in the actual probe positions are possible. However, a more probable cause is significant poloidal asymmetries in the edge parameters of Alcator C, which have been observed using a full poloidal Langmuir probe array, DENSEPACK[10,13].

The edge density increases as the central density is increased. However, the edge density increase does not scale linearly with respect to the central density increase. Typically the edge density profile, in the shadow region behind the

limiters, follows an exponential decay profile (see Chapter 2 and section 5.2.4). Therefore, the measured density value depends on the plasma density at the limiter radius and the transport mechanisms, thus variations of bulk density profiles can strongly influence the edge density measurement.

Similar to the two-sided temperature asymmetry, the electron side plasma density is also larger than the ion side density. The electron side/ion side density ratio is much larger for measurements made with the top mount geometry as compared with the side mount case. On the top, the ratios for both the 16.5 and 12.5 cm limiters vary from 10-15 at low central densities and 8-10 at high $\bar{n}_e$'s. On the side, the density ratio starts from 2-3 at low density, but increases quickly and levels off at a ratio of ~ 5 as $\bar{n}_e$ is increased. Consistent with the DENSEPACK measurements, the edge plasma densities at the side are much lower than the densities at the top of Alcator C.

The interpretation of the exact meaning of the floating potential, V_{float}, is unclear for Langmuir probes in a magnetized environment. Often, significant variation of the floating potential is detected corresponding to the onset of peculiar edge phenomena. Although the floating potential is not used as part of the interpretations of the edge phenomena in this thesis, the dependence of V_{float} as a function of the operating parameters is included for future references.

The electron side V_{float} is typically more positive than the ion side V_{float} when the probe enters Alcator C from the top. At low densities, the potential difference between the two sides is larger. This difference is reduced as $\bar{n}_e$ is increased. For the "12.5 cm Top" configuration, the ion side V_{float} starts at a more positive value than the electron side V_{float}, but the potential difference between the two sides reverses sign beginning at $\bar{n}_e \sim 2.5 \times 10^{14}\,\mathrm{cm}^{-3}$. As for the "12.5 cm Side" case, the ion side V_{float} is always more positive than the electron side value. At low densities, where we found very small electron side/ion side density ratios, the potential difference between the two sides of Janus is largest.

5.2.2 Maximum Plasma Current

One of the major achievements of the Alcator C device is the successful demonstration of current drive using lower hybrid waves[12]. However, current drive can only support plasmas at very low plasma densities ($\bar{n}_e \leq 1 \times 10^{14}\,\mathrm{cm}^{-3}$). Normally the Alcator C operates at much higher central densities and plasma currents as compared with the lower-hybrid-driven plasmas. As previously mentioned, the operating parameters for the 12.5 cm limiter are very limited. This prevents us from conducting a reasonable current scan at the smaller limiter. The current dependence of the smaller limiters will be incorporated into the presentation of the next section.

Figure 5.7 plots the edge parameters as a function of the plasma current, I_p, for the "16.5 cm Top" configuration. The probe is positioned between 17.5 and 17.6 cm with $\bar{n}_e \sim 1.6 - 2.1 \times 10^{14}\,\mathrm{cm}^{-3}$. At low I_p, the edge plasma is found to be cooler. The electron side V_{float} also becomes more negative as I_p is decreased. The two-sided asymmetry has a slight dependence on I_p. The ratio of electron side/ion side n_p decreases by about a factor of 2 over the range of I_p in this scan.

5.2.3 $\bar{n}_e/I_p$ Dependence

Looking back at the two previous sections, we found that the effects of I_p and $\bar{n}_e$ on the edge parameters oppose each other. Therefore, $\bar{n}_e/I_p$ arises as a possible scaling parameter for studying the edge parameter dependences. Interestingly similar scaling parameter has been observed on other tokamak devices. $barn_e/I_p$ is also used as a scaling parameter of the Marfe phenomenon observed on Alcator C[10].

Figures 5.8-5.10 plot the edge parameters as a function of $\bar{n}_e/I_p$ for the "16.5 cm Top", "12.5 cm Top", and "12.5 cm Side" cases respectively. For each case the probe is located at the position defined previously in section 5.2.1.

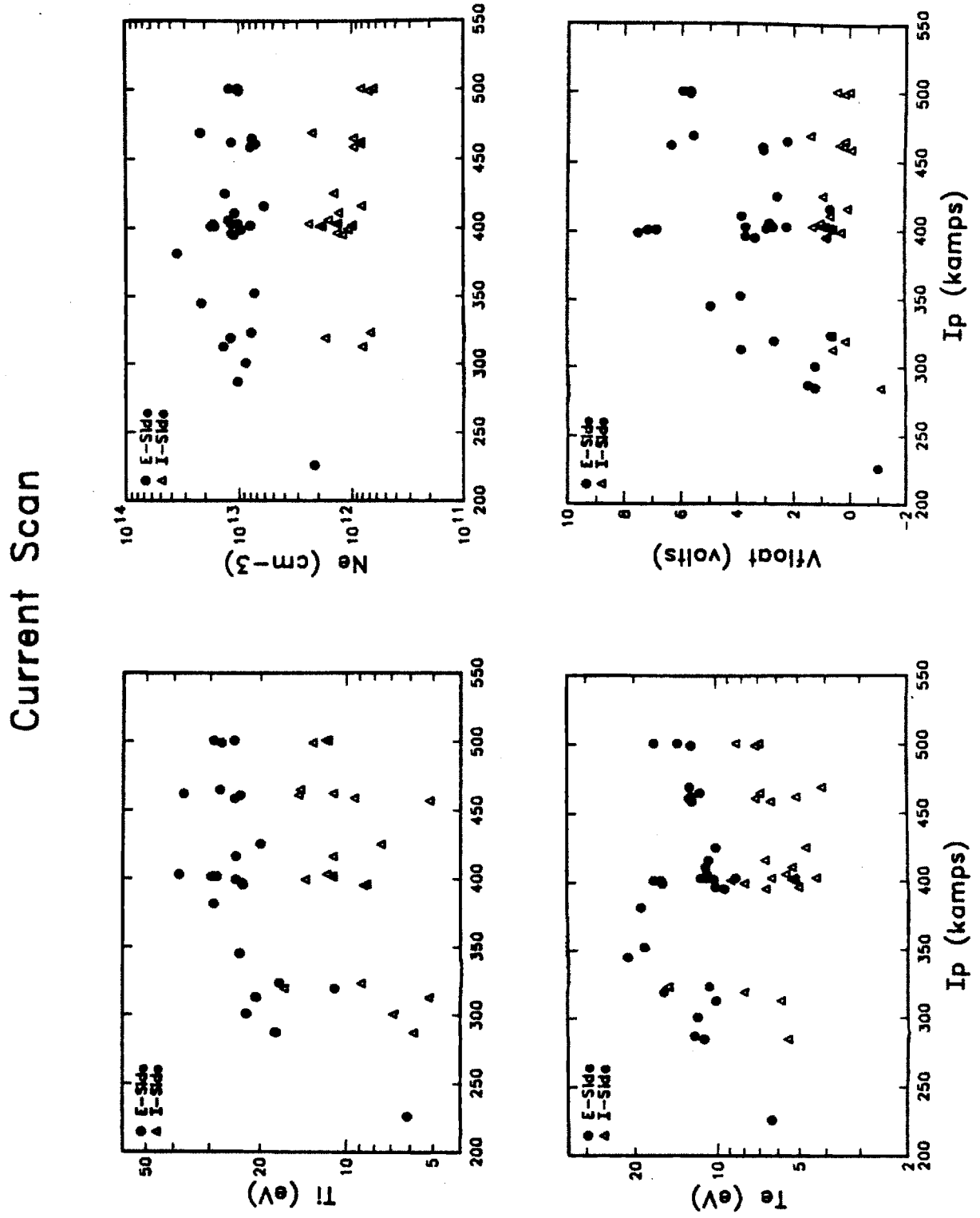

Figure 5.7 Edge parameters as a function of I_p for the "16.5 cm Top" configuration.

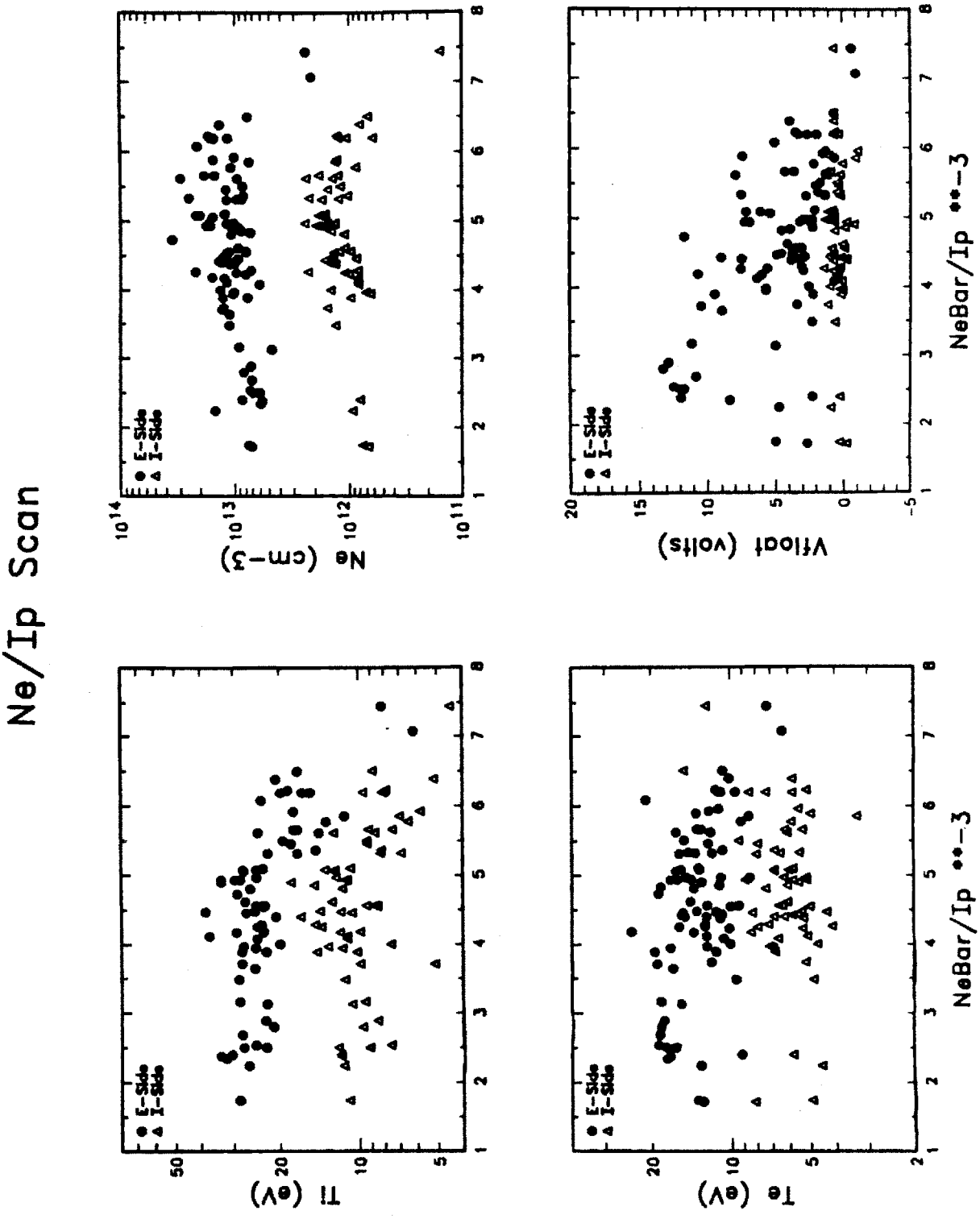

Figure 5.8 Edge parameters as a function of $\bar{n}_e/I_p$ for the "16.5 cm Top" configuration.

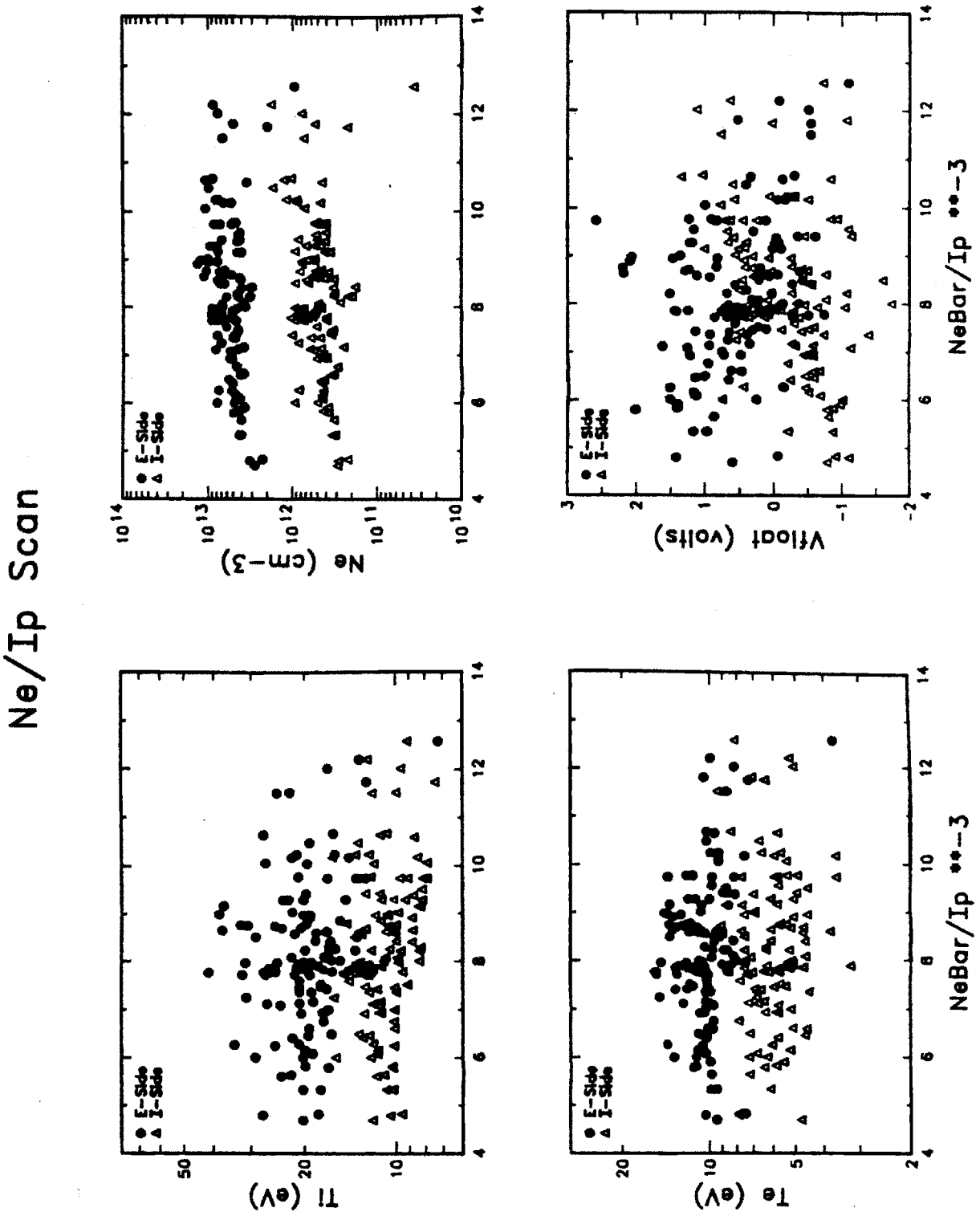

Figure 5.9 Edge parameters as a function of $\bar{n}_e/I_p$ for the "12.5 cm Top" configuration.

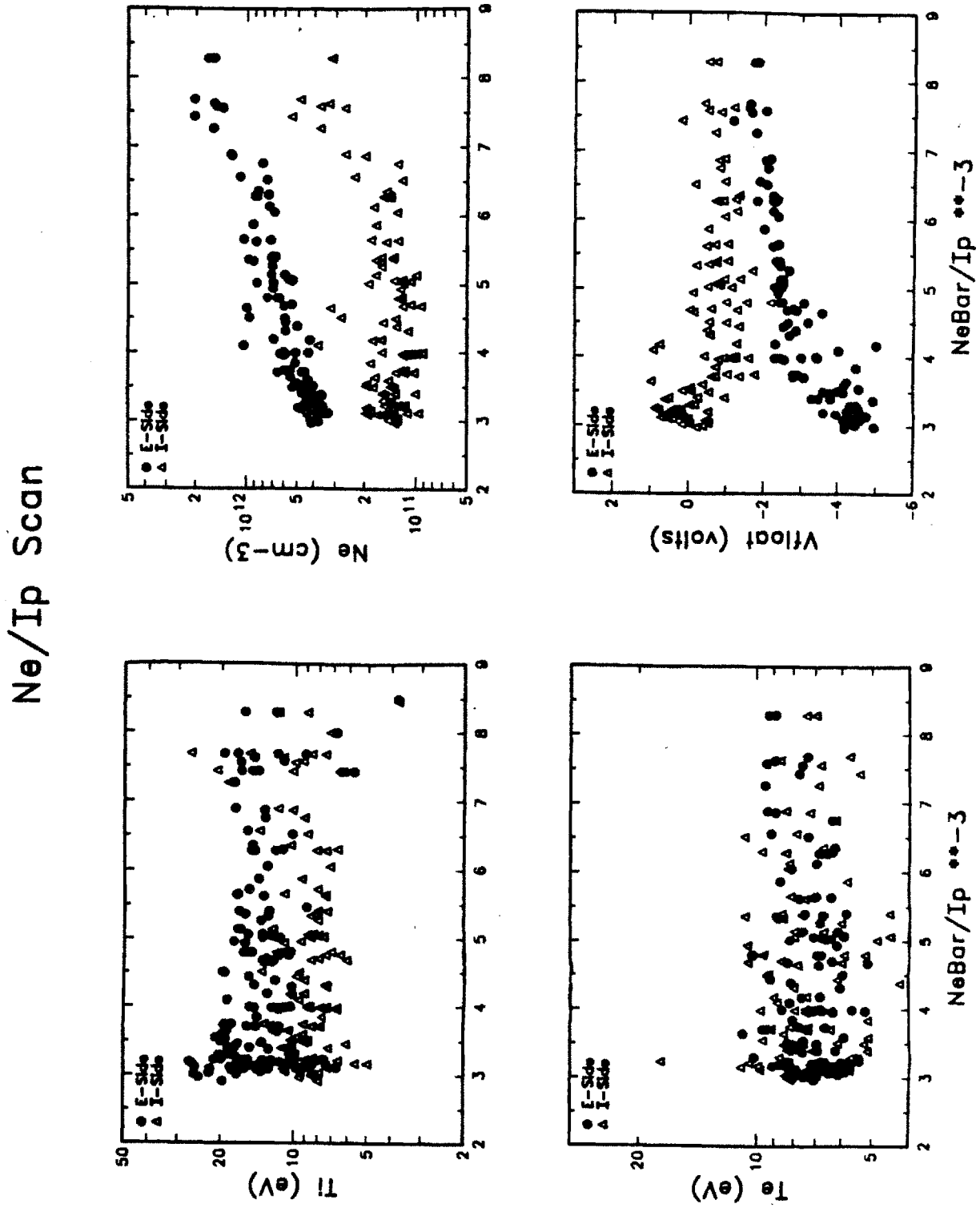

Figure 5.10 Edge parameters as a function of $\bar{n}_e/I_p$ for the "12.5 cm Side" configuration.

At small values of $\bar{n}_e/I_p$, the behaviors of the edge parameters follow the trends predicted by the $\bar{n}_e$ dependences described in section 5.2.1. The edge plasma enters a peculiar regime at large $\bar{n}_e/I_p$ values. For the top mount geometry, beyond a certain transition value, both the electron side and ion side T_i values drop; the electron side T_e drops while the ion side T_e stay roughly unchanged; and the plasma densities on both sides also beyond the transition point. The floating potential difference between the two sides is reduced as $\bar{n}_e/I_p$ increases. Beyond the transition point, the electron side V_{float} drops under the ion side V_{float}.

It is possible to relate the transition point to the onset of Marfe[10,13], where the edge plasma region enters a radiation-dominated regime. The transition point for the "16.5 cm Top" case agrees very well with the experimentally determined[10,13] Marfe threshold, which for a 16.5 cm limiter is located at $\bar{n}_e/I_p \sim 5-5.5\times10^{-3}$, where $\bar{n}_e$ is in 10^{14} cm^{-3} and I_p is in kA. The transition point for a different limiter radius is not studied. For the "12.5 cm Top" case, a similiar transition point is located at about $\bar{n}_e/I_p \sim 1.0\times10^{-2}$.

The transition phenomenon for the side mount geometry is unclear. Although the electron side T_i begins to drop as $\bar{n}_e/I_p$ exceeds 8×10^{-3}, no other phenomenology that is seen for the top mount geometry can be distinguished.

5.2.4 Radial Profiles of the Edge Parameters

In order to evaluate the transport properties of the edge region, it is necessary to determine the spatial dependences of the plasma parameters in order to calculate the spatial derivative terms. Janus is designed to be able to scan in the minor radial direction. The scan range is limited by the vacuum vessel wall at one end and the limiter radius at the other end. However, there exist operating limits on how close the probe can approach the limiter radius. As the probe approaches the limiter radius, the plasma is hotter and denser, thereby

setting a limit for the RFEA power supply in terms of maximum bias voltage and maximum current limitation.

Figures 5.11-5.13 plot the radial profiles for the three different geometric configurations. For the "16.5 cm Top" configuration, the central parameters sit in the range of $I_p \sim 310 - 350\,\mathrm{kA}$, and $\bar{n}_e \sim 1.3 - 1.7 \times 10^{14}\,\mathrm{cm}^{-3}$. For both 12.5 limiter configurations, the operating parameters are at $I_p \sim 270 - 300\,\mathrm{kA}$, and $\bar{n}_e \sim 2.2 - 2.4 \times 10^{14}\,\mathrm{cm}^{-3}$.

Edge modelling typically assumes that the spatial dependences of the edge parameters follow exponential-decay profiles. This assumption allows us to replace the spatial derivative, d/dr, with the variable $-1/\lambda$, where λ is the e-folding scale length for the parameter in question. Looking at the measured radial profiles, we found that both the electron side and ion side density profiles for all three cases can very well be approximated by simple exponential profiles. The density scrape-off length, λ_n, is longer for a larger limiter radius. For the "12.5 cm Side" case, the electron side λ_n is slightly longer than the ion side value. Therefore the electron side/ion side asymmetry grows from 3 to 10 as the probe is retracted from the bulk plasma. For the "12.5 cm Top" case, λ_n values on both sides are approximately the same, with λ_n's around 0.25-0.3 cm, yielding constant electron side/ion side ratios of $\sim 10 - 15$. For the 16.5 cm limiter case, λ_n(electron side) $\sim$ 0.42 cm, while λ_n(ion side) $\sim$ 0.61 cm. The electron side/ion side n_p ratios decrease from ~ 10 close to the limiter edge to ~ 6 near the wall.

The temperature scrape-off length, λ_T, is much longer than λ_n, and the measurements are much more uncertain. The ion temperature scrape-off length, λ_{Ti}, is always shorter than the electron temperature scrape-off length, λ_{Te}. Therefore the T_i/T_e ratio is largest as the probe approaches the limiter edge and reduces as the probe is drawn back toward the wall. $T_i/T_e \rightarrow 1$ near the wall. The ion side λ_T's are typically much longer than the electorn side λ_T's. With few exceptions, λ_{T_e}(ion side) is so large that λ_{T_e}(ion side) $\sim \infty$. On the

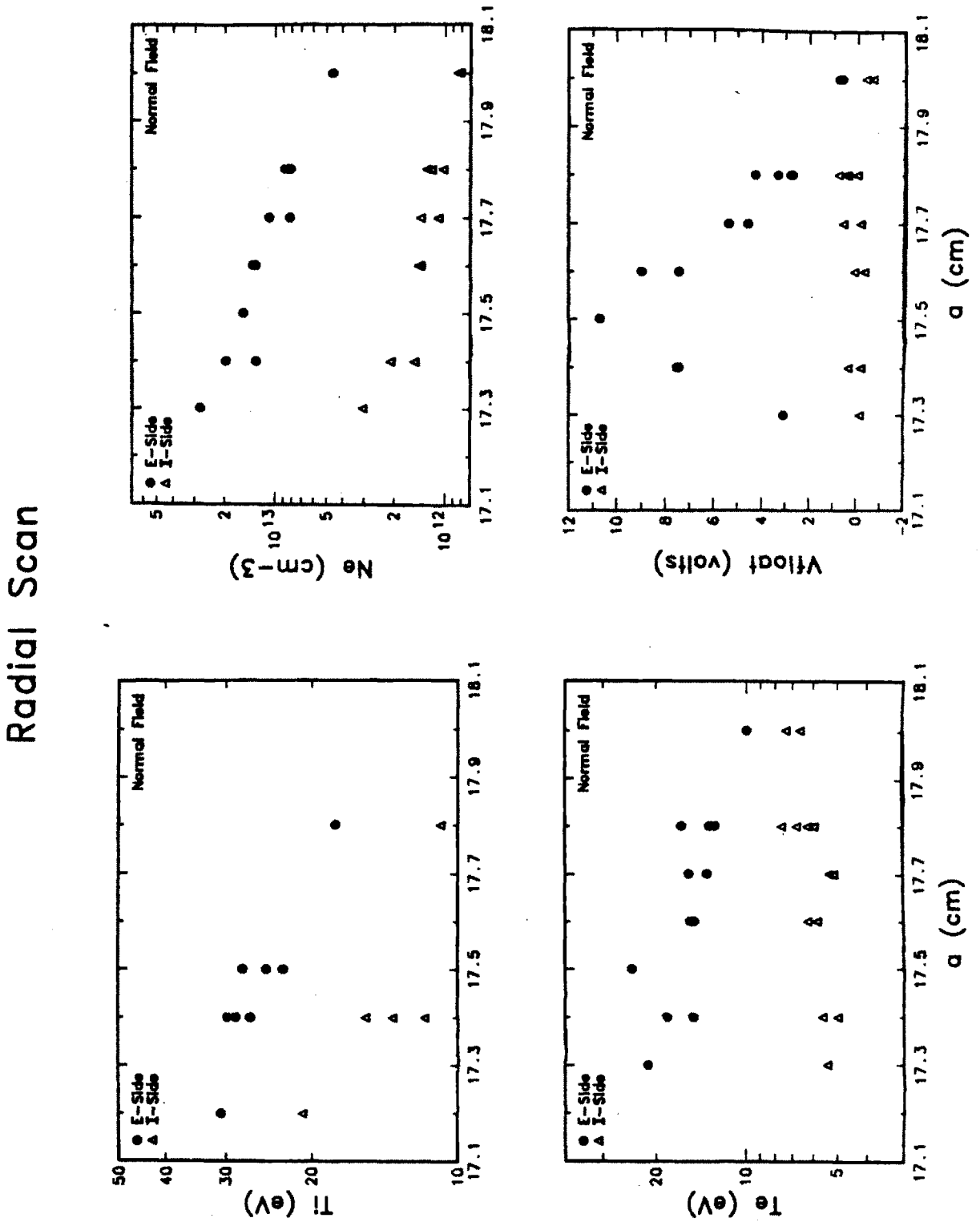

Figure 5.11 Edge parameters as a function of minor radius for the "16.5 cm Top" configuration.

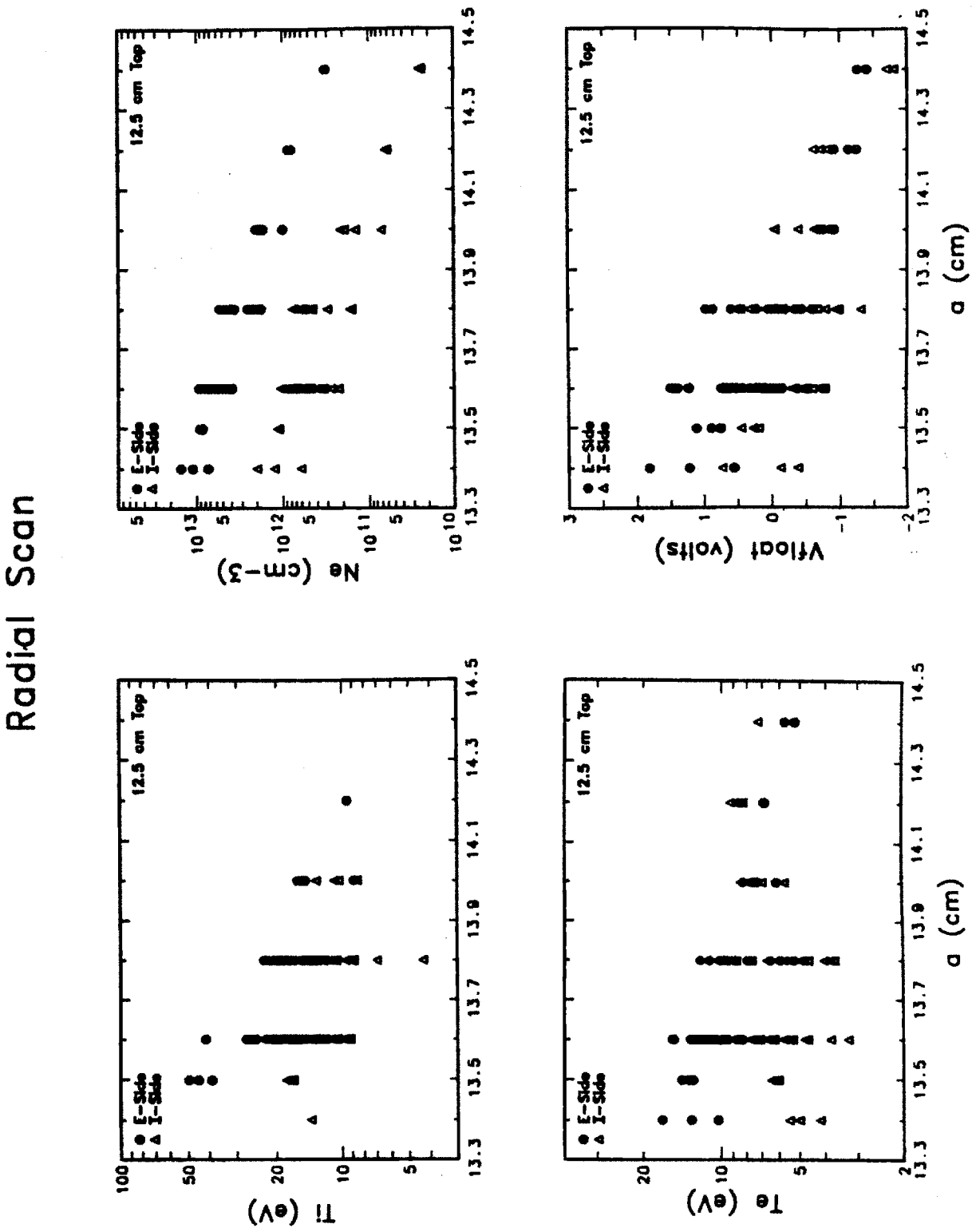

Figure 5.12 Edge parameters as a function of minor radius for the "12.5 cm Top" configuration.

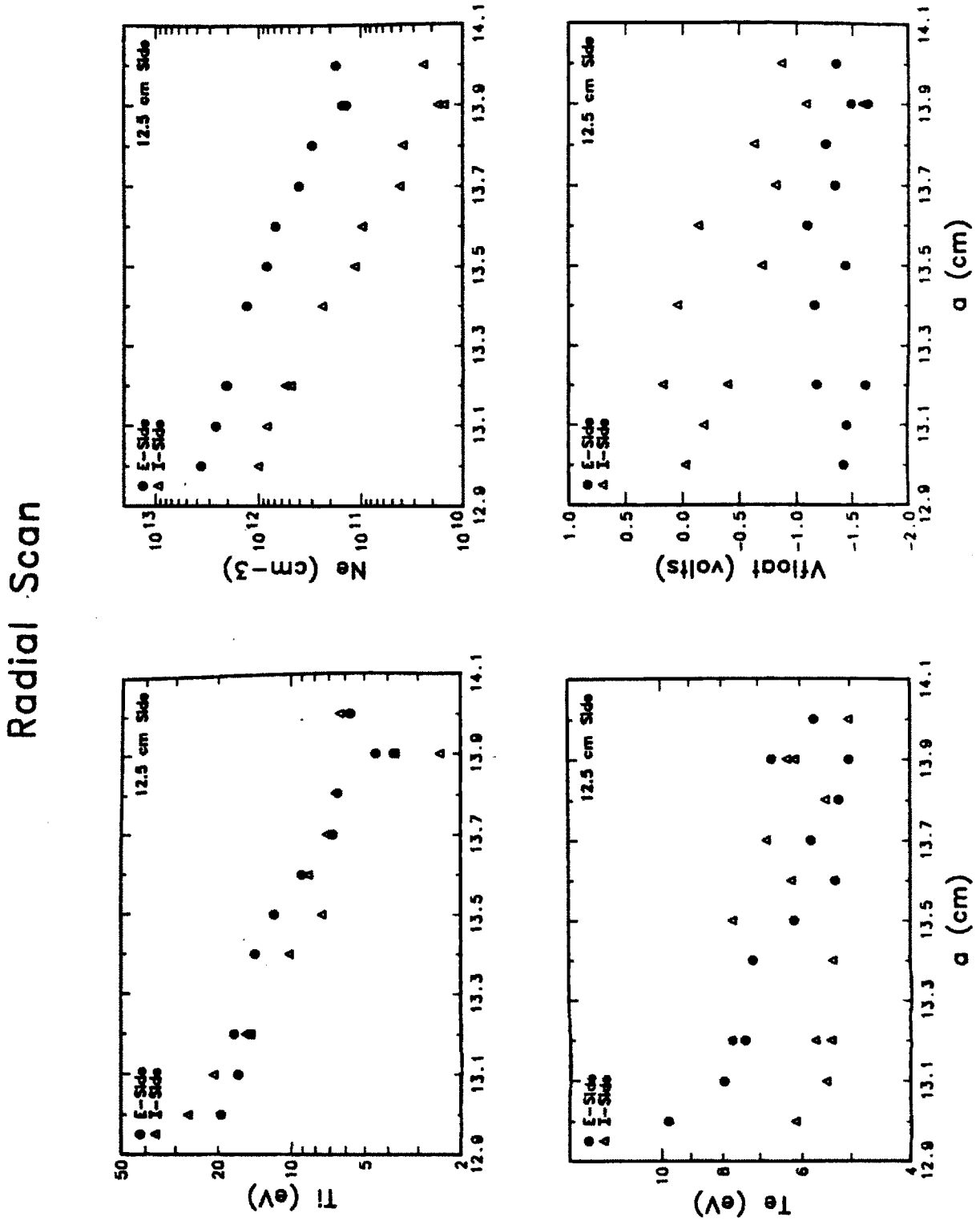

Figure 5.13 Edge parameters as a function of minor radius for the "12.5 cm Side" configuration.

electron side, for the "16.5 cm Top" case, λ_{Te} and λ_{Ti} are both $\sim$ 1.0 cm. The two 12.5 cm limiter cases have similiar electron side temperature scrape-off lengths, $\lambda_{Te} \sim 1.5 - 2$ cm, and $\lambda_{Ti} \sim 0.7$ cm.

As the probe moves away from the limiter edge, the floating potential difference between the two sides drops. The electron side V_{float} is more positive than the ion side V_{float} when Janus is inserted from the top of Alcator C. The behavior reverses when the probe is mounted from the side.

5.2.5 Toroidal Field Magnitude and Direction

Alcator C is a high magnetic field device with operating range of $|B_t|$ from 6.5 to 13 tesla. Figure 5.14 plots the edge parameters as a function of toroidal magnetic field strength. The scan is conducted at $I_p \sim 280 - 300$ kA and $\bar{n}_e \sim 2.0 - 2.2 \times 10^{14}$ cm^{-3}. Both the electron side T_i and T_e decrease as B_t is increased while the ion side temperatures stay either constant or increase slightly, thus reducing the electron side/ion side temperature ratios down toward one. The behavior of V_{float} follows the temperature behavior. Both the electron and ion side densities decrease as B_t inceases. However, the decreases are uniform, maintaining the electron side/ion side ratio at ~ 10.

Normally the toroidal field direction is aligned antiparallel with respect to the plasma current direction. This is defined as the *normal* field configuration. The direction of the toroidal field can be reversed such that $\underline{B}_t \parallel \underline{I}_p$. This is defined as the *reverse* field configuration.

The reverse field experiment was only performed for the 16.5 cm limiter with Janus located at the top. Looking at similiar experimental conditions, we found that the reversal of $\underline{B}_t$ has a pronounced impact on the edge plasma. Figure 5.15 plots the edge parameters as a function of $\bar{n}_e/I_p$ for a probe positioned between 17.5 and 17.6 cm. Despite the large scattering of the data points, an obvious difference between the "normal" and "reverse" configurations is the change

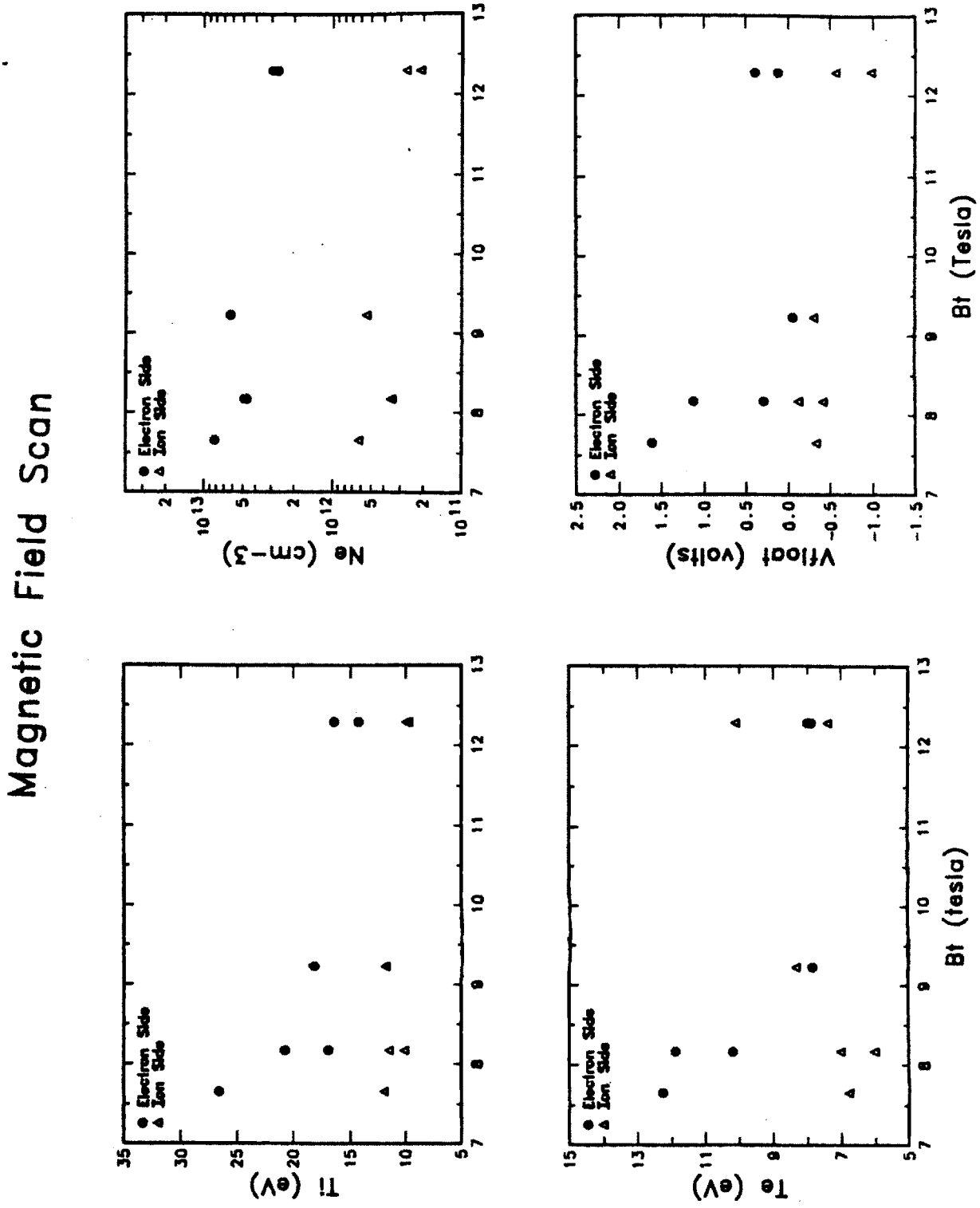

Figure 5.14 Edge parameters as a function of the toroidal field magnitude.

in magnitudes for all the edge parameters. The ion side parameters approach the magnitudes of the electron side parameters such that the electron side/ion side ratios approach one. Throughout the entire $\bar{n}_e/I_p$ scan, the ion side floating potential is either greater than or approximately equal to the electron side value. This is a reversal from the "normal" field case.

The effect of reversing the $\underline{B}_t$ direction on the two-sided asymmetry is most visible by examining the radial profiles of plasma parameters. Figure 5.16 plots a radial profile of edge parameters for similiar operating conditions as shown in figure 5.11. For the "normal" field configuration, the ion side density and temperature scrape-off lengths are much longer than the corresponding electron side values, thus yielding large electron side/ion side ratios as the probe is pushed toward the limiter radius. For the "reverse" field case, the ion side scrape-off lengths are smaller than the normal field case. The electron side scrape-off lengths typically do not vary much when the direction of $\underline{B}$ changes. Close to the limiter radius, the magnitudes of the ion side parameters exceed the electron side values. The floating potentials on both sides are approximately equal far away from the limiters, but the ion side V_{float} becomes more and more positive with respect to the electron side V_{float} as the probe is pushed toward the limiter radius. This trend is opposite from the "normal" field trend.

5.2.6 Plasma Positions

Changing the plasma position can lead to a large perturbation of the edge parameters. The in-out and up-down plasma positions are diagnosed by using a carefully wound poloidal array of magnetic pickup coils positioned at the vacuum vessel[14]. The in-out position can be determined by a linear combination of the pick up voltage readings from the cosine and saddle coils, or V_{c-s}, and the up-down position can be determined by the voltage reading of the sine coil, V_{sin}.

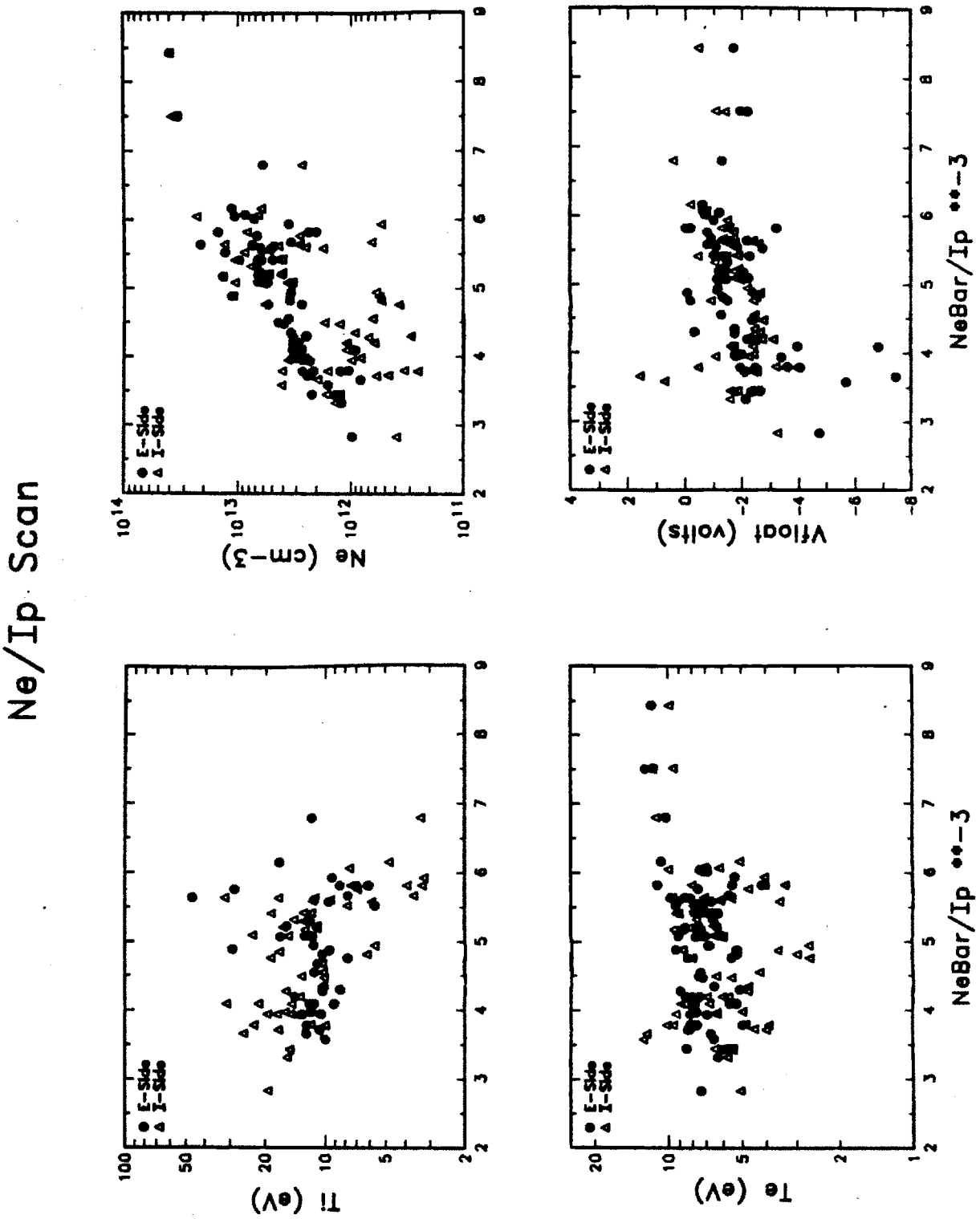

Figure 5.15 Edge parameters as a function of $\bar{n}_e/I_p$ for "16.5 cm Top" reversed field configuration.

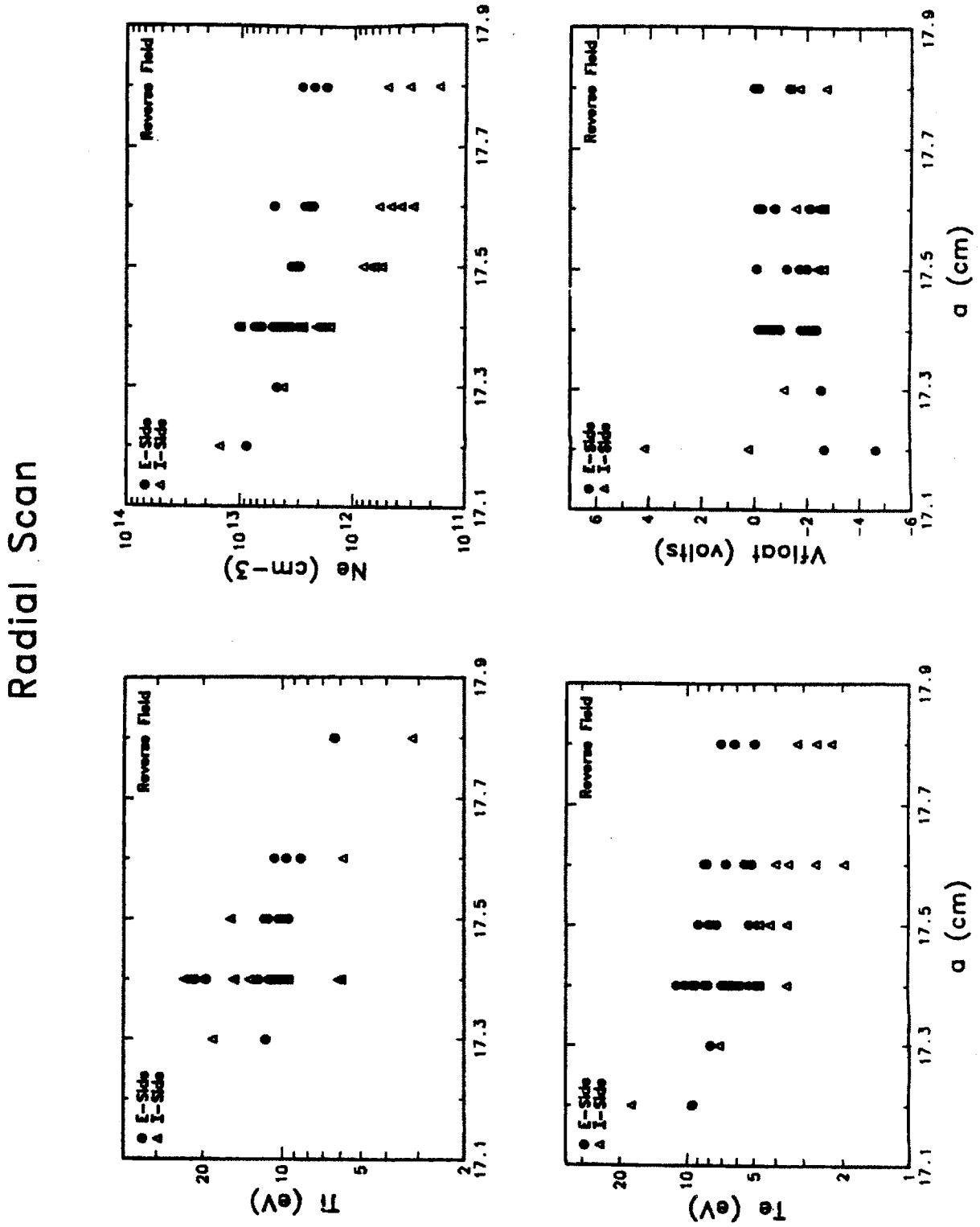

Figure 5.16 Edge parameters as a function of minor radius for the "16.5 cm Top" reverse field configuration.

The only systematic study of the effects of plasma positions on the edge parameters is conducted by varying the in-out position. During an in-out scan, the up-down positions are held fixed on axis. Figure 5.17 plots the edge parameter dependences of the in-out positions at one radial position (12.6 cm) while all other parameters are fixed. The scan is conducted in deuterium with $I_p \sim 247$ kA, $\bar{n}_e \sim 2.6 \times 10^{14}$ cm^{-3}, and $B_t \sim 8.5$ tesla. Both the electron side temperature and density increase as the plasma position is shifted inside (high field side). No systematic change of the ion side density is evident. Although the ion side temperature appears to decrease a little as the plasma is shifted inside, the variation is only a few eV.

A more extensive study of the effect of plasma positioning on the electron and ion side edge parameters is displayed in figures 5.18 and 5.19. The central plasma parameters are fixed at $I_p \sim 250 - 260$ kA, $\bar{n}_e \sim 2.0 - 2.3 \times 10^{14}$ cm^{-3}, and $B_t \sim 7.3$ tesla. The fuel is hydrogen. The study is comprised of 4 radial scans at the plasma in-out positions of +0.8 cm, +0.7 cm, +0.2 cm, and –0.25 cm, where positive values signify position toward the outside, or low field side, and negative values mean inward positions.

On the electron side, there is a clear trend, at all radii, toward increasing edge density and T_e as the plasma is shifted toward the inside. A similiar trend exists for T_i at small minor radii. Decreasing T_i is seen at large minor radius, $a_s > 13.0$ cm. As the plasma is shifted toward the inside, V_{float} also becomes more positive at all radial locations.

On the ion side, the edge parameter dependence is less clear. The temperature values fluctuate as the plasma position changes. The ion side V_{float} is more negative than the electron side V_{float} for $a_s \leq 12.8$ cm. No significant potential difference is seen at large minor radii. At $a_s \geq 12.8$ cm, there is some general trend of density increase as the plasma shifts inward. Figure 5.20 plots the fitted density scrape-off lengths on both the electron and ion sides for the four plasma in-out positions studied. When the plasma is shifted outward, the electron side

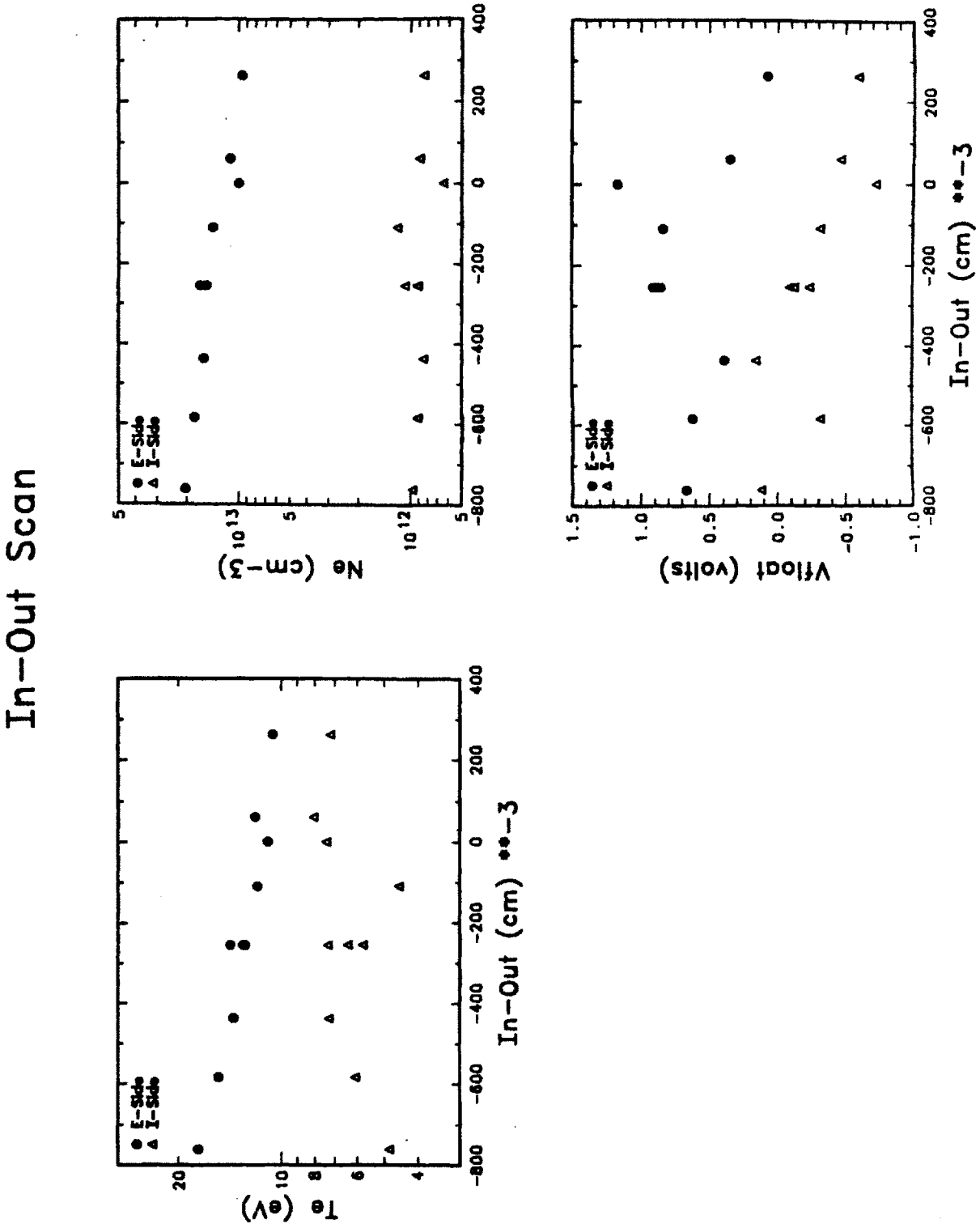

Figure 5.17 Edge parameters as a function of the plasma in-out positions for a probe located at 12.6 cm.

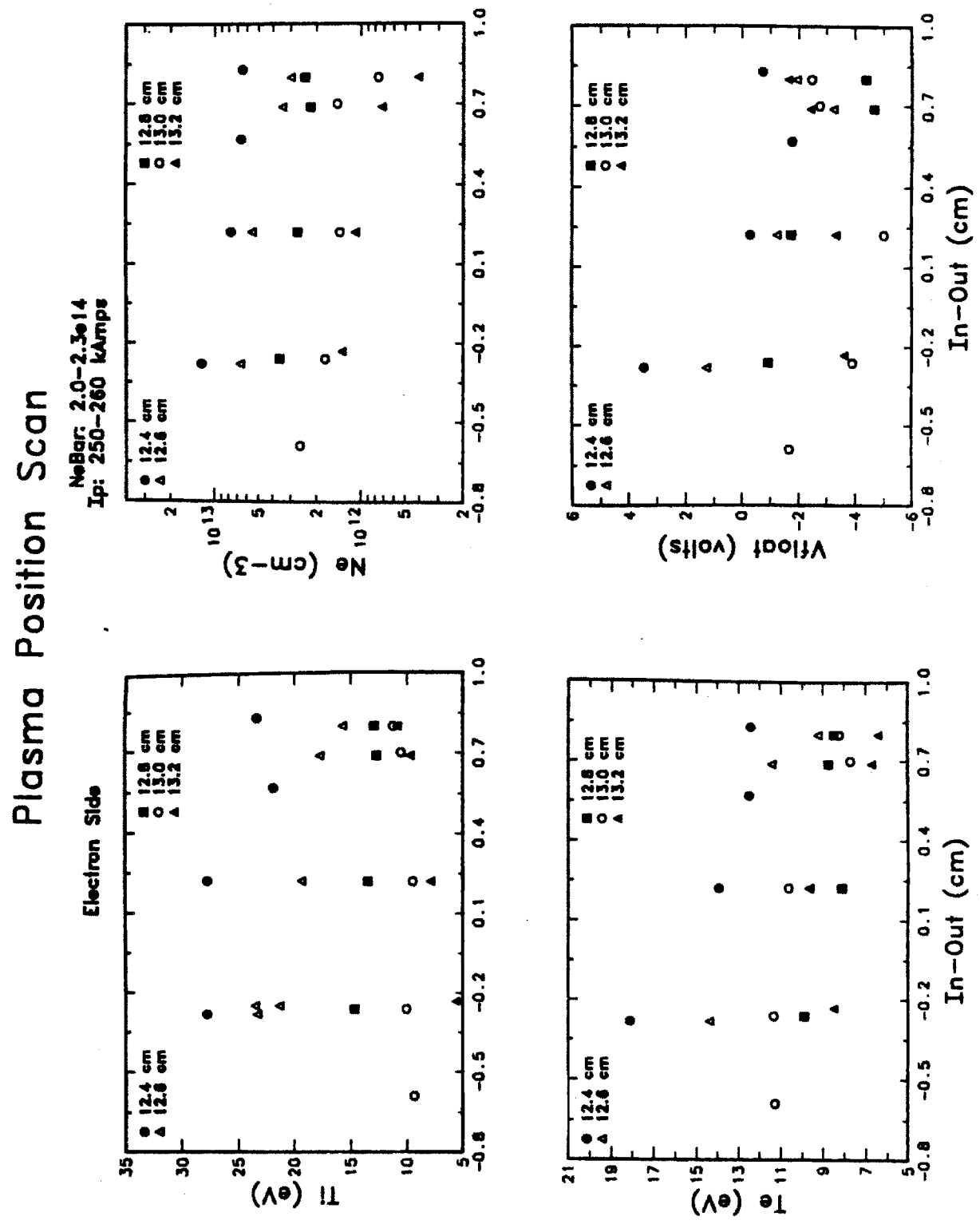

Figure 5.18 Variations of electron side parameters as a function of plasma in-out positions and minor radius.

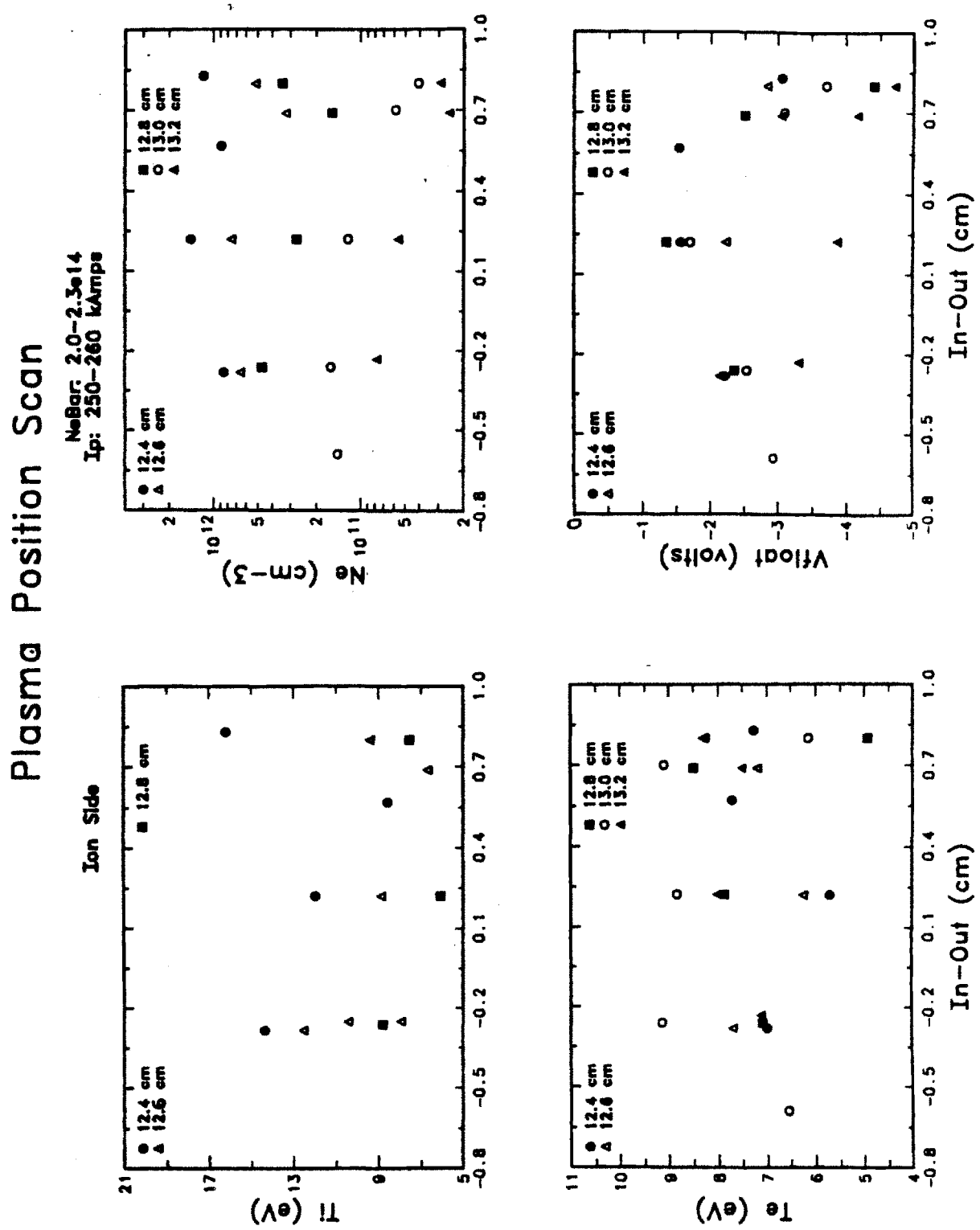

Figure 5.19 Variations of ion side parameters as a function of plasma in-out positions and minor radius.

λ_n's are longer than ion side λ_n's. When the plasma is shifted inward, the λ_n's on both sides are approximately the same.

As the result of the changes in magnitudes of edge parameters and λ_n as the plasma position shifts in and out, the two-sided asymmetry also changes. Figure 5.21 plots the electron side/ion side density and T_e ratios. As the plasma shifts inward, there is a systematic trend, at all radial positions, for greater electron side T_e as compared with the ion side T_e. For $a_s \leq 12.6$ cm, the density asymmetry favors the electron side as the plasma shifts toward inside. For larger minor radii, there appears to be a reversal of asymmetry, favoring larger electron side density as the plasma shifts *outward*. However, at the one lone data point from an extreme inside position and large minor radial position ($a_s = 13.0$ cm), the ratio appears to have a well-shape dependence, favoring larger electron side density as the plasma shifts *either* inward or outward.

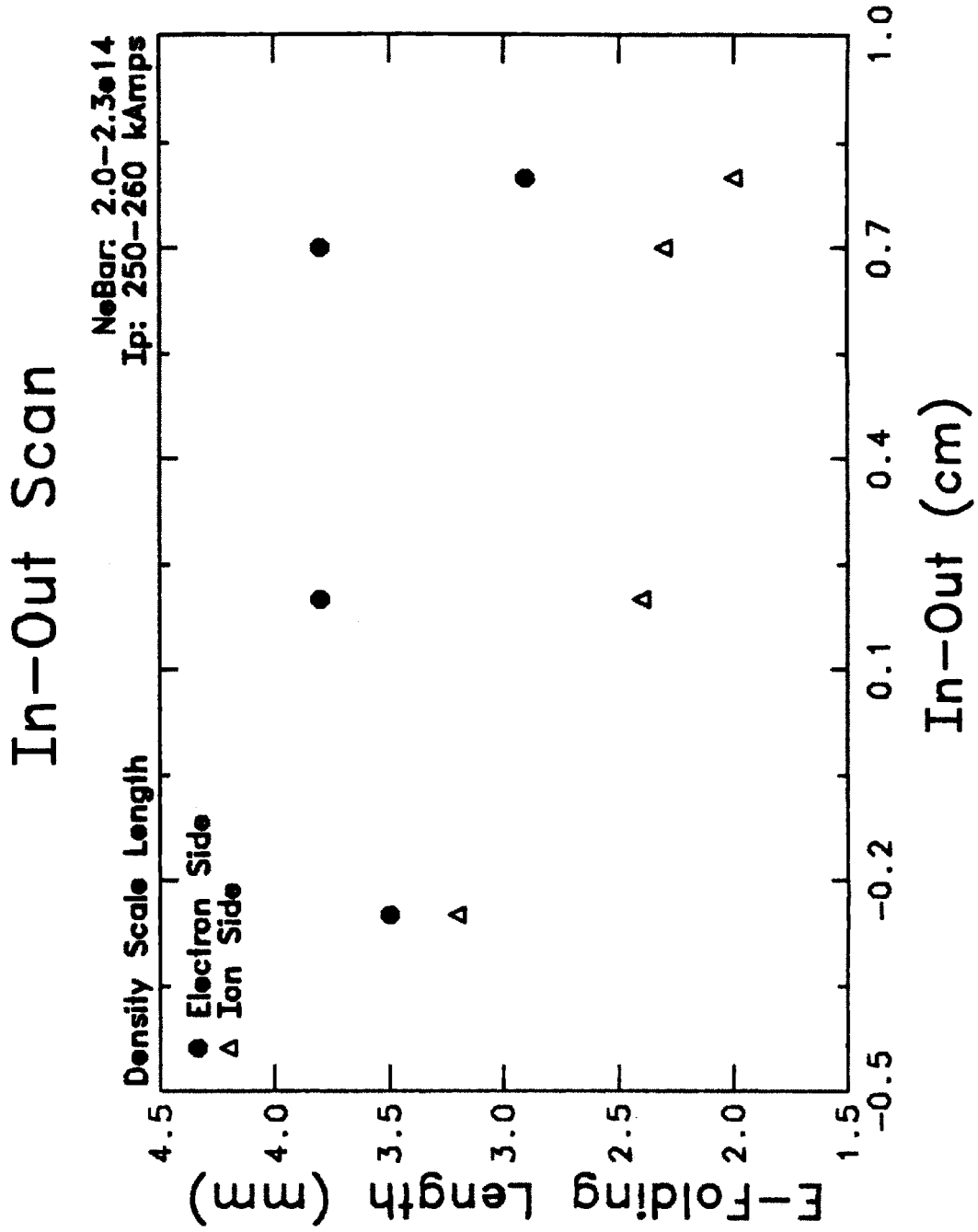

Figure 5.20 Variations of the electron and ion side density scrape-off scale lengths as a function of the plasma in-out positions.

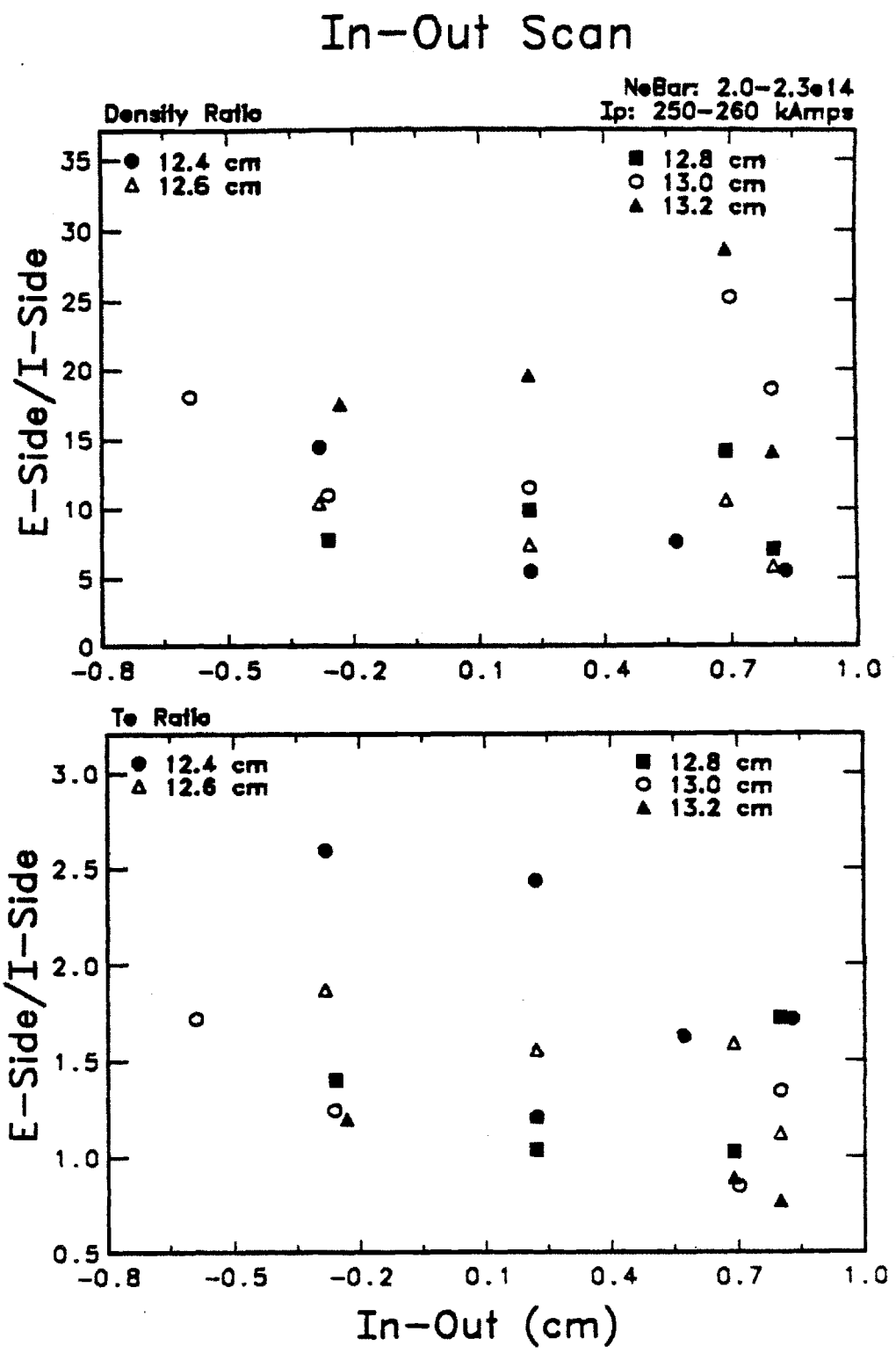

Figure 5.21 Electron side/ion side density and electron temperature ratios at different radii and plasma in-out positions.

References

[1] Gierszewski, P. J., "Plasma/Neutral Gas Transport in Divertors and Limiters," M.I.T. ScD Thesis, September 1983.

[2] Prinja, A. K., Conn, R. W., "An Axially Averaged-Radial Transport Model of Tokamak Edge Plasmas," *J. Nucl. Matt.* **128 & 129**, 135–140 (1984).

[3] Ulrickson, M., Post, D. E., "Particle and Energy Transport in the Plasma Scrape-Off Zone and Its Impact on Limiter Design," *J. Vac. Sci. Technol. A* **1**, 907 (1983).

[4] Waltz, R. E., Burrell, K. H., "Tokamak Boundary in Contact with a Limiter," *Nuclear Fusion* **17**, 1001 (1977).

[5] Braams, B. J., Harbour, P. J., Harrison, M. F. A., Hotston, E. S., Morgan, J. G.,, "Modelling of the Boundary Plasma of Large Tokamaks," *J. Nucl. Mat.* **121**, 75 (1984).

[6] Moody, J. D., McDermott, F. S., Porkolab, M., Parker, R. R., Besen, M., Takase, Y., Alcator C Group, "The Alcator C Ion Bernstein Wave Heating Experiment," *Bull. Amer. Phys. Society* **30**, paper 5Q9, 1495 (1985).

[7] Shepard, T. D., Besen, M., McDermott, F. S., Parker, R. R., Porkolab, M., "A Matched Fast Wave Coupler for the Alcator C ICRF Heating Experiment," *Bull. Amer. Phys. Society* **30**, paper 5Q10, 1495 (1985)

[8] Greenwald, M., Gwinn, D., Milora, S., Parker, J., Parker, R., Wolfe, S., and Alcator Group, "Energy Confinement of High-Density Pellet-Fueled Plasmas in the Alcator C Tokamak," *Phys. Rev. Let.* **53**, 352 (1984).

[9] Designed and operated by S. Wolfe.

[10] LaBombard, B., "Poloidal Asymmetries in the Limiter Shadow Plasma of the Alcator C Tokamak," M.I.T. Doctoral Thesis, April 1986.

[11] Liewer, P. C., "Measurements of Microturbulence in Tokamaks and Comparisons with Theories of Turbulence and Anomalous Transport," *Nuclear Fusion* **25**, 543 (1985).

[12] Porkolab, M., et al., "Lower Hybrid Heating and Current Drive, and Ion Cyclotron Heating Experiments on the Alcator C and Versator II Tokamaks," Proceedings of the 10^{th} Int'l. Conf. on Plasma Physics and Controlled Nuclear Fusion Research, London, (September 1984).

[13] Lipschultz, B., LaBombard, B., Marmer, E. S., Pickrell, M. M., Terry, J. L., Watterson, R., Wolfe, S. M., "MARFE: An Edge Plasma Phenomenon," *Nuclear Fusion* **24**, 977 (1984).

[14] Pribyl, P., "Plasma Position Control on Alcator C," M.I.T. Plasma Fusion Center Report, PFC/RR-81-21 (May 1981).

CHAPTER 6

Ion and Electron Energy Balances

The ions play an important role in the edge plasma region. A large number of edge processes and plasma-surface interactions are dependent on the ion temperature, T_i. Yet direct measurement of T_i is seldom achieved in the edge plasma region. An excellent review of the techniques of ion temperature measurement is given by Matthews[1]. Using the three diagnostics within Janus, a number of important edge plasma parameters can be monitored directly and simultaneously, including the plasma density, and ion and electron temperatures. From the measured values of the edge parameters and using the simple edge model derived in Chapter 2, we can examine the Alcator C edge plasma and investigate the possible edge phenomena that may affect the edge plasma. In this chapter, energy balances for both the ions and electrons will be performed. Unfortunately a number of unknowns, principally the neutral and impurity parameters, along with the existence of edge potentials, will directly affect the energy balance. In addition, the edge transport mechanisms are anomalous, thus accurate ion and electron energy balances are difficult. An alternative to studying the energy balances is to study the degree of impact for various energy loss or gain mechanisms which will influence the edge energy balance picture.

A simple energy balance, using a model proposed by Stangeby[2], is presented in the next section. Section 6.2 reiterates some of the important findings relevant to the ion and electron energies that were previously presented in Chapter 5. Then ion and electron energy balances, using the model derived in Chapter 2, will be carried out for the edge parameters measured on the Alcator C using Janus. Finally, in section 6.4, we will attempt to perform an accounting of the total energy deposited in the edge region.

6.1 A Simple Energy Balance Picture

Assuming that the edge region is collisionless, and neglecting the presence of both neutrals and impurities, Stangeby[2] simplifies the edge energy balance picture to a balance between parallel loss to the limiters and perpendicular gains due to diffusion and conduction. The terminology used in this chapter is defined in Chapter 2.

In the Stangeby model, the continuity equation is expressed by equation (2.28). The energy equation is approximated as

$$\nabla \cdot q_{\perp}^{j} \sim \frac{q_{\parallel}^{j}}{L_{\parallel}}, \tag{6.1}$$

where $q_{\perp}^{j}$ and $q_{\parallel}^{j}$ are the perpendicular and parallel heat fluxes for species j. The perpendicular heat flux as a function of the minor radius r can be approximated as

$$q_{\perp}^{j} \sim n_p \chi_{\perp}^{j} \frac{d(kT_j)}{dr} + 2kT_j D_{\perp} \frac{dn_p}{dr}. \tag{6.2}$$

r_{lim} is defined as the limiter edge. The parallel ion and electron heat fluxes are described by equations (2.53) and (2.55). For this analysis, Stangeby uses $f(\tau) \sim 0.5$ and $\mu_E \sim 1$.

The radial profiles in the scrape-off plasma are assumed to be:

$$n_p(r) \equiv n_{p0}\, e^{-(r-r_{lim})/\lambda_n}, \tag{6.3}$$

$$T_e(r) \equiv T_{e0}\, e^{-(r-r_{lim})/\lambda_e}, \quad \text{and} \tag{6.4}$$

$$T_i(r) \equiv T_{i0}\, e^{-(r-r_{lim})/\lambda_i}, \tag{6.5}$$

where λ's are the scrape-off density and temperature scale lengths, and the subscript 0 signifies the value at the limiter radius. The radial dependence of the ion sound speed is assumed to be dominated by the ion temperature profile. By using equations (6.3)-(6.5), Stangeby integrates through the continuity and energy equations from the limiter radius to the wall at $\sim \infty$. The perpendicular ion conduction term is negligible if $\lambda_i \rightarrow \infty$. By using the continuity equation, $D_\perp$ is given by equation (2.34). Therefore, the electron energy equation can be reduced to

$$1 + \frac{\lambda_n}{\lambda_e} = \frac{\gamma_e}{2 + (\chi^e_{\perp 0}\lambda_n / D_{\perp 0}\lambda_e)}. \tag{6.6}$$

γ_e is the sheath transmission coefficient for electrons. It is a function of plasma, material, and geometrical effects. Figure 6.1 plots the function λ_e/λ_n against the transport function $\chi^e_{\perp 0}/D_{\perp 0}$ for different values of γ_e. At the Alcator C edge, $\lambda_e/\lambda_n \sim 2.5$. For typical value of $\gamma_e \sim 6$, $\chi^e_{\perp 0}/D_{\perp 0} \sim 6$. The INTOR[3] design study used $\chi^e_{\perp 0}/D_{\perp 0} \sim 5 - 10$.

Assuming that all the particle and energy fluxes that diffuse into the edge plasma region will be removed by the limiters, the rate of total particle (P_p) and energy (P^j_E for species j) removal at the limiter can be expressed as

$$P_p = N_s w \int_{r_{lim}}^{\infty} \Gamma_\parallel \, dr, \quad \text{and} \tag{6.7}$$

$$P^j_E = N_s w \int_{r_{lim}}^{\infty} q^j_\parallel \, dr, \tag{6.8}$$

where $\Gamma_\parallel$ is the parallel particle flux (see section 2.2.1), N_s is the total number of limiter or divertor surfaces, and w is the breadth of the scrape-off tube.

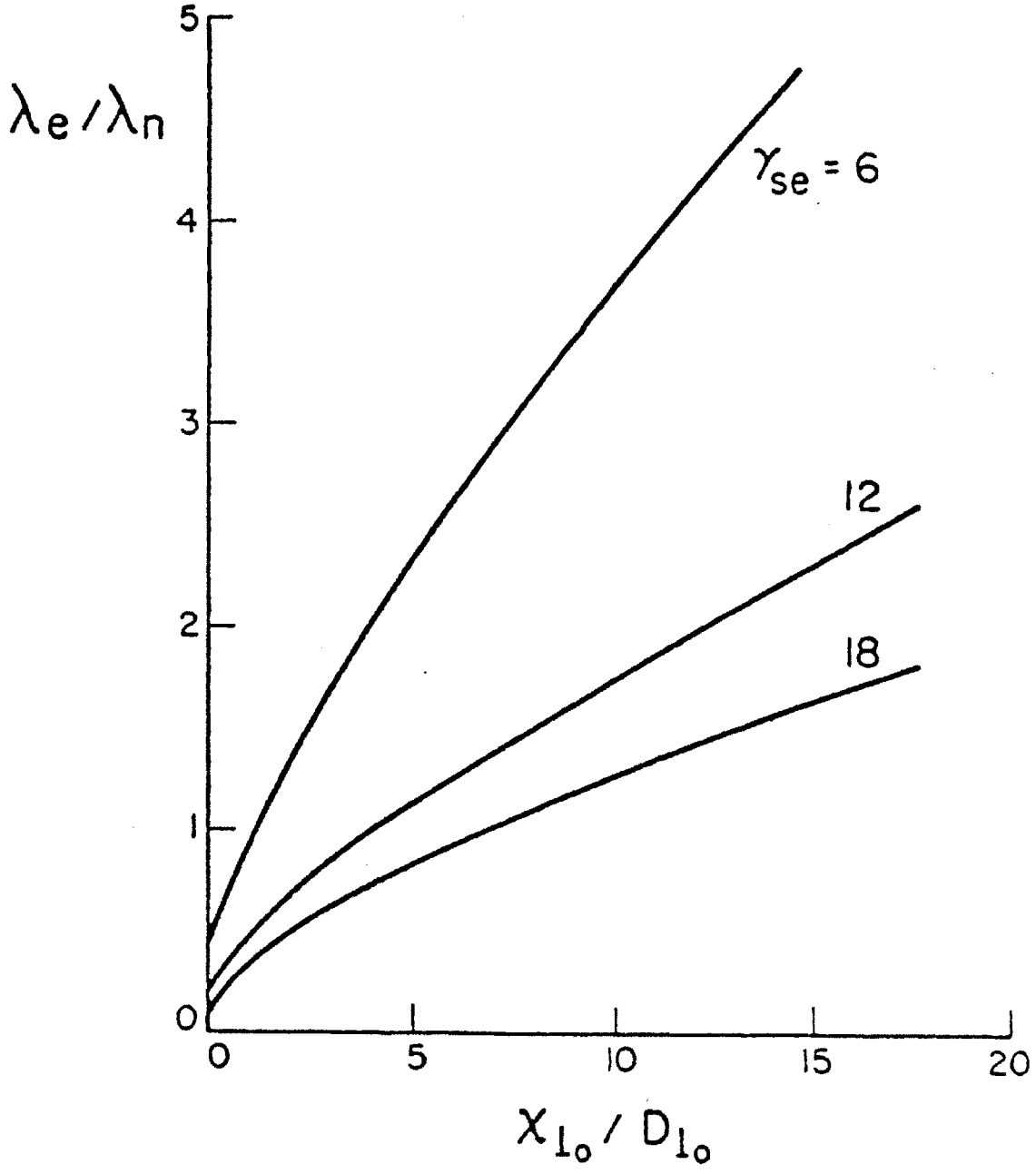

Figure 6.1 The ratio of λ_e/λ_n as a function of the ratio $\chi^e_{\perp 0}/D_{\perp 0}$ plotted for various values of the electron sheath transmission factor γ_e.

$w = 2\pi r_{lim}$ for a full poloidal ring limiter. Given the radial profiles of the densities and temperatures, and by predicting the dependence of γ_e as a function of both T_e and T_i, the values of T_{i0}, T_{e0}, n_{p0} can be deduced as functions of P_E's, and P_p, or vice versa.

Stangeby's model provides a simple, intuitive picture of the edge plasma. However, a number of the approximations he has to make in order to achieve the final result are not applicable to the Alcator C edge, mainly the negligence of the neutral and impurity contributions, ignoring collisional effects, and assuming a flat T_i profile. Furthermore, Stangeby's edge model, although simple and intuitive, fails to properly model the perpendicular convection term while neglecting the parallel compression contribution due to the presence of the presheath. A more complete model of the energy equations that is more appropriate for the Alcator C edge region is derived in Chapter 2.

6.2 Effect of Operating Parameters on T_i and T_e

Using the RFEA to measure T_i and the Langmuir probe to measure T_e, we can monitor the variation of ion and electron energies contained within a finite flux tube as a function of the Alcator C operating conditions. First let us re-examine the single shot time history presented in section 5.1. The shot presented is a low density discharge with $\bar{n}_e \sim 8 \times 10^{13}$ cm^{-3} operating at 280 kA. Ion temperatures on both the ion and electron side are much larger than the electron temperature. The ratio of T_i/T_e ranges from $2 \sim 4$, indicating strong ion and electron energy decoupling. The 90° collision frequency is directly proportional to the local density while inversely proportional to the temperatures. Therefore, at low central, and thus low edge densities, T_i and T_e will not equilibrate.

The single shot data also point out the difference between the temperatures measured at the electron side and ion side. The possible mechanisms of generating such side-to-side asymmetry will be discussed in more detail in the

next chapter. In analyzing the ion and electron energy balances, we will only treat the case as energy balances within the flux tube extended from the Janus diagnostics back into the edge plasma.

Looking at the temperature variations as a function of the operating parameters presented in section 5.2, we found large scattering of the measured temperatures for every operating parameter scan. Furthermore, the temperature variations behave differently for each of the three limiter-probe configurations. From the $\bar{n}_e/I_p$ scans, for the 12.5 cm limiter cases, we measured larger electron side T_i and T_e, by factors of 1.5-2, for a probe located at the top as compared with the side. The ion side temperatures are approximately the same for both cases. Keep in mind that the probe's minor radial position is closer to the limiter, by ~ 4 mm, for the side-mount case as compared with the top-mount case.

For the temperature measurements made on the electron side of Janus, there is a systematic trend of decreasing temperatures as $\bar{n}_e/I_p$ increases. This is consistent with Stangeby's simple model presented above. However, the ion side temperatures do not exhibit similiar trends. As $\bar{n}_e/I_p$ increases, the ion side temperatures either stay constant, or in some cases even show signs of increase. Unfortunately there is no simple explanation that may resolve this issue. For conventional Langmuir probe measurements, the probe tip collects current from both the electron and ion sides. So the actual temperature measured is really an "averaged" quantity weighted by the total flux collected on each side. For the Alcator C geometry, if a conventional Langmuir probe replaces Janus, then the temperature measurement likely reflects the electron side value since the flux collected at the electron side is much greater than the ion side.

The electron side/ion side temperature ratio also depends on the poloidal position of the probe and $\bar{n}_e/I_p$. For Janus locating at the top, the electron side temperatures are larger than the ion side temperatures. However, the electron side/ion side temperature ratio approaches 1 as $\bar{n}_e/I_p$ increases. On the side,

the electron side/ion side T_i ratio still exceeds 1, but the ratio drops from 1.5-3 for the top-mount case to 1-2 for the side-mount case. The T_e ratio on the side hovers at ~ 1 throughout the entire range of $\bar{n}_e/I_p$.

The ions are typically hotter than the electrons. For all three geometric configurations presented in Chapter 5, the T_i/T_e ratio varies from 1.5 to 3 on both the electron side and ion side for low values of $\bar{n}_e/I_p$. As $\bar{n}_e/I_p$ increases, there is a general trend of reducing T_i/T_e.

The radial profiles of the ion and electron temperatures act differently for different probe locations and at different sides. In general, the ion side temperature profiles are much flatter than the electron side profiles, thus the electron side/ion side temperature ratio decreases as the probe moves away from the limiter radius. The T_i profiles are either steeper than or approximately the same as the T_e profiles for all cases studied, so the T_i/T_e ratio typically increases as the probe moves toward the limiter radius.

Several operating parameters have significant influence on the temperature behaviors of the ions and electrons. By reversing the toroidal field, for the range of $\bar{n}_e/I_p$ studied, the electron side temperatures decrease while the ion side temperatures either stay constant or increase slightly. The electron side/ion side ratio drops and in some cases goes below 1. T_i remains larger than T_e, with T_i/T_e ratio ranges from 1-4. The radial profile also changes. The ion side profiles are now steeper than the electron side profiles.

Change in the magnitude of the toroidal field also affects T_i and T_e. Increasing $|B_t|$ results in the decrease of both T_i and T_e on the electron side while the ion side temperatures either stay constant or increases slightly; thus the electron side/ion side ratio decreases as $|B_t|$ increases. T_i/T_e ratio remains in the range of 1.5-2 thoughout the entire field scan.

Shifting the plasma positions in and out also has a strong impact on the measured temperatures. On the electron side, the difference between shifting the

plasma position in and out by 1 cm could produce temperature changes of as much as 60%, favoring higher temperatures at inward positions. The changes in the temperatures appear more pronounced for probe locations closer to the limiter radius. On the ion side, the impact of shifting the plasma positions on the temperatures is not obvious. Temperature measurements fluctuate for different radii and different plasma positions.

6.3 Energy Balances

It is difficult to perform detailed energy balances in the edge region. Unknown parameters such as the neutral and impurity populations and the types of impurity species present will directly influence the energy balance. In addition, the perpendicular transport is anomalous, thus the transport coefficients, $D_\perp$ and $\chi_\perp$, are difficult to estimate. Further uncertainties arise from the actual influence of potential perturbation, such as sheath and presheath effects, on the energy balances. In view of these uncertainties, accurate energy balances in the edge region are not possible. One useful exercise in studying the edge plasma, however, is to examine the degree of impact of every possible energy loss and gain mechanism. In this fashion the dominant processes may be isolated.

Janus is a large probe, large in the sense that the length required for balancing the parallel flux loss with the perpendicular flux gain is longer than the connection length to the next limiter surface. Therefore the parameters measured by Janus are not "unperturbed" parameters, but rather they reflect the averaged values of the plasma within the sampling flux tubes. It is in these flux tubes that ion and electron energy balances are performed.

From Chapter 2, the ion and electron energy equations are expressed as

$$\frac{3}{2} D_\perp \left(\frac{dn_p}{dr}\right)\left(\frac{dT_i}{dr}\right) + \frac{d}{dr}\left(n_p \chi_\perp^i \frac{dT_i}{dr}\right) = n_p T_i \nabla \cdot \underline{v}^i + \frac{q_\parallel^i}{L_\parallel} + Q_{ie} + Q_{cx} + Q_{iz}^i, \text{ and } (6.9)$$

$$\frac{3}{2} D_\perp \left(\frac{dn_p}{dr}\right)\left(\frac{dT_e}{dr}\right) + \frac{d}{dr}\left(n_p \chi_\perp^e \frac{dT_e}{dr}\right) = n_p T_e \nabla \cdot \underline{v}^e + \frac{q_\parallel^e}{L_\parallel} + Q_{ei} + Q_{rad} + Q_{iz}^e. \quad (6.10)$$

In performing the energy balances, we chose to analyze the radial profile data presented in figure 5.11, which includes data points from 17.2-18.0 cm in the minor radial direction. The operating parameters for this set of data are $I_p \sim 310 - 350$ kA, $\bar{n}_e \sim 1.3 - 1.7 \times 10^{14}$ cm^{-3}, $\underline{B}_t \sim 8$ tesla and antiparallel with respect to $\underline{I}_p$. At each radial position the edge parameters are averaged. Even with the averaging some scattering exists in the data such that accurate spatial derivatives are not possible. To this effect each parameter is fitted with an exponential profile of the form

$$\varrho^{(e,i)}(r) = \varrho^{(e,i)}(r = r_{lim}) \exp\left(\frac{-(r - r_{lim})}{\lambda^{(e,i)}}\right), \quad (6.11)$$

where ϱ is just a dummy variable, λ is the e-folding scale length, and the superscript (e,i) represents either the electron side or ion side. This spatial profile assumption allows us to replace the spatial derivative d/dr by $(-1/\lambda)$. For the data of figure 5.11, on the electron side, $\lambda_n^e \sim 0.42$ cm, $\lambda_e^e \sim 0.96$ cm, and $\lambda_i^e \sim 1.05$ cm. On the ion side, $\lambda_n^i \sim 0.61$ cm, $\lambda_e^i \sim \infty$, and $\lambda_i^i \sim 0.91$ cm. λ_n is the density scale length, λ_e is the T_e scale length, and λ_i is the T_i scale length. Figure 6.2 plots the fitted electron side and ion side profiles of T_i, T_e, and n_p along with the averaged data points.

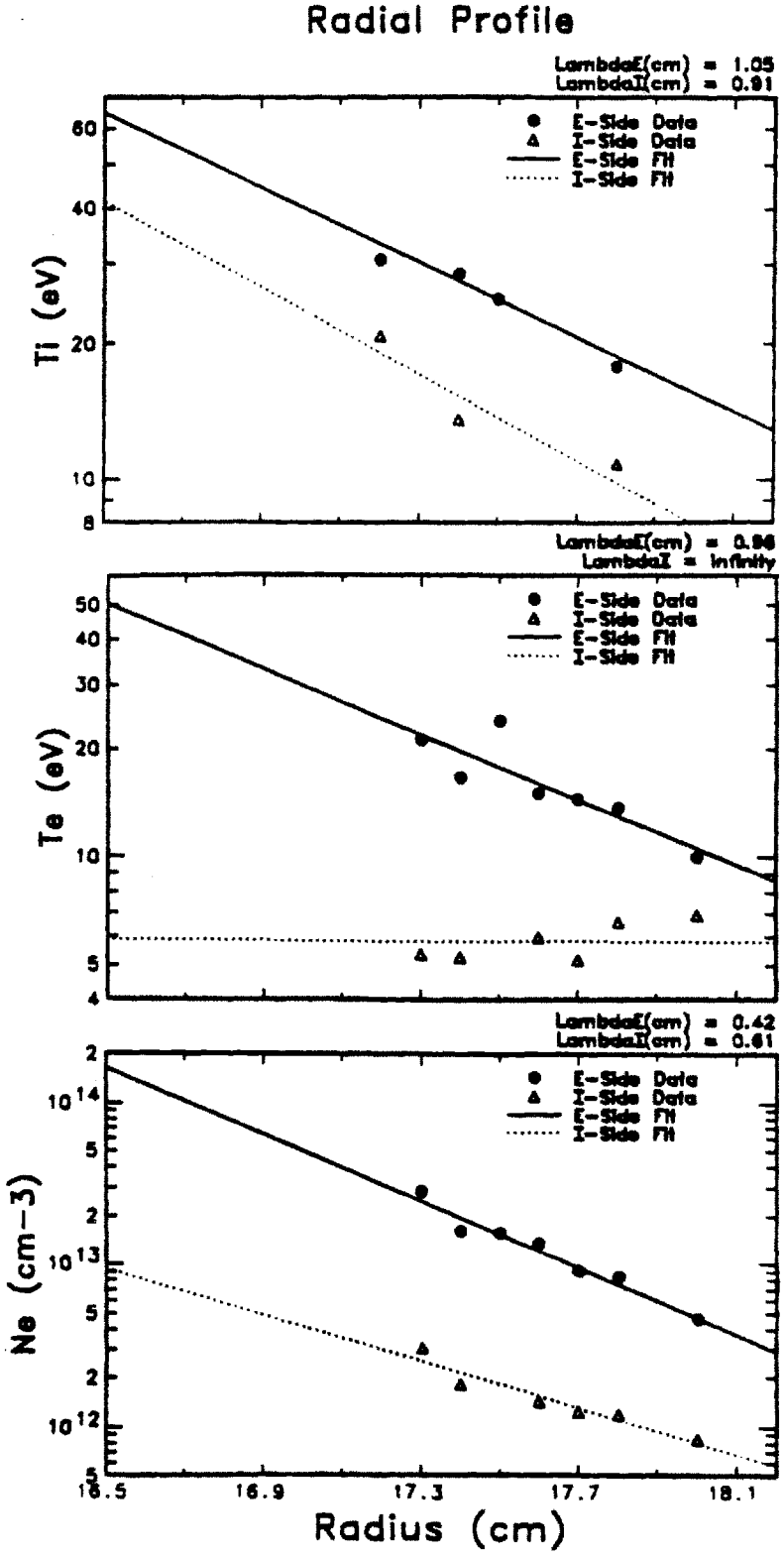

Figure 6.2 Averaged values of T_i, T_e, and n_p as a function of minor radius.

Using these fitted profiles, the ion and electron energy balances can be performed for minor radii between 17.2-18.0 cm. The behavior of the edge parameters beyond this range is unknown. It is possible that the edge plasma in this region, close to the core plasma, behaves quite differently due to changes in transport mechanisms. Using an axially averaged radial transport model, Prinja and Conn[4] found that near the limiter edge the temperature scrape-off lengths decrease significantly due to the change of energy transport from conduction to parallel convective flow. Unfortunately the geometric constraints on the Janus design limits the diagnostic sensors from sampling the plasma to within 5 mm of the limiter edge.

6.3.1 Ion Energy Balance

The first two terms of equation (6.9) represent the perpendicular convection and conduction of the ions. Using the fitted exponential profiles, the spatial derivatives can be evaluated such that

$$\frac{3}{2} D_\perp \left(\frac{dn_p}{dr}\right)\left(\frac{dT_i}{dr}\right) + \frac{d}{dr}\left(n_p \chi_\perp^i \frac{dT_i}{dr}\right) = \frac{3 D_\perp n_p T_i}{2 \lambda_n \lambda_i} + \frac{\chi_\perp^i n_p T_i}{\lambda_i}\left(\frac{1}{\lambda_n} + \frac{1}{\lambda_i}\right). \quad (6.12)$$

For λ's greater than zero, or when the parameters constantly decay toward lower values as the probe is drawn toward the wall, the perpendicular convection and conduction mechanisms act as the energy source terms in the edge region. In other words, these two terms characterize the heat flux across the limiter boundary, from the hotter core region into the cooler edge region.

The parallel convection term, $q_\parallel^i / L_\parallel$, represents the amount of ion energy deposited onto the probe due to parallel convective flow. $q_\parallel^i$ is defined in equation

(2.53) and includes the effects of the presheath potential. Keep in mind that the derivation of equation (2.53) assumes a floating probe. In reality this assumption is not valid in the tokamak edge since the limiters are made of conducting metals (molybdenum for Alcator C) and are typically grounded to the torus vacuum vessel. For this exercise we will continue to use this parallel convection model due to the lack of better alternatives.

The compression term, $n_p T_i \nabla \cdot \underline{v}^i$, is also difficult to assess. Assuming that the divergence of the perpendicular velocity is negligible, then the divergence of the parallel velocity, due to the acceleration of the ion distribution up to the speed of sound, can be expressed by equation (2.46). Due to this presheath effect, the incident flux must also be modified by the factor $f(\tau)$.

The energy exchange due to collisions with the electrons and neutrals are expressed by Q_{ie} and Q_{cx} respectively. Energy equipartition with the electrons is expressed by equation (2.63). If this term is small compared with other energy loss or gain mechanisms, then the ion temperature profile would not be coupled with the T_e profile. The charge exchange process is typically a loss term due to lower neutral energy as compared with T_i. Typically the neutral energy, E_n, is ~ 3 eV. Q_{cx} is given by equation (2.67) and the charge exchange reaction rate for hydrogen ions and neutrals is given by equation (B.12). As the result of electron impact ionization of neutrals, an energy source is added into the ion energy balance. This term, Q^i_{iz}, is expressed by equation (2.66), and the electron impact ionization rate is given by equation (B.9).

Assuming that no neutral and impurity species are present, we can perform an energy balance between the parallel and equipartition ($T_i > T_e$) losses and perpendicular gains, similar to Stangeby's simple model (equation (6.6)). Using equation (2.34) to express $D_\perp$, we get

$$\frac{\chi^i_\perp}{D_\perp} = \frac{(\lambda_i/\lambda_n)^2}{1+(\lambda_i/\lambda_n)}\left[1 + 2\mu_E - \frac{3}{2}\frac{\lambda_n}{\lambda_i} + \frac{Q_{ie}\, L_\parallel}{n_p\, C_s\, kT_i\, f(\tau)}\right]. \qquad (6.13)$$

The equipartition contribution is small ($\sim 2\%$) as compared with the other terms. Therefore, substituting in the λ's and assuming $\mu_E \sim 1$, then on the electron side, $\chi_\perp^i/D_\perp \sim 4.3$, and on the ion side, $\chi_\perp^i/D_\perp \sim 1.8$.

After adding in the neutrals and impurities, the perpendicular conduction term must be increased to compensate further energy losses in the edge region. For this analysis, the $\chi_\perp^i/D_\perp$ ratio is assumed to be a constant at every radial point. Using $\chi_\perp^i/D_\perp \sim 5$ on the electron side and ~ 2 on the ion side, energy balances are performed by varying the neutral and impurity densities at every radial position in order to balance the excess source due to perpendicular conduction. The neutral density can affect the ion energy balance through charge exchange and electron impact ionization while the presence of impurities only affects the electron energy balance as the result of impurity radiation.

Figure 6.3 plots the plasma, neutral, and impurity (molybdenum) density profiles on both the electron and ion sides that results in the balancing of the ion and electron energies throughout the entire scrape-off region. The ion side impurity profile is left out as the result of the flat T_e profile. This is discussed further in the next section. Concentrating on the ion energy balance, we found that for the $\chi_\perp^i$ values specified above, the necessary neutral density is $\sim 5.4 \times 10^{11}$ cm^{-3} on the electron side, and $\sim 5.4 - 8.7 \times 10^{11}$ cm^{-3} on the ion side. For higher $\chi_\perp^i$ values, larger neutral density would be required to increase the charge exchange loss in order to balance the increasing perpendicular conduction.

One way to look at the relative importance of each term is to define a "pseudo" confinement time for each mechanism and compared the difference. The total ion energy content within the flux tube, E_i, can be expressed as

$$E_i = \frac{3}{2} n_p k T_i. \tag{6.14}$$

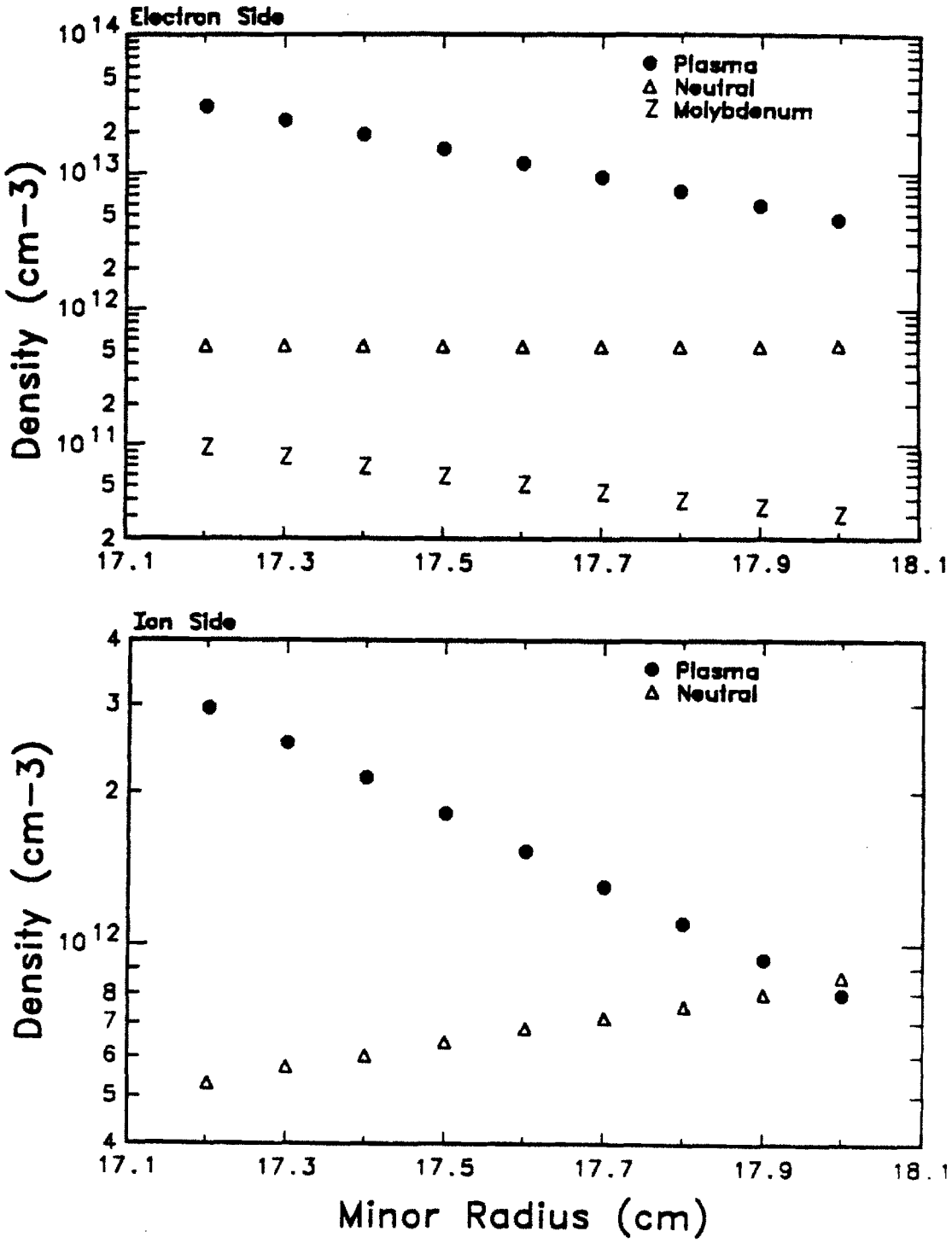

Figure 6.3 Plasma, neutral, and impurity (molybdenum) density profiles on both the electron side and ion side that satisfy the electron and ion energy balances for the data of figure 6.2.

Therefore we can define an energy confinement time, τ_E, for a specific mechanism j as

$$\tau_E^j \equiv \frac{E_i}{Q^j}, \tag{6.15}$$

where Q^j is the power density of mechanism j, such as Q_{cx}. Table 6.1 lists the values of Q^j and τ_E^j, on both the electron and ion sides, for all energy loss and gain mechanisms at 17.2 cm. The principal energy loss mechanisms are the parallel convection and parallel compression, with the charge exchange loss serving as a fine tuning knob. The source terms are the perpendicular conduction and convection terms. Ionization and equipartition losses are insignificant as compared with the other terms. Figure 6.4 shows the detailed ion energy balance, on both the electron side and ion side, as a function of minor radius.

For this set of data the T_i/T_e ratio is of order 1.5. As shown in Chapter 5, T_i/T_e ratios could be as large as 3-4. However, comparison between Q_{cx} and the parallel loss terms shows that even at large T_i/T_e values, the parallel losses remain as the dominant loss mechanism. Therefore, it is not surprising that T_i and T_e profiles do not couple together. Their respective energy balances must be determined separately.

One of the uncertainties in performing the energy balance is the negligence of the viscosity term. Poloidal and radial variations of the parallel flow velocities have been observed on DITE[5]. The presence of significant gradient of parallel velocities would require the inclusion of the viscosity term into the energy equation. The effect of the viscosity term is neglected due to insufficient data and lack of proper larger probe data to analyze the parallel flow phenomenon. More discussion on the parallel flow is presented in Chapter 7.

Electron Side

Mechanism	Q (W/cm^3)	τ_E (μs)
Parallel Convection	-2.40×10^1	-10.4
Parallel Compression	-1.20×10^1	-20.7
Perpendicular Convection	7.20	34.5
Perpendicular Conduction	3.36×10^1	7.4
Charge Exchange	-4.24	-58.6
Ionization	1.34×10^{-1}	1.86×10^3
Equipartition	-6.92×10^{-1}	-360.0

Ion Side

Mechanism	Q (W/cm^3)	τ_E (μs)
Parallel Convection	-2.01	-6.7
Parallel Compression	-1.00	-13.5
Perpendicular Convection	1.01	13.4
Perpendicular Conduction	2.25	6.0
Charge Exchange	-1.75×10^{-1}	-77.4
Ionization	6.17×10^{-4}	1.23×10^4
Equipartition	-7.03×10^{-2}	-192.4

Table 6.1 Q^j and τ_E^j values, on both the electron and ion sides, for all possible ion energy loss or gain mechanisms.

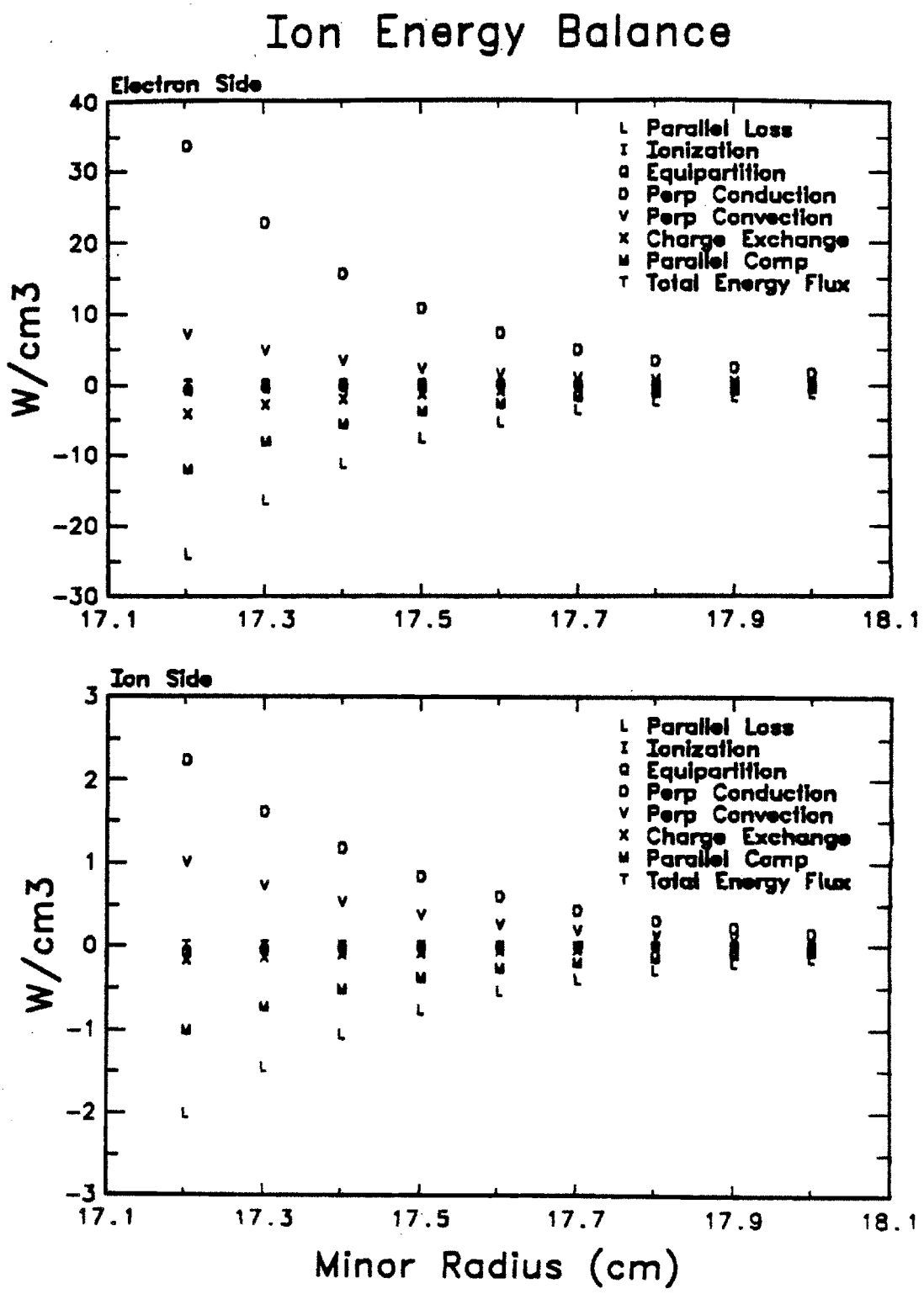

Figure 6.4 Radial variations in the ion energy balances on both the ion and electron side.

6.3.2 Electron Energy Balance

The reduction of the electron energy equation follows the previous treatment of the ion energy equation. The perpendicular terms are simplified to

$$\frac{3}{2} D_\perp \left(\frac{dn_p}{dr}\right)\left(\frac{dT_e}{dr}\right) + \frac{d}{dr}\left(n_p \chi_\perp^e \frac{dT_e}{dr}\right) = \frac{3\, D_\perp\, n_p\, T_e}{2\, \lambda_n\, \lambda_e} + \frac{\chi_\perp^e\, n_p\, T_e}{\lambda_e}\left(\frac{1}{\lambda_n} + \frac{1}{\lambda_e}\right). \quad (6.16)$$

Since both the ions and electrons must flow together, quasineutrally, toward the sheath edge, the divergence of the parallel velocity can be similarly described by equation (2.46), and the flux be reduced by $f(\tau)$. The parallel convection term is given by equation (2.55). Using the coefficient γ_e, which is defined as the electron portion of the sheath transmission coefficient, the contributions of both the electron thermal energy and the energy required to maintain the negative sheath potential are

$$\gamma_e = \frac{2}{1-\nu_e} + \frac{e|V_{sheath}|}{kT_e}, \quad (6.17)$$

where ν_e is the secondary electron emission coefficient which is set at 0.3. The sheath potential contribution is derived from the kinetic model proposed by Emmert[6].

$Q_{ei} = -Q_{ie}$, and Q_{iz}^e is now an energy loss term since electron must exert a certain amount of energy to excite the impurities. Q_{iz}^e is given by equation (2.65) where $\xi_e \sim 30$ eV for T_e in the range of 10-30 eV[7] and $n_p \leq 1 \times 10^{13}$ cm^{-3}. Finally, due to radiative decay and recombination processes, a fraction of the electron energy is lost via radiation. Q_{rad} is given by equation (2.64).

Neglecting the presence of neutrals and impurities, the $\chi_\perp^e/D_\perp$ relationship can be derived (using equation (6.13))

$$\frac{\chi_\perp^e}{D_\perp} = \frac{(\lambda_e/\lambda_n)^2}{1+(\lambda_e/\lambda_n)}\left[1+\gamma_e-\frac{3}{2}\frac{\lambda_n}{\lambda_e}+\frac{Q_{ei}\,L_\parallel}{n_p\,C_s\,kT_e\,f(\tau)}\right]. \qquad (6.18)$$

Neglecting the electron-ion equipartition term, and plugging in the λ's, we get $\chi_\perp^e/D_\perp \sim 8.6$ The perpendicular terms on the ion side are negligible due to the flat T_e gradient. Unless $\chi_\perp^e \to \infty$, this behavior raises an interesting question as to what kind of energy source is present in the flux tube to maintain the flat T_e profile. Clearly the equipartition of the ion-electron energies cannot sustain the observed T_e profile.

Using the same neutral profile necessary for the ion energy balance, we can manipulate the impurity profile and balance the electron energies. From Appendix B, we found that using low-Z impurities such as carbon and oxygen, due to their low cooling rates, would require an improbably high quantity of impurities to generate the necessary radiative loss in order to balance the perpendicular source terms. The electron side portion of figure 6.3 plots the necessary molybdenum profile for electron energy balance. On the ion side, due to the flat T_e profile, the presence of impurities would just increase the total losses since the perpendicular source is nonexistence.

Table 3.2 gives the Q^j and τ_E^j values, at both the electron side and ion side, for the electron energy balance at 17.2 cm. Figure 6.5 plots the radial profile of the energy balances. For this set of calculations, the ion side molybdenum profile is assumed to be the same as the electron side profile. The radiative energy loss term, in this case, replaces the charge exchange term as the tuning knob. The ionization and equipartition terms are still small in comparison.

The parallel convective term is by far the dominant energy loss mechanism. This is because of the large γ_e value due to the presence of the negative sheath

Electron Side

Mechanism	Q (W/cm^3)	τ_E (μs)
Parallel Convection	-4.28×10^1	-4.2
Parallel Compression	-8.73	-20.7
Perpendicular Convection	5.73	31.6
Perpendicular Conduction	4.94×10^1	3.7
Radiation	-2.94	-61.6
Ionization	-1.36	135.4
Equipartition	6.92×10^{-1}	-261.4

Ion Side

Mechanism	Q (W/cm^3)	τ_E (μs)
Parallel Convection	-1.43	-2.9
Parallel Compression	-3.10×10^{-1}	-13.5
Radiation	-2.79×10^{-1}	-15.0
Ionization	6.17×10^{-3}	677.6
Equipartition	-7.03×10^{-2}	-59.4

Table 6.2 Q^j and τ_E^j values, on both the electron and ion sides, for all possible electron energy loss or gain mechanisms.

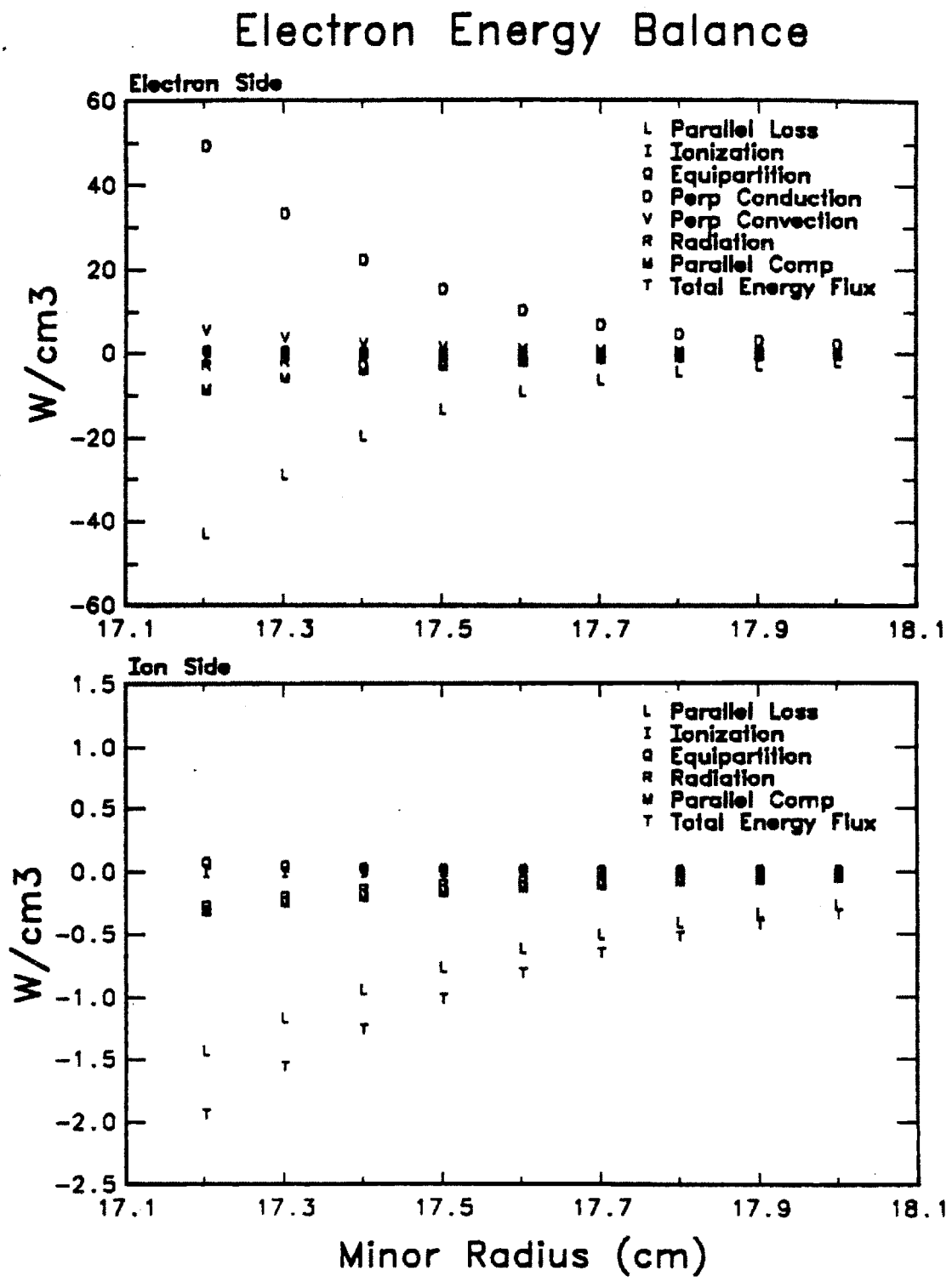

Figure 6.5 Radial variations in the electron energy balances on both the ion and electron side.

potential and secondary electron emission. If the value of ν_e is greater than the value (0.3) used for this study, then the parallel loss term will increase. However, keep in mind that the parallel loss terms are derived with the asumption of the ideal situation where the plasma is in contact with a floating plate. Clearly, given the limiter configuration of Alcator C, this asumption may not be valid. The profile of potential difference between the plasma and a conduction limiter (or wall) is quite complicated. It is dependent on the limiter geometry and material property, parallel and perpendicular transport, and the operating parameters of the experiment. It is possible that the potential difference between Janus and the plasma prohibits the formation of a negative sheath. Then the parallel loss terms can no longer be expressed by our present model.

One possible evidence in support of this argument is from the V_{shift} measurement of the RFEA. It is difficult to obtain an accurate and consistent measurement of V_{shift} due to edge fluctuations. In general the ion side V_{shift} is 0 for all discharges. The electron side V_{shift} increases as the probe approaches the limiter radius. But the value eV_{shift}/kT_e is typically smaller than the $e|V_{sheath}|/kT_e$ value predicted by theory. $eV_{shift}/kT_e \sim 1-2$ is typical. If the sheath formation under our geometry does not agree with the theoretical predictions, then the parallel loss terms must be re-evaluated. However, given our present understanding and experimental observations, it is difficult to assess the validity of this assumption.

6.4 Energy Accounting

From the previous section, we found that the loss mechanism is dominated by parallel convective loss to the limiters. Neglecting the rest of the loss terms, we can attempt to perform a simple accounting of total energy loss in the edge plasma region. The total power flux at the probe, on both the electron side and ion side, can be obtained using equation (2.57), which states

$$q_{\parallel}^{total} = (2\tau\mu_E + \gamma_e)\, kT_e\, n_p\, C_s\, f(\tau), \qquad (6.19)$$

where $\tau = T_i/T_e$. Figure 6.6 plots the electron side and ion side $q_{\parallel}^{total}$ as a function of the minor radius from 17.2-18.0 cm, using the fitted profiles from the previous section.

The total power deposited at this poloidal location can be obtained simply by integrating $q_{\parallel}^{total}$ over the minor radius. To get the total power deposited into the edge region, P_{total}, knowledge of the poloidal profile of $q_{\parallel}^{total}$ is necessary. Assuming poloidal symmetry, the total power deposited on the electron side of one limiter and ion side of the other limiter (see figure 3.1) could be expressed as

$$P_{total} = \sum_{sides} \int_{r_{lim}}^{\infty} q_{\parallel}^{total}\, 2\pi r\, dr. \qquad (6.18)$$

The total power deposited between 17.2 and 18.0 cm is approximately 120 kW. Given that the spatial profiles of T_i, T_e, and n_p remain constant throughout the edge region, we can obtain the total power deposited in the edge region, which must be multiplied by 2 due to the presence of two sets of limiters. For the data presented in the previous section, $P_{total} \sim 3.6$ MW. This is far greater than the total ohmic power input, which is ~ 600 kW for these discharges.

In reality the assumption of poloidal symmetry is not valid. From the data measured by a poloidal array of Langmuir probes[8], the edge region of Alcator C is highly asymmetric in the poloidal direction. Furthermore, Janus is located at or near the peak pressure position. Therefore, to obtain P_{total}, a poloidal profile factor is needed. For non-rf discharges, radiation power typically accounts for up to 50% of the total ohmic power[9]. To match the experimental results, a poloidal peak to average factor of ~ 12 is needed to justify the Janus measurements. Keep

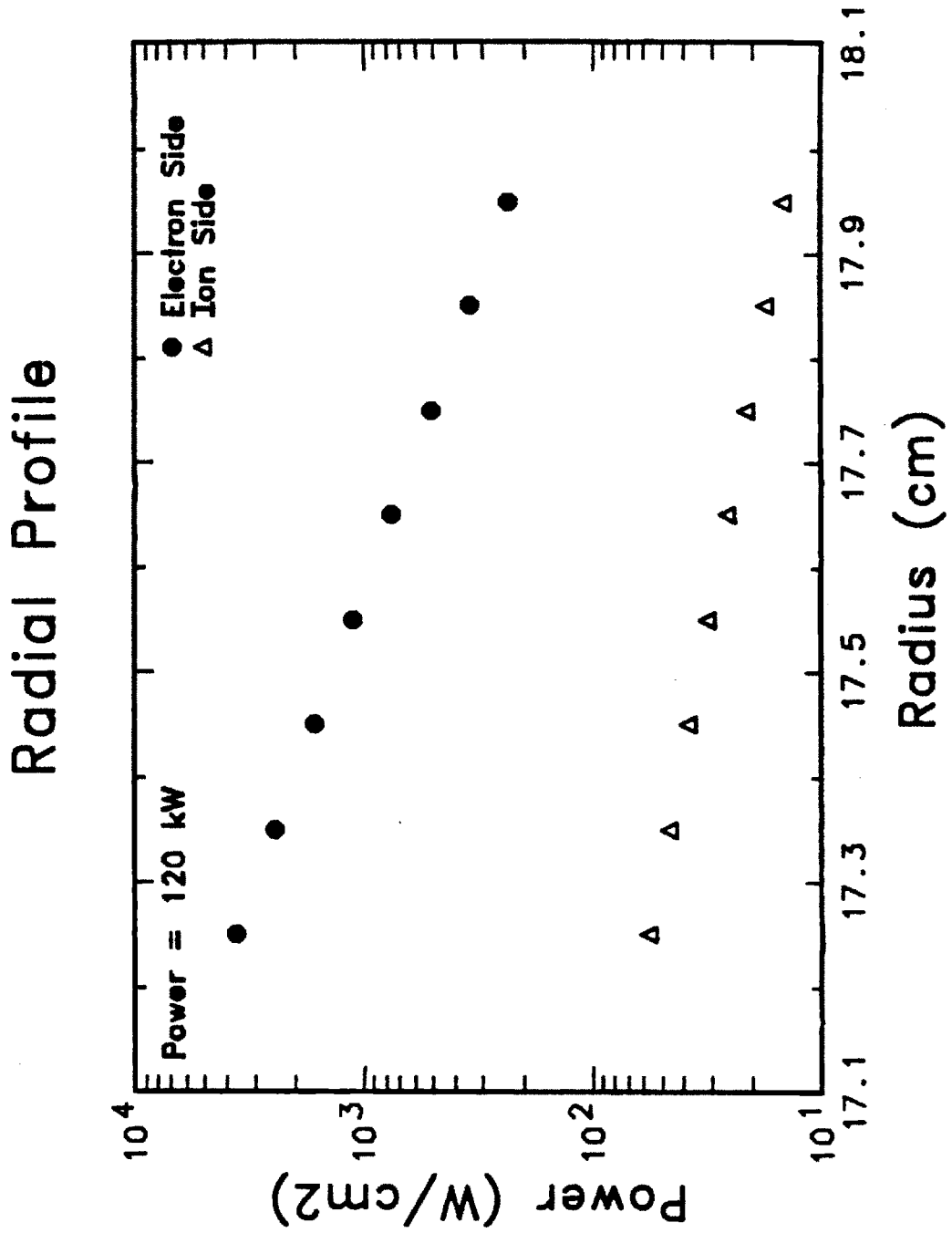

Figure 6.6 Electron side and ion side $q_{\parallel}^{total}$ as a function of the minor radius.

in mind that these results assume the consistency of the radial temperature and density profiles throughout the entire edge region.

References

[1] Matthews, G. F., "The Measurement of Ion Temperature in Tokamak Edge Plasmas," Oxford Doctoral Thesis, 1985.

[2] Stangeby, P. C., "Large Probes in Tokamak Scrape-Off Plasmas. Analytical Model for the Collisionless Scrape-Off Plasma," *Phys. of Fluids* **28** (2), 644–651 (1985).

[3] "International Tokamak Reactor, Phase Two A, Part I, Report of the INTOR Workshop 1981-83," 196 (IAEA, Vienna, 1983).

[4] Prinja, A. K., Conn, R. W., "An Axially Averaged-Radial Transport Model of Tokamak Edge Plasmas," *J. Nucl. Mat.* **128 & 129**, 135 (1984).

[5] Proudfoot, G., Harbour, P. J., Allen, J., Lewis, A. "Poloidal and Radial Variations in Plasma Transport in a Limiter Scrape-Off Layer in DITE," *J. Nucl. Mat.* **128 & 129**, 180–185 (1984).

[6] Emmert, G. A., Wieland, R. M., Mense, T. A., Davidson, J. N., "Electric Sheath and Presheath in a Collisionless, Finite Ion Temperature Plasma," *Phys. Fluids* **24**, 803 (1980).

[7] Janev, R. K., Post, D. E., Langer, W. D., Evans, K., Heifetz, D. B., Weisheit, J. C., "Survey of Atomic Processes in Edge Plasmas," *J. Nucl. Mat.* **121**, 10–16 (1984).

[8] Labombard, B., "Poloidal Asymmetries in the Limiter Shadow Plasma of the Alcator C Tokamak," M.I.T. Doctoral Thesis (April 1986).

[9] Pickrell, M. M., "The Role of Radiation on the Power Balance of the Alcator C Tokamak," M.I.T. Doctoral Thesis (November 1982).

CHAPTER 7

Electron Side/Ion Side Asymmetries

The proof-of-principle experiment[1] (see also section 3.2) used a simple RFEA that was able to both rotate with respect to the toroidal field, $\underline{B}_t$, and move radially. During this experimental period, the Alcator C ran with a limiter radius of 16.5 cm and $\underline{B}_t$ was aligned antiparallel with respect to the plasma current, $\underline{I}_p$. This magnetic configuration is the normal operating configuration of Alcator C. Since the RFEA measures parallel parameters, we expect maximum flux entering through the slit when the probe is aligned parallel to the magnetic field. Experimentally, this is indeed observed. As the probe is rotated away from the parallel position, the signal becomes weaker and eventually disappears below the noise level at approximately 40° away from the parallel position. However, when the probe is aligned parallel (ion side) and antiparallel (electron side) with respect to I_p, we found large asymmetries favoring higher temperatures and densities on the electron side.

Looking back at previous experiments conducted on Alcator C, we found several results in support of the observed electron side/ion side asymmetries during the proof-of-principle experiment. Figure 7.1 shows a sketch of the limiter damage and redeposition pattern for a small (10 cm radius) ring limiter[2]. Concentrating on the damage pattern, we found that the primary damaged regions are located at the inside-top region on surface facing the electron side and at the inside-bottom region on the ion side surface. The damage was most likely caused by thermal effects, such as evaporation (see Appendix A), indicating that the edge plasmas surrounding these damaged regions are hotter and denser than the plasmas at undamaged regions. Therefore, from the limiter damage pattern, we conclude that there are some electron side/ion side parameter asymmetries. The damage pattern supports the proof-of-principle experiment since the experiment

was located at the top of Alcator C, where the limiter damage occurred on the electron side.

Further supporting evidence came from a careful experimental study, conducted by Hayzen and co-workers[3], of the Alcator C boundary plasma using Langmuir and thermocouple probes located at various poloidal and toroidal positions. Among the probes were two sets of bi-directional thermocouple probes located at the bottom sections of Alcator C. These probes are designed to measure the total thermal flux on both the electron side and ion side. In the *normal* magnetic configuration, or when $\underline{B}_t \not\parallel \underline{I}_p$, Hayzen found that the ion side thermal flux is larger than the electron side thermal flux. The ratio of ion side/electron side thermal flux increases as the probe is pushed toward the limiter radius. Extrapolating the ratio to the limiter radius, the ion side thermal heat flux would greatly exceed the electron side flux, thus producing the preferential limiter damage pattern previously discussed.

The Janus experiment is designed with two sets of edge diagnostics such that both the ion side and electron side edge parameters can be monitored simultaneously. The Langmuir probe and the RFEA results for various operating parameters have been presented in Chapter 5. Looking at the single shot data presented in section 5.1, we found large asymmetries between the electron side and ion side parameters. The single shot data use the "16.5 cm Top" configuration (see section 5.2) while the probe is at a radial position of 17.8 cm. Comparing the two sides, we found larger temperatures and densities on the electron side. The two-sided ion and electron temperature ratios are about 2 to 3. The density ratio is ~ 5. We also found a greater floating potential (Langmuir probe) and shift potential (RFEA) on the electron side.

Unfortunately there is no simple answer that can satisfactorily explain the cause of this electron side/ion side asymmetry. This chapter focuses on the two-sided asymmetry and attempts to come up with plausible scenarios that might lead to the observed asymmetry. In the first section, operating parameters

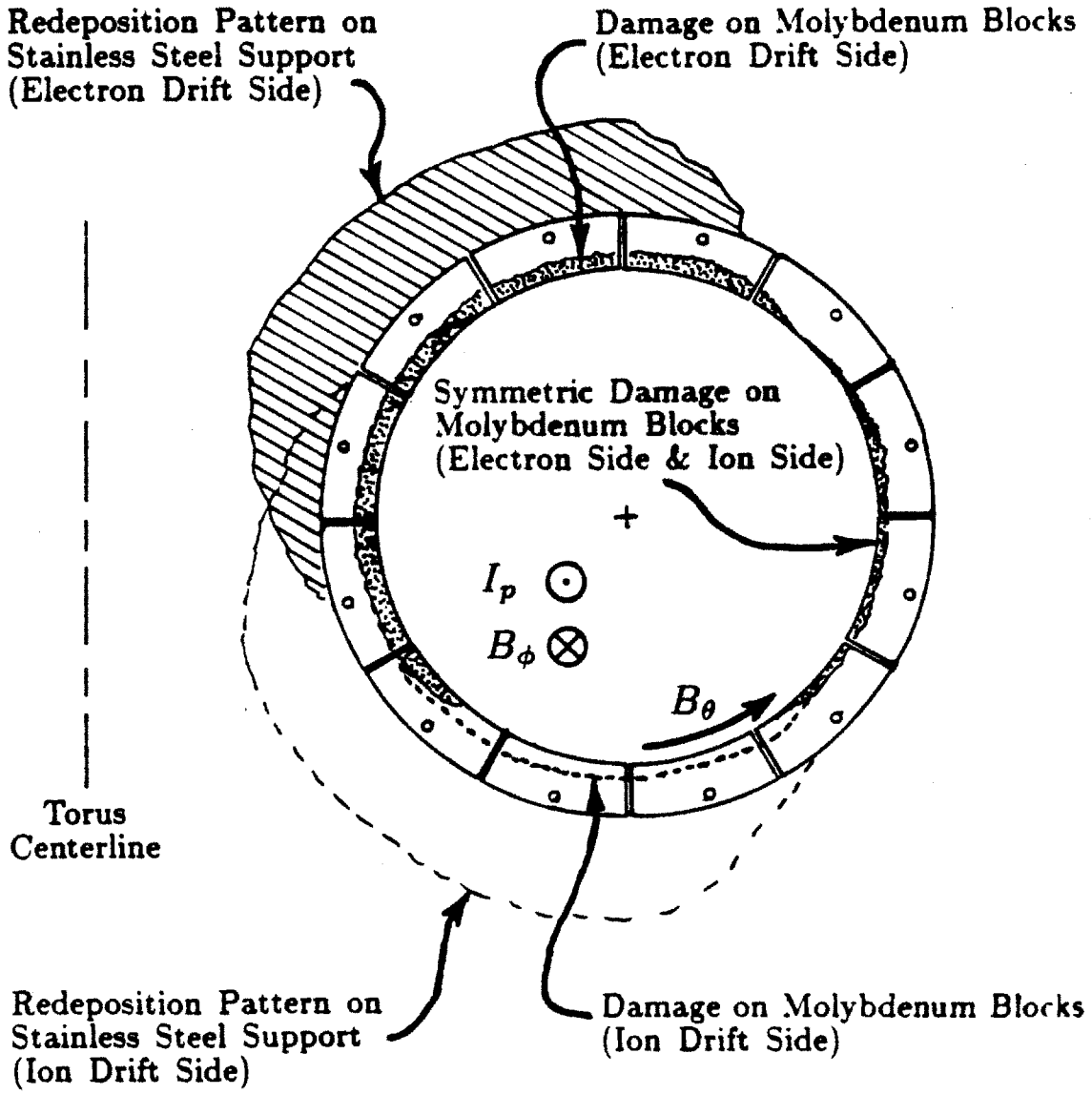

Figure 7.1 Limiter damage pattern for a 10 cm (radius) limiter operating in normal field configuration.

that most strongly influence the asymmetry are extracted from Chapter 5 and reiterated. Possible mechanisms that could drive the asymmetry are presented in the following sections.

7.1 Effect of Operating Parameters on the Asymmetry

The data presented in Chapter 5 include detailed characterization of the electron side and ion side edge plasma parameters as functions of various operating parameters. In particular, there are several operating parameters which have significant impact on the electron side/ion side asymmetry pattern, including the radial position of the probe, the toroidal magnetic field magnitude and direction, and plasma in-out positions.

The effect of $\underline{B}_t$ on the asymmetry was first observed by Hayzen[3]. Focusing on their bi-directional thermocouple probe located on the bottom region of Alcator C, Hayzen found that by reversing the toroidal field direction, the asymmetry pattern also reverses. In the normal field configuration, the probes on the ion side detect stronger thermal heat flux, by factors of $2 \sim 3$, than the electron side probes. When the toroidal field direction is reversed, the electron side signals become stronger. The magnitude of the electron side/ion side thermal flux ratio is dependent on both the poloidal position of the probe and the limiter configuration. Hayzen found that the thermal flux peaks at approximately 0 to 5 degrees, with the magnetic axis defined as 0°; 5° is toward the low field side of the axis. The asymmetry is stronger near the axis than off axis. The asymmetry is also stronger as the number of limiters in the machine is increased, despite the fact that the heat flux is larger for fewer limiters. For a single poloidal limiter in reverse field configuration, the magnitude of asymmetry is of order $1 \sim 2$. The asymmetry ratio grows to $2 \sim 7$ as the number of limiters is doubled.

Most of the Alcator C discharges sampled by Janus employed the normal field configuration. Only a few days of experiments were conducted in the reverse

field configuration. Comparing these discharges with the normal field discharges, the effect of the toroidal field configuration on the two-sided asymmetry is most visible when a series of radial profile experiments was conducted in otherwise similar discharge conditions. The parameter that is used to examine the asymmetry is the ion satuation current, I^i_{sat}, measured by the Langmuir probe when the probe characteristic flatten out at large negative probe biases (see section 4.2). I^i_{sat} is a particularly desirable quantity since its measurement does not require the application of any probe theories. If the Bohm Sheath Criterion is satisfied, then I^i_{sat} reflects both the density and temperature variations, although the temperature dependence is only reflected in term of $\sqrt{T_e + T_i}$ (equation (4.16)).

Figure 7.2 plots the radial profiles of the I^i_{sat} ratio, electron side/ion side, for both normal (solid circle) and reverse (open triangle) field configuations. These scans are done with 16.5 cm molybdenum ring limiters, at 8 tesla, with peak plasma current of $\sim$ 330 kA and peak line-averaged electron density of $\sim 2 \times 10^{14}$ cm^{-3}. Janus is inserted from the top of Alcator C. Far away from the limiter radius, both ratios are of order 10. As Janus is pushed closer to the limiter radius, the normal field ratio increases to a ratio of $\sim$ 60 when the probe edge approaches the limiter radius. For the reverse field configuration, the pattern is reversed. As Janus approaches the limiter radius, the ratio of electron side/ion side I^i_{sat} starts to decline until eventually the ion side dominats. Keep in mind that the ion side has a much shorter connection length to the nearest limiter surface as compared with the electron side (see figure 3.1).

Varying the magnitude of B_t can also affect the electron side/ion side asymmetry. This is evident from the data presented in figure 5.14. The two-sided temperature asymmetry reduces as $|B_t|$ is increased. The density asymmetry does not vary as a function of $|B_t|$, despite changes in the absolute magnitude of the densities on both sides.

Another operating parameter that can strongly perturb the two-sided asymmetry is the plasma position. Figure 7.3 plots the electron side/ion side I^i_{sat},

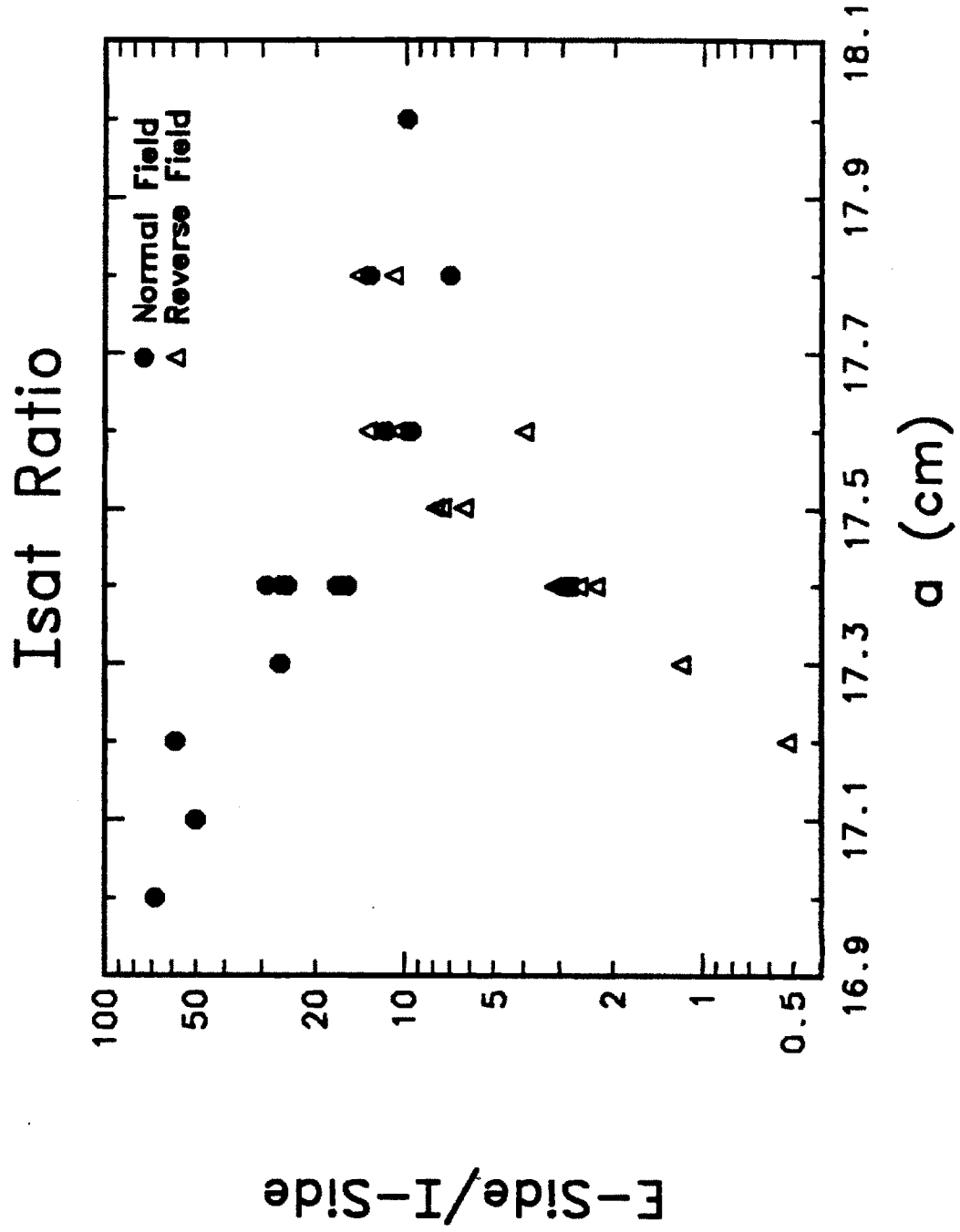

Figure 7.2 Radial profiles of the ratios of the electron side/ion side I^i_{sat} for both the normal and reverse magnetic field configurations.

T_e, and n_p ratios for the data presented in figure 5.17. From figure 7.3, we see that as the plasma position is shifted toward the inside (−), the electron side/ion side ratio grows. As the plasma position starts to shift outward (+), the trend reverses.

Other operating parameters also affect the asymmetry, but not as strongly as $\underline{B}_t$ and the plasma positions. For operation in normal field configuration, from section 5.2, we found that regardless of the limiter radius, both the electron side/ion side temperature and density ratios always exceed 1.

The next two sections offer two possible mechanisms which may drive the electron side/ion side asymmetry. Unless otherwise defined, the variables used in this chapter follow the terminology of the previous chapters. Using the Janus data in relation with other Alcator C measurements, we can examine the validity of each mechanism in terms of the observed asymmetry ratios.

7.2 Flux Tube Model

As discussed in Chapter 2, the measured edge parameters are just reflections of the properties of the plasma residing in the flux tube connecting to the diagnostic sensors. The flux tube is defined by tracing the magnetic field lines, which intersect the diagnostic sensors, back into the plasma (see figure 2.5). The measured parameters are strongly dependent on the flux tube geometry (figure 7.4(a)), which can be affected by plasma in-out positions (figure 7.4(b)). The parameters also depend on on the transport processes along the entire length of the flux tube. Therefore, if the transport mechanism and plasma parameters are different for the electron side and ion side flux tubes, then the measured values on the two sides will also be different (figure 7.4(c)). The *flux tube model* uses possible variations of the properties along the sampling flux tubes to develop plausible explanations for the two-sided asymmetry.

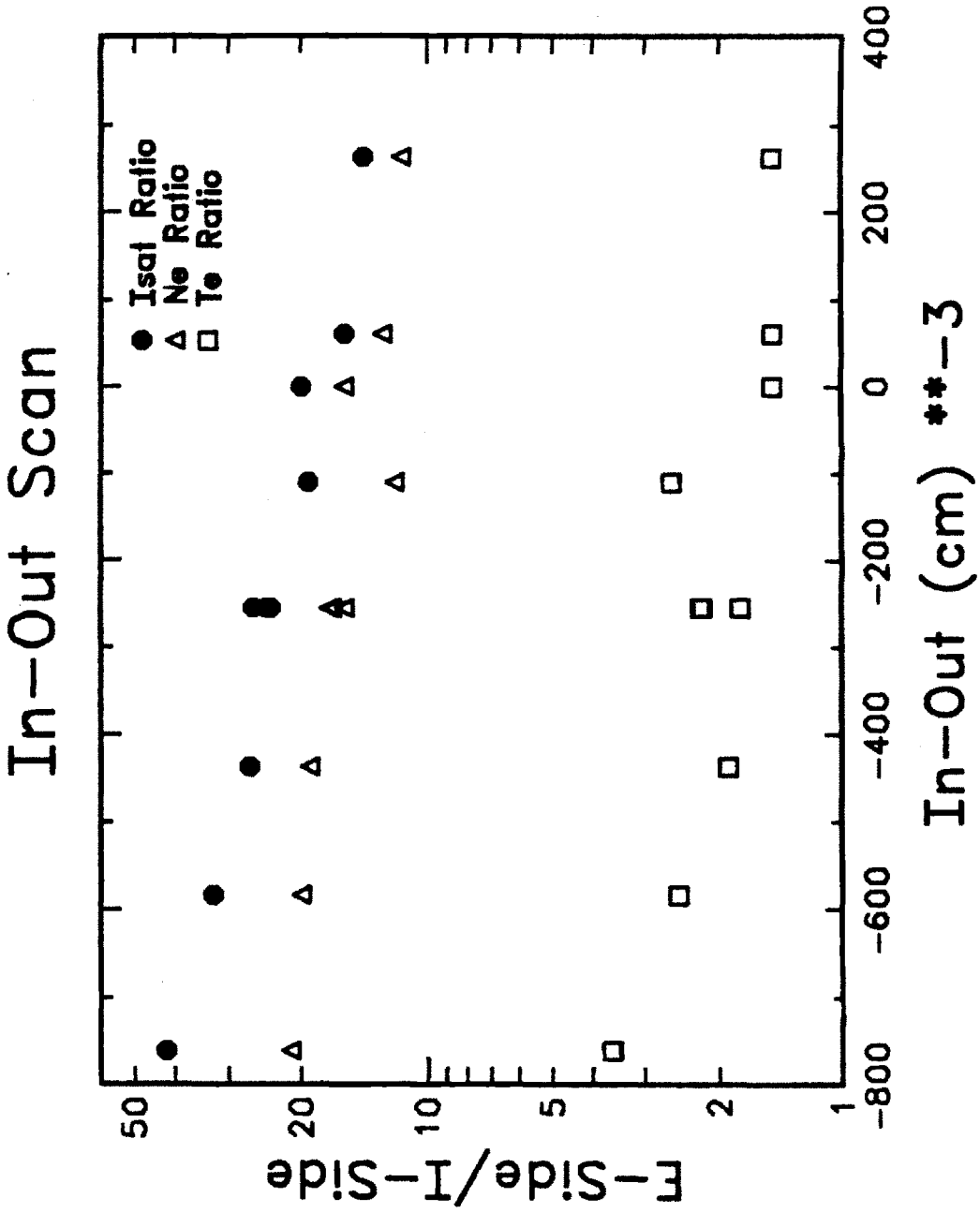

Figure 7.3 Ratios of electron side/ion side I^i_{sat}, T_e, and n_p as a function of plasma in-out positions under normal field configuation.

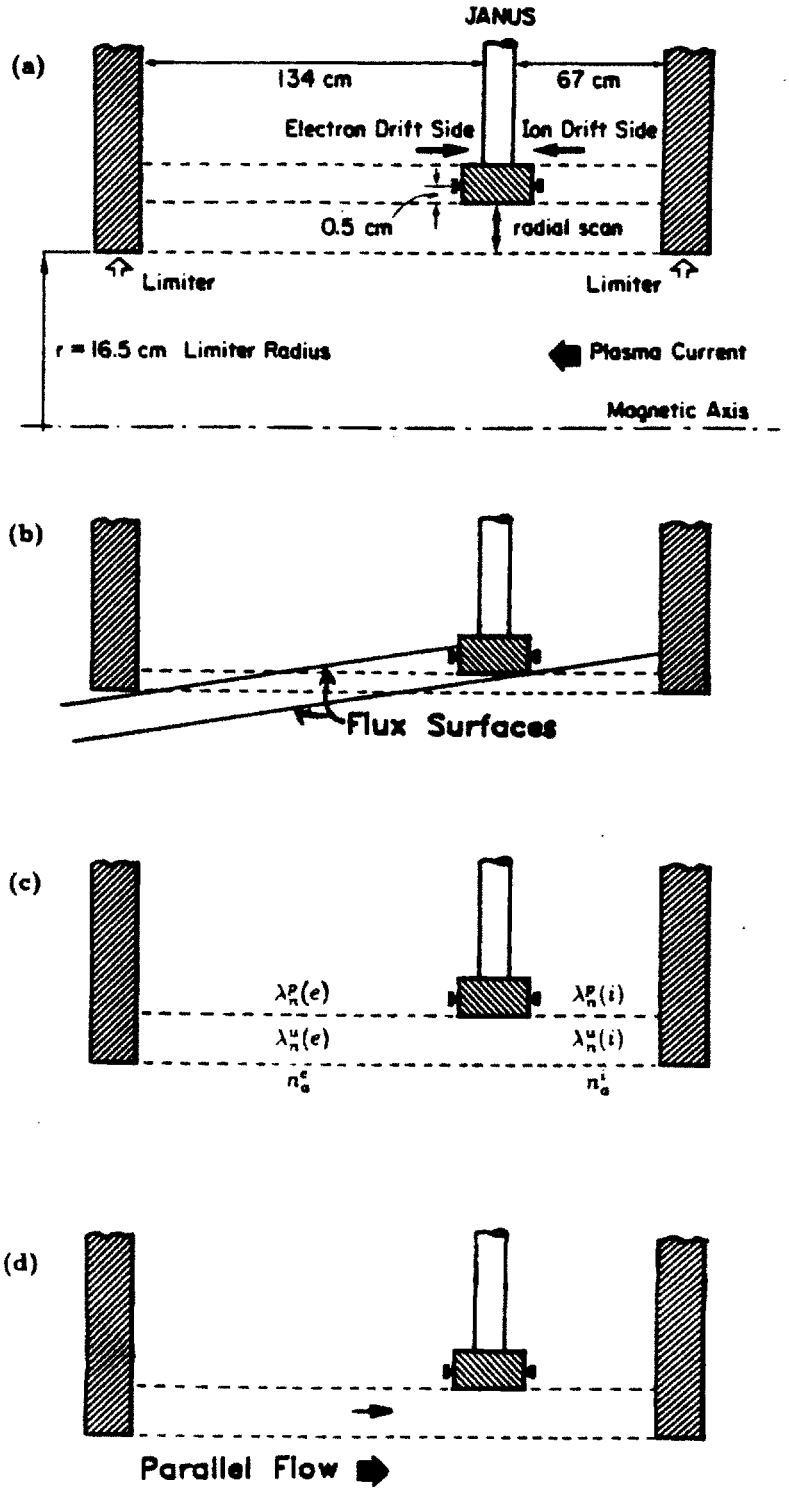

Figure 7.4 Figure (a) shows the variation of connection length for the Janus diagnostics; (b) shows the effect due to plasma position shifts; (c) shows the effect due to different perpendicular transport for different sampling flux tubes; and (d) includes the effect of parallel plasma flow.

7.2.1 Connection Length Variation

One possible method to produce asymmetric diffusion in the two flux tubes is to have different flux tube connection lengths. A unscaled artist's conception of the geometric configuration of Janus is shown in figure 7.4(a). Regardless of the poloidal location, Janus is always located at same toroidal location, with the same limiter configuration. Therefore, the electron side and ion side flux tube connection lengths, $L_{\|}$, always maintain the relationship of

$$L_{\|}(\text{e-side})/L_{\|}(\text{i-side}) \quad \sim \quad 2. \tag{7.1}$$

Assuming that the spatial dependences of the parameters in the limiter shadow follow exponential profiles, then the electron side/ion side ratio between a measured parameter, ϱ, on the two sides of the recessed (by $\Delta_p \sim 0.5$ cm) diagnostic sensors, defined as $R_{e/i}(\varrho)$, can be represented by

$$R_{e/i}(\varrho) \quad = \quad \frac{\varrho^e \, e^{-\Delta_p/\lambda^e}}{\varrho^i \, e^{-\Delta_p/\lambda^i}}, \tag{7.2}$$

where λ^e and λ^i are the electron side and ion side scrape-off scale lengths, and ϱ^e and ϱ^i are the magnitudes of the electron side and ion side parameters at the edge of the probe housing. If the plasma parameters at the probe edge are the same on both sides of Janus, then $\varrho^e \sim \varrho^i$. As previously addressed in Chapter 6, the temperature measurements are subjected to greater degree of fluctuations due to the uncertainties in the transport mechanisms and the degree of impact of the neutrals and impurities. Therefore radial dependences of the temperatures are difficult to determine, and the plasma density, n_p, or the ion saturation current, I^i_{sat}, is used as the representative parameter since simple and useful models of their behaviors can be more easily derived. The density

scale length can be approximated by using the continuity equation assuming insignificant particle sources

$$\lambda_n \sim \sqrt{\frac{D_\perp L_\parallel}{f(\tau) C_s}}. \tag{7.3}$$

Combining equations (7.1)-(7.3), the electron side/ion side ratio is reduced to

$$R_{e/i}(n_p) \sim \exp\left(0.414\,\Delta_p \sqrt{\frac{f(\tau) C_s}{D_\perp L_\parallel^e}}\right). \tag{7.4}$$

In the absence of a momentum source, $L_\parallel$ can be approximated by half the length between two connecting solid surfaces. $L_\parallel^e \sim 67$ cm. Taking typical edge plasma values of $T_i \sim 25$ eV, $T_e \sim 15$ eV, $D_\perp \sim 8000$ cm^2/s, and approximating $f(\tau) \sim 0.5$, then $R_{e/i}(n_p) \sim 1.65$. Typical ratios of $R_{e/i}(n_p)$ for the normal field, top insertion configuration, range from 5 to 30, depending on the probe's minor radial position. Therefore, based on the connection length difference to the next limiter alone, the magnitude of the experimentally observed $R_{e/i}(n_p)$ cannot be justified.

By shifting the plasma positions, due to the change of relative positions between the flux surface and limiter, the connecting length to different poloidal locations of the edge region will also be different. If the outer flux surfaces are shifted by sufficient displacements, then it is possible for field lines connection to one side of the Janus diagnostics to escape the next connecting limiter surface and must travel around the torus several times before rerconnecting onto another solid surface. This is illustrated in figure 7.4(b).

Simplemindedly, the flux surfaces can be described by concentric circles with centers shifted by the plasma position shift with respect to the limiter center. By comparing the field line position on a flux surface with respect to

the limiter position as field lines rotate poloidally, the number of turns each field line will go around the torus before intersecting the limiter can be monitored. The rotational transform can be made either clockwise or counterclockwise to simulate the following of field lines parallel or antiparallel with respect to $\underline{I}_p$. Therefore, we can examine the variation of the connection lengths for field lines intersecting either the electron side or ion side of Janus as the plasma position shifts.

For $q_{lim} = 3.6$ and assuming an inward flux surface shift of 0.7 cm, figure 7.5 shows the poloidal variations of the connection length to an electron side limiter surface and an ion side limiter surface. The solid circles trace out the inner limiter boundary. Longer connection lengths are characterized by denser and darker dots. Clearly large poloidal variations exist. On the electron side, the connection length is longer on the upper-inside region, while on the ion side, the longer connection length region resides on the lower-inside. Interestingly these patterns correspond to the observed limiter damage patterns of figure 7.1.

Typically Janus operates at large minor radii such that the flux tubes connect only to the next limiter surface. Although by shifting the flux surface positions would change the connection length profile both poloidally and radially, impacting the plasma parameter magnitude as observed experimentally, the shifts would not have major impact on the directional asymmetry. Experimentally, the measured density ratios between the two sides vary from 10-20, and the plasma positions are typically up-down and in-out symmetric.

7.2.2 Nonuniform Plasma Parameters Along Flux Tubes

Using a full poloidal array of 80 Langmuir probes at three different minor radii (DENSEPACK), LaBombard[2] found strong poloidal asymmetries in the Alcator C edge region. The poloidal asymmetry is present throughout the entire

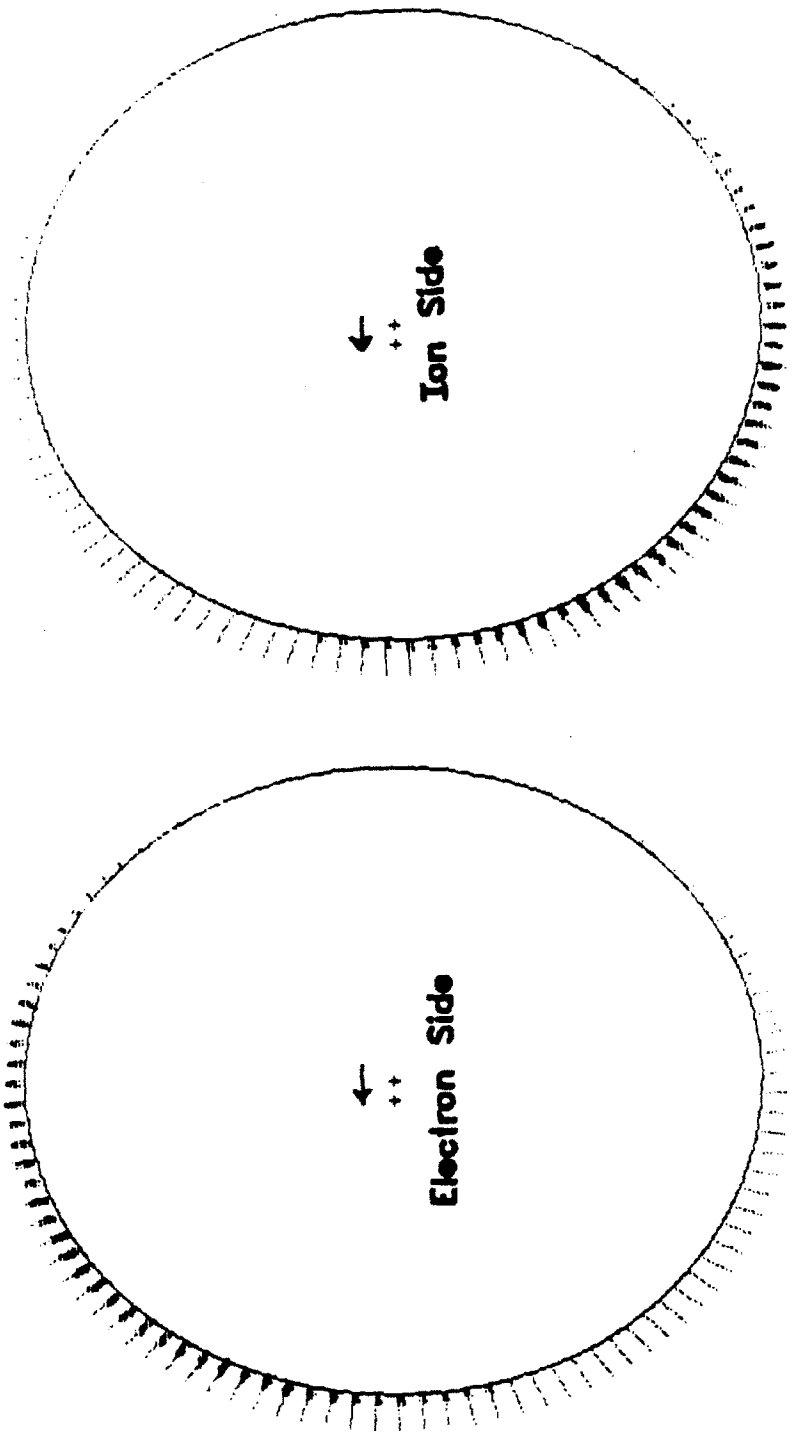

Figure 7.5 Variations in the field line connection lengths intersecting the limiter surfaces on the electron side and ion side. The flux surface is shifted inward by 0.7 cm.

discharge, at various operating conditions, despite intuitive belief in the presence of strong parallel field transport that should readily equilibrate parameters along field lines. Variations of $\sim 4-20$ in plasma density, $\sim 1-2$ in T_e, and $\sim 3-8$ in λ_n are observed. Figure 7.6 shows the poloidal profiles of n_p and T_e at minor radii of 16.8 cm, 17.2 cm, and 17.6 cm, and the fitted λ_n profile from the n_p measurements. The experiment is conducted with the normal field configuration using 16.5 cm (radius) full-poloidal ring, molybdenum limiters. No significant variation of the poloidal asymmetry pattern was observed for running with reverse field configuration as compared with running with normal field configuration[4].

DENSEPACK was installed at the same toroidal position as Janus. Unfortunately there are no DENSEPACK probes located at the region occupied by Janus, or 270° in the poloidal angle defined by figure 7.6, which is also the region where largest poloidal gradients for all edge parameters were observed. The DENSEPACK Langmuir probes are small in dimension ($\sim$ 1 mm), and do not perturb the plasma to the degree of the Janus. Therefore the λ_n measurement should not reflect change in the connection length, but rather change in the perpendicular diffusion coefficient, $D_\perp$. The unperturbed (without Janus) e-folding length is defined as λ_n^u. From equation (7.3), modified, or perturbed, e-folding density scale lengths, defined as λ_n^p, can be inferred from the DENSEPACK measurements by adjusting the connection lengths for each of the electron side and ion side flux tubes. Therefore, λ_n^p is given by

$$\lambda_n^p = \lambda_n^u \sqrt{\frac{L_\parallel(\text{Janus connection length})}{L_\parallel(\text{Total connection length})}}. \tag{7.5}$$

From equation (7.1), we can then obtain

$$\lambda_n^p(\text{e-side}) = \lambda_n^u(\text{e-side})\sqrt{\frac{2}{3}}, \quad \text{and} \tag{7.6}$$

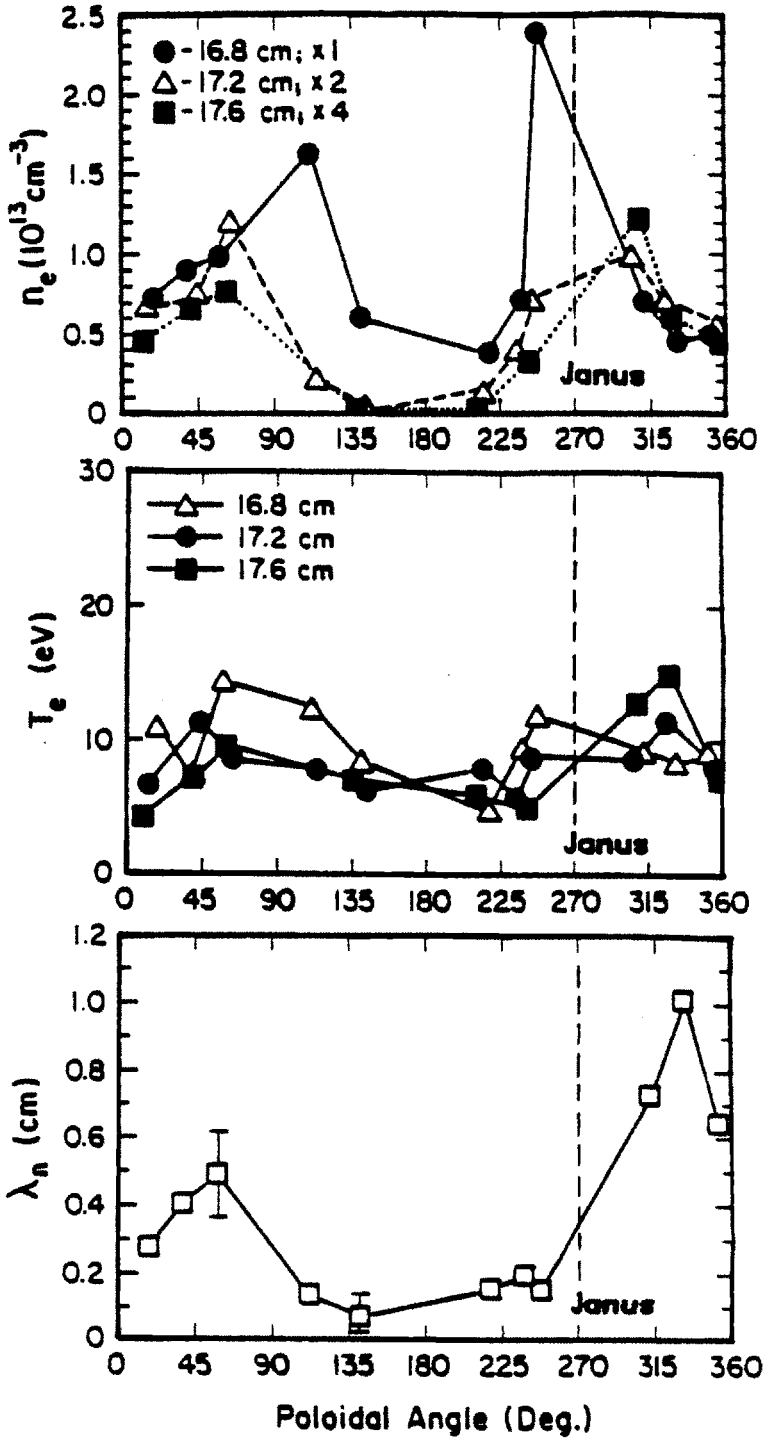

Figure 7.6 Poloidal profiles of n_p and T_e at 16.8 cm, 17.2 cm, and 17.6 cm, and the fitted λ_n from the n_p profiles.

$$\lambda_n^p(\text{i-side}) \quad = \quad \lambda_n^u(\text{i-side})\sqrt{\frac{1}{3}}. \tag{7.7}$$

Using the DENSEPACK results, we can now go back to our previous models and determine the effect of a poloidally asymmetric edge plasma on the measured parameters on both the electron and ion sides. Using the fitted λ_n profile, we can estimate *averaged* λ_n's for both the electron side and ion side flux tubes. From figure 7.6, $\langle\lambda_n^u(\text{e-side})\rangle \sim 0.48$ cm, and $\langle\lambda_n^u(\text{i-side})\rangle \sim 0.28$ cm, where $\langle\ \rangle$ is an averaged value over the entire sampling flux tube. Using equations (7.6) and (7.7), $\langle\lambda_n^p(\text{e-side})\rangle \sim 0.39$ cm, and $\langle\lambda_n^p(\text{i-side})\rangle \sim 0.16$ cm. Assuming that the densities at the probe edge on both sides are approximately the same, $R_{e/i}(n_p) \sim 6.15$ at the diagnostic sensors. However, DENSEPACK also measured large poloidal density variations, suggesting that the densities feeding the electron side and ion side flux tubes are different. Combined with the T_e profile, DENSEPACK measurements show that pressure is not constant along the flux surfaces in the limiter shadow region where field lines do not reconnect. The density asymmetry effect can be accounted for by using equation (2.79) to estimate the magnitude of the densities at the sensors for different probe positions. Rewritting equation (2.79), we get

$$n_p^{e,i}(r_p + \Delta_p) \quad = \quad \left[n_p(r_{lim})\, e^{-r_p/\langle\lambda_n^u(e,i)\rangle}\right] e^{-\Delta_p/\langle\lambda_n^p(e,i)\rangle}, \tag{7.8}$$

where (e,i) denotes either the electron or ion side, r_p is the probe edge position in minor radius, and $n_p(r_{lim})$ is the plasma density at the limiter edge, r_{lim}, which can be extrapolated from the data presented in figure 7.6.

The inferred $n_p^{e,i}$ values and thus the $R_{e/i}(n_p)$ values are strong functions of r_p. Since the λ_n^u values differ, favoring higher perpendicular transport on the electron side, then the density difference at the probe edge will increase as r_p is

increased. Using an averaged n_p value at the limiter of 9×10^{13} cm^{-3} on the ion side and 6×10^{13} cm^{-3} on the electron side, $R_{e/i}(n_p) \sim 4$ as the probe edge is flush with the limiter. However, when $r_p = 1$ cm into the limiteer shadow, $R_{e/i}(n_p) \sim 18$, which is much closer to the observed values. However, the model breaks down for large minor radii since the electron side/ion side ratio of the [] term in equation (7.8) is limited to the range 0.5-2 due to parallel momentum considerations.

The DENSEPACK results can also explain the different behavior of the asymmetry for different magnetic field configurations. DENSEPACK measurements indicate that the poloidal asymmetry is independent of the direction of $\underline{B}_t$. Therefore the perpendicular particle transport is much weaker (smaller λ_n) at the inner regions (high field side) of the torus as compared with the outer regions. For the magnitude of λ_n measured, beginning at 3 mm into the scrape-off region, the plasma density on the outer regions would exceed n_p on the inside. Since $\Delta_p = 0.5$ cm, from the point of view of the flux tubes connecting to the Janus diagnostics, the outer portion of the torus is always a high density, high perpendicular transport region and the inner portion a low density, low perpendicular transport region.

Figure 7.7 shows a view from the top of the flux tubes connecting to the Janus diagnostics for both the normal and reverse field configurations. Normally the electron side flux tube intersects the outer regions of the torus or a region with high edge density (for $r_p > 3$ mm) and high perpendicular particle transport. Therefore, in a normal field configuration, in addition to the favorable connection length ratio, the electron side measurements should also dominate over the ion side measurements due to favorable transport. When $\underline{B}_t$ changes direction, the direction of the flux tube also changes direction. Now the ion side flux tube intersects the high density, high particle transport region. So despite shorter connection length as compared with the electron side, the ion side parameters eventually dominate over the electron side. This is observed

experimentally.

A major problem with using variation of λ_n's for different Janus flux tubes is with the radial dependence of the asymmetry. Although the poloidally asymmetric λ_n measurement indicates a high density, high perpendicular diffusion region on the outer half (low field side) of the torus, which aids in the explanation of the asymmetry, for both the normal and reverse field magnetic field configurations, the radial profiles of the edge parameters as measured by Janus suggest conflicting phenomena. If the perpendicular transport follows the suggested behavior of equation (7.8), then with higher λ_n on the outside, the two-sided asymmetry should become stronger at larger minor radii for the normal field configuration, and weaker for the reverse field configuration. Looking at the data presented in figure 7.2, the dependences of $R_{e/i}(n_p)$ as functions of both the minor radius and $\underline{B}_t$ direction are opposite to the dependence inferred by DENSEPACK. Although the interpretation of the radial profile measurements for a large probe is unclear (see section 2.3), the inconsistency between the Janus results and DENSEPACK results suggests the existence of other possible mechanisms that might drive the two-sided asymmetry.

7.3 Parallel Plasma Flow

Another possible mechanism that will produce the two-sided asymmetry phenomenon observed by Janus is the existence of toroidal flow parallel to magnetic field lines (figure 7.4(d)). Parallel flow with flow velocity on the order of sound speed has been observed experimentally[5,6]. However, we must first evaluate the possible existence of parallel flow in the scrape-off region of Alcator C. Experimentally, the limiter damage pattern shown in figure 7.1 suggests the possible existence of parallel flow. The presence of parallel flow would add a preferential momentum source which would produce asymmetric energy deposition onto the limiter surfaces. The damage pattern of figure 7.1 suggests that

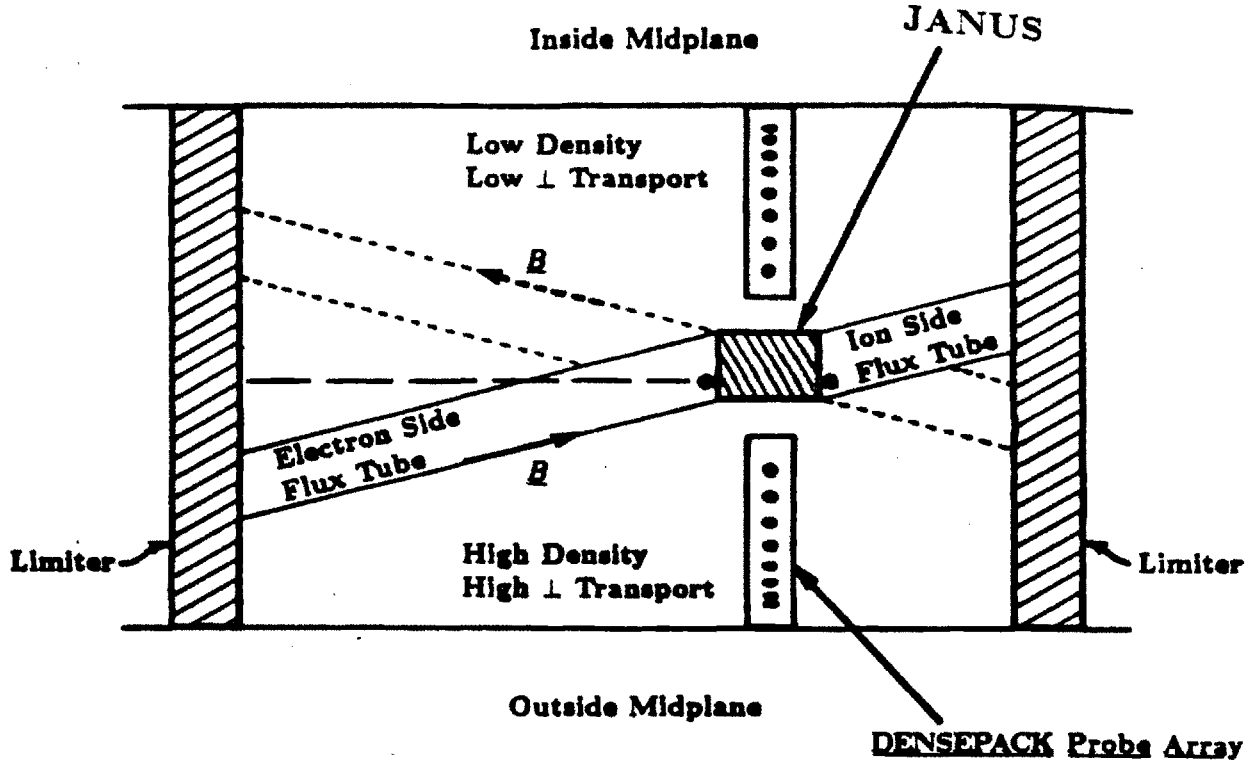

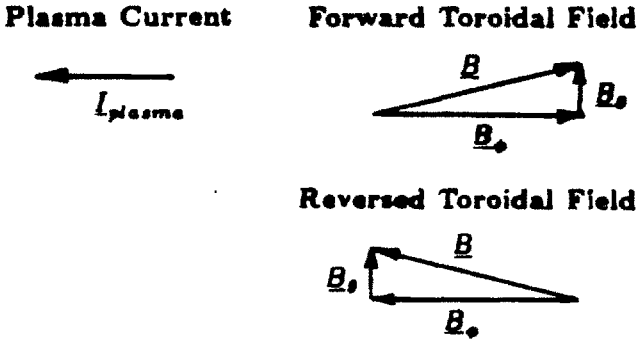

Figure 7.7 A view from the top of the Janus electron side and ion side flux tubes for both the normal and reverse field configurations.

there is flow toward the electron side at the top portion of the edge plasma, and toward the ion side at the bottom.

In the edge region of Alcator C, two mechanisms that would drive parallel flows appear most likely. The first mechanism is the effect of the plasma presheath, which requires both the ions and electrons to flow together, reaching the speed of sound at the sheath edge. This criterion, known as the Bohm Sheath Criterion, is derived in Chapter 2. If there is no preferential momentum source, then the flow will start at the midpoint between two connecting limiter surfaces. For Janus (see figure 3.1), the parallel flow would then be toward the electron side sensors.

If the plasma position is shifted such that the connection length between the limiters changes, then the flow direction in relation with the Janus diagnostic positions is no longer certain. The possible influence of the plasma in-out positions on $R_{e/i}$ is demonstrated in figure 7.3. By shifting the position in and out, a field line launched from one limiter surface might not intersect the next limiter surface, causing the limiter surface to make an apparent "down" shift. Therefore, depending on the "shifting" of the limiter positions relative to a field line, the flow might be either toward or away from the electron side sensors. Figure 7.8 shows two conceptual Janus-limiter configurations that would influence the flow directions. In figure 7.8(a), the limiter facing the electron side sensors is downshifted, causing a flow toward the electron side of Janus. In figure 7.8(b), the ion side limiter is downshifted. Now the flow is toward the ion side. The effect of the parallel flow on the two-sided asymmetry will be derived later in this section.

The second likely mechanism that might drive parallel flows is the tendency of the plasma to reach an equilibrium along field lines. DENSEPACK[10] measured large parameter asymmetry in the poloidal direction. Parallel flow could be driven along the field lines inside the limiter radius. Such flow will attempt to resymmetrize the asymmetry in the edge region and will carry the momentum

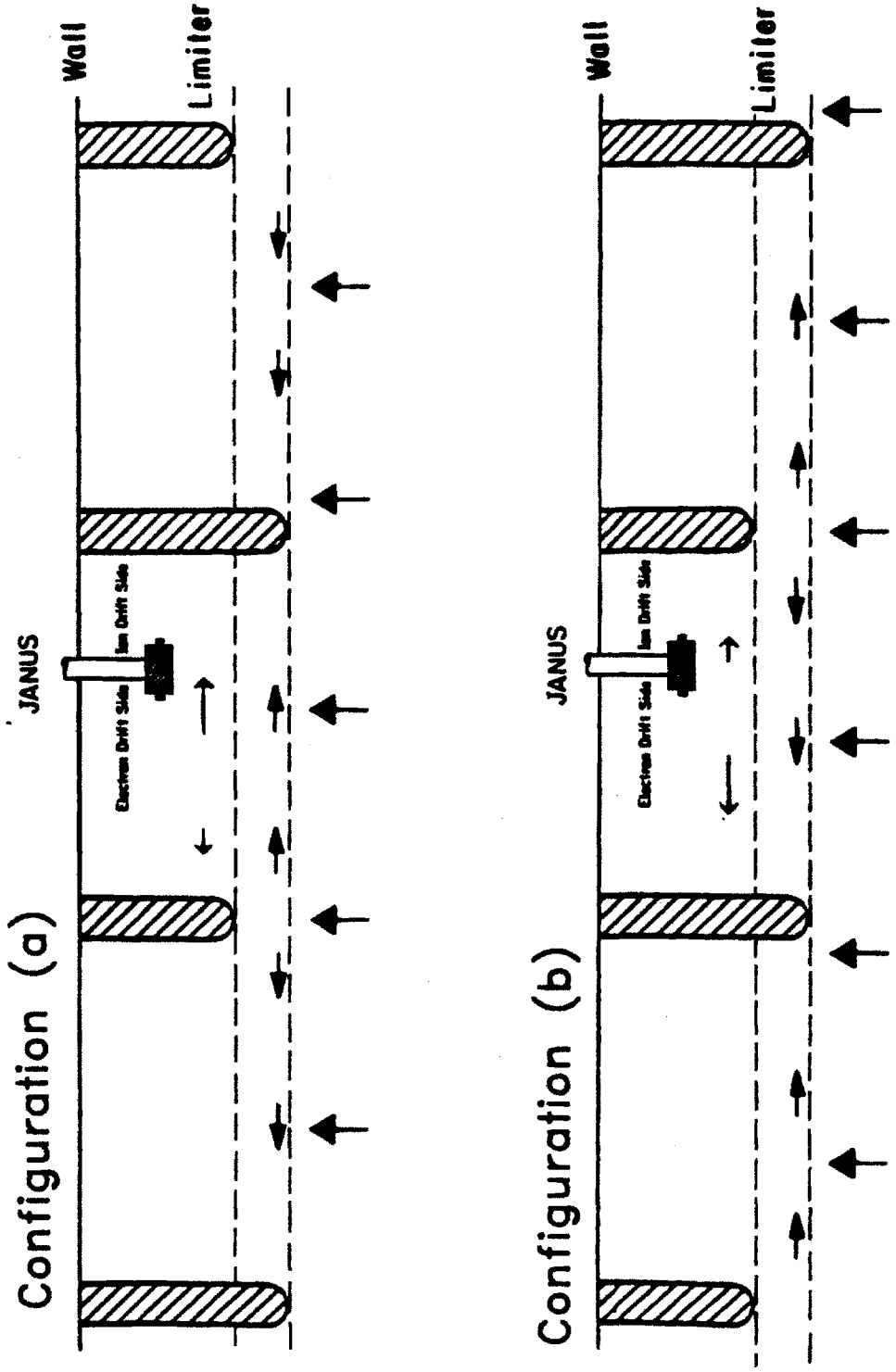

Figure 7.8 Two Janus-limiter configurations that would influence the parallel flow directions.

source into the edge. Possible reasons behind the poloidal asymmetry are given by LaBombard[2,9]. By reversing the $\underline{B}_t$ direction, the parallel flow also reverses. Therefore, if the poloidal profile stays constant with respect to the $\underline{B}_t$ direction, then the flow direction could be directly related to the direction of $\underline{B}_t$, matching our normal and reverse field observations. The flow direction is dependent on the poloidal profile and should flow from high density regions toward low density regions; for the Alcator C edge plasma, the high density regions are located at the top and bottom regions of the machine. Unfortunately Janus is located at a unknown region where the poloidal gradient is largest, thus producing a large uncertainty in our hypothesis.

Chapter 2 presented a simple derivation of the momentum equation which includes the contribution of momentum sources. The theory was first presented by Stangeby[7]. From equation (2.40), the imposed criterion of sound speed flow at the electron side and ion side surfaces of the probe would yield a difference between the collected particle fluxes on both sides. Substituting in $M = 1$ and $M = -1$ at the upstream and downstream probe surfaces, equation (2.40) is reduced to

$$\frac{n_p(\text{upstream})}{n_p(\text{downstream})} = \frac{2 - M_0}{2 + M_0}, \tag{7.9}$$

where M_0 is the initial particle velocity, divided by the sound speed, when it enters the flux tube. If sonic flow at the edge region is observed, then equation (7.9) can also describe the ratio of the total ion flux between the two sides if T_i and T_e are the same on both sides. Substituting in $M_0 = -0.5$, or an initial flow at half the sound speed from the upstream side, then

$$\frac{\Gamma^i_{sat}(\text{upstream})}{\Gamma^i_{sat}(\text{downstream})} \sim \frac{n_p(\text{upstream})}{n_p(\text{downstream})} = \frac{5}{3}. \tag{7.10}$$

Therefore, the upstream side, which faces into the flow, would expect a larger particle flux as compared with the downstream side.

The Stangeby Flow Model encounters some problems if $M_0 \geq 1$. Looking at equation (2.41), for downstream flow, the denominator will pass through a singularity as M passes through the value of -1. Furthermore, the two-sided ratio will approach ∞ as the initial velocity reaches twice the sonic speed. Assuming that only subsonic flows are possible, then the maximum two-sided ratio one can obtain using Stangeby's fluid model is 3. Experimentally I^i_{sat} and n_p ratios between the electron and ion sides typically exceed 10 throughout all radii in the scrape-off layer. Therefore, we could not explain the observed side-to-side asymmetry by using this fluid model with sonic flow.

Harbour and Proudfoot[6] revised the Stangeby model and obtained a two-sided ratio for $M_0 \geq 1$. In their model the value of M at the probe surface is at sound speed if $M_0 \leq 1$ and $M(\text{edge}) = M_0$ for $M_0 > 1$. Assuming that the temperatures on both sides are equal, or neglecting the variation of C_s in calculating the collected ion flux (see equation (4.16)), then equation (7.9) is modified to

$$R^f_{u/d} = \frac{2 - M_0}{2 + M_0}, \quad \text{for } M_0 \leq 1, \text{ and} \tag{7.11}$$

$$R^f_{u/d} = M_0\,(2 + M_0), \quad \text{for } M_0 > 1. \tag{7.12}$$

$R^f_{u/d}$ is the ratio of the collected upstream and downstream ion fluxes using the modified fluid model.

Assuming that the ion velocity distribution function is a Maxwellian with a superimposed drift, then the current density of ions with velocities greater (upstream flow) and less (downstream flow) than 0 can be calculated kinetically. A simplistic model was proposed by Harbour and Proudfoot[6]. The ratio between

the current density of upstream and downstream sides, $R^p_{u/d}$, using this particle model, can be derived and compared with the fluid model. Figure 7.9 plots the functions $R^f_{u/d}$ and $R^p_{u/d}$, as derived by Harbour and Proudfoot, versus M. For a typically observed $R_{e/i}$ ratio of 30, the fluid model predicts a Mach number of ~ 5 and the particle model predicts $M \sim 1$. A large discrepancy between the two models exists. Both models have their own flaws and more theoretical modelling is required before the actual impact of the existence of parallel flow on the edge plasma parameters can be properly assessed. However, this exercise points out the possible impact of a parallel flow on the two-sided asymmetry.

A major constraint of both the particle and fluid models, however, is that the probe dimension must be small enough that the probe is a unperturbing probe. Unfortunately Janus is a large, perturbing probe which violates the assumptions of both models. A further complication in the determination of the influence of parallel flow on the observed two-sided asymmetry arises from the observation of Proudfoot and co-workers[6]. Using a semi-poloidal array of scannable, bi-directional Langmuir probes on DITE, they found poloidal and radial variations in the parallel flow velocities. The Mach number decreases as the minor radius decreases, corresponding to the increase in connection length between the limiters, and also to possible increase of recycling at the limiter surface. They also found greater M at the lower-outside region of DITE, but that variation can be attributed to the variation of connection length at different poloidal locations. If strong radial and poloidal variations of M exist in the scrape-off region of Alcator C, then all the measured edge parameters would depend on the local flow velocity. Furthermore, the transport mechanisms at the edge region would also be affected. A gradient in the parallel flow velocity can also give rise to nonnegligible viscosity terms in the energy equation which we ignored in the derivation of the 1-D edge plasma model presented in Chapter 2.

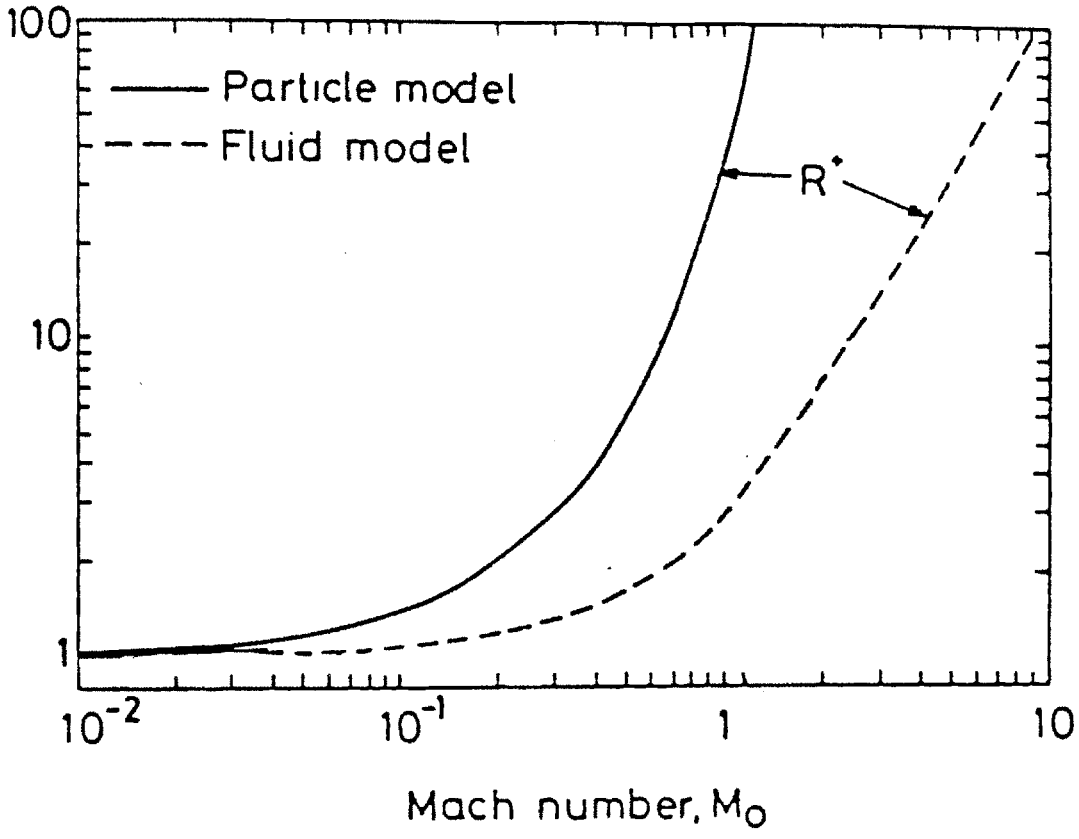

Figure 7.9 $R^f_{u/d}$ and $R^p_{u/d}$ as a function of the Mach number M.

References

[1] Wan, A. S., Yang, T. F., Parker, R. R., "A Localized, Directional Edge Plasma Diagnostic on Alcator C," *Bull. Amer. Phys. Society* **29**, paper 2V7, 1223 (Nov 1984).

[2] LaBombard, B., "Poloidal Asymmetries in the Limiter Shadow Plasma of the Alcator C Tokamak," M.I.T. Doctoral Thesis, April 1986.

[3] Hayzen, A. J., Overskei, D. O., Moreno, J., "Probe Measurements of the Boundary Plasma in Alcator C," M.I.T. Plasma Fusion Center Report PFC/JA 81-10 (April 1981).

[4] LaBombard, B., private communication (1986).

[5] Harbour, P.J., Proudfoot, G., "Mach Number Deduced from Probe Measurements in the Divertor and Boundary Layer of DITE," *J. Nucl. Mat.* **121**, 222 (1984).

[6] Proudfoot, G., Harbour, P. J., Allen, J., Lewis, A., "Poloidal and Radial Variations in Plasma Transport in a Limiter Scrape-Off Layer in DITE," *J. Nucl. Mat.* **128 & 129**, 180–185 (1984).

[7] Stangeby, P. C., "Measuring Plasma Drift Velocities in Tokamak Edge Plasma using Probes," *Phys. Fluids* **27**, 2699–2704 (1984).

[8] Mott-Smith, H. M., Langmuir I., *Phys. Rev.* **28**, 727 (1926).

[9] Labombard, B., Lipschultz, B., "Poloidal Asymmetries in the Scrape-Off Layer Plasma of the Alcator C Tokamak," M.I.T. Plasma Fusion Center Report PFC/JA-85-43 (April 1986).

CHAPTER 8

Calorimeter Data and Analysis

An important consideration in designing any edge component for a fusion device is the amount of incident heat flux that will strike the surface. The extent of the material damage depends on both the magnitude of the heat flux and the material's thermal properties. (Appendix A describes the possible plasma-surface interaction mechanisms in the edge region of a fusion device.) Therefore, to design an edge component it is important to predict the kind of environment the component must withstand. Although we can measure the heat flux on existing devices[1-7], it is necessary to understand the importance of various contributing terms that form the total heat flux.

This chapter is devoted to the analysis of calorimeter data. The next section (8.1) presents a brief introduction to the sheath transmission coefficient. Section 8.2 includes the presentation of some calorimeter data and the analysis of the data with the good of further understanding the heat flux.

8.1 Sheath Transmission Coefficient

A simple, heuristic derivation of the total parallel heat flux, $q_{\parallel}^{total}$, is derived in Chapter 2. Using a detailed kinetic model[8], $q_{\parallel}^{total}$ to a floating surface can be estimated. This is given by equation (2.57), which states

$$q_{\parallel}^{total} = (2\,\mu_E\,\tau + \gamma_e)\,kT_e\,n_p\,C_s\,f(\tau), \tag{8.1}$$

where $\tau \equiv T_i/T_e$. $f(\tau)$ is a density reduction factor ranging from 0.487 to 0.798 for T_i/T_e values from 0 to ∞. The $2\mu_E\tau$ factor represents the contribution from the ion thermal energy. μ_E is an enhancement of the energy flux over

ions possessing a half-space Maxwellian at the sheath edge. For $T_i/T_e \geq 1$, $\mu_E \rightarrow 1$. γ_e is given by equation (6.17). It represents the electron contributions which include both the electron thermal energy and the sheath potential, V_{sheath}. From equation (8.1) we can define a total sheath transmission coefficient[9], γ_{total}, such that

$$\gamma_{total} = 2\mu_E\tau + \frac{2}{1-\nu_e} + \frac{e|V_{sheath}|}{kT_e}. \tag{8.2}$$

ν_e is the secondary electron emission coefficient. Physically the quantity $\gamma_{total}kT_e$ can be defined as the total amount of energy deposited onto the incident material by an ion-electron pair. Stangeby[10] has proposed further refinement to the γ_{total} value which includes the backscattering of ion and electron energies and particles, presheath adjustments, and atomic physics effects.

To predict the amount of heat flux incident to an edge component, knowledge of γ_{total} as a function of the edge parameter is necessary. Then, given the parameters T_i, T_e, and n_p, $q_{\|}^{total}$ can be predicted. It is also possible to control the edge parameters by using different operating conditions. For example, the attainment of H-Mode would significantly alter the edge conditions[11].

8.2 Data and Analysis

The measurement of the parallel heat flux is typically achieved by using a calorimeter, which measures the incremental temperature due to the deposition of plasma energy onto a calorimeter plate. The calorimeter must withstand high heat loads while maintaining a fast thermal response time. The design and analysis techniques of the calorimeter used on Janus were previously described in Chapters 3 and 4 respectively. Curiously, the Janus calorimeter performed sporadically. It is likely that the weld between the tungsten calorimeter plate and the chromel-alumel thermocouple did not hold up. The measurement is also

plagued by electrical pickup noise, especially during ohmic and toroidal field ramp-up and ramp-down periods. Only the discharges during the early life time of Janus yielded satisfactory calorimeter results. The presentation in this section is limited to these discharges.

The deduction of γ_{total} using equation (8.2) requires a knowledge of the edge densities and T_i, T_e. Previous experiments[1-4] used a third lead on the calorimeter to bias the calorimeter like a Langmuir probe. Therefore, by predicting the value of γ_{total}, it is possible to deduce the ion temperature given the knowledge of $q_{\parallel}^{total}$ from the calorimeter, and n_p and T_e from the Langmuir probe. For Janus, T_i is provided by the RFEA while the Langmuir probe measures T_e and n_p. Therefore, we can measure γ_{total} directly by combining the results of all three diagnostics of Janus. Furthermore, the Langmuir probe also measures the ion saturation current, I_{sat}^{i}. In actuality the ion saturation current can be related to the total ion flux that will impact the Langmuir probe surface. Using this fact and equation (8.1), the total sheath transmission coefficient is approximately equal to

$$\gamma_{total} = \frac{q_{\parallel}^{total}\, e\, A_{lp}}{I_{sat}^{i}\, kT_e}, \tag{8.3}$$

where A_{lp} is the Langmuir probe area. Substituting in the Janus geometries, equation (8.3) can be rewritten as

$$\gamma_{total} = 5.07 \times 10^{-2}\, \frac{q_{\parallel}^{total}}{I_{sat}^{i}\, T_e}, \tag{8.4}$$

where $q_{\parallel}^{total}$ is in W/cm^2, I_{sat}^{i} is in amperes, and T_e is in eV.

Figure 8.1 plots the core plasma parameters, I_p and $\bar{n}_e$, for a discharge during the "operating" period of the calorimeter. This shot used hydrogen fuel, and was run at 8.2 tesla normal toroidal field. Janus (RFEA slit) is located at

17.5 cm in minor radius, ~ 1 cm into the limiter shadow. Only the electron side calorimeter data are presented here since the ion side calorimeter detected no significant temperature rise beyond the noise level. The temperature evolution of the electron side calorimeter plate, as measured by the thermocouple at the back of the plate, is shown in figure 8.2. Initially the plate temperature, T_c, stays relatively constant, near the initial plate temperature. Then the temperature rises sharply during the flattop period ($\sim 220 - 510$ ms) of the discharge, and finally levels off at the end of the discharge (> 510 ms).

Figure 8.3 shows the three main heat flux components on the electron side (see equation (4.22)). During the flattop period, energy radiating and conducting away from the calorimeter plate is negligible compared with the parallel plasma heat flux. The measurement of the total parallel heat flux is proportional to the time rate of change of the calorimeter plate temperature, or dT_c/dt. Looking at the temperature profile of figure 8.2, we see that dT_c/dt fluctuates wildly throughout the shot. Therefore, heavy numerical smoothing is required before $q_{\parallel}^{total}$ can be obtained. This calculation also assumes that 50% of all the incident energy is backscattered.

To deduce the γ_{total} value, we need to know the relevant edge parameters. Figure 8.4 plots the time histories of T_i, T_e, n_p, I_{sat}^i, and V_{shift} using the RFEA and Langmuir probe measurements. Averaging the parameters during flattop, we found $\langle T_e \rangle \sim 17.3$ eV, $\langle T_i \rangle \sim 24.3$ eV, $\langle n_p \rangle \sim 3.33 \times 10^{13}$ cm^{-3}, $\langle I_{sat}^i \rangle \sim 0.951$ A, and $\langle q_{\parallel}^{total} \rangle \sim 816$ W/cm^2. Plugging these values into equation (8.4), $\gamma_{total} \sim 2.51$. Using equation (8.1), or modelling the flow to the Langmuir probe by sound speed, $\gamma_{total} \sim 2.87$. Both values are far lower than any theoretically predicted value of γ_{total}, which typically ranges from 6 to 10. Using the averaged edge values during flattop, using V_{shift} to replace V_{sheath}, and assuming $\nu_e \sim 0.3$, then from equation (8.2), $\gamma_{total} \sim 6.97$, which is greater than the measured value by a factor of $\sim 2.5 - 3.0$.

Few measurements of γ_{total}[5-7] in the edge region of tokamaks have been

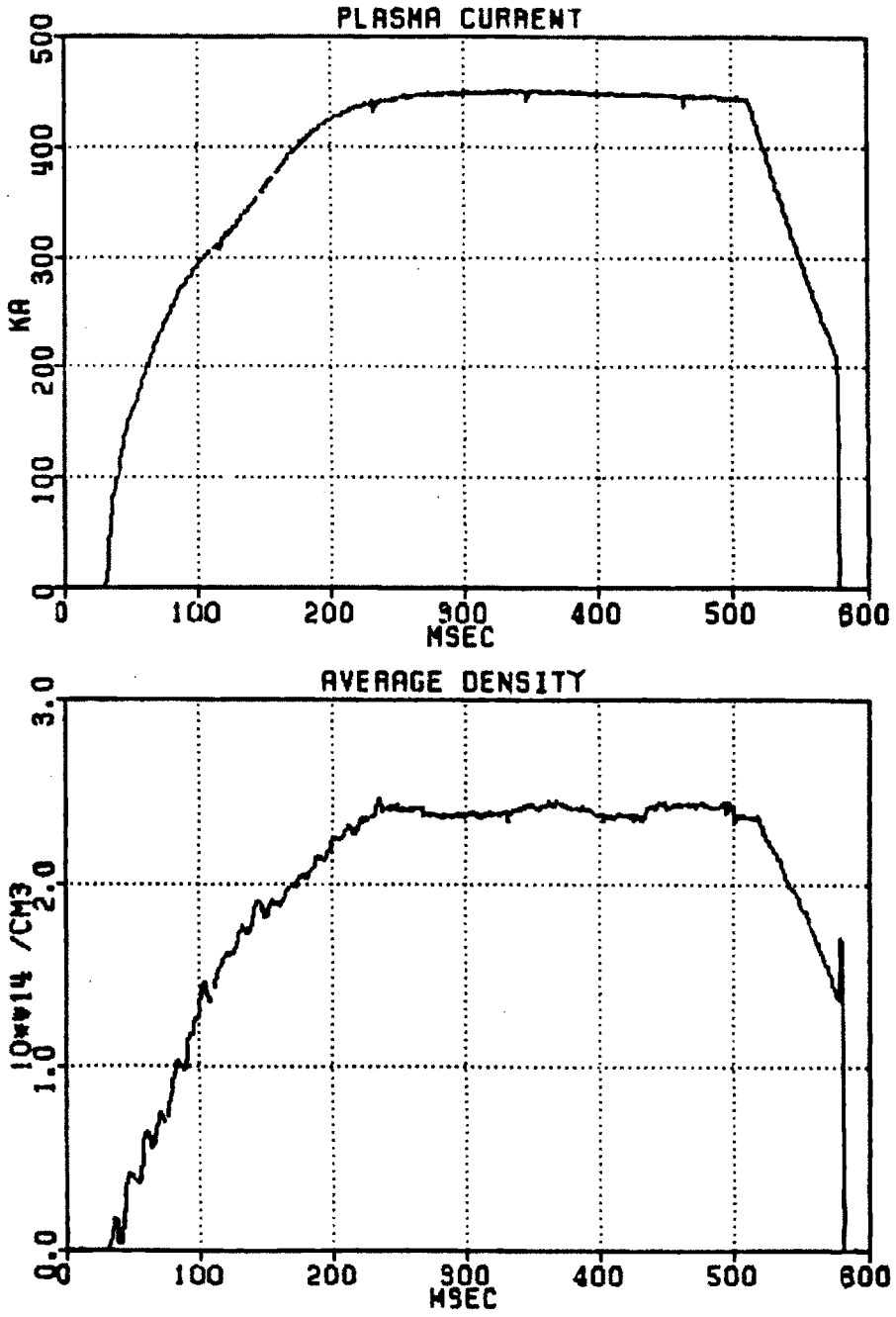

gure 8.1 I_p and $\bar{n}_e$ for a discharge used in obtaining the calorimeter data.

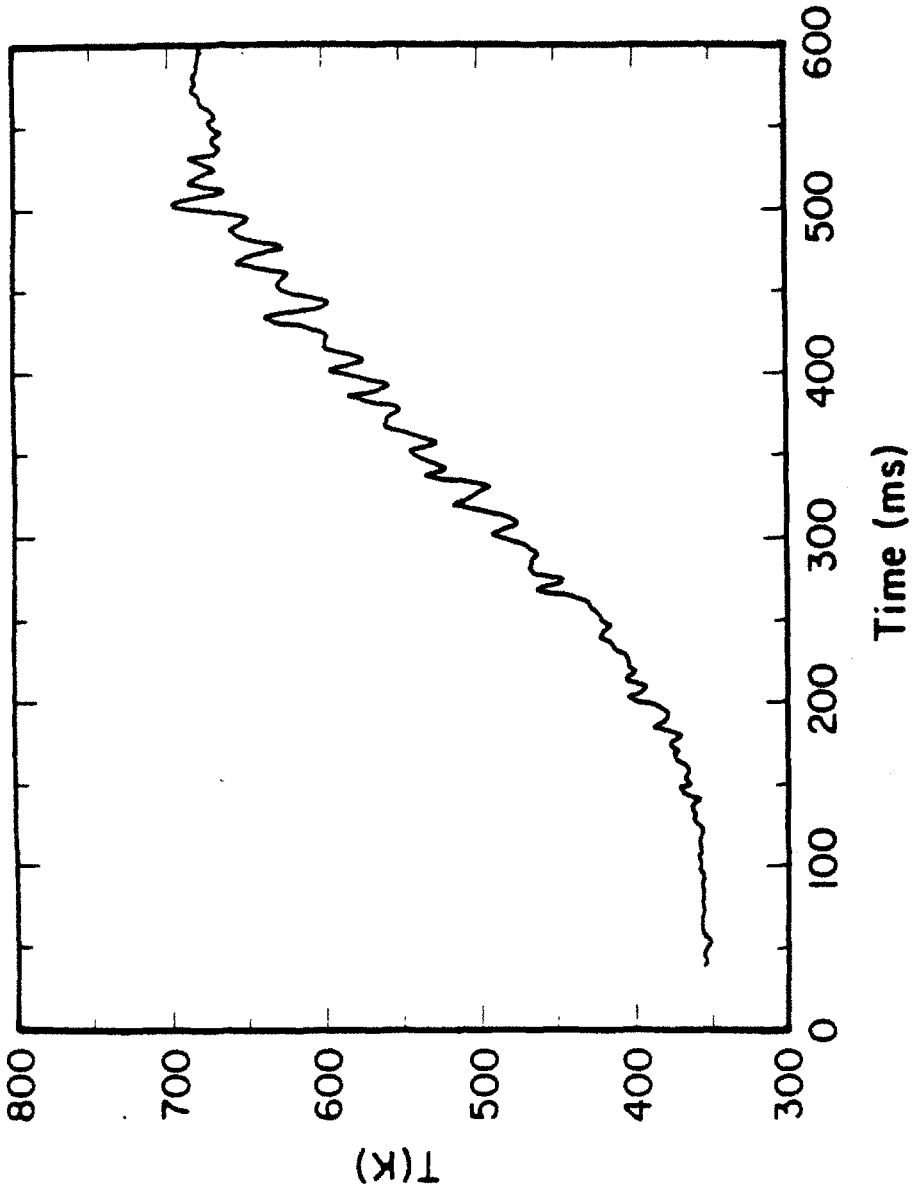

Figure 8.2 Temperature evolution at the back of the electron side calorimeter plate.

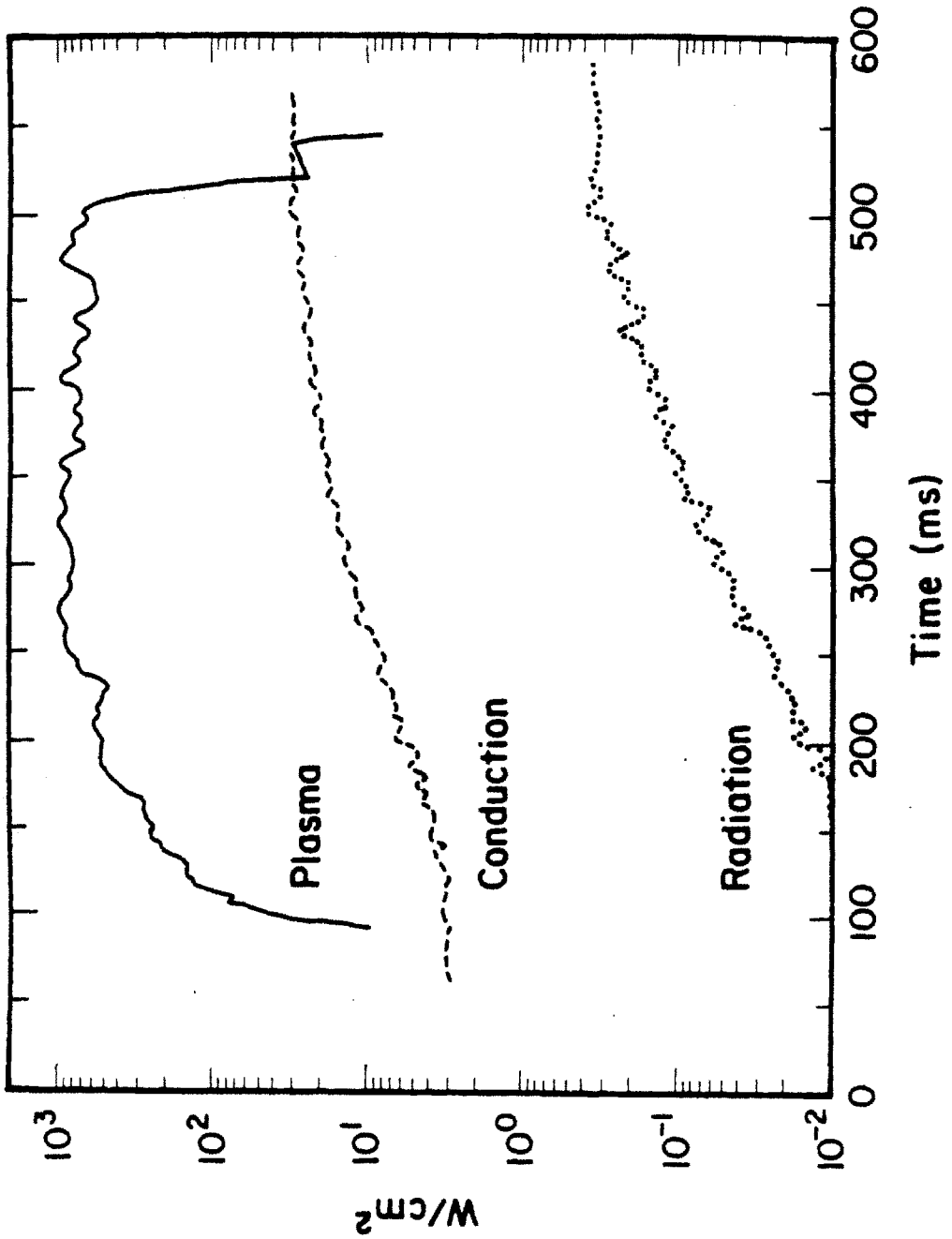

Figure 8.3 Time histories of the parallel plasma heat flux, radiation, and conduction terms on the electron side.

attempted. On Macrotor[7], without any limiters, large asymmetric heat fluxes, favoring the electron side over the ion side, were observed. Adding limiters or adding a small scraper plate at the tip of the heat flux probe would restore the symmetry. It is believed that the principal cause of this asymmetry is the presence of high energy electron tails. Without limiters or scrapers, $\gamma_{total} \sim 25$ is deduced. On DIVA[5], large heat fluxes were also observed. Once again, a high energy electron tail, and thus a two-component electron distribution function, was judged as the primary mechanism.

The JFT-2 experiment[6] measured toroidal and radial variations of γ_{total}. On the ion side near a rail limiter, γ_{total} varies from ~ 7 at the limiter radius to ~ 3.5 at 7 cm into the limiter shadow. 180° away toroidally, the heat flux and γ_{total} are both much larger than the other location. $\gamma_{total} \sim 14$ at the limiter radius and decreases to ~ 5 at 1 cm behind the limiter. 0.5 cm beyond the limiter, $\gamma_{total} \sim 20$ was measured. The Janus measurement presented here is for a probe location at 1 cm into the limiter shadow.

The large discrepancy between the measured and predicted values of γ_{total} needs explanation. The first and most likely possibility is due to some error during either the measurement or the analysis. In view of the trouble we had with the calorimeter in the later period of the experiment, the integrity of the thermocouple junction at the calorimeter plate is a major question mark. In addition, the induced emf for a chromel-alumel thermocouple is of the order of 10 mV. The experimental measurements of the floating potential at the calorimeter plate are of the order of volts. Therefore, it is difficult to achieve high accuracy without extraordinarily high common mode rejection ratios for the operational amplifier. For the Janus design this is about 80.

The biggest uncertainty in the analysis of the calorimeter data is the value of the particle and energy reflection coefficients, which are a function of the particle energetics, the material properties and the averaged incident angle of the particles[12-14]. An overall energy reflection coefficient of 0.5 for tungsten is

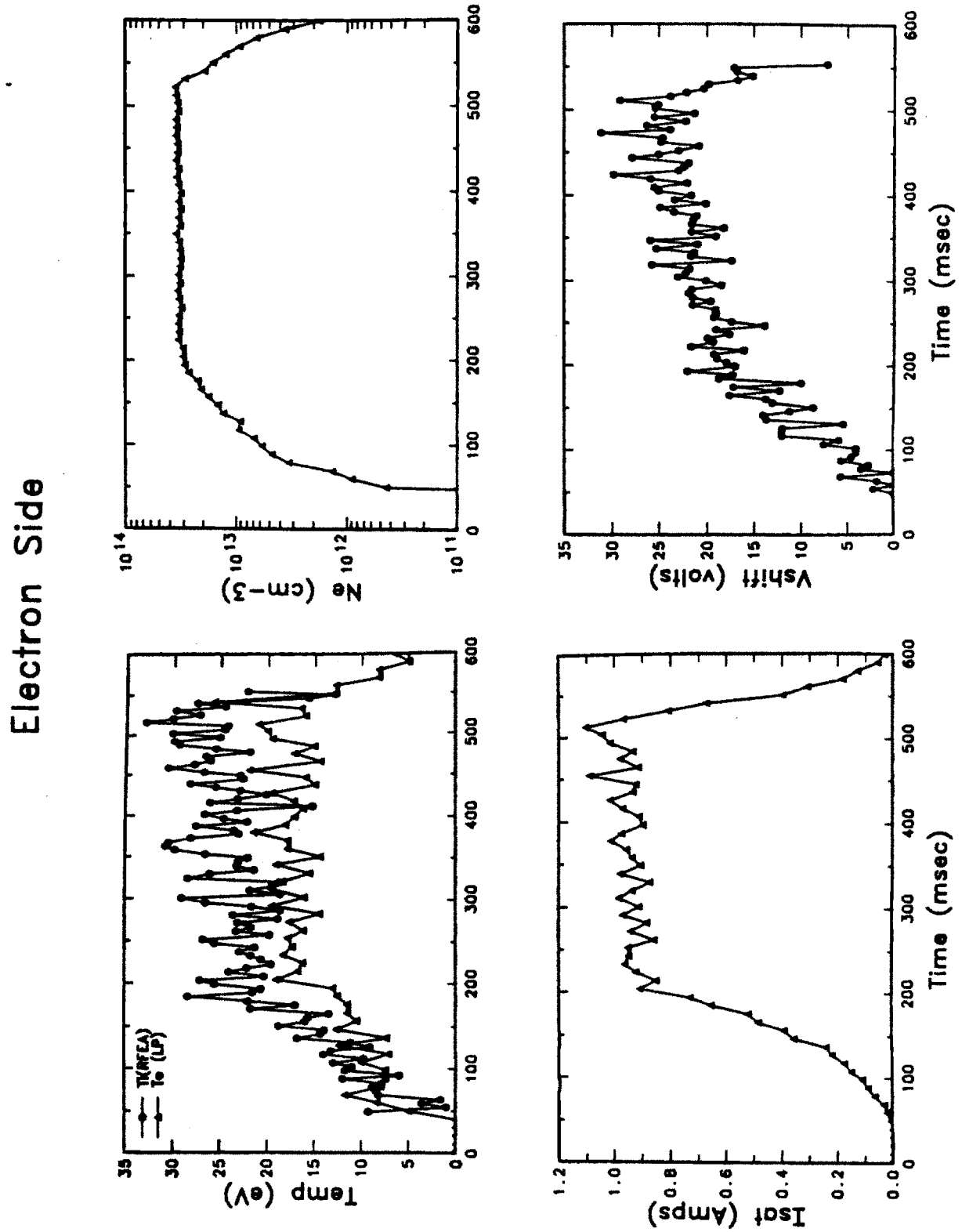

Figure 8.4 T_i, T_e, n_p, I_{sat}^i, and V_{shift} time histories.

used for the analysis. This coefficient accounts for both fractions of the ion and electron energies backscattered away from the material surface. The energy reflection coefficient is a difficult parameter to quantify. Few, if any, experiemental measurements have been performed to determine the coefficient. Most of the low energy data are obtained using computational models. For normal incident deuterons on tungsten, the projected energy reflection coefficient is approximately 0.6[13]. The electron energy reflection coefficient is typically smaller than the ion energy reflection coefficient[10]. If the energy reflection coefficient is larger than expected, then the measured $q_{\|}^{total}$ would also increase. To justify our discrepancy, the energy reflection coefficient needs to be ~ 0.8.

The calorimeter plate is also subjected to metallic deposition from the plasma, where the principal metallic impurities are molybdenum (limiter) and iron (vacuum vessel). Due to these coating, it is likely that the reflection coefficient should also be affected. It is also assumed that the deposition neither affects the thermal properties of the calorimeter plate nor does it cause significant increase in the plate mass. Both effects would change the analyisis, resulting in greater $q_{\|}^{total}$.

The energy reflection coefficient is also dependent on the incident angle of the incident particle. In a magnetized plasma the charged particles, on average, can strike the material surface at an oblique angle despite normal alignment of the surface with respect to the magnetic field and the presence of the sheath potential[14]. For a normal alignment of the material surface with respect to $\underline{B}$, and assuming Maxwellian distributed ions drifting to the sound speed at the sheath edge followed by acceleration toward the wall potential at $V_{sheath} = -2.5T_e$, the averaged incident angle is $\sim 20°$, where 0° is defined as normal incidence to the material surface. For $T_i \sim 20$ eV, the particle reflection coefficient is increased by $\sim$ 20% for 20° incidence as compared with normal incidence. The energy reflection coefficient scales roughly as a fraction of the particle reflection coefficient plus a constant. Therefore, it is possible that the

increase in energy reflection coefficient due to the change of incident angle could also account, in part, for the low measured value of γ_{total}.

One possible explanation of the low γ_{total} value, of course, is due to incorrect theory. From Chapter 6, we found that in order to balance the parallel loss terms, which couple the data with theoretical formulations, it is necessary to have anomalously large perpendicular convection and conduction sources. A $\chi_\perp/D_\perp$ ratio exceeding 1 is always necessary to arrive at proper ion and electron energy balances using the model derived in Chapter 2. If γ_{total} is actually lower than the theoretically predicted value, than the parallel convection term will also be reduced, thus lowering the necessary $\chi_\perp/D_\perp$ ratio for the electron and ion energy balances.

Further uncertainties could arise if parallel flows are present. Poloidal and radial variations of the parallel flow have been observed on DITE[15]. The influence of parallel flow on the formulation of the sheath transmission coefficient is unknown. Possible impact of the parallel flow at the edge region of Alcator C is presented in Chapters 6 and 7.

References

[1] Manos, D. M., Budny, R., Satake, T., Cohen, S. A., "Calorimeter Probe Studies of PDX and PLT," *J. Nucl. Mat.* **111 & 112**, 130–136 (1982).

[2] Manos, D. M., Budny, R., Cohen, S. A., *J. Vac. Sci. Technol. A* **1**, 845 (1983).

[3] Stangeby, P. C., *et al.*, "Edge Measurements of T_e, T_i, n, E_r on the DITE Tokamak Using a Biased Power Bolometer," *J. Vac. Sci. Technol. A* **1**, 1302 (1983).

[4] Erents, S. K., "Measurements of Edge Temperature and Density Profiles in the DITE Tokamak, using a Voltage Scanned Heat Flux Probe," *Fusion Technology* **6**, 453 (1984).

[5] Kimura, H., et al., "Heat Flux to the Material Surfaces in a Tokamak," *Nucl. Fusion* **18**, 1195 (1978).

[6] Gomay, Y., et al., "Particle and Energy Fluxes Observed in the Scrape-Off Layer of JFT-2 Tokamak," *Nucl. Fusion* **18**, 849 (1978).

[7] Zweben, S. J., Taylor, R. J., "Edge-Plasma Properties of the UCLA Tokamaks," *Nucl. Fusion* **23**, 513 (1983).

[8] Emmert, G. A., Wieland, R. M., Mense, A. T., Davidson, J. N., "Electric Sheath and Presheath in a Collisionless, Finite Ion Temperature Plasma," *Phys. Fluids* **23**, 803 (1980).

[9] Stangeby, P. C., "Plasma Sheath Transmission Factors for Tokamak Edge Plasmas," *Phys. Fluids* **27**, 682 (1984).

[10] Stangeby, P. C., "Sheath Lecture," Proceedings of NATO Advanced Study Institute on Plasma Surface Interactions, Val Morin P.Q., Canada (August 1984).

[11] Wagner, F., Keilhacker, M., and the ASDEX and NI Teams, "Importance of the Divertor Configuration for Attaining the H-Regime in ASDEX," *J. Nucl. Mat.* **121**, 103–113 (1984).

[12] Eckstein, W., Verbeek, H., "Data on Light Ion Reflection," Max-Planck Institute Report IPP 9/32 (August 1979).

[13] Ito, R., Tabata, T., Tioh, N., Morita, K., Kato, T., Tawara, H., "Data on the Backscattering Coefficients of Light Ions from Solids (a Revision)," Institute of Plasma Physics (Nagoya University) Report No. IPPJ-AM-41.

[14] Knize, R. J., "Plasma Particle and Energy Reflection at a Wall with an Obliquely Incident Magnetic Field," *Nucl. Fusion* **25**, 1498 (1985).

[15] Proudfoot, G., Harbour, P. J., Allen, J., Lewis, A., "Poloidal and Radial Variations in Plasma Transport in a Limiter Scrape-Off Layer in DITE," *J. Nucl. Mat.* **128 & 129**, 180–185 (1984).

CHAPTER 9

Effect of ICRF Heating on the Edge Plasma

In Chapters 5-8 we presented a detailed experimental investigation of the edge ion and electron parameters on Alcator C. We found that ions and electrons are energetically decoupled, and anomalously large perpendicular transport mechanisms are necessary to balance the parallel losses to the limiters. We also found parameter asymmetry between the electron and ion sides of Janus, which may be caused by a combination of different processes, including variations of the transport behaviors at the connecting flux tubes and the possible existence of parallel toroidal flow. Combining all three Janus diagnostics, we measured much smaller sheath transmission coefficients than predicted theoretically.

The ultimate purpose of this thesis is to perform a detailed study of the Alcator C edge plasma such that the effect of various plasma-surface interactions can be better understood. The impurity release mechanisms are directly connected to the adjacent edge plasma parameters[1] which can be monitored using Janus. Coupling the Janus measurements with various spectroscopic measurements[2,3] on Alcator C, we can attempt to correlate the behaviors of various impurity species with possible impurity release mechanisms and isolate the dominant mechanisms. Using simple Langmuir probes, studies of impurity generation mechanisms in association with rf heating have been performed, both on Alcator C[4,5] and on various other tokamaks[6-13]. In this chapter, we will investigate the relations between the change of edge parameters with the spectroscopically observed change in the impurity concentrations, both before and during ICRF fast wave[14] and Bernstein wave[15] experiments.

For both ICRF experiments, the Alcator C limiter configuration consists of two sets of full poloidal ring limiters made of molybdenum. A limiter radius of 12.5 cm was used for both the Bernstein wave and fast wave antennae. In

addition, sets of smaller limiters with 11.5 cm radii were used for the fast wave experiment. At 18.0 cm in the minor radius, there are four sets of virtual limiters located at every port. The vacuum chamber has a minor radius of 19.2 cm. Both the vacuum chamber and the virtual limiters are made of stainless steel. Figure 9.1 presents a view from the top of Alcator C, showing the locations of limiters, the grazing incidence VUV spectrograph, ICRF antennae, and Janus.

The fast wave antenna is a half loop antenna located at the same toroidal position as Janus. Janus is always located at the top of Alcator C during the fast wave experiments. Figure 9.2 shows an exploded view of the fast wave antenna. The outer Faraday shield is made of stainless steel. When the smaller limiter was used, the alumina insulators were removed and the outer Faraday shields were coated with molybdenum. Previous experiment using pure molybdenum Faraday shields was not successful due to embrittlement of the molybdenum shield[16]. The tip of the Faraday shield is located at ~ 13.0 cm.

The Bernstein wave antenna is approximately a quarter loop antenna inserted from the side of Alcator C. Figure 9.3 shows an exploded view of the Bernstein wave antenna. Once again the Faraday shields are made of stainless steel. During the tenure of Janus, the alumina insulators were removed. The antenna can be moved in the radial direction to adjust the coupling of RF fields and plasma. Typically the tip of the Bernstein wave antenna is located ~ 0.5 cm into the shadow of the limiter. When the Bernstein wave antenna is on the machine, Janus is also positioned at the side, 180° away toroidally.

The first section of this chapter focuses on the observation of the impurity behavior during both ICRF experiments. Section 9.2 presents the Janus data during the ICRF experiments, for various operating conditions. Correlation of the edge parameter variations with possible impurity release mechanisms is presented in section 9.3.

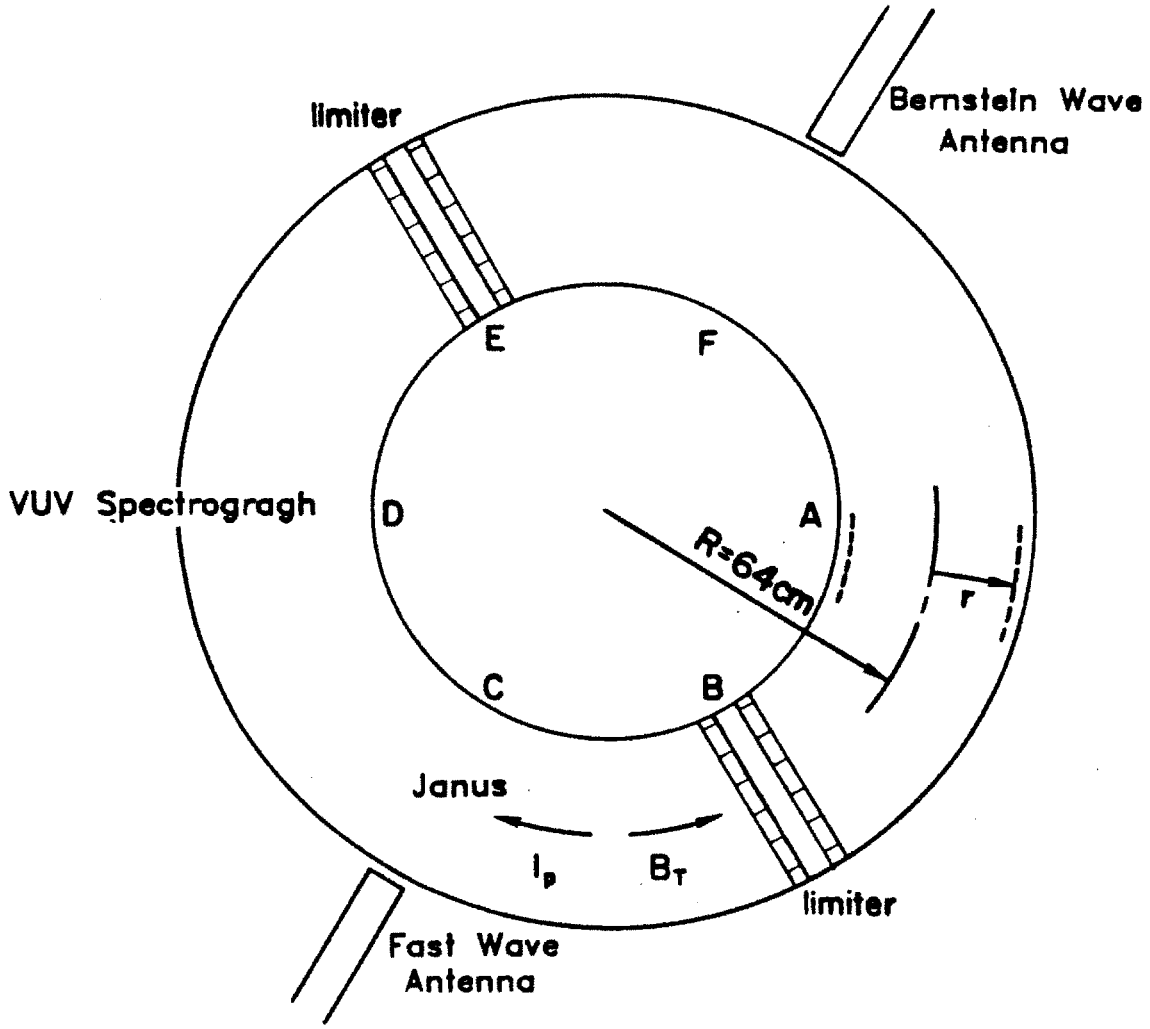

Figure 9.1 A top view of Alcator C showing the toroidal positions of the molybdenum limiters, the VUV spectrograph, the ICRF antennae, and Janus.

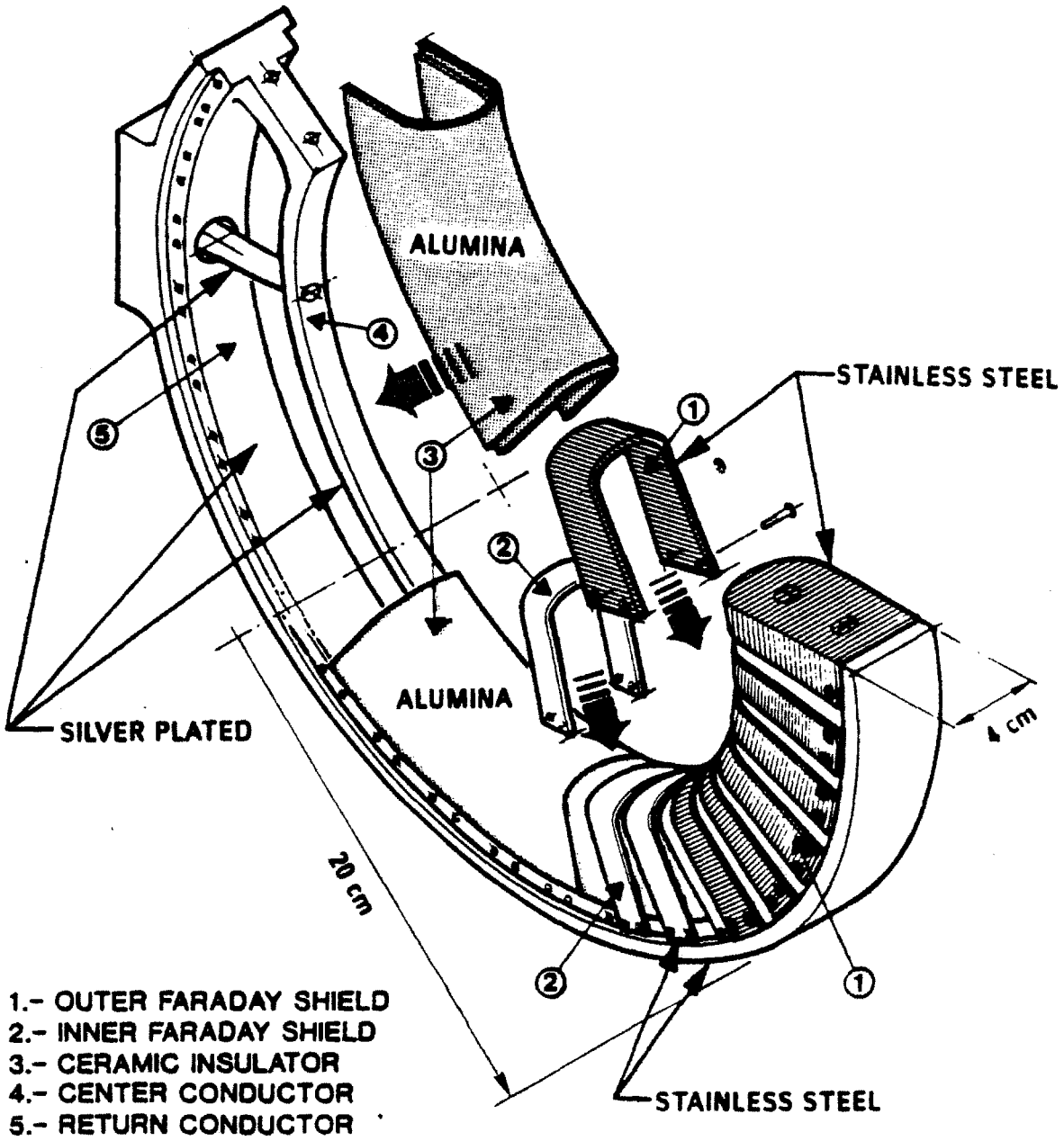

Figure 9.2 Exploded view of the ICRF fast wave antenna.

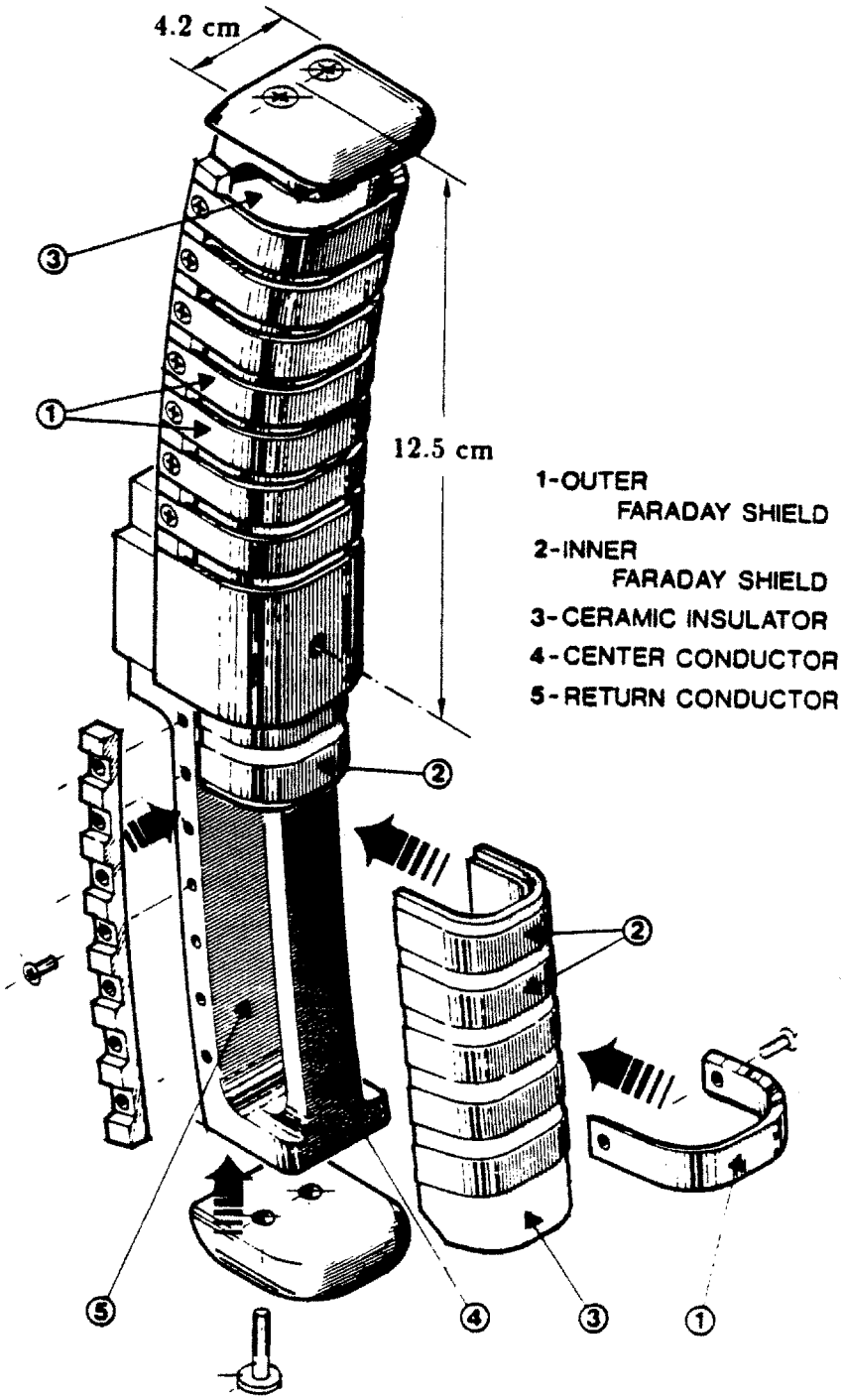

Figure 9.3 Exploded view of the ion Bernstein wave antenna.

9.1 Impurity Behaviors During ICRF Experiments

The measurement of the behavior of impurities is achieved using a 2.2 meter grazing incidence time-resolving vacuum ultra-violet (VUV) spectrograph, which monitors impurity line radiation[4]. The VUV spectrograph has a spectral range of 20-1160 Å, and is capable of simultaneously covering $\sim$ 20 Å when centered at 30 Å and $\sim$ 100 Å when centered at 1100 Å. For the ICRF experiments here, the operating range of the VUV spectrograph ranges from $328 - 373$ Å, which includes an iron line at $\sim$ 335 Å and a molybdenum line at $\sim$ 341 Å.

For a high power ($\sim$ 450 kW) fast wave heating discharge and 11.5 cm limiters, figure 9.4 plots the time and spectral dependent brightness profile. For this discharge, the plasma parameters are $I_p \sim 217$ kA, $\bar{n}_e \sim 2.5\times10^{14}$ cm^{-3}. The toroidal field current is set at 97 kA, or $\sim$ 7.3 tesla, which places the resonance layer at $\sim$ 5.5 cm toward the high field side. The ICRF is on from 185-280 ms after the plasma commutation. During this time, the brightness of the impurity line radiation increased dramatically. Figure 9.5 shows the time histories of the brightness of both the iron and molybdenum lines. When the ICRF is turned on, the magnitudes of the brightness for both lines increased significantly. The brightness of the iron line increased by a factor of $\sim$ 5 and the molybdenum line increased by a factor of $\sim$ 7. Keep in mind that for this specific discharge, the outer Faraday shield is coated with molybdenum. The only source of iron is either from the inner Faraday shield, the wall, or possibly from the loss of the molybdenum coating at the outer Faraday shield. The iron densities increase by factors of 10 to 20 during previous experiments using uncoated Faraday shields while the molybdenum density increase stays roughly constant regardless of the Faraday shield condition[17,18].

The change in the impurity brightness during ICRF need further analysis. Clearly, the plasma-surface interaction mechanisms are changed when the ICRF is turned on. More interestingly, we found a large increase in the iron brightness. Further examination of the geometrical configuration of the fast wave experiment

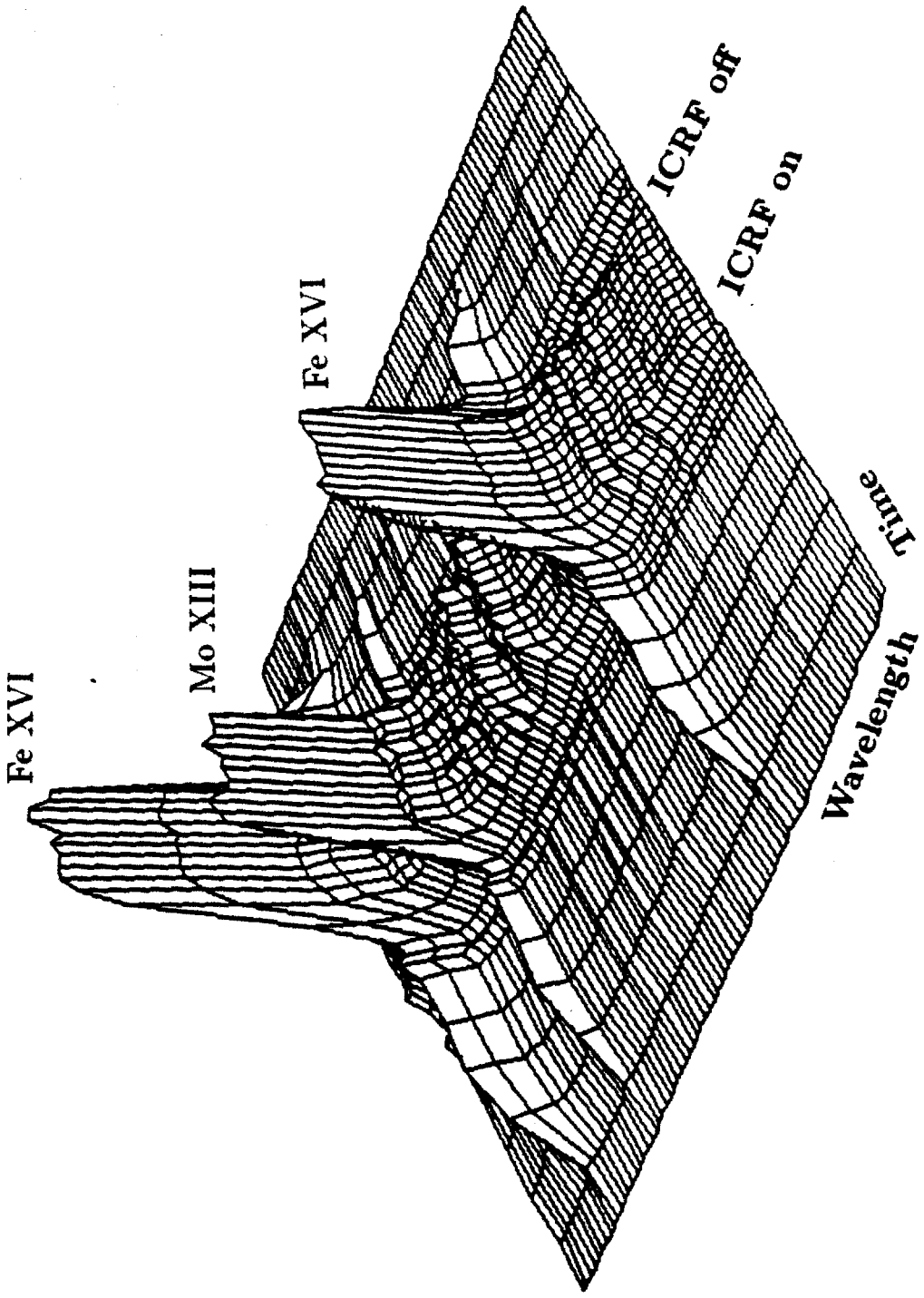

Figure 9.4 Time and spectral profiles of the brightness of the impurity line radiation.

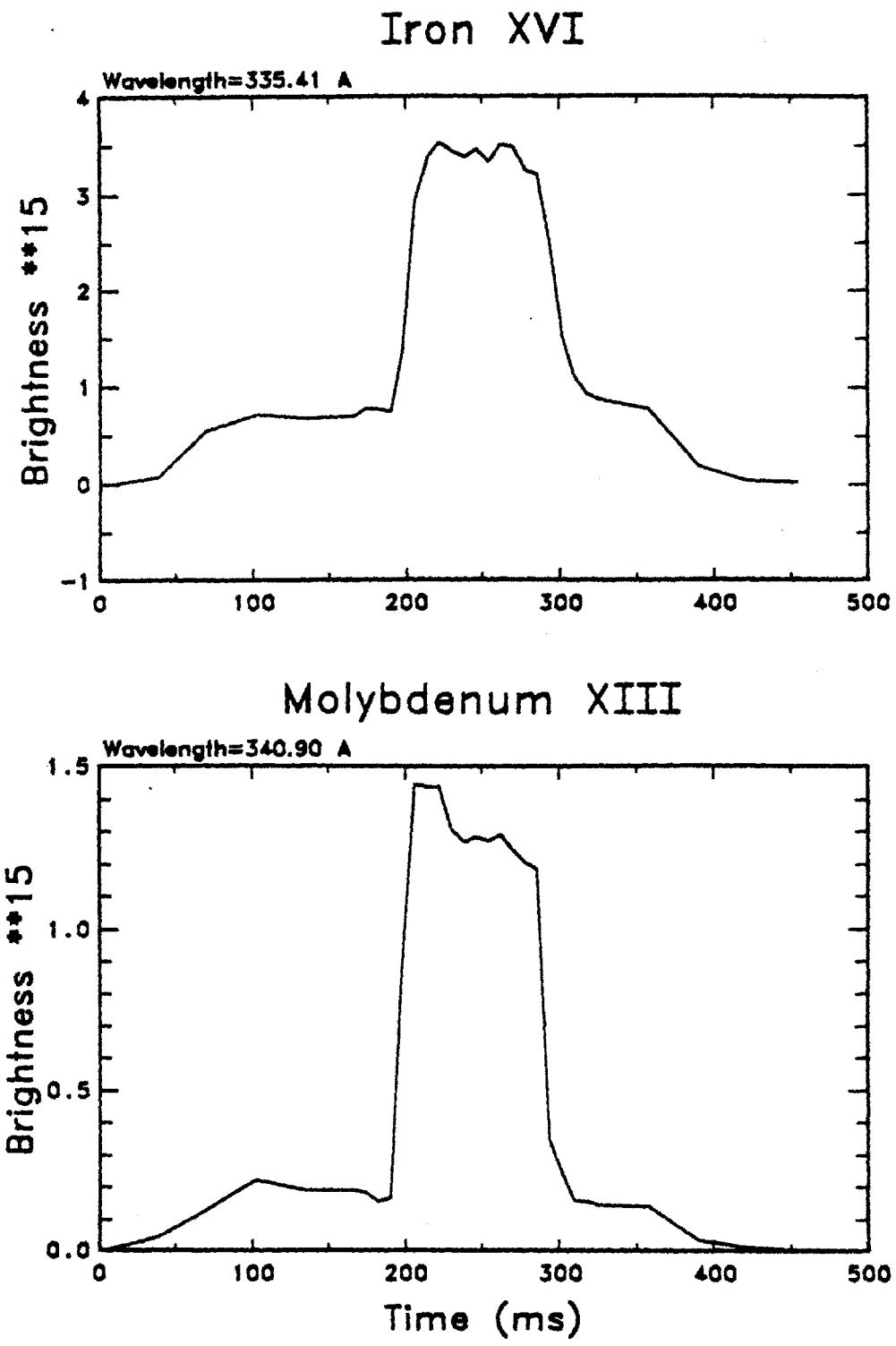

Figure 9.5 Time histories of the iron and molybdenum brightnesses.

indicates that the stainless steel Faraday shield must be a major contributor of the impurities. The next closest stainless steel structures are the virtual limiters, which are $\sim$ 5 cm behind the ICRF antenna. In addition, the proportionally larger iron brightness increase as compared with molybdenum, despite the relatively smaller exposed area of Faraday shield to the total limiter surface area, points out the possibility of preferential impurity releases at the Faraday shield. During the previous ICRF experiment[18] similiar impurity behavior was also observed, indicating that the Faraday shield was a primary source of impurities during ICRF[3].

One interesting behavior of the impurity time history is the reduction of the initial levels of impurity brightness during an intermittent rf discharge where the antenna faulted for a short period of time during the pulse. The impurity radiation level jumps back up when the rf is restored.

Unfortunately the spectrograph did not monitor all of the Bernstein wave and fast wave experiments. Of those shots monitored, the impurity line radiation always increased dramatically during ICRF. The behaviors match those presented in figures 9.4-9.5, although the absolute magnitude of the brightness increase may vary. Previous experiments[3] also point out that the change in the magnitude of the iron brightness increases as the ICRF power level is increased. No such systematic study of the impurity concentration was performed for the more recent ICRF experiments. However, for the 11.5 cm limiter fast wave experiment, there is supporting evidence of larger iron brightness increase in comparison with the molybdenum brightness when the amount of ICRF power is increased[19].

9.2 Effect of ICRF on the Edge Plasma Parameters

To investigate the cause of increasing impurity concentrations during ICRF, it is necessary to know the behavior of the edge plasma near the antennae and

limiters. This section presents a systematic study of the edge plasma parameters using Janus for both the fast wave and Bernstein wave experiments. The most thorough study was conducted for the fast wave experiment using 11.5 cm limiters. This set of data is presented in the first subsection. A study of the fast wave experiment with 12.5 cm limiters is presented in the second subsection, while the Bernstein wave experiment is presented in the third subsection. The implication of the effects of these parameter changes during ICRF will be discussed in more detail in section 3 of this chapter.

9.2.1 The Fast Wave Experiment with 11.5 cm Limiters

For this set of experiments the radii of the molybdenum limiters are reduced to 11.5 cm. The tip of the stainless steel Faraday shield is located at ~ 13 cm, 1.5 cm in back of the limiter edge. Since the only operating limitation of Janus is the relative position of the probe edge and the limiter edge, Janus can now scan across the fast wave antenna and investigate the plasma conditions between the antenna and the limiter edge. For the sake of convenience, the region between the antenna and the limiter ($11.5 \leq r < 13.0$ cm) is herein defined as the limiter zone, and the region starting at the Faraday shield ($r \geq 13.0$ cm) is defined as the antenna zone.

Edge Parameter Variations

Plotted in figure 9.6 are time histories of T_i, T_e, n_p, and V_{float}, on both the electron and ion sides, for Janus located at 12.6 cm. Keep in mind that the Janus position is defined as the minor radial position of the RFEA slit, and the data acquisition system for Janus is turned on 30 ms before plasma commutation. For figure 9.6, the rf is on from $\sim 210 - 310$ ms. For this discharge, ~ 460 kW of rf power is injected into the plasma. During ICRF, both the electron side and ion side T_e rise sharply. Electron side T_e increases by ~ 15 eV, and ion side T_e increases by ~ 35 eV. Due to limitations of the power supply, which can provide

up to ±90 volts, T_e exceeding 40-50 eV is difficult to resolve. T_i on the ion side increases by ~ 30 eV while the electron side T_i, on average, shows no apparent increase. The T_i measurements are highly uncertain since the RFEA has been operating for an extended period of time without any mesh change. Therefore, for this and other ICRF results, T_i results are not emphasized. The behaviors of T_i, however, matches the Langmuir probe T_e behaviors. No significant density variations during ICRF are seen, althought for this discharge n_p on both sides drop slightly after the antenna is turned off. This is not typically observed. The floating potential changes drastically during ICRF. Although the electron side V_{float} exhibits no major variation, the ion side V_{float} jumps up by ~ 15 volts during ICRF.

The edge parameters returned to approximately the pre-rf values immediately (within one Janus sweep period, ~ 5 ms) after the termination of rf. This drastic change of the edge parameters is also noticed during intermittent rf pulses, when the rf faults for a short period of time during the pulse. The edge parameters recover as the rf is restored. The time behavior of the edge parameters is exactly the same as that exhibited by the impurity radiation measured by the VUV spectrograph.

Using the database code mentioned in Chapter 5, we can monitor the edge plasma variations for various operating parameters both when the ICRF is turned on and when it is off. For constant rf power of 95 kW, figure 9.7 plots the electron side (circles) and ion side (triangles) radial profiles of T_i, T_e, n_p, and V_{float} during ICRF (solid symbols) and without ICRF (open symbols). For this set of discharges, $\bar{n}_e \sim 2.7 \times 10^{14}$ cm^{-3}, $I_p \sim 247$ kA, the fuel is hydrogen, and the toroidal field is set up such that the cyclotron resonance layer for second harmonic hydrogen is ~ 5.5 cm toward the high field side.

The most interesting observation is the T_e profile. Previous radial scans without ICRF have always shown that the T_e radial profiles either decay or stay roughly constant for increasing minor radius; thus the source of edge energy

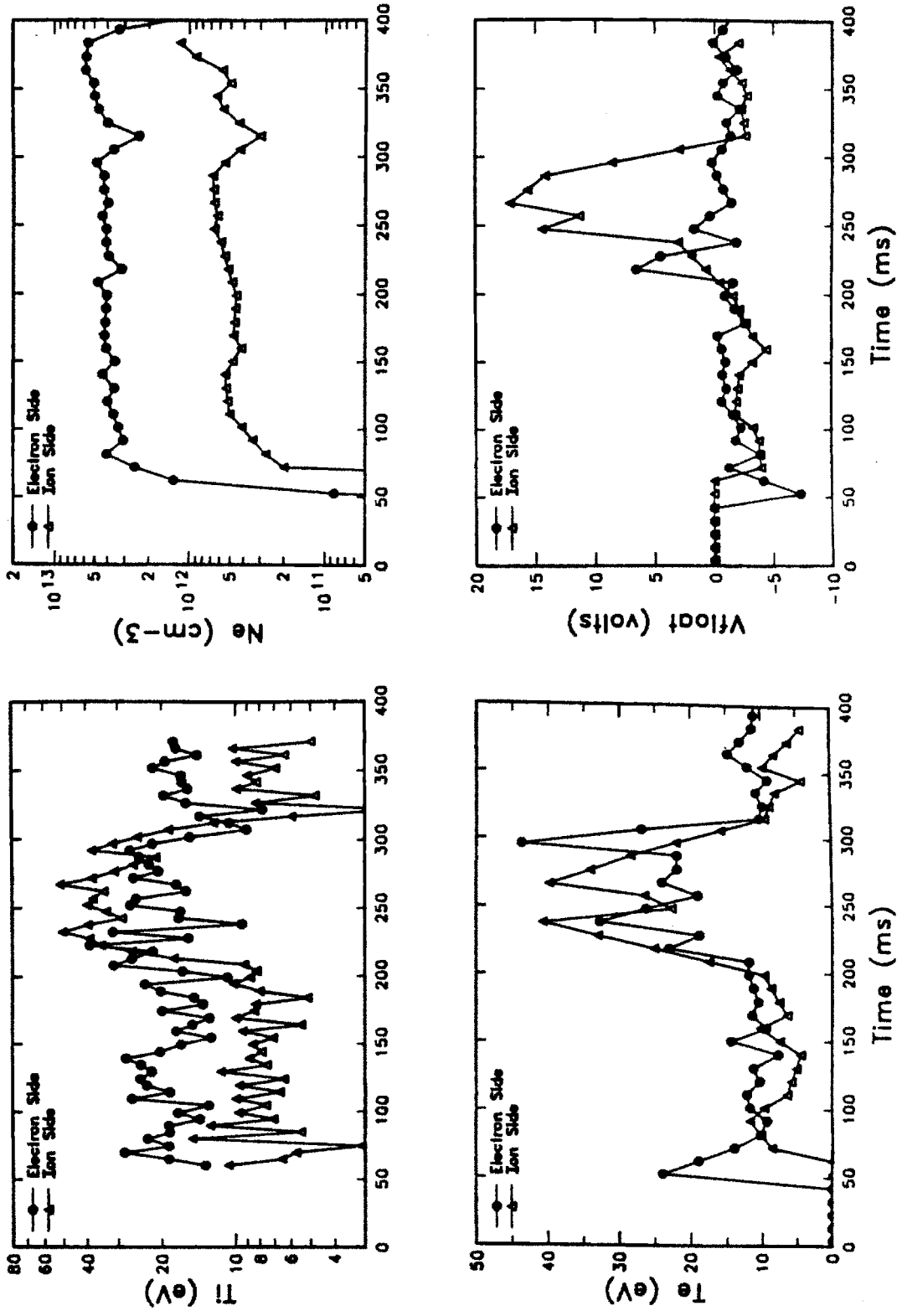

Figure 9.6 Time histories of T_i, T_e, n_p, and V_{float}, on both the electron and ion sides, for an ICRF fast wave experiment.

is predominantly due to perpendicular convection and conduction from the bulk plasma. However, when the rf is turned on, figure 9.7 shows increasing T_i and T_e on both the electron and ion sides in the antenna zone. In the limiter zone, the temperature profiles still resembles the pre-rf profiles, although the magnitudes of both T_i and T_e are increased when the rf is turned on. These temperature behaviors indicate a localized energy source in the antenna zone. The mechanism behind the coupling mechanism between the edge plasma and the antenna rf field is unknown. Possible edge heating mechanisms include coupling to the slow wave at the edge region[9], damping of coaxial modes or surface waves[20], or absorption at the lower hybrid resonance layer. The temperature increase in the limiter zone could be due to increased perpendicular transport from either the bulk plasma or the plasma in the antenna zone.

When the ICRF is turned on, the densities on both the electron and ion sides drop. No noticeable plasma position shifts were observed corresponding to these density reductions. Other experiments have observed edge density increases corresponding to rf[6]. The density increase is attributed to increasing desorption processes due to hotter plasma and material surface. The scrape-off lengths in the limiter zone are not strongly affected by the rf. On the electron side, n_p still decreases in the antenna zone during rf. However, on the ion side, increasing n_p is observed during rf, indicating a localized particle source in the antenna zone.

The particle source, S_p, could be caused by either increasing desorption or neutral ionization as the result of a hotter edge plasma. For ionization processes S_p is defined by equation (2.24), which states

$$S_p = n_p n_n \langle \sigma v \rangle_{ioniz}, \tag{9.1}$$

where n_n is the neutral density. For electron impact ionization of atomic hydrogen, $\langle \sigma v \rangle_{ioniz}$ can be approximated by equation (B.9). Using $T_e \sim 10$ eV for the no-rf case, $\langle \sigma v \rangle_{ioniz} \sim 3.6 \times 10^{-9}$ cm^3/s. During rf, $T_e \sim 35$ eV, and

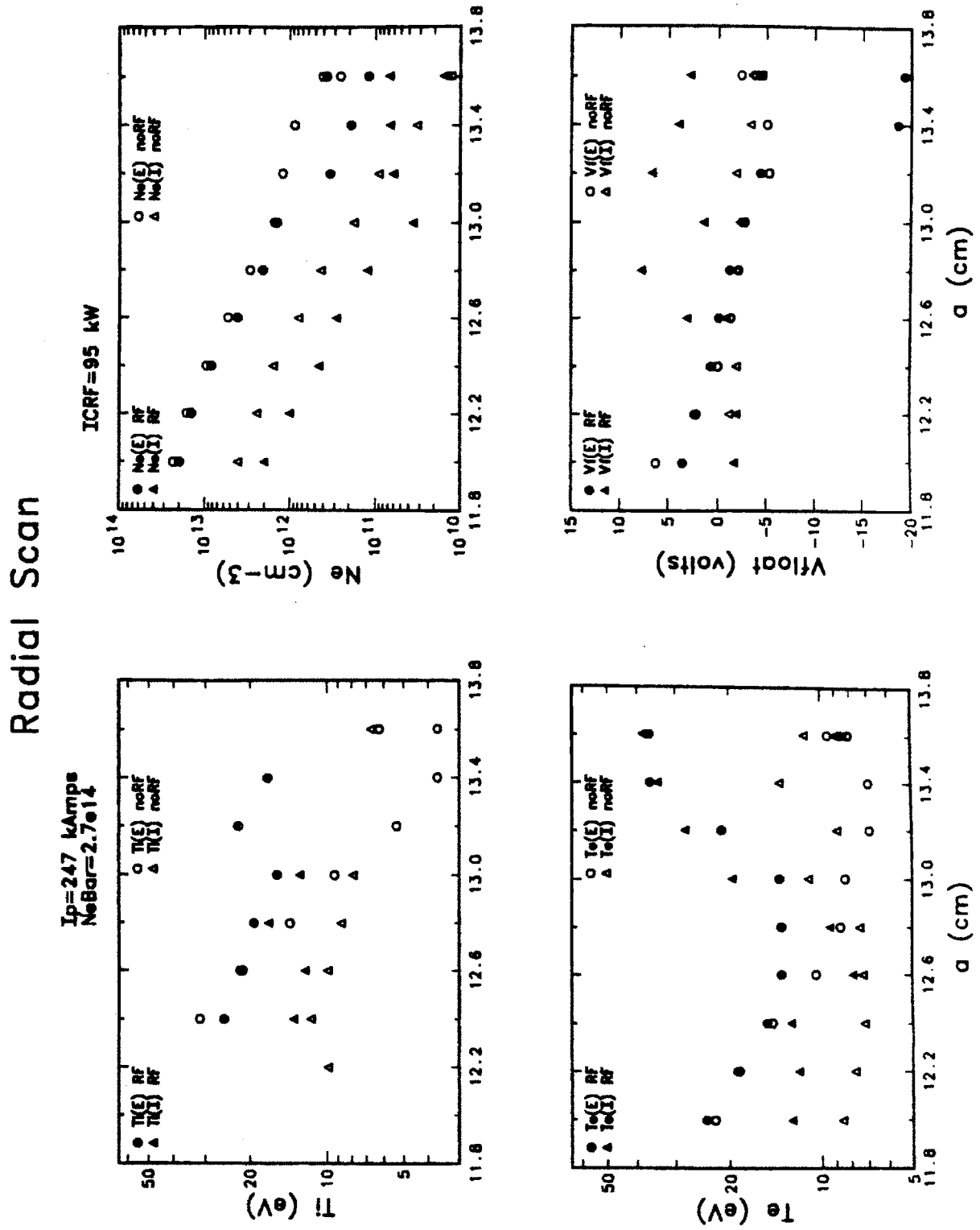

Figure 9.7 Radial profiles of T_i, T_e, n_p, and V_{float} on the electron and ion sides, both with (95 kW) and without ICRF.

$\langle \sigma v \rangle_{ioniz} \sim 1.6 \times 10^{-8}$ cm^3/s. The relative importance of the ionization source in balancing the edge particles with the parallel losses can be expressed by equation (2.32):

$$\frac{f(\tau) C_s}{L_\parallel} \gg n_n \langle \sigma v \rangle_{ioniz}. \tag{9.2}$$

The two competing variables for edge particle balance are C_s and $\langle \sigma v \rangle_{ioniz}$. C_s is proportional to $\sqrt{T_i + T_e}$ which would yield a no-rf to RF ratio of ~ 2 while a $\langle \sigma v \rangle_{ioniz}$ variation of a factor of ~ 4 is reached earlier. Therefore, if the edge neutral density stays constant throughout the entire discharge, then it is possible that ionization could play an important role in the edge particle balance during rf.

The floating potentials are not strongly perturbed during rf until the probe approaches the antenna zone. Before the onset of rf, ion side and electron side V_{float} are both slightly negative with respect to the probe ground. In the antenna zone, during rf, the ion side V_{float} increases while the electron side V_{float} decreases, thus setting up a large potential difference between the two sides.

Fixing the toroidal field constant so the resonance layer stays fixed, and increasing the total rf power to $\sim$ 460 kW, figure 9.8 plots the same set of edge parameters as figure 9.7. The averaged central parameters are reduced slightly, $\bar{n}_e \sim 2.3 \times 10^{14}$ cm^{-3} and $I_p \sim 217$ kA, but the initial edge parameters (before rf) stay approximately the same as for the low power case. The edge region behavior for these high power discharges is very different as compared to behavior for low power discharges. The temperature profiles no longer show the bump in the antenna zone. Now the temperature profiles are nearly flat during rf. The previously observed hollow profile in the limiter zone near the antenna edge is filled up as the amount of rf power is increased. A T_e increase of $\sim 10 - 20$ eV is observed on the ion side. The electron side T_e increase is

most dramatic in the antenna zone. Near the limiter radius ($r \sim 12.0$ cm), no T_e variation is observed when the rf is turned on.

A flattening of the density profiles on both the electron and ion sides is now observed. n_p still drops slightly near the limiter radius. However, from $r \geq 12.6$ cm onward, the electron side and ion side plasma densities during rf both exceed the pre-rf values. The density increase is more pronounced in the antenna region. A large variation in the floating potential is once again observed. During rf, the potential difference is smallest near the limiter radius. As r is increased, the ion side V_{float} remains very positive with respect to the probe ground while the electron side V_{float} decreases until flattening out at ~ -15 volts in the antenna zone.

Keeping the operating parameters at roughly the same values, a toroidal magnetic field scan was performed. By increasing the toroidal field strength, the cyclotron resonance layer will be shifted from the high field side toward the low field side. Resonance layer positions at 2.6 cm, 5.5 cm, and 8.4 cm away from the magnetic axis, toward the high field side, are used in the field scan. Fixing the total injected power at $\sim 400 - 460$ kW, no apparent difference in the edge parameters was observed. The radial parameter profiles all resemble the data presented in figure 9.8. If the operating parameters are held fixed, it appears that the dominant criterion in edge parameter variations is the total amount of ICRF power injected.

Focusing on the parameter change during ICRF, figure 9.9 shows the change of T_e and n_p during and before the firing of ICRF antenna as a function of the injected ICRF power. The change in T_e is defined as ΔT_e, or the difference between the averaged T_e during and before ICRF. The density variation is expressed by the ratio of the change of n_p over the measured density before ICRF:

$$\frac{\Delta n_p}{n_p} \equiv \frac{\langle n_p(\text{no rf})\rangle - \langle n_p(\text{rf})\rangle}{\langle n_p(\text{no rf})\rangle}. \tag{9.3}$$

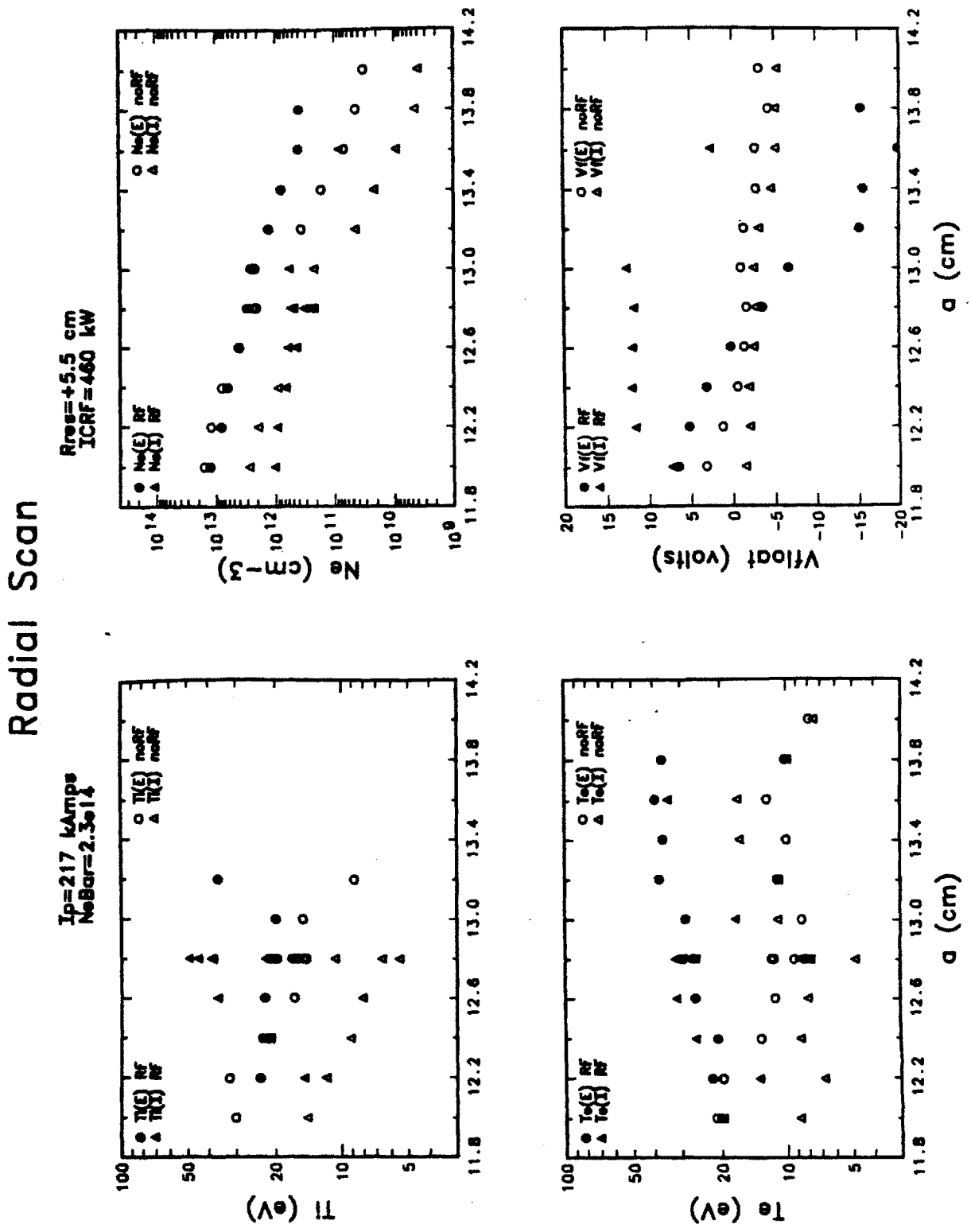

Figure 9.8 Radial profiles of T_i, T_e, n_p, and V_{float} on the electron and ion sides, both with (460 kW) and without ICRF.

The power scan presented in figure 9.9 is conducted with Janus located at 12.8 cm, 2 mm beyond the tip of the Faraday shield. It is at this position that the edge varies most as a function of input power. From figure 9.9, we found that the ion side T_e increase is much greater than the corresponding electron side increase. A significant ion side T_e increase of ~ 20 eV is observed even at ~ 200 kW. Although large ΔT_e scatterings are observed, there is a general trend toward greater ΔT_e at higher injected power.

From equation (9.3), positive $(\Delta n_p)/n_p$ indicates decreasing density during ICRF as compared with the pre-rf status. At low input power, there is a trend toward increasing $(\Delta n_p)/n_p$ as a function of rf power. However, this trend starts to reverse itself near 300 kW. At high power levels, $(\Delta n_p)/n_p$ becomes negative. The relative change of density is more pronounced on the electron side at low powers, and more pronounced on the ion side at high powers. This observation is consistent with the radial profiles presented in figures 9.7 and 9.8. At a low rf power of 95 kW, the densities in the limiter zone drop during rf. However, at high power (460 kW), the densities at positions close to the antenna zone also increase. This could be caused by diffusion of particles from the antenna zone into the limiter zone, or by increased particle source at these regions.

Energy Accounting

Assuming that the loss mechanisms in the edge region are dominated by the parallel convective flow to the limiters, we can attempt a simple analysis of energy accounting, similiar to the analysis conducted in section 6.4 above. The object of this exercise is to determine the amount of ICRF power deposited in the edge region and is not a proper analysis of the global energy balance.

The total (ions plus electrons) parallel loss, $q_{\parallel}^{total}$, can be expressed by equation (2.57), which states

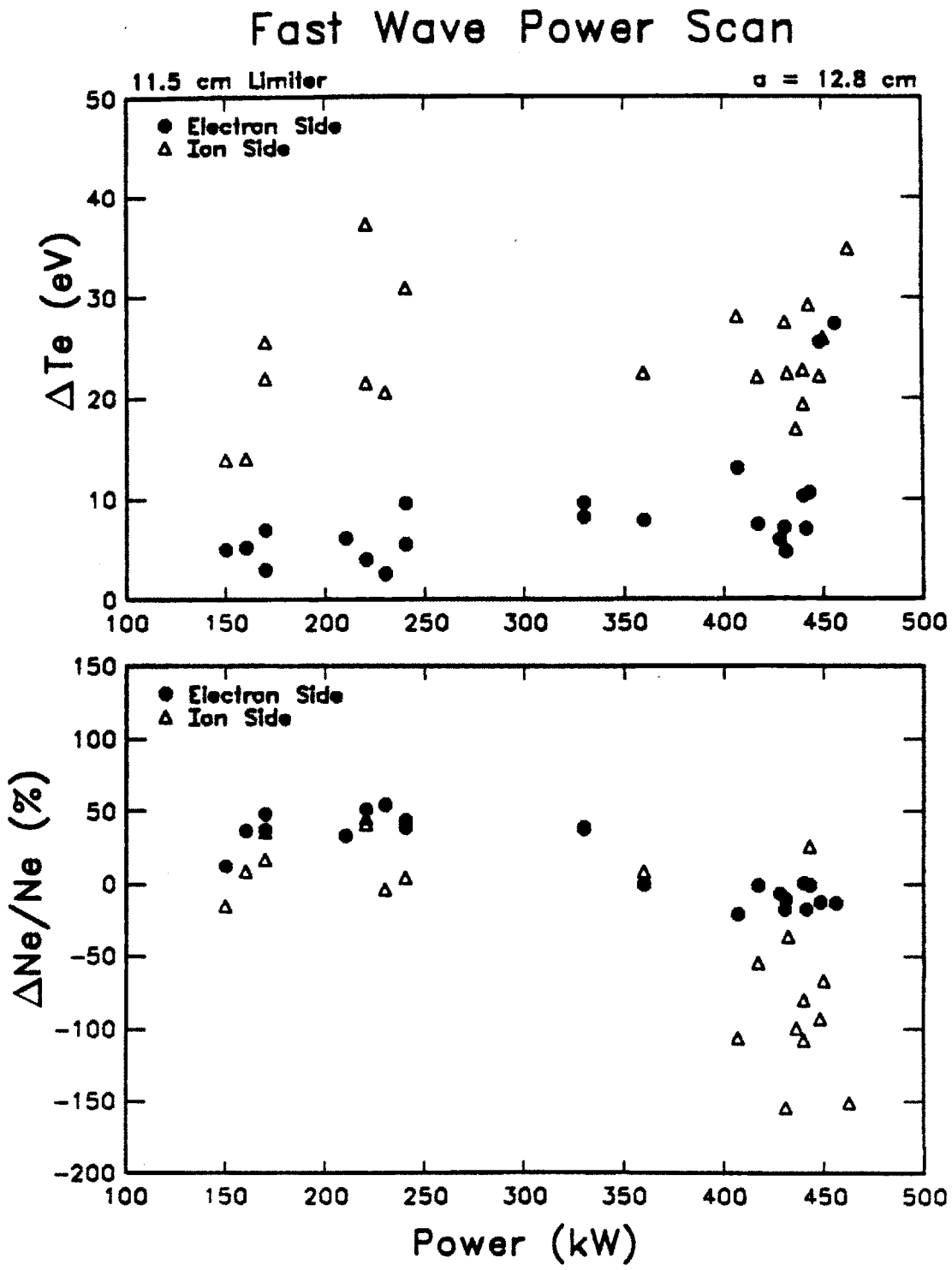

Figure 9.9 Electron side and ion side ΔT_e and $(\Delta n_p)/n_p$ as a function of total injected ICRF fast wave power, operating at second harmonic hydrogen heating with 11.5 cm limiters.

$$q_{\|}^{total} = (2\tau\mu_E + \gamma_e)\, kT_e\, n_p\, C_s\, f(\tau). \qquad (9.4)$$

The terminology and typical values have all been given in Chapter 6. As previously discussed, γ_e includes both the electron thermal energy and the sheath potential contributions. Figures 9.10 and 9.11 include the electron and ion side radial $q_{\|}^{total}$ profiles, both with (solid circles) and without (open triangles) ICRF, for the low (95 kW) and high (460 kW) power fast wave experiments respectively. The relevant edge parameters are presented in figures 9.7 and 9.8.

The variation of $q_{\|}^{total}$ depends on both temperature and density variations. For the low power case, the electron and ion side $q_{\|}^{total}$s are lower during rf in the limiter zone. The principal cause of this decrease is the magnitude of the n_p reduction during rf such that the temperature increase could not compensate the density loss. Near the antenna zone $q_{\|}^{total}$ is greater during rf as the result of large temperature increase. In the region sampled by Janus alone, we can obtain the total power deposited into the region, P^{total}, by integrating the function $(q_{\|}^{total} 2\pi r)$ over minor radii. Due to the lack of the poloidal profile data for 11.5 cm limiters, poloidal symmetry is assumed. The total ICRF power deposited into the region, P^{total}(ICRF), will equal the difference between the total deposited power during rf and without rf. For the low power data, P^{total}(ICRF) on the electron side is ~ -4.1 kW while P^{total}(ICRF) on the ion side is ~ -0.2 kW. The reason behind the loss of power to the limiters during ICRF is because of the large density reduction in the limiter zone which brings down the $q_{\|}^{total}$ in that region. Due to the large n_p difference over 2 cm, a small fractional reduction in n_p would produce the results derived here.

For the high power case, with the exception of several points on the electron side near the limiter radius, the temperature increase throughout the entire sampling region far outweights the density reductions. P^{total}(ICRF) on the electron and ion sides are approximately 25.1 kW and 6.8 kW respectively. However,

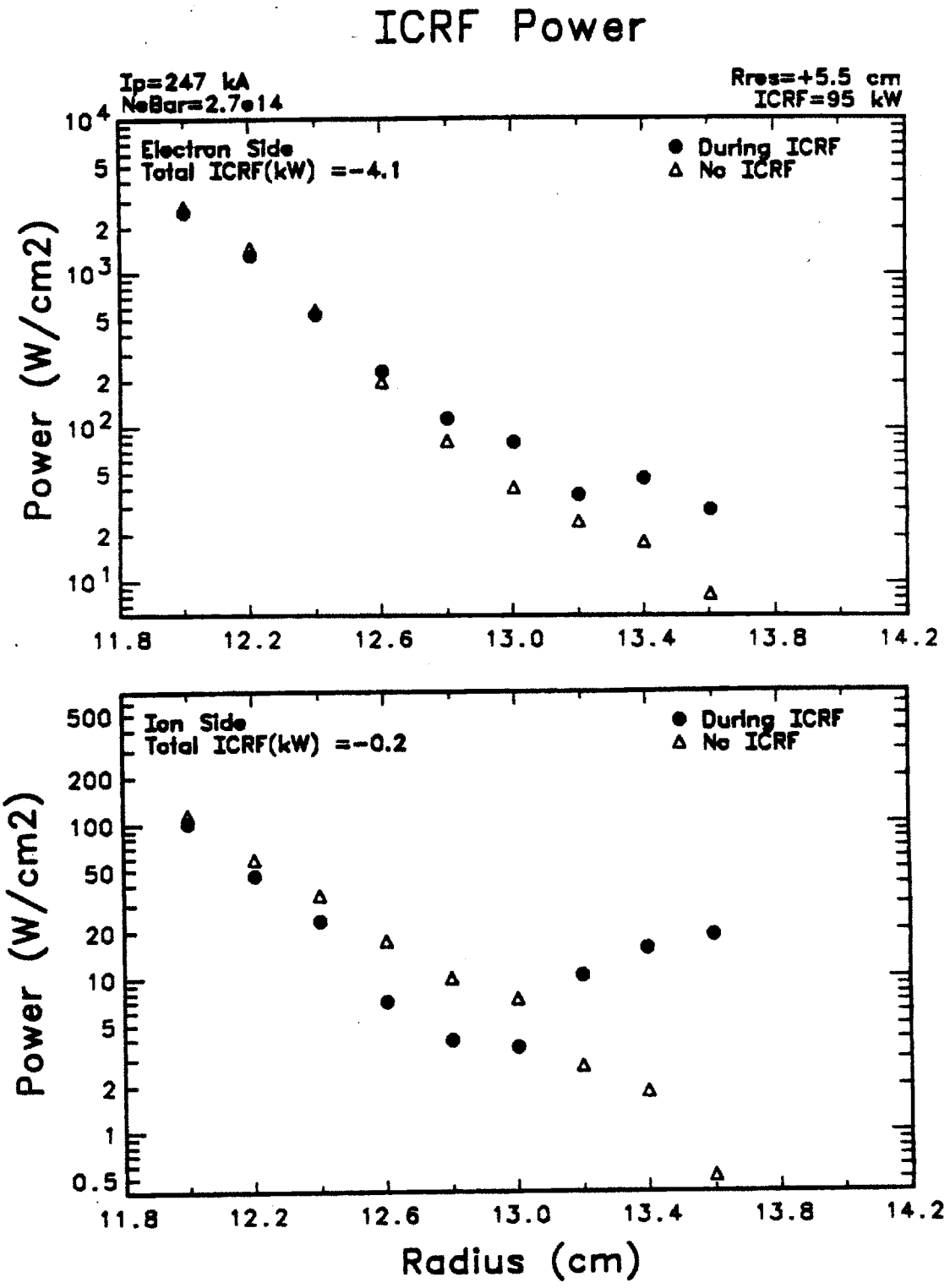

Figure 9.10 The electron and ion side radial $q_{\|}^{total}$ profiles with and without 95 kW of ICRF power.

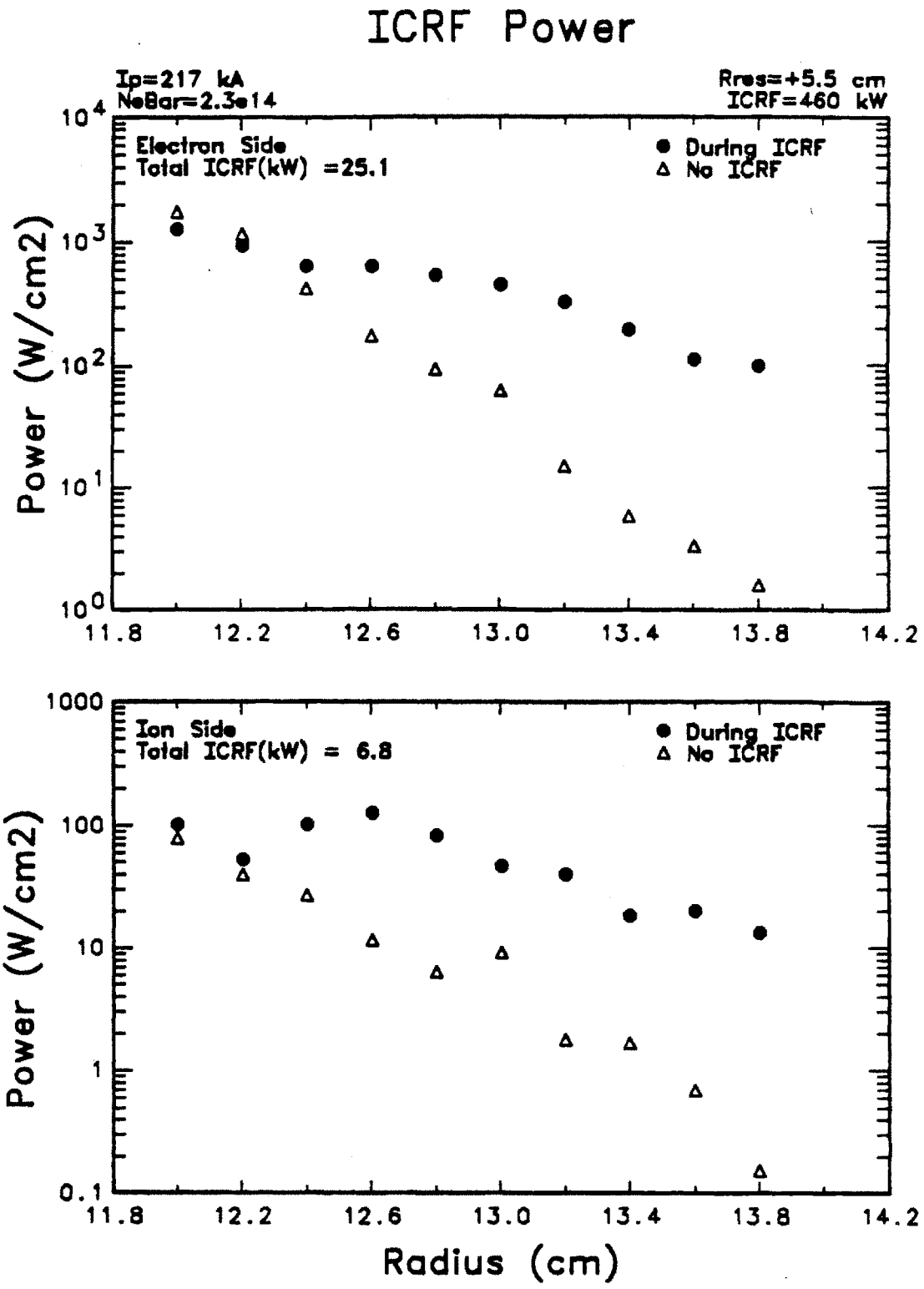

Figure 9.11 The electron and ion side radial $q_{\|}^{total}$ profiles with and without 460 kW of ICRF power.

the total power on both sides still only account for less than 10% of the total injected power, indicating that most of the ICRF power is still deposited in the bulk plasma, probably in the form of large velocity tails[21].

9.2.2 The Fast Wave Experiment with 12.5 cm Limiters

This set of experiments was performed using 12.5 cm molybdenum limiters, so the tip of the Faraday shield is only 0.5 cm away from the limiter edge. The Faraday shields are made of uncoated stainless steel and all the alumina insulators shown in figure 9.2 are in place as sketched. Due to geometrical limitations, Janus can not reach the limiter zone defined in the previous subsection. The majority of the ICRF discharges in this configuration use the minority hydrogen heating scheme with deuterium as the primary fuel species. The toroidal magnetic field strength is typically set at ~ 12 tesla.

Figure 9.12 shows the radial profiles of the electron side and ion side edge parameters with and without ICRF. Once again, the definitions of the symbols are given in figure 9.7. For this set of scans, $\bar{n}_e \sim 2.1 \times 10^{14}$ cm^{-3} and $I_p \sim 290$ kA. When turned on, the fast wave antenna injects between 250-300 kW into the plasma. The temperature profiles behave similarily as the limiter region of the high power experiment discussed previously, staying essentially flat during rf. Comparing the temperature behavior in the antenna zone, the temperature increase here is much less than the 11.5 cm limiter case. However, keep in mind that the antenna edge is only 0.5 cm away from the limiter edge. The density at the antenna edge is thus much larger for the 12.5 cm limiter case. The density difference between the two cases, on both the ion and electron sides, can be as large as an order of magnitude. The densities on both sides drop as the rf is turned on. Unfortunately the antenna can only be pushed to this power limit. Therefore, the rising n_p phenomenon at high power is not observed. There is also no significant floating potential variation.

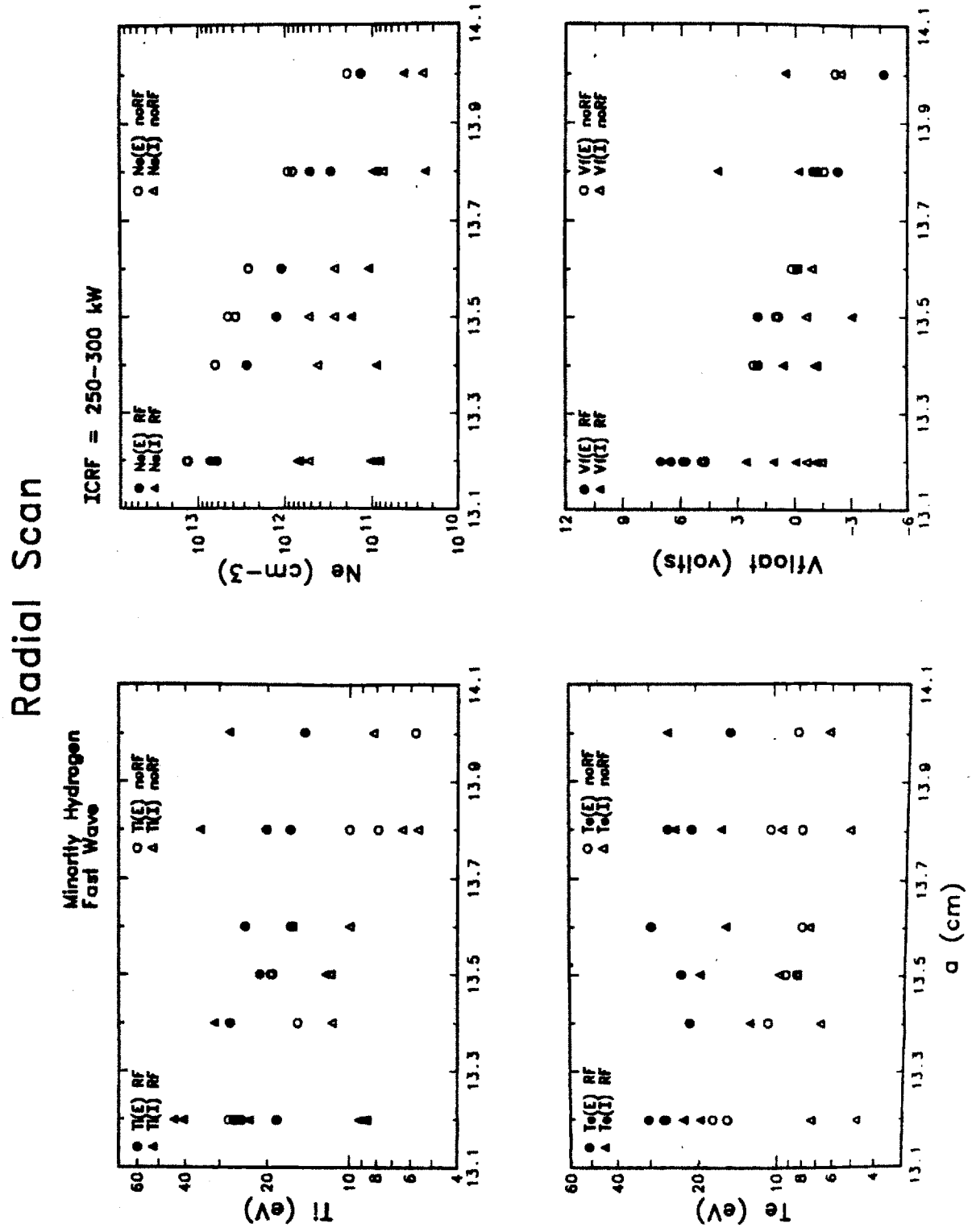

Figure 9.12 Radial profiles of T_i, T_e, n_p, and V_{float} on the electron and ion sides, both with and without ICRF, operating at minority hydrogen heating with 12.5 cm limiters.

Using the previously defined variables of ΔT_e and $(\Delta n_p)/n_p$, we can investigate the effect of various input power level on the edge parameters. Figure 9.13 plots the two functions, on both the electron and ion sides, against total input rf power. Unlike the previous experiments where the ion side change is more dramatic, the changes on both sides are roughly equal. Both ΔT_e and $(\Delta n_p)/n_p$ increase roughly linearly with increasing input power, although the scattering become much larger as the rf power is increased.

9.2.3 Bernstein Wave Experiment

The Bernstein wave experiment used 12.5 cm molybdenum limiters. The antenna itself can be moved radially to maximize the coupling. For most of the time the antenna edge (as defined by the Faraday shield) was $\sim$ 0.5 cm away from the limiter edge. Unfortunately Janus was installed from the side of Alcator C for this experiment, thus direct comparison of the edge parameters between the effects of the Bernstein wave and fast wave antennae can not be made. Furthermore, the Bernstein wave antenna is a quarter loop antenna located 180° away toroidally. Since the edge region is divided by the molybdenum limiters, it is possible that the edge parameter variation is more pronounced in the other half of torus. Typically the Bernstein wave experiment operates in the $1\frac{1}{2}$ harmonic cyclotron resonance of hydrogen.

Figure 9.14 plots the electron and ion side radial profiles of the edge parameters with and without rf. For this set of radial scans the Bernstein wave antenna inputs in $\sim$ 80 kW of power. Several operating regimes are used for the Bernstein wave experiment. For these discharges $\bar{n}_e \sim 8 \times 10^{13}$ cm^{-3} and $I_p \sim 230$ kA. The effect of the Bernstein wave on the edge plasma is not as strong as the fast wave heating scheme. The amount of injected power and the toroidal location of the antenna with respect to Janus may be partially responsible. Both T_i and T_e increases during rf are not as pronounced as the fast

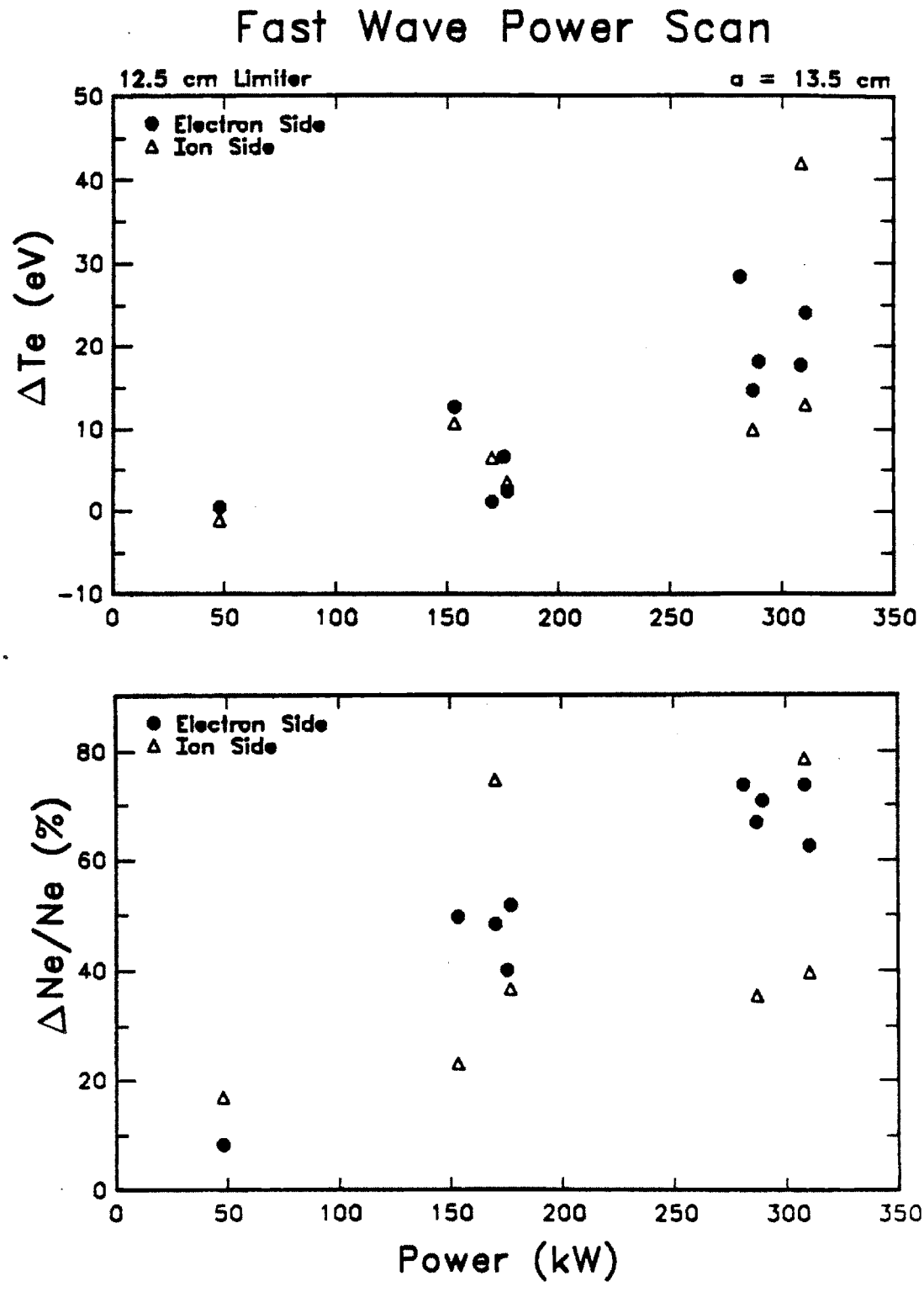

Figure 9.13 Electron side and ion side ΔT_e and $(\Delta n_p)/n_p$ as a function of total injected ICRF fast wave power, operating at minority hydrogen heating with 12.5 cm limiters.

wave cases. n_p drops on both sides when the rf is firing. During rf, slight V_{float} increases on both sides, at all radial positions, are also observed.

The maximum Bernstein wave power level sampled by Janus is only about 120 kW, thus the effect of the power level on the edge parameters is inconclusive. For a limited range of rf power, T_e and n_p appear to increase for increasing rf power.

When the Bernstein wave antenna operates at a particular density regime, i.e. $\bar{n}_e \sim 1 \times 10^{14}$ cm^{-3}, a large $\bar{n}_e$ rise corresponding to the firing of the Bernstein wave antenna is observed, although no increase of gas puffing was programmed. Figure 9.15 shows the $\bar{n}_e$ behavior corresponding to the rf. A trace amount of silicon was injected into the machine both before and during the density rise, and the impurity confinement time can be measured by monitoring the decay of helium-like silicon lines as a function of time[2]. Figure 9.16 plots the time histories of the He-like silicon injected before rf (at t_1) and during rf (at t_2). The impurity confinement time, τ_{Si}, before the density rise, and thus before the onset of the Bernstein wave, was ~ 9 ms. τ_{Si} doubled during the operating period of the Bernstein wave antenna, which, if linking the impurity confinement time scale with the bulk plasma confinement characteristic, would result in the observed increase of the line-averaged central electron density. The total particle flux diffused into the edge region is inversely proportional to the particle confinement time. Therefore, if the central particle confinement is increased, then the reduction of particle flux into the edge region would naturally result in the uniform decrease of edge densities. However, the $\bar{n}_e$ increase is only observed for a very finite operating window. A similar silicon injection experiment performed in conjunction with the fast wave experiment did not show significant impurity confinement time variation.

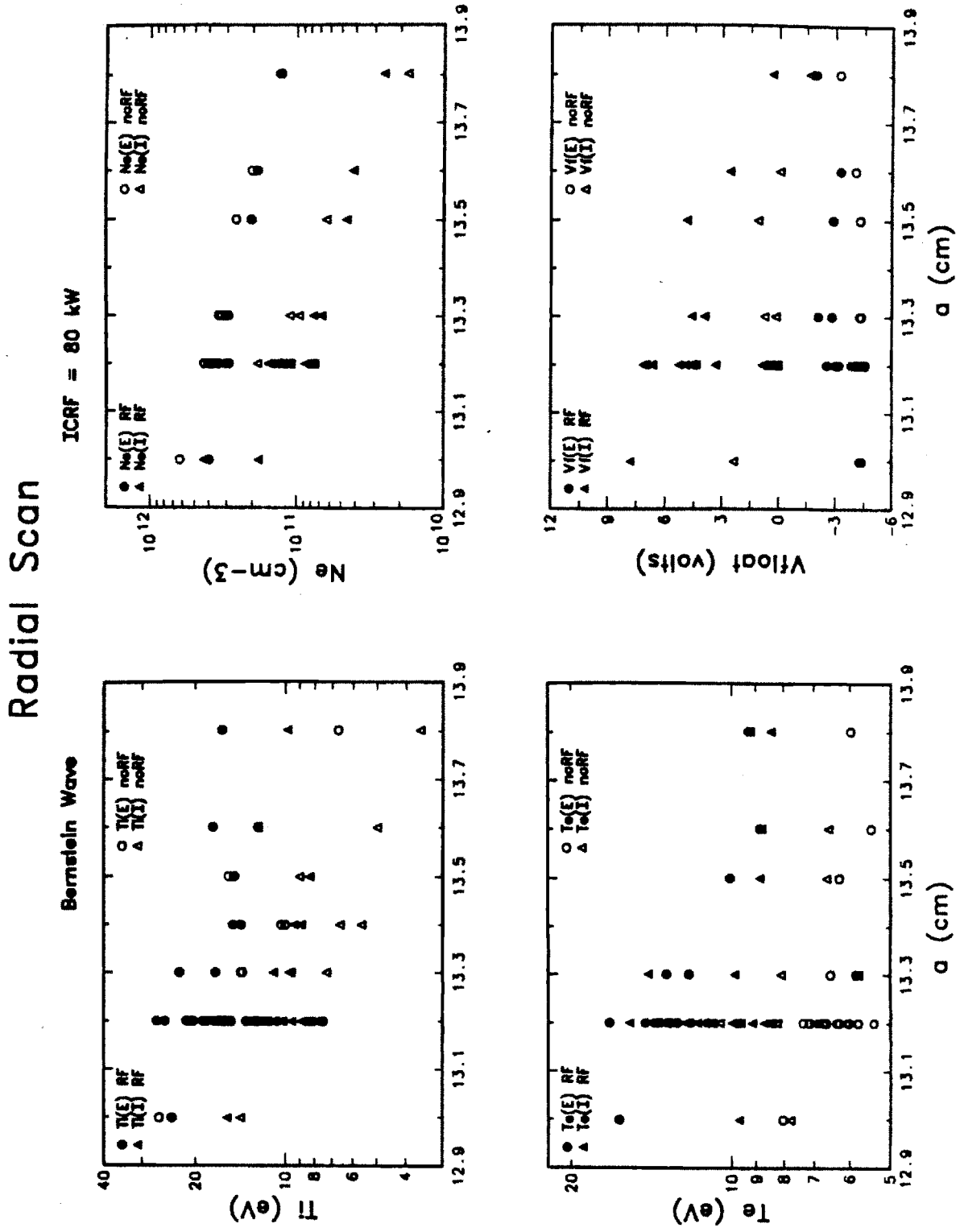

Figure 9.14 Radial profiles of T_i, T_e, n_p, and V_{float} on the electron and ion sides, both with and without ion Bernstein waves, operating with 12.5 cm limiters.

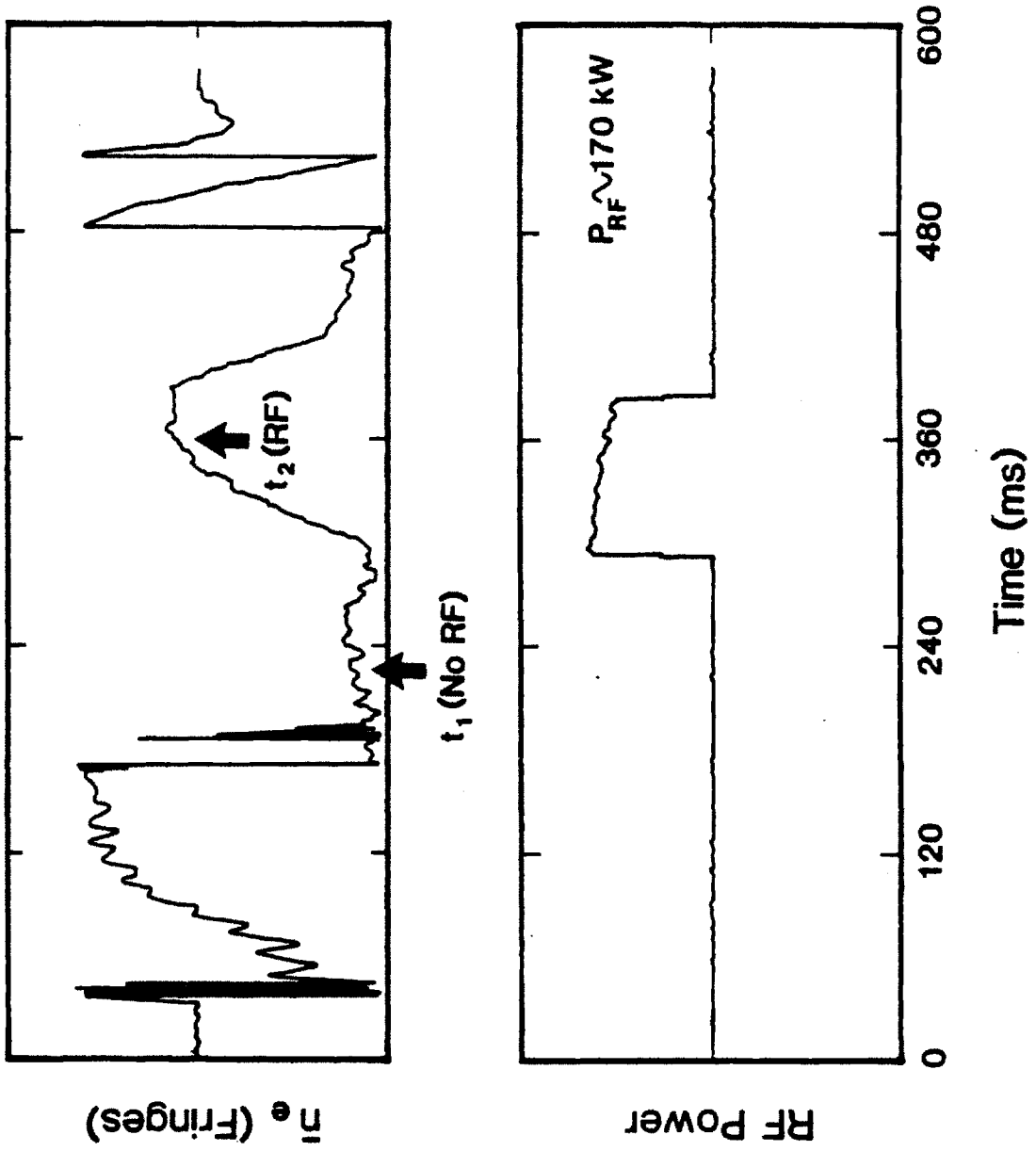

Figure 9.15 Change of $\bar{n}_e$ during Bernstein wave operation.

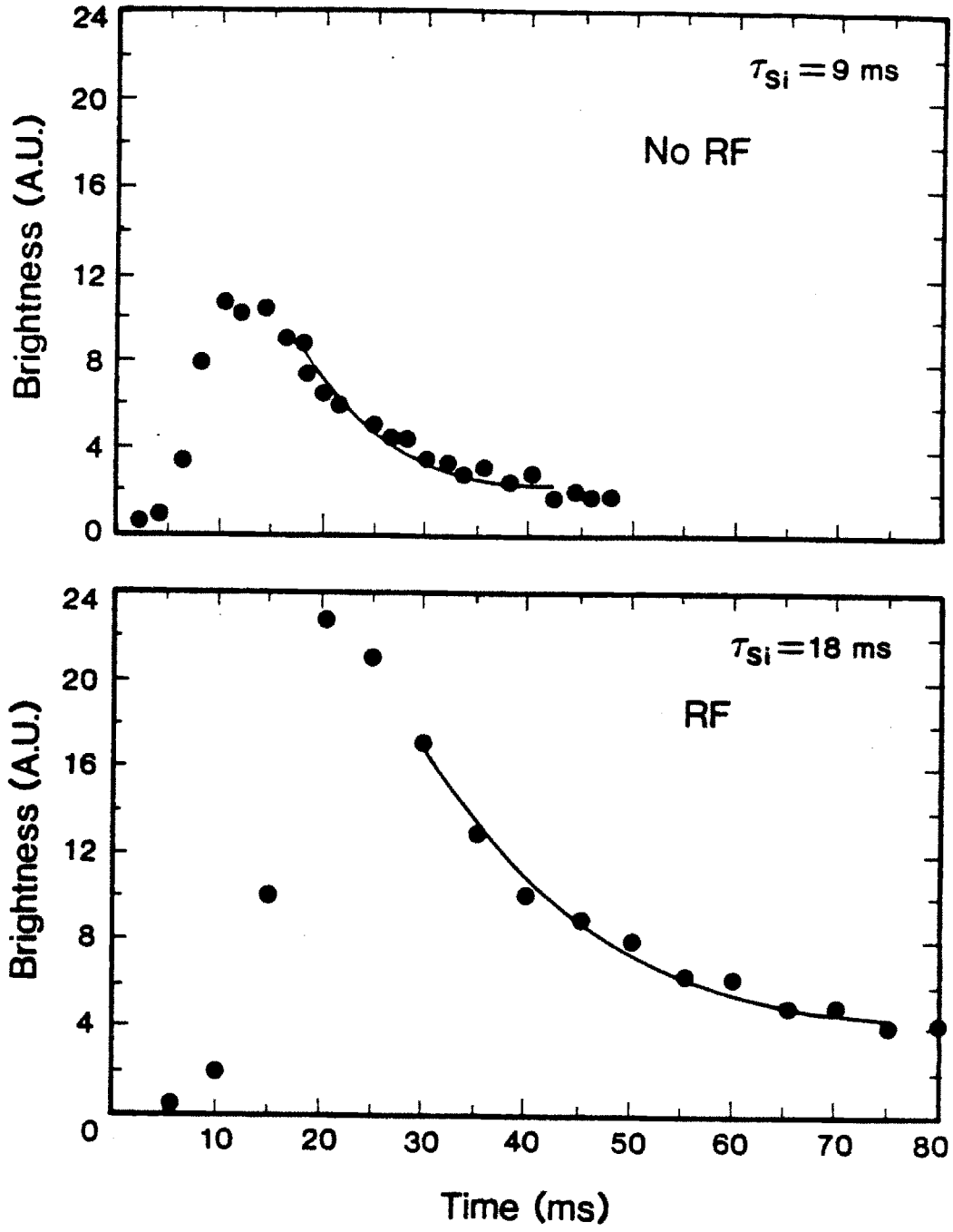

Figure 9.16 τ_{Si} before and during Bernstein wave operation.

9.3 Impurity Release Mechanisms During ICRF

Given the edge variations observed by the Janus diagnostics, it is necessary to correlate the impurity behavior with possible plasma-surface interaction mechanisms. The possible mechanisms dealing with the release of limiter materials are described in Appendix A. These processes include: evaporation, arcing, blistering and flaking, and sputtering due to high energy neutrals, fuel ions, or impurities. Detailed impurity generation mechanisms on Alcator C during lower hybrid heating[5] and ion cyclotron heating[3] have been previously investigated.

Blistering and flaking can be eliminated right away since their time behavior for the impurity releases would be erratic, unlike the consistent nature of the observed impurity radiation. Evaporation is also unlikely since the calculated heat load to the surfaces is too small to account for the quantity of impurity released. Furthermore, the time response of the impurity variation corresponds very well with the on/off of the antenna. Such behavior would not be possible if the nature of the impurity release mechanism is associated with the thermal loading on the material surfaces since the cooling time for either the antenna or the limiters would be much longer than the observed impurity decay time scale.

Arcing between the antenna and the vacuum vessel can be eliminated since visual inspection of the antenna surfaces did not reveal any arc tracks. Furthermore, the antenna design includes an arc detector such that the antenna would shut down upon the detection of an arc between the antenna and the vacuum chamber. However, the possibility of many unipolar arcs between the antenna and the plasma cannot be ruled out. Unipolar arcs can form when high T_e causes a sufficiently negative sheath potential such that cathode spots are initiated. The arcs can be sustained as long as the cathode spots are maintained by the deposited electrons.

The most likely cause of the impurity increase is due to physical sputtering, which is directly proportional to the energies and masses of the striking neutrals

or ions. During rf, large increases of both T_i and T_e are observed. T_i figures directly into the ion energy increase. T_e can be related to the increase in the sheath potential, V_{sheath}. Therefore, when an ion enters the sheath region, it would pick up an amount of energy equal to $q_i V_{sheath}$, where q_i is the ion charge state. The possible generation of a strong reactive field near the antenna[10] has also been proposed as an ion acceleration mechanism in place of V_{sheath}. If large quantities of highly charged impurities are present in the edge region, then the impurity energy striking the material surface would be further increased due to the large q_i. Neutral sputtering could also contribute to the impurity release mechanisms. From charge exchange measurements[21], large ion tails are generated during ICRF. When charge exchanged, the neutrals would possess very large energies ($\sim 1 - 10$ keV) such that neutral sputtering could also be important. However, neutral induced sputtering would not explain the fact that larger iron impurities were observed for the noncoated Faraday shield experiments since neutrals have no preferential sputtering location.

A previous study[3] of ICRF generated impurities on Alcator C revealed a roughly linear increase of iron brightness as a function of RF power. Similar trends have been observed in more recent experiments[19]. In addition, the edge temperatures also increase as a function of rf power. For the 11.5 cm limiter case, with fast wave heating, there appears to be some direct heating to the edge species in the antenna zone. This evidence suggests that the dominant impurity release mechanism at both the limiter and antenna surfaces is likely to be due to physical sputtering. Due to the higher mass of molybdenum over iron, the sputtering yield of hydrogen on stainless steel is about an order of magnitude greater than that of molybdenum. This and the larger temperature change in the antenna zone may help explain the relative magnitude of iron increase during ICRF.

Using an edge erosion code[22], which calculates the thermal sputtering rates, and heating, evaporation/sublimation rates, we can model the time behavior of

the impurities by incorporating the edge plasma parameters and the physical properties of the exposed material. The total sputtering yield includes contributions from both the fuel ions and partially stripped impurities. The code was used to model the previous ICRF experiment[3] and predicts negligible evaporation yields. Modelling the physically sputtering yields, the results agree with the observed impurity behaviors qualitatively, and within a factor of 2, quantitatively.

References

[1] McCracken, G. M., Stott, P. E., "Plasma-Surface Interactions in Tokamaks," *Nucl. Fusion* **19**, 889 (1979).

[2] Terry, J. L., private communication (1986).

[3] Manning, H. L., Terry, J. L., Lipschultz, B., LaBombard, B., Blackwell, B., Fiore, C., Foord, M., Marmer, E. S., Moody, J., Parker, R. R., Porkolab, M., Rice, J., "Impurity Generation During ICRF Heating Experiments on Alcator C," M.I.T. Plasma Fusion Center Report PFC/JA-86-17 (March 1986).

[4] Manning, H. L., "Grazing Incidence Spectroscopy Measurement of ICRF Generated Impurities on Alcator C," Harvard Doctoral Thesis (May 1986).

[5] Lipschultz, B., LaBombard, B., Manning, H. L., Terry, J. L., Knowlton, S., Marmer, E. S., Porkolab, M., Rice, J., Takase, Y., Texter, S., Wan, A., "Impurity Sources During Lower-Hybrid Heating on Alcator C," M.I.T. Plasma Fusion Center Report PFC/JA-85-45 (Dec. 1985).

[6] TFR Group, Sand, F., "ICRF Heating Experiments in TFR Using a Low-Field-Side Antenna," *Nucl. Fusion* **25**, 1719 (1985).

[7] Stratton, B. C., Moos, H. W., Hodge, W. L., Suckewer, S., Hosea, J. C., Hulse, R. A., Hwang, D. Q., Wilson, J. R., "Changes in Impurity Radiation During ICRF Heating of PLT Tokamak Plasmas," *Nucl. Fusion* **24**, 767 (1984).

[8] Suckewer, S., Hinnov, E., Hwang, D., Schivell, J., Schmidt, G. L., et al., *Nucl. Fusion* **21**, 981 (1981).

[9] Kimura, H., Matsumoto, H., Odajima, K., Konoshima, S., Yamamoto, T., et al., in *Plasma Physics and Controlled Nuclear Fusion Research*, Proc. 9th Int. Conf., Baltimore (1982), Vol. 2, IAEA, Vienna, 113 (1983).

[10] Ogawa, H., Odajima, K., Ohtsuka, H., Matsumoto, H., Kimura, H., et al., *J. Nucl. Mat.* **128 & 129**, 298 (1984).

[11] Noda, N., Watari, T., Toi, K., Kako, E., Sato, K., et al., *J. Nucl. Mat.* **128 & 129**, 304 (1984).

[12] Cohen, S. A., Bernabei, S., Budny, R., Chu, T. K., Colestock, P., et al., *J. Nucl. Mat.* **128 & 129**, 280 (1984).

[13] deChambrer, A., Collins, G. A., Duperrex, P.-A., Heym, A., Hofmann, F., "Effect of rf Heating on Edge Parameters in the TCA Tokamak," *J. Nucl. Mat.* **128 & 129**, 310–316 (1984).

[14] Shepard, T. D., Besen, M., McDermott, F. S., Parker, R. R., Porkolab, M., "A Matched Fast Wave Coupler for the Alcator C ICRF Heating Experiment," *Bull. Amer. Phys. Society* **30**, paper 5Q10, 1495 (1985)

[15] Moody, J. D., McDermott, F. S., Porkolab, M., Parker, R. R., Besen, M., Takase, Y., Alcator C Group, "The Alcator C Ion Bernstein Wave Heating Experiment," *Bull. Amer. Phys. Society* **30**, paper 5Q9, 1495 (1985).

[16] Blackwell, B., Besen, M., private communication (1984).

[17] Manning, H. L., Terry, J. L., private communication (1986).

[18] Porkolab, M., Blackwell, B., Bonoli, P., Griffin, D., Knowlton, S., et al., "Lower Hybrid Heating and Current Drive, and Ion Cyclotron Heating Experiments on the Alcator C and the Versator II Tokamaks," in *Plasma Physics and Controlled Nuclear Fusion Research*, Proc. 10th Int. Conf., London (1984).

[19] Shepard, T. D., Manning, H. L., private communication (1986).

[20] Messiaen, A. M., Koch, R., Bhatnagar, V. P., Vandenplas, P. E., Weynants, R. R., in *Heating in Toroidal Plasmas*, (Proc. 4^{th} Intl. Sympos., Rome, 1984), Vol. I, Intl. School of Plasma Physics, Varenna, 315 (1984).

[21] Fiore, C., private communication (1986).

[22] Lipschultz, B., private communication (1986).

CHAPTER 10

Summary

An important issue in designing future fusion devices is the role played by the edge plasma. Present understanding of the behavior of edge plasma is very limited. The focus of this thesis is to experimentally investigate the relevant ion and electron parameters in the edge, or scrape-off region of the Alcator C tokamak. The issues addressed in this thesis include the development and application of an edge diagnostic capable of monitoring the relevant edge plasma parameters. The observed edge phenomena are explained using simple, heuistic arguments. During ICRF heating, measured edge parameters can be correlated with plasma-surface interaction mechanisms in conjunction with spectroscopic observations of impurity behaviors.

10.1 Conclusions

The instrument used to study the edge ion and electron parameters, denoted as Janus, is a bi-directional, multi-functional plasma diagnostic. Janus is designed to measure most of the relevant edge parameters simultaneously along both directions of a field line. The two sides are defined by the direction of the plasma current, and are labelled as the electron and ion sides. On each side of Janus there is an identical set of three diagnostics: a Langmuir probe, a calorimeter, and a retarding-field energy analyzer (RFEA). All Janus components are designed to withstand high heat fluxes. The probe head is detachable to allow for easy maintenance. Physically, Janus is a "large" probe such that the probe's perturbing length is longer than the connection length to the next limiter surface. Therefore, the edge parameters measured by Janus are not equal to the unperturbed plasma parameters, but rather they reflect the averaged characteristics of the plasma within the sampling flux tubes.

The RFEA measures the parallel energy distributions of the ions and electrons. A typical RFEA requires a narrow entrance slit, at least two biasable grid electrodes, and a collector. The slit must be shaped like a knife edge to maximize transmission, be narrow enough to maintain a continuous sheath across the opening, and tough enough to withstand high incident heat fluxes. The grid design must consider space charge limitation, Debye-shielding, and nonperturbing transmission characteristics. The transmission characteristics for both the slit and the grids were examined using a 3-D Monte-Carlo, true orbit particle following code and, for the operating regime of Janus, found to exhibit little dependence on the particle energetics, analyzer geometry, and biasing schemes. Using a programmable function generator, the Janus RFEA can be alternatively biased to allow for measurements of both the electron and ion distribution functions during the same discharge. Both distribution functions follow closely the expected Maxwellian form. From these distributions, values of the ion and electron temperatures can be inferred. An energy shift in the integrated ion current corresponds to the potential difference between the unperturbed plasma and the RFEA entrance slit. Density measurements are difficult to obtain due to uncertainties in the particle transmission coefficients at the grids.

The Langmuir probe is used to measure the electron temperature, plasma density, and floating potential. The Langmuir probe protrudes out of the Janus housing and is aligned normal with respect to magnetic field lines. The electron temperature measurement is obtained by using a simple Langmuir probe theory which fits only the exponential portion of the probe characteristic. T_e obtained by this Langmuir probe analysis agrees well with the value obtained by the RFEA. T_e obtained by using a more complete magnetized probe theory which accounts for the perturbing effect of the probe size yields a lower value as compared with both the RFEA measured T_e and the exponential fitted T_e. A difference of $\sim 30\%$ is commonly observed.

The calorimeter is designed to measure the total parallel heat flux incident

on an electrically floating plate. Measurements of the parallel heat flux indicate much lower total sheath transmission coefficients than those predicted theoretically. Uncertainties due to the energy reflection coefficient and the 3-D thermal transport effect need to be resolved in order to measure accurately the total heat flux. The calorimeters are also plagued by pickup problems.

Using Janus we conducted a detailed, localized investigation of the plasma in the scrape-off region. The relevant edge parameters include the electron side and ion side ion temperature from the retarding-field energy analyzers, and T_e, n_p, V_{float} measurements from the Langmuir probes. During the tenure of Janus, three different limiter geometries and various operating conditions were employed. The operating parameters studied include line-averaged central electron density, plasma current, magnetic field magnitude and direction (with respect to I_p), and plasma positions. Furthermore, Janus could be scanned in the minor radial direction in order to study the spatial profiles of the edge parameters.

The parameter $\bar{n}_e/I_p$ is found to be an appropriate scaling variable for the edge parameters. To some extent, the effect of increasing central density offsets some of the effect of increasing plasma current. Using 16.5 cm limiters, at $\bar{n}_e/I_p \geq 6 \times 10^{11}$ cm^{-3}/kA, the edge temperatures and densities both drop appreciably. This threshold matches the Marfe threshold found by LaBombard and Lipschultz. The threshold increases as the limiter radius is decreased.

The measurements on the two sides of Janus revealed strong directional asymmetry. The asymmetry is most strongly influenced by the magnetic field direction and plasma in-out positions. Normally $\underline{B}_t$ is aligned antiparallel with respect to $\underline{I}_p$. In this configuration the asymmetry favors larger temperatures and densities on the electron side. The asymmetry grows stronger as Janus approaches the limiter edge. The radial dependence of the asymmetry reverses when $\underline{B}_t \parallel \underline{I}_p$. Near the limiter radius the ion side parameters dominate despite a shorter connection length. For normal magnetic configurations, shifting plasma

position toward the strong field side also forces the asymmetry to grow in favor of the electron side.

The magnitude of directional asymmetry can not be explained by the connection length alone, although simple modelling shows that the shift in plasma position could affect the asymmetry through connection length variation near the limiter edge. A poloidal Langmuir probe array measured strong poloidally asymmetric densities and T_e. Poloidal asymmetric diffusion into different (electron and ion sides) flux tubes would magnify the asymmetry but fails to account for the radial dependence of the asymmetry. Lack of flow velocity measurements and supporting theory leaves the parallel flow as a possible but not verified mechanism of generating the observed directional asymmetry.

Ion temperature is always found to equal or exceed the electron temperature. Comparison between the equipartition time scale and time scales associated with other energy loss or gain mechanisms indicates weak ion and electron energy coupling in the scrape-off region of Alcator C. For all limiter configurations studied, at ~ 1 cm into the limiter shadow, the T_i/T_e ratio varies from 1.5 to 3 on both the electron and ion sides for low values of $\bar{n}_e/I_p$. The ratio reduces toward 1 as $\bar{n}_e/I_p$ increases. Typically the T_i profile is steeper than the T_e profile, so that the T_i/T_e ratio increases as Janus approaches the limiter radius.

The electron and ion temperature profiles are different as the result of weakly coupled energy transport mechanisms in the scrape-off region. Detailed energy balance in the scrape-off region is difficult due to unknown neutral and impurity concentrations and spatial profiles. For both ions and electrons, the gain mechanisms are dominated by perpendicular convection and conduction from the bulk plasma, and the loss mechanisms are dominated by parallel convection to the limiter surfaces and parallel compression in the presheath region. Assuming the formation of the sheath potential, large $\chi_\perp/D_\perp$ ratios are necessary for balancing both the ion and electron energy equations. $\chi_\perp/D_\perp$ for the electrons are greater than the ions to satisfy the requirement of maintaining the sheath

potential. Charge exchange, electron impact ionization, and radiation processes serve as the adjustment terms for the ion and electron energy equations. They also determine the necessary neutral and impurity densities at different spatial locations. Using the parallel convection term to model the loss and assuming that the spatial profiles of the temperatures and densities stay exponential, the total energy deposited into the edge region is found to exceed the total ohmic input power. Poloidal and spatial profile adjustments are needed to properly determine the total deposited edge power.

Large quantities of high-Z impurities were observed during both ion Bernstein wave and ion cyclotron fast wave heating experiments. For fast wave experiments using 11.5 cm limiters, radial profile measurements at low rf power indicate direct edge heating in the region immediately adjacent to the antenna. Localized particle sources in the antenna zone, possibly due to increasing ionization or desorption, are also observed. Near the limiter radius the edge density drops during rf. The strong edge heating is extended beyond the antenna region, into the limiter region (between the antenna and the bulk plasma), when the injected rf power is increased. Simple energy accounting for both the limiter and antenna regions show little or no power deposited into the edge region at low power due to a stronger density decrease as compared with the temperature increase. At the high power level, $< 10\%$ of the total ICRF power can be accounted for in the edge region. Similiar edge heating and density decreases were found for Bernstein and fast wave experiments using 12.5 cm limiters. For a specific operating window, at $\bar{n}_e \sim 1 \times 10^{14}$ cm^{-3} and $I_p \sim 260$ kA, a large central density increase was observed during Bernstein wave operation without increased fueling. Spectroscopic measurements of He-like silicon time histories show a factor of two increase in impurity confinement time during rf. However, no similar confinement time increase was observed for other operating regimes.

The impurity increase is most likely caused by increased physical sputtering due to the temperature increase. Unipolar arc is another possibility but visual

inspection of the antenna surfaces failed to show any evidence of arc tracks. Evaporation is unlikely due to insufficient temperature rise at the material surfaces and the rapid decrease of impurity concentration upon the termination of the rf pulse. Blistering and flaking have erratic release behaviors, which do not match the spectroscopically observed time histories of the impurity radiation. The edge erosion code used to model previous ICRF experiments also points to sputtering as the dominant impurity release mechanism.

10.2 Suggestions for Future Work

The application of Janus to study the edge parameter variations for different operating conditions has uncovered many edge phenomena that cannot be satisfactorily explained without further experimental verification. The fundamental issue concerns the relationship between the Janus measured parameters and the actual plasma parameters without the probe being present. Due to the dimension of Janus, the probe is a "perturbing," or large probe. The only theory developed for interpreting the large probe data is not valid for the typical operating regime of Alcator C. Without proper interpretation of valid large probe theory, the parameters measured by Janus only reflect the averaged values of the plasma within the sampling flux tube.

To determine the perturbing effect of the large probe, it is desirable to have a separate scannable, nonperturbing probe, such as a simple Langmuir probe, positioned in front of the large probe. Then with the large probe present, the nonperturbing probe can scan, along the minor radius, from a perturbing region into the shadow of the large probe, to a unperturbed region beyond the large probe. Such a radial profile would help resolve the question regarding different transport processes at different regions.

The diagnostics within the Janus package can also be modified to allow the probe to become a more versatile and powerful instrument. A simple upgrade

of the RFEA could be achieved by employing multiple slits and corresponding collectors located at different radial locations. The grid electrodes can be shared by all slit-collector combinations. The only restriction of the design would be the ability to machine the tightly spaced slits. The slits and the collectors must be separated by at least a couple of gyroradii so the signals at different radial positions would not be mixed up. The power supplies for the grid electrodes must be able to deliver high power and high voltage since power supply saturation has already been observed in some cases for the present single slit design. The employment of such a multi-positional RFEA would enable us to map out a radial profile of the edge parameters without moving the probe, which will also add another piece to the missing information regarding the large probe effect.

The major disappointment of the Janus experiment is the failure of the calorimeters to operate consistently and reliably. The initial design guideline for the calorimeter plate did not include the energy reflection characteristics of the plate material. A better choice for the calorimeter plate would be carbon. Then the thermocouple could be attached to the back of the plate by using special vacuum compatible epoxy. It would also be desirable to attach a third, biasable lead to the calorimeter plate. Then the biasable calorimeter would be able to measure the contribution of a specific portion of the particle distribution function.

Observation of directional asymmetry leads to the question of the possible existence of parallel flow. Knowledge of the magnitude of the flow velocity and its spatial variations would also enable us to determine the relative importance of the viscosity contribution in the ion and electron energy equations. In Chapter 7 possible mechanisms of generating parallel flow have been proposed. To measure the parallel flow velocity experimentally, nonperturbing, bi-directional Langmuir probes can be employed. The flow velocity can be determined by the ratio of the parameters on the two sides. Unfortunately, parallel flow theory is still in the developmental stage. Another alternative in measuring the parallel flow would

be to use spectroscopic techniques. By focusing the viewing angle along a field line, flow velocity can be inferred by measuring the Doppler broadening of a specific impurity line. Such a technique has been successfully employed in fusion devices to measure poloidal rotation.

The primary function of Janus is to measure the edge ion and electron parameters. However, as uncovered in Chapter 6, the impurity and neutral concentrations and spatial profiles could contribute toward the ion and electron energy balances. Furthermore, knowledge of the quantitative behaviors of the neutral and impurity species would help us understand the mechanisms of plasma-surface interactions and edge atomic and molecular processes. The impurity parameters can be monitored by using spectrometers or surface deposition probes. Previous attempts at using a low-energy neutral time of flight energy analyzer were not successful due to large background noises. Efforts in monitoring the edge neutral and impurity parameters should be continued and intensified since they play a vital part in both the edge and bulk plasma behaviors.

APPENDIX A

Recycling and Impurity Release Mechanisms

In either limiter or divertor-controlled plasma discharges, the edge region is where plasma first intersects a solid material surface. As the result of plasma-surface interactions, particles are released from the solid into the edge plasma region. There are three separate catagories of plasma-surface interaction mechanisms: recycling, low-Z, and high-Z impurity release. An excellent review is given by McCracken and Stott[1]. These three mechanisms are now discussed in turn.

A.1 Recycling

Recycling includes all processes which allow a fuel ion incident on a material surface to return to the edge plasma. The released ions could come from two different catagories, from either the trapped gas already in the solid or backscattering of the original incident ions.

As ions or neutrals strike a solid material, they experience a series of elastic and inelastic collisions. A certain fraction of the particles, R_p, incident on the solid is released, or *backscattered*, back into the edge plasma region, carrying away a certain fraction of energy, R_E. R_p and R_E are functions of the reduced energy ϵ_E, where

$$\epsilon_E = \frac{a_0 m_2 E}{e^2 (m_1 + m_2) Z_1 Z_2 \sqrt{(Z_1^{\frac{2}{3}} + Z_2^{\frac{2}{3}})}}, \qquad (A.1)$$

and Z_1, m_1 and Z_2, m_2 are the mass and charge numbers of the incident ion and target atom respectively , $e = 1.6 \times 10^{-19}$ coulomb, a_0 is the Bohr radius, and E is the incident ion energy. Therefore, R_p and R_E increase as E decreases and m_2

increases. However, as E is reduced below 1 keV, the backscattering coefficients become very difficult to measure[2,3]. These values can only be obtained by using computational models. For hydrogen incident on molybdenum, typical values are $R_p \sim 0.4$ and $R_E \sim 0.3$. For tungsten, $R_p \sim 0.8$, and $R_E \sim 0.6$. Furthermore, in a magnetized environment, plasma is gyrating about magnetic field lines and can, on average, have an oblique incident angle with respect to the surface[4]. The reflection coefficients increase as the incident angle deviates away from normal or 90° incident angle.

The incident particles that are not backscattered will slow down and become *trapped* in the solid. Once implanted, particles can diffuse within the solid and be reemitted when they reach the solid surface. The rate of reemission depends on the types of trapped particles, and also on the condition of the solid such as temperature and degree of damage. Hydrogen has a high diffusion coefficient in metals, even at room temperature. Increased solid temperature will enhance diffusion.

Ion impact can also affect particle recycling. The detailed mechanism is not fully understood, but in practice the rate of recycling can be quite well described by cross sections. The ion-induced detrapping cross section does not strongly depend on the solid temperature, but it does vary for different target solids. Typically the cross section peaks at around 5-10 keV and decreases sharply as the incident energy is decreased and a more gradual change is seen as the energy is increased.

The backscattered particles are principally neutrals, carrying away a fraction of the original incident energy equal to R_E. Compared to the reemitted neutrals, the backscattered particles possess much higher energy and will travel further back toward the bulk plasma region before ionization or charge exchange. A detailed description of the plasma-neutral interactions is given in Appendix B.

A.2 Low-Z Impurity Release Mechanisms

The low-Z impurities arise from the release of low-Z gases, such as oxygen, carbon, and nitrogen, that are previously adsorbed on the solid surface. These gases can be adsorbed on surfaces by a variety of mechanisms, including the low-binding-energy ($\sim$ 0.5 eV) Van der Waal's forces, more strongly bound (several eV) chemical forces, or by trapping at imperfect sites within the solid. The impact of low-Z impurities on the bulk plasmas is described in Chapter 1. Low-Z impurities can be released by a range of desorption processes which include: thermal, particle, and chemical mechanisms.

The rate of thermal desorption can be described as

$$\frac{dc(t)}{dt} \propto e^{-E_b/kT}, \qquad (A.2)$$

where c is the concentration of the low-Z impurity, E_b is the binding energy, and T is the solid temperature. A large fraction of the weakly bound particles can be baked out to reduce the low-Z impurity concentration during experiment. During the experiment, thermal desorption is believed to play a minor role in the release of low-Z impurities.

Particle desorption includes desorption due to the bombardment of energetic ions and neutrals, electrons, and photons. For ion and neutral bombardments, the desorption mechanism depends on many parameters, including particle flux, incident particle mass, energy and incident angle, and the concentration and binding energy of the impurity. From a simplistic point of view, ion and neutral-induced desorptions are the direct result of momentum transfer from the incident particles to the trapped particles, causing the detrapping of low-Z impurities which can diffuse through the solid lattice and be reemitted. Glow discharge cleaning is just an extension of this type of desorption process.

Electrons, due to their light mass, have insignificant impact on momentum transfer. However, they can excite the atoms or molecules into unbound states, which are repelled from the surface. Photon-induced desorption is just an extension of the electron-induced desorption. Photoelectrons are produced in the first stage of the process before the electron excitations take place.

Low-Z impurities such as carbon and oxygen are very susceptible to chemical reactions with incident ions or atoms, leading to the formation of more weakly bound molecules. The molecules can then be more readily desorbed. This mechanism is also referred to as chemical sputtering. For limiters made of low-Z materials such as carbon and silicon, the chemical desorption mechanism can play a dominant role in the release of limiter materials over other processes that will be described in the next section.

A.3 High-Z Impurity Release Mechanism

The high-Z impurities are either wall or limiter materials. Their release mechanisms are different than the two previously described mechanisms, and include processes such as evaporation and thermal shocks, sputtering, arcing, and blistering. For a reactor regime plasma, the control of high-Z impurities is crucial in reducing the radiative energy losses which would quench an otherwise ignited plasma. Even for present day experiments, radiation can play an important role in the overall energy balance of bulk plasma[6], especially during rf heating experiments[7,8].

A.3.1 Evaporation and Thermal Shock

Evaporation and thermal shocks arise from surface heating due to the plasma heat flux deposited on the material surface. The evaporation rate can be described as

$$\frac{dc(t)}{dt} \propto \frac{\alpha\, p_0}{\sqrt{A\,T(t)}}\, e^{-\Delta H_{sub}/kT(t)}, \qquad (A.3)$$

where c is the concentration, α is the sticking coefficient of the atom at the surface, A is the atomic number, T is the surface temperature, p_0 is a constant associated with the vapor pressure of the solid, and ΔH_{sub} is heat of sublimation of the evaporated material. The higher the melting of a material, the higher the ΔH_{sub} will usually be.

The surface temperature rise corresponding to an incoming heat pulse depends largely on the material's thermal properties. During the plasma discharge, the time scale of the heat pulse is short ($\sim$ 100 ms) in comparison with the thermal decay time which is on the order of seconds. Therefore the solid surface could heat up to high temperatures which would cause evaporation. From equation (A.3), the characteristic of evaporation-induced impurities release is approximately exponential. Therefore evaporation can be monitored by using spectrometers looking at the time behavior of the impurities in question.

A.3.2 Sputtering

Physical sputtering is predominantly a momentum transfer process. When an energetic ion or neutral strikes a solid it produces a collision cascade by collisions with the lattice atoms. Sputtering takes place when this cascade results in a surface atom receiving enough energy to exceed its binding energy and escape. The sputtering yield is inversely proportional to the material's sublimation

energy and directly proportional to the energy transferred from the incident particle to the lattice atoms. Therefore the sputtering yield is larger for low melting point materials and for low mass incident particles such as hydrogen and helium.

Theoretically there is a general sputtering energy threshold E_{limit} below which insufficient energy is transferred to the lattice atom for sputtering to take place:

$$E_{limit} = \frac{E_{sub}}{\gamma_r(1-\gamma_r)}, \qquad (A.4)$$

$$\text{where } \gamma_r = \text{reduced mass}$$

$$\equiv \frac{4m_1m_2}{(m_1+m_2)^2}. \qquad (A.5)$$

m_1 and m_2 are as defined in section A.1. For molybdenum, the threshold energies are 176 eV, 94 eV, and 53 eV for incident hydrogen, deuterium, and helium respectively. Above the threshold the sputtering yield increases roughly linearly with energy, but reaches a maximum in the range of 1-10 keV (for light ions) and slowly decreases above 10 keV. The sputtering yield is also dependent on the incident angle. This can be tied to the angular dependence of the particle and energy reflection coefficients previously discussed.

In the edge region of tokamaks, material in contact with the plasma will develop a sheath potential in order to balance the incident ion and electron fluxes. Along the field line, this potential is negative due to the electron's high mobility. Section 2.1 gives a simple review of the physics behind the formation of a stable sheath. Since ions dominate the sputtering process, the negative sheath will further accelerate the ions toward the material surface, increasing the sputtering yield.

When the sputtered particle is ionized and returns to the material, this process, called *self-sputtering*, can cause further sputtering. Since the wall par-

ticles are usually high-Z, and thus highly ionized, a high-Z impurity particle can pick up a large quantity of energy as it accelerates through the sheath potential. Therefore a very small impurity concentration may lead to a runaway situation where the sputtering yield exceeds 1. It is conceivable that impurity self-sputtering may be more important than the sputtering caused by fuel particles.

A.3.3 Arcing

Arcing can occurs between the plasma and the material surface when the local potential difference exceeds the requirement to sustain an arc. This potential difference can arise from sufficiently high electron temperature which increases the negative sheath potential. When a cathode spot is initiated on the material surface, strong local electron emission will reduce the sheath potential so more electrons can reach the surface, setting up a circulating current. The arc is sustained as long as the hot cathode spot can be maintained by the deposited electrons.

The amount of material removed as the result of arcing is directly proportional to the charge transfered. The erosion rate is highest for metals of low melting point and low thermal conductivity. A typical erosion rate for molybdenum is approximately 0.05 atoms/electron.

A.3.4 Blistering

When a material is subjected to a large dose of incident ions, and the range of the ion implantation, R_m, is large while the sputtering yield, S_{yield}, is small, *blistering* can occur when a large concentration of gas is built up near the surface, causing pieces of surface material to break off and fall into the plasma. The occurrence of blisters is primarily due to light ions such as hydrogen

and helium. The exact mechanism of blistering, however, is still subject to controversy. Current theories contend that blistering is either gas-pressure driven or due to differential expansion of the implanted layer due to radiation damage.

There is a critical dosage for blistering, D_c, proportional to

$$\frac{D_c}{n_l} < \frac{R_m}{S_{yield}}, \qquad (A.6)$$

where n_l is the atomic density of the lattice. Below D_c essentially all incident ions are trapped in the surface and blistering yield is low. A large chunk of material may be released into the plasma as the result of blistering. The diameter of the blisters, d_b, increases with incident particle energy. In many cases, the blister thickness, t_b is also found to increase as d_b increases.

References

[1] McCracken, G. M., Stott, P. E., "Plasma-Surface Interactions in Tokamaks," *Nucl. Fusion*, **19** 7, 889 (1979).

[2] Eckstein, W., Verbeek, H., Max-Planck Institute Report IPP 9/32 (August 1979).

[3] Ito, R., Tabata, T., Itoh, N., Morita, K., Kato, T., Tawara, H., "Data on the Backscattering Coefficients of Loght Ions from Solids (a Revision)," Institute of Plasma Physics (Nagoya University) Report No. IPPJ-AM-41.

[4] Knize, R. J. "Plasma Particle and Energy Reflection at a Wall with an Obliquely Incident Magnetic Field," *Nucl. Fusion* **25**, 1498 (1985).

[5] Tabata, T., Ito, R., Itikawa, Y., Itoh, N., Morita, K., Tawara, H., "Dependence of the Backscattering Coefficients of Light Ions upon Angle of Incidence," Institute of Plasma Physics (Nagoya University) Report No. IPPJ-AM-34.

[6] Pickrell, M., "The Role of Radiation on the Power Balance of the Alcator C Tokamak," M.I.T. Doctoral Thesis (February 1982).

[7] Lipschultz, B., LaBombard, B., Manning, H. L., Terry, J. L., Knowlton, S., Marmer, E. S., Porkolab, M., Rice, J., Takase, Y., Texter, S., Wan, A., "Impurity Sources During Lower-Hybrid Heating on Alcator C," M.I.T. Plasma Fusion Center Report PFC/JA-85-45 (Dec. 1985).

[8] Manning, H. L., Terry, J. L., Lipschultz, B., LaBombard, B., Blackwell, B., Fiore, C., Foord, M., Marmer, E. S., Moody, J., Porkolab, M., Parker, R. R., Rice, J., "Impurity Generation During ICRF Heating Experiments on Alcator C," M.I.T. Plasma Fusion Center Report PFC/JA-86-17 (March 1986).

APPENDIX B

Edge Molecular and Atomic Processes

As the result of plasma-surface interactions and refueling, large amount of neutral atoms and molecules reside in the edge plasma region. These neutrals may be fuel particles from refueling and recycling, or impurities due to various plasma-surface interaction mechanisms. Thus the edge region is an extremely complex region dominated by not only plasma physics phenomena, but also strongly influenced by molecular and atomic processes. This appendix offers a brief review of some of the important molecular and atomic processes that may occur in the scrape-off layer of Alcator C. The processes reviewed include ionization and dissociation, charge exchange, and radiation.

B.1 Ionization and Dissociation

Both molecular and atomic hydrogens are present in the edge region. Most of the molecules reside near the wall and limiters while atoms populate the regions closer to the bulk plasma, away from any surface structures and gas puffing ports. Interactions with both types of neutral particles must be considered in modelling the edge region.

The ionization and dissociation processes are dominated by electron impact. In the energy range of interest (10 eV $\leq T_i, T_e \leq$ 10 keV) to fusion plasmas, the important electron impact processes include

$$e^- + H_2 \rightarrow H_2^+ + 2e^-, \quad \text{molecular ionization,} \tag{B.1}$$

$$e^- + H_2 \rightarrow 2H + e^-, \quad \text{molecular dissociation,} \tag{B.2}$$

$$e^- + H_2 \rightarrow H + H^+ + 2e^-, \quad \text{molecular dissociative ionization,} \tag{B.3}$$

$$e^- + H_2^+ \rightarrow 2H, \quad \text{molecular dissociative recombination,} \tag{B.4}$$

$$e^- + H_2^+ \rightarrow H + H^+ + e^-, \quad \text{molecular dissociation, and} \tag{B.5}$$

$$e^- + H \rightarrow H^+ + 2e^-, \quad \text{atomic ionization.} \tag{B.6}$$

These processes can also be induced by photons. However, the photon-induced cross-sections are much lower and the photon population is also much smaller than the electron density, so the electron impact processes are expected to dominate.

The reaction rate for a specific electron impact process j is defined as

$$\text{electron impact reaction rate} \equiv n_j\, n_e\, \langle \sigma\, v \rangle_j, \tag{B.7}$$

where n_e is the electron density, n_j is the density of the neutral in question, and $\langle \sigma v \rangle_j$ is the reaction rate. For $n_e \sim 1 \times 10^{13}$ cm^{-3}, the solid curves of figure B.1 plot the function $n_e \langle \sigma v \rangle$ for the 6 dominating electron impact processes[1] listed in equations (B.1) - (B.6).

In the edge plasma region, 5 eV $\leq T_e \leq$ 30 eV, where T_e is the electron temperature. In this temperature range, we found that the molecular processes are in general larger than the atomic process by factors ranging from 2 to 10. The overall reaction rate, however, depends on the concentrations of both molecular and atomic hydrogen. Due to their large reaction rates, molecular hydrogen

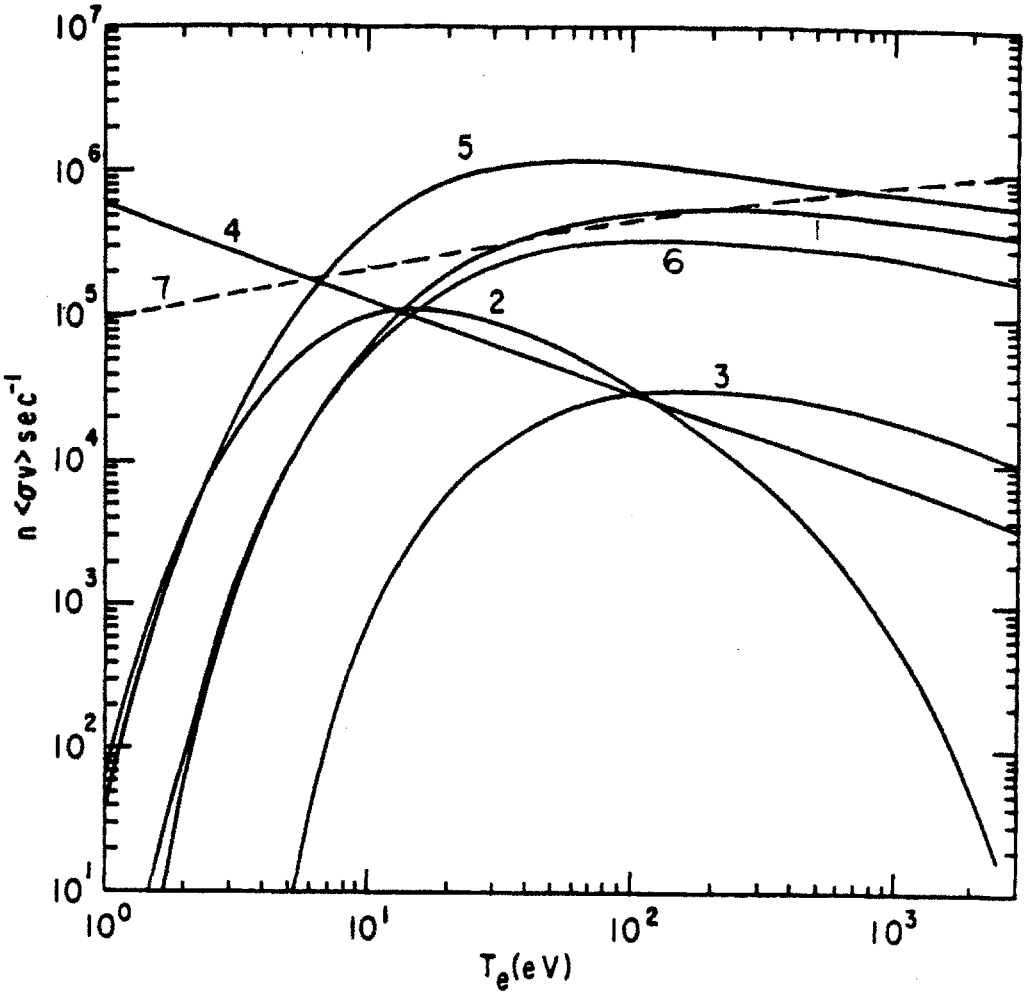

Figure B.1 Electron impact ionization, dissociation, and recombination reaction rates (solid lines), and charge exchange reaction rate for atomic hydrogen (dashed line).

is quickly ionized, and through dissociation and recombination processes, converts to atomic hydrogen.

Using a simple model, we can estimate the mean free path of a hydrogen molecule in the edge region of Alcator C. The effective mean free path, λ_{mfp}, is approximately equal to the molecular velocity $V_{molecule}$, divided by the function $n_e \langle \sigma v \rangle_j$

$$\lambda_{mfp} \sim \frac{V_{molecule}}{n_e \langle \sigma v \rangle_j}. \qquad (B.8)$$

Assuming a 3 eV molecule, and using the total reaction rate of the electron impact process on H_2, $\lambda_{mfp} \sim 4$ cm. As soon as the neutral hydrogen molecules are ionized, the dissociation and recombination processes take over and H_2^+'s are quickly converted to neutral and ionized hydrogen atoms.

The edge probe experiment described in this thesis is located approximately 67 cm away from the nearest limiter surface and 130 cm away from the main gas puffing port. The vacuum wall is located at a minor radius of approximately 19.3 cm. For the 16.5 cm limiter radius experiment, the impact of molecular hydrogen on the overall particle and energy balance could be significant. For the 12.5 cm and 11.5 cm limiter radii experiments, atomic processes should dominate as most of the molecules should already be ionized and dissociated into atomic forms.

Reference 2 tabulates all the reaction rates of the electron impact processes and fits them with a complex polynomial function. For electron impact ionization of atomic hydrogen

$$\langle \sigma v \rangle_{ioniz}(H) \sim \frac{(2.94 \times 10^{-5} T_e)^4}{1 + (0.099 T_e)^{3.1} + (0.059 T_e)^{4.25}}, \qquad (B.9)$$

where $\langle \sigma v \rangle_{ioniz}$ is in m^3/s and T_e is in eV. Once T_e, n_e, and n_H are known, the reaction rate of of this process can be easily calculated. In actual experiment, n_H is the only unknown. Therefore the ionization energy loss is also unknown.

B.2 Charge Exchange

When a charged particle collides with a neutral particle, the resonant electron could be transferred from one particle to the other; this process is defined as *charge exchange*. When the neutral energy is much different, usually lower, as compared with the ion energy, charge exchange processes may play a major role in the overall energy balance in the edge plasma region. The principal resonant charge exchange processes are

$$H_2^+ + H_2 \rightarrow H_2 + H_2^+, \qquad \text{molecular charge exchange, and,} \qquad (B.10)$$

$$H^+ + H \rightarrow H + H^+, \qquad \text{atomic charge exchange.} \qquad (B.11)$$

The dashed line of figure B.1 plots the function $n_i \langle \sigma v \rangle_{cx}$ for the atomic process assuming n_i, the proton density, is $\sim 1 \times 10^{13}$ cm^{-3}. The molecular resonant charge exchange rate is lower than its atomic counterpart by about an order of magnitude. Combined with lower molecular density, the process described in equation (B.10) can be neglected. For 10 eV $\leq T_i \leq$ 100 eV, the charge exchange reaction rate is tabulated in functional form in reference 3

$$\langle \sigma v \rangle_{cx}(H) \quad \sim \quad 1 \times 10^{-8} \; T_i^{0.36} \quad cm^3/s, \qquad (B.12)$$

where T_i is in eV.

The ion temperature, T_i, is typically 1-3 times T_e. In addition, the neutral energy is typically 2-3 eV. Therefore the charge exchange energy loss could play a major role in the ion energy balance if the atomic concentration is large enough.

B.3 Radiation

When a test charged particle interacts with the Coulomb field of a field particle, inelastic collisions with the field particle's atomic electrons or nucleus would produce a significant change in energy that may cause the production of photon, or *radiative* energy loss. In either collisional process, the rate of energy radiated is inversely proportional to powers of the mass of the test particle. Therefore, for $T_i \sim T_e$, electron interaction dominates the radiation phenomena[4,5].

B.3.1 Bremsstrahlung and Cyclotron Radiation

When an electron moves by the Coulomb field of the nucleus, it could experience an acceleration and as a result emit continuous radiation in the range of near infrared to X-ray wavelengths. This radiation is referred to as *bremsstrahlung radiation*[4,5]. The energy radiated per unit time classically is given by

$$Q_{brem} = \frac{dE_{rad}^{brem}}{dt} = \frac{2\,e^2\,Z\,a^2}{3\,c^3}, \qquad (B.13)$$

where c is the speed of light and a is the acceleration. For bremsstrahlung radiation, a is deduced from the Coulomb force. The total bremsstrahlung radiation, therefore, is equal to

$$Q_{brem} \simeq 5.35 \times 10{-}31\, n_e\, T_e^{\frac{1}{2}} \sum_j (n_j\, Z_j^2) \quad \mathrm{W/cm^3}, \qquad (B.14)$$

where the total radiative power is summed over all the ion species in the plasma. T_e is in keV and the densities are in cm^{-3}. From equation (B.14), bremsstrahlung radiation increases for higher electron temperature and density, and also for increasing ion density and its associated charge states.

When an electron gyrates about a magnetic field line, the centripetal acceleration replaces the the Coulomb field induced acceleration in equation (B.13) and *cyclotron radiation* in the infrared to microwave ranges would be emitted. The cyclotron radiation, unlike the bremsstrahlung, is emitted in discrete frequencies which are different harmonics of the cyclotron frequency (equation 2.70)). Electron cyclotron emission in the bulk plasma region can be used to infer central electron temperature[6] and the energy distribution function[7].

Cyclotron radiation can be reabsorbed by an optically thick plasma at the emitted cyclotron frequency. For an optically thin Maxwellian plasma, the total cyclotron radiation can be approximated as

$$Q_{cyc} \simeq 5 \times 10^{-32} n_e^2 T_e^2 \quad \mathrm{W/cm^3}. \qquad (B.15)$$

T_e and n_e have the same units as in equation (B.14).

B.3.2 Radiative Decay and Recombination

When a free electron Coulomb collides with a bound state electron, the loss of the kinetic energy is equal to the energy gained by the bound electron. Since each atom has fixed electronic energy levels the free electron cannot transfer any variable amount of energy to the bound electrons, but rather it must excite the atom to allow the bound state electron to jump to a specific excited level. Photons are emitted as the excited bound state electron *decays* to a lower energy level. A complete derivation of this problem can be found in reference 8.

Free electrons can also be captured by ions. Radiation is emitted as the result of this *recombination*. The total photon energy released per recombination event corresponds to the ionization potential plus the kinetic energy of the incident electron.

In the edge plasma region, large populations of bound state electrons are present in both the neutral hydrogens and neutral or partially stripped impurities. Both the bremsstrahlung and electron cyclotron radiations are small in comparison with the radiative decay and recombination processes.

In the edge region where the particles are lost quickly to the limiters through parallel convection, the edge plasma is seldom found in *coronal equilibrium* where the radiative decay and recombination processes along with the ionization and excitation processes must have sufficient time to establish an equilibrium. Nevertheless, coronal equilibrium models are still used frequently due to simple cross section calculation techniques. Post, Jensen, and co-workers[9] used a modified coronal equilibrium model and calculated the charge states and radiative cooling rates for different impurities in the range of $2 \leq Z \leq 92$. In their model, they accounted for all the radiation phenomena discussed in this section. For an impurity density, n_Z, the total radiated power from all ionization states can be expressed as

$$Q_{rad} = n_e n_Z P_Z, \qquad (B.16)$$

where P_Z is a cooling rate coefficient. Figure B.2 plots P_Z as a function of the electron temperature for carbon, oxygen, and molybdenum. We found that for carbon and oxygen, P_Z peaks at the T_e range of interest. For molybdenum, P_Z is at least an order of magnitude larger than the low-Z impurities. However, the concentration of molybdenum is also smaller than the low-Z impurities. Depending on the type of impurity and its concentration, radiation could play an important role in the overall electron energy balance in the edge plasma region.

The onset of Marfe[10], a poloidally asymmetric edge phenomenon where the inner portions of the plasma near the edge region become denser and cooler, is a possible manifestation of a thermal instability where the impurity radiation becomes the dominant energy loss mechanism in the edge plasma region.

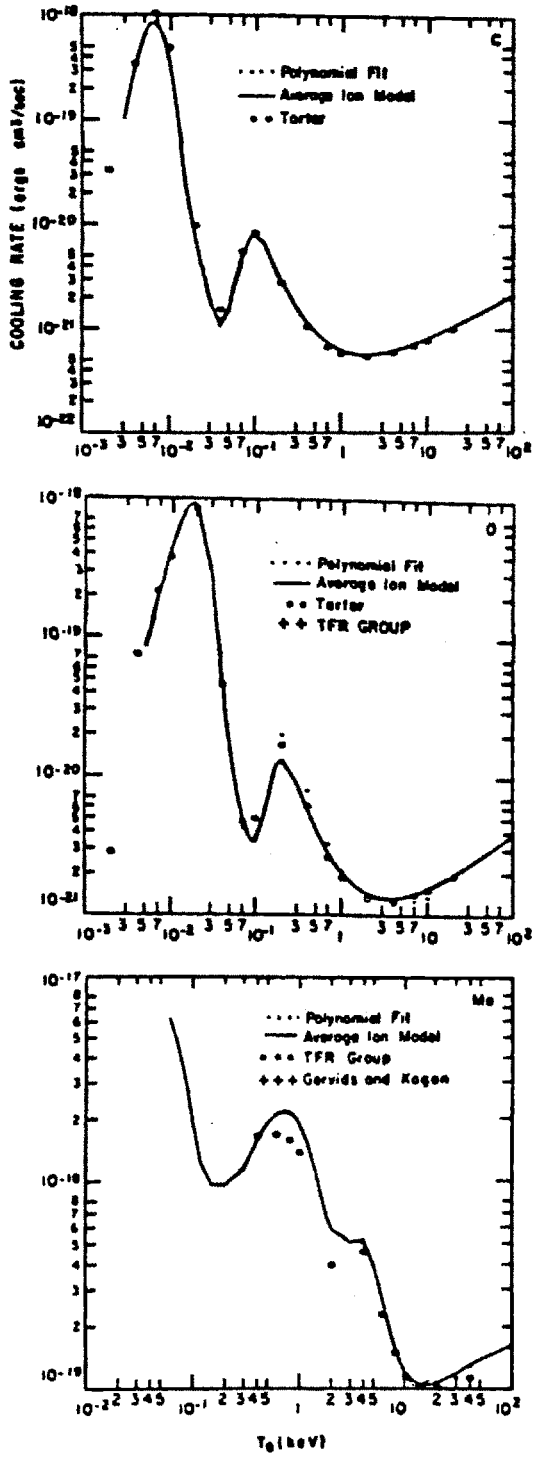

Figure B.2 Radiative cooling coefficient of carbon, oxygen, and molybdenum as a function of the electron temperature.

References

[1] Post, D. E., Heifetz, J., Petravic, M., "Models for Poloidal Divertors," Princeton Plasma Physics Lab. Report PPPL-1913 (July 1982).

[2] Gierszewski, P. J., "Plasma/Neutral Gas Transport in Divertors and Limiters," M.I.T. Doctoral Thesis (September 1983).

[3] Matthews, G. F., "The Measurement of Ion Temperature in Tokamak Edge Plasmas," Oxford Doctoral Thesis (1985).

[4] Yip, S., class lecture notes for M.I.T. course 22.111 – Nuclear Physics, September–December 1980.

[5] Kammash, T., Ch. 2 in Fusion Reactor Physics - Principles and Technology, Ann Arbor Science, Ann Arbor, Michigan (1975).

[6] Gomez, C., M.I.T. Doctoral Thesis (April 1986).

[7] Kato, K., M.I.T. Doctoral Thesis, in progress.

[8] Evans, R. D., The Atomic Nucleus, McGraw-Hill, New York (1955).

[9] Post, D. E., Jensen, R. U., Tarter, C. B., Grasberger, W. H., Lokke, W. A., "Steady State Radiative Cooling Rates for Low-Density, High-Temperature Plasma," *Atomic Data and Nuclear Tables* **20**, 397 (1977).

[10] Lipschultz, B., LaBombard, B., Marmer, E. S., Pickrell, M. M., Terry, J. L., Watterson, R., Wolfe, S. M., "MARFE : An Edge Plasma Phenomenon," *Nucl. Fusion* **24**, 977 (1984).

APPENDIX C

A 3-D Monte-Carlo, True-Orbit Particle Following Code

It is very difficult to predict the particle transmission characteristics in complicated geometries with strong electric and magnetic field variations, such as the environment inside a retarding-field energy analyzer (RFEA). Furthermore the particle energy can only be characterized by distribution functions. Particles residing in different velocity regions can exhibit very different transmission characteristics through different RFEA components. In order to show the viability of an RFEA-type of edge plasma diagnostic, it is important to study the influence of the analyzer geometry, applied electric and magnetic fields, and particle energetics on the collected distribution. To this purpose we developed a true-orbit particle-following code using the Monte-Carlo technique to generate particle velocity distributions.

The code handles the analysis of ion transmission only. Electrons have very small Larmor radii, ρ_e, as compared with the geometrical scale length of the RFEA. Thus we can treat the electron transmission problem like photon transmissions, without the magnetic field effect. The ion Larmor radius, ρ_i, on the other hand, is on the same order as the RFEA scale length. Therefore we must rely on this code to study the detailed ion transmission characteristics.

C.1 Code Principles and Assumptions

In a magnetized environment a charged particle travels along the magnetic field line in an helical motion. To solve for the particle motion we must first solve for the equation of states:

$$m_i \frac{\partial \underline{v}}{\partial t} = q_i \left(\underline{E} + \underline{v} \times \underline{B} \right), \text{ and} \qquad (C.1)$$

$$\frac{\partial \underline{x}}{\partial t} = \underline{v}, \qquad (C.2)$$

where q_i is the ion charge and m_i the mass; $\underline{E}$ is the external electric field and $\underline{B}$ the external magnetic field; $\underline{v}$ and $\underline{x}$ are the particle velocity and position vectors respectively.

The external electric and magnetic fields are prescribed analytically. For simplicity of calculation the direction parallel to the magnetic field is defined as the z direction. This is also the direction in which the RFEA is designed to diagnose. The direction parallel to the slit is the y direction, and the perpendicular to the slit is the x direction.

To simulate the RFEA geometry we installed 3-D spatial grids. The grid dimensions are variable to form "boxes" that can be designated to be either a solid or vacuum. These features allow us to model each component of the RFEA with the flexibility of varying the geometry in order to study the geometrical effects, for example, to study the influence of various slit geometries (section 3.2.1). The solids are assumed to be fully absorbent, i.e. the particles are immediately absorbed when they intersect a solid-vacuum interface.

An additional feature in modelling the mesh geometries is the inclusion of a "random" starting position for the mesh with respect to the slit position. Two random numbers generated at the start of the code allow the mesh position to shift in both the horizontal (y) and/or vertical (x) directions. This feature is incorporated since we have no knowledge of the exact mesh position with respect to the slit location. It is also needed to study the effect of mesh geometry and the Markoff behavior of the particles described in section 3.2.2.2.

C.2 Particle Tracing Model - Leap-Frog Technique

The numerical technique for solving equations C.1 and C.2 is different for each particle tracing model used. It is important to choose an accurate particle tracing model to minimize error build-up for every incremental time step. Section C.3 will be devoted to the error analysis of the technique. Another important criterion is the speed and efficiency of the technique as a particle is pushed forward one time step at a time.

Base on these criteria the Leap-Frog Method (LFM)[1] was chosen. LFM finds new velocity components at every half time step while calculating the displacements at every time step. The method solves for the following equation of states:

$$\underline{v}^{n} = \underline{v}^{n-\frac{1}{2}} + \frac{q_i \Delta t}{2 m_i}(\underline{E}^{n} + \underline{v}^{n-\frac{1}{2}} \times \underline{B}^{n}); \qquad (C.3)$$

$$\underline{v}^{n+\frac{1}{2}} = \underline{v}^{n-\frac{1}{2}} + \frac{q_i \Delta t}{m_i}(\underline{E}^{n} + \underline{v}^{n} \times \underline{B}^{n}); \qquad (C.4)$$

$$\underline{v}^{n+1} = \underline{v}^{n+\frac{1}{2}} + \frac{q_i \Delta t}{2 m_i}(\underline{E}^{n+1} + \underline{v}^{n+\frac{1}{2}} \times \underline{B}^{n+1}); \text{ and} \qquad (C.5)$$

$$\underline{x}^{n+1} = \underline{x}^{n} + \underline{v}^{n+\frac{1}{2}} \Delta t. \qquad (C.6)$$

Here Δt represents the time step for each calculation, and n represents a specific time step. Therefore at the beginning of each new time step the initial state of the particle is changed by substituting in $\underline{v}^{n+\frac{1}{2}}$ as the "previous" $\underline{v}^{n-\frac{1}{2}}$, and $\underline{x}^{n+1}$ as the previous $\underline{x}^{n}$.

If $\underline{x}^{n+1}$ falls within a solid grid boundary, the code is reversed such that a new Δt is calculated which would force the particle to intersect right on the solid-vacuum interface instead of somewhere inside the solid.

C.3 LFM Error Analysis

C.3.1 Perpendicular Component Error Analysis

We can monitor the accuracy of the LFM by monitoring the change in the ion Larmor radius (ρ_i) for each time step. ρ_i is defined as:

$$\rho_i = \frac{m_i v_\perp}{q_i B}, \tag{C.7}$$

$$\text{where } v_\perp^2 = v_x^2 + v_y^2, \text{ and} \tag{C.8}$$

$$B = |\underline{B}|. \tag{C.9}$$

Since the magnitude of B does not change in time and space (uniform magnetic field), and if there are no stray electric field present in the RFEA chamber (E_z only), the perpendicular velocity ($v_\perp$) should not change as the particle marches forward in time. Therefore the perpendicular error analysis is simply achieved by monitoring the change in the perpendicular energy, or equivalent to the change in $v_\perp^2$ for each time step. This monitor is defined by the ratio β, where

$$\beta = \frac{({v_\perp}^{n+1})^2}{({v_\perp}^n)^2}. \tag{C.10}$$

Using equations C.3-C.5, we can analytically calculate β:

$$\beta = 1 + \frac{1}{2}(\omega_i \Delta t)^2 + \frac{5}{16}(\omega_i \Delta t)^4 + \cdots. \tag{C.11}$$

ω_i is the ion gyrofrequency defined in equation 3.8. β calculates the incremental perpendicular energy for each time step Δt. The error in ρ_i is just equal to

$\sqrt{\beta}$. Since ω_i is fixed, Δt must be "small" such that the total error of the perpendicular component is small.

For typical Alcator C parameters (see Table 1.1) and a deuterium plasma, we found $\omega_i = 3.86 \times 10^8$ Hz. Choosing $\Delta t = 1 \times 10^{-11}$ s, we obtain $\sqrt{\beta} = 1.0000037$. For typical RFEA analysis an ion travels through the entire analyzer chamber in about 1×10^{-7} second. Therefore, even if we follow the particle through the entire analyzer region, the total error is approximately 3.8%. Since we routinely only follow the particles for a much shorter time when following them through only a single RFEA component, $\Delta t = 1 \times 10^{-11}$ second is quite adequate for our analysis.

C.3.2 Parallel Component Error Analysis

Parallel to the magnetic field there is no B dependence in the equation of motion and the velocity increment for each time step is given as

$$v_z^{n+1} = v_z^n + \frac{q_i \Delta t}{2 m_i}(E_z^n + E_z^{n+1}). \qquad (C.12)$$

Since there is no velocity dependence in equation C.12, there should be no parallel component error unless the presription of E_z as a function of space is not sufficiently accurate.

Inside the RFEA there is no region except at the mesh-vacuum interface where E_z would be changing drastically. This can be remedied by changing Δt at the interface such that the particle stops at the interface, thereby avoiding jumping across a boundary where E_z changes abruptly. Also in equation C.12 the applied E_z is taken to be the average of the E_z values at two spatial positions $\underline{x}^n$ and $\underline{x}^{n+1}$ in order to minimize the error in regions where E_z is changing.

C.4 Selecting Particle Launching Velocities

The RFEA measures the parallel energy distribution of the incoming ions and electrons. As shown in section 4.1, the parallel ion energy distribution is approximately equal to a Maxwellian shifted by a uniform energy corresponding to the potential difference between the slit and the plasma. In the perpendicular directions, the potential should not perturb the distribution functions and they should remain as Maxwellians.

To simulate a Maxwellian distribution we launch particles in a Monte- Carlo fashion using a random number generator and appropriate transforms[2]. There are several ways to generate a Gaussian distribution using random numbers, ξ_i. The simplest method is to follow the Central Limit Theorem. Statistics. The Theorem states that if the ξ_i are independent random numbers with mean $\bar{\xi}$ and variance $\sigma_\xi{}^2$, then

$$\eta = \sum_{i=1}^{n} \xi_i \qquad (C.13)$$

is normally distributed with mean $n\bar{\xi}$ and variance $n\sigma_\xi{}^2$. In practice, n, approximately 4 to 8 is adequate and the resulting distribution is primarily valid for $|v - v_{th}| < \frac{nv_{th}}{2}$. The transformation between normal distributions is

$$\frac{v_i - \bar{v}_i}{\sigma_v} = \frac{\eta - \bar{\eta}}{\sigma_\eta}, \qquad (C.14)$$

$$\text{where } \sigma_v = \sqrt{\frac{\kappa T_i}{m_i}}, \qquad (C.15)$$

$$\bar{\eta} = n\bar{\xi}, \text{ and} \qquad (C.16)$$

$$\sigma_\eta = \sqrt{n\sigma_\xi{}^2}. \qquad (C.17)$$

v_i is defined as the velocity of a particle in one direction. Defining $\bar{v}_i = 0$, we can obtain v_i by:

$$v_i = \frac{\sigma_v}{\sigma_\eta}\left(\sum_{i=1}^{n}\xi_i - n\bar{\xi}\right). \qquad (C.18)$$

Using $n = 5$ in equation C.18 we obtain:

$$v_i = 1.095\, v_{th}^i \left(\sum_{i=1}^{5}\xi_i - 2.5\right), \qquad (C.19)$$

$$\text{where } v_{th}^i = \sqrt{\frac{2\kappa T_i}{m_i}}. \qquad (C.20)$$

In the parallel direction the velocity distribution must be modified by including an energy shift. This can be easily modified by defining a new v_z

$$v_z^{new} = \sqrt{v_z^2 + \frac{2q_i V_{shift}}{m_i}}, \qquad (C.21)$$

where $q_i V_{shift}$ corresponds to the amount of energy picked up by a charged particle as it travels through a potential drop, i.e. like an ion accelerating through a negative sheath potential.

Figure C.1 displays a set of launched distributions for all three velocity components totaling 3000 particles. For this case, $T_i = 25\,\text{eV}$, $T_e = 15\,\text{eV}$, and the parallel velocity component is shifted by a sheath component $\sim 2.8\,T_e$ (see figure 2.2). Each velocity component is normalized by the ion thermal velocity. The open squares are the launched distributions obtained by finding the total number of particles launched within a finite velocity strip and normalized to the total launched particles. The solid lines are the theoretical fit expected for

each velocity component. Increasing the total number of launched particles improves the statistics, but at the cost of computer time. Typically 3000 particles, launched one at a time, are sufficiently accurate for our purpose.

C.5 Running the Code

Figure 3.5 shows a cross sectional view of the RFEA geometry. It is very expensive to launch a large number of particles and then follow them through the entire geometry, for example, from before the slit entrance to the point of collection. To minimize the computation time while retaining good statistics, it is necessary to examine the transmission characteristics of a single component of the RFEA. For example, one can look at only the slit transmission for different slit geometries or at different applied mesh potentials for mesh transmissions. The overall transmission characteristics can simply be multiplied together provided that the transmission characteristics of any single component would not depend on the transmission characteristics of any other RFEA component. Thus we can refer to each transmission as a Markoff process, i.e. the previous process is erased from the particle's "memory" and the next process is an entirely new and independent task.

It is necessary to use a step-by-step particle following code to keep track of the positions and velocities of each particle as they travel through the RFEA components. In doing so it is necessary for us to install a number of diagnostics within the code in order to examine the transmission characteristics. The crucial parameters that we monitor include the particle's initial and final positions and velocities. In doing so we can determine each velocity component's transmission characteristic in order to evaluate the RFEA's viability as a diagnostic to measure the parallel energy distribution function. These transmission coefficients for different components of the RFEA are further examined in section 3.2.

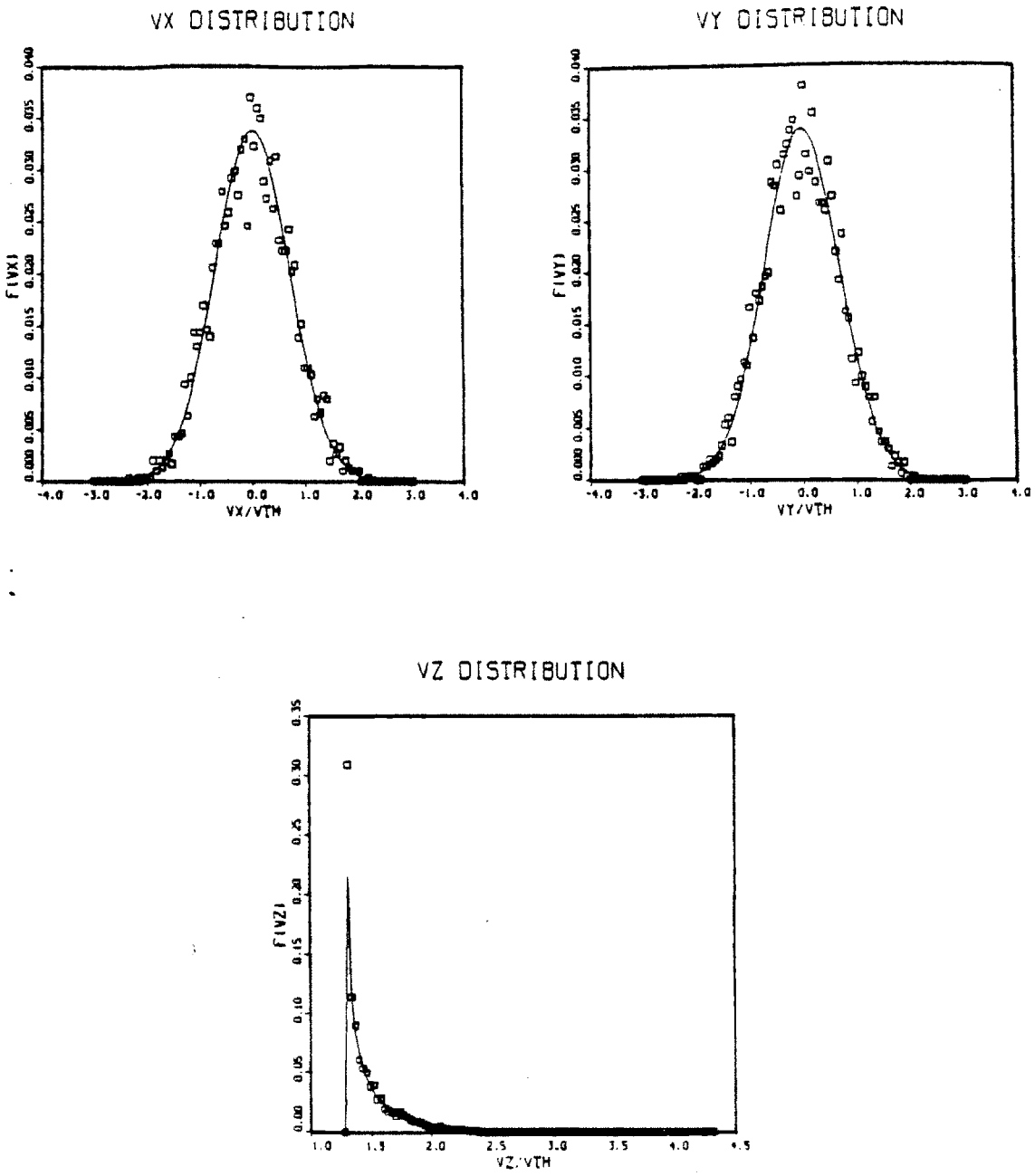

Figure C.1 The launched distribution functions of the v_x, v_y, and v_z velocity components (dots) and their theoretical Maxwellian fits (solid lines).

Another important parameter is the location of the particle when it is absorbed. This parameter allows us to determine whether the particles are absorbed on the front surface of a RFEA component or on the side of the component. The front incident particles are in general not a function of the magnetic field. If the particles absorbed on the sides of the component are assumed to be transmitted, the total transmission coefficient actually comes very close to the geometric transmission coefficient determined by the mesh dimensions. Thus the side absorbed particles reflect the magnetic effect of the particle transmission characteristic. This effect is tabulated and incorporated as the true ion transmission coefficient used in the analysis of the RFEA output, and it is described in more detail in section 4.1.

References

[1] Hewitt, D., private communication 1982.

[2] Gierszewski, P. J., "Plasma/Neutral Gas Transport in Divertors and Limiters", M.I.T. Doctoral Thesis, September 1983.